Master of Science Thesis

Drag Effect of Dented Surfaces in Turbulent Flows.

E. Vervoort

August 20, 2007

Faculty of Aerospace Engineering

Delft University of Technology

Drag Effect of Dented Surfaces in Turbulent Flows.

Master of Science Thesis

For obtaining the degree of Master of Science in Aerospace Engineering at Delft University of Technology

E. Vervoort

August 20, 2007

Faculty of Aerospace Engineering · Delft University of Technology

Delft University of Technology

Copyright © Aerospace Engineering, Delft University of Technology
All rights reserved.

DELFT UNIVERSITY OF TECHNOLOGY
DEPARTMENT OF
AERODYNAMICS

The undersigned hereby certify that they have read and recommend to the Faculty of Aerospace Engineering for acceptance the thesis entitled **“Drag Effect of Dented Surfaces in Turbulent Flows.”** by **E. Vervoort** in fulfillment of the requirements for the degree of **Master of Science**.

Dated: August 20, 2007

Supervisors:

Prof.dr.ir. P.G. Bakker

Dr.ir. L.L.M. Veldhuis

Dr.ir. B.W. van Oudheusden

Summary

The subject of this thesis is the development of a method for reducing drag in turbulent flows, by means of the application of dented surfaces. This drag changing phenomenon is called the Dented Surface Effect (DSE). DSE makes use of dent-like cavities in the surface of an object, which influence the fluid flow over the surface. The literature presently known about DSE is not clear about the drag reducing capabilities of DSE. Research confirming drag reduction exists, but there are also experiments which do not support the drag reducing capabilities of DSE. First goal of this research is confirming if DSE is able to reduce drag. This is done by trying to recreate the results found in an experiment [Vida, 2004] which claims to reduce drag. If indeed a drag reduction is encountered the most important objective of this thesis is to discover the drag-reducing mechanism of DSE, because it is not known why DSE does reduce drag. Last objective of this thesis is the optimization of the drag reduction.

This research on drag reduction is performed making use of Computational Fluid Dynamics (CFD) simulations, which calculate the flow over a dented surface, and by making use of windtunnel tests, where a model of the dented plate is subjected to a flow to measure the drag of the plate. Advantage of researching DSE with both these methods is that the results of both research methods can be compared. Also from a literature study it is known that drag reduction is only obtained in experimental research, numerical research has not resulted in drag reduction. But with these numerical research it is more easy to visualize the flow and, maybe, discover the phenomenon causing the drag reducing.

The CFD-simulations are used to test the influence of a number of geometrical dent parameters on the drag reduction. The depth of the dent is varied over a specific range. This results in two characteristic flow patterns which are developed. For shallow dented surfaces the flow will stay attached to the surface, increasing both the skinfriction and the pressure drag, thus increasing the total drag. For deep dents the flow separates in the dents. Here, in the dents, reversed flow causes the skinfriction to be negative. The pressure drag increases due to the separated flow. The total drag, which is the sum of the skinfriction and the pressure drag, is found to increase for all dent configurations tested.

The windtunnel tests do result in drag reduction, up to 13%, for a specific combination of dent configurations and flow conditions. Shallow dents are proven to reduce drag on the entire velocity regime, while very deep dents are found to always create an increasing drag. Dent with intermediate depths cause drag reduction for low velocites, while high velocities result is drag increase. Thus it is possible to reduce drag by means of DSE, which was not yet concluded from the CFD-simulations. The windtunnel tests also show that the pattern in which the dents are arranged is an important parameters to obtain drag reduction. The lateral distances between the dents is varied, which influences the interacting of the flow coming out of a dent with dents at downstream positions. Here

the windtunnel tests show differences in drag reduction.
The drag reduction capabilities of DSE are presumably caused by the decreasing skinfriction for separated flows, which if larger then the increased pressure drag, causes the total drag to decrease. But for all dent geometries numerically tested in this thesis the increasing pressure drag dominates the decreasing skinfriction. For a total drag reduction the pressure drag should be limited, which is presumed to happen if the flow exiting a dent interacts in a specific way with dents downstream. This interacting should be investigated in future research.

Samenvatting

Het onderwerp van deze afstudeeropdracht is het ontwikkelen van een methode om de weerstand van een object in turbulente stromingen te reduceren, door middel van het toepassen van gedeukte oppervlakken. Het fenomeen wat de weerstandsverlaging veroorzaakt wordt ook wel het "Dented Surface Effect" (DSE) genoemd. DSE maakt gebruik van deuken in oppervlakken, welke de stroming beïnvloeden. Uit gevonden literatuur blijkt dat het niet duidelijk is hoe DSE de weerstand verlaagd. Ook zijn er in het verleden experimenten geweest die de weerstand verlaging aangetoond hebben, maar er zijn ook onderzoeken bekend waarbij de weerstand reductie niet is aangetroffen. Het eerste doel van dit onderzoek is om aan te tonen dat het toepassen van DSE echt weerstandreductie tot gevolg heeft. Dit zal gedaan worden door het reproduceren van resultaten uit een experiment [Vida, 2004] waarbij weerstandsverlaging gevonden is. Wanneer er werkelijk weerstandreductie optreedt, is het volgende, en tevens belangrijkste, doel om te verklaren waarom de weerstand wordt verlaagd. Laatste doel van dit onderzoek is het optimaliseren van de weerstandreductie.

Dit onderzoek maakt gebruik van experimenten met behulp van Computational Fluid Dynamics (CFD) simulaties, hiermee wordt de stroming over een gedeukt oppervlak doorgerekend. Ook wordt gebruik gemaakt van windtunnel experimenten, waarbij de weerstand van de gedeukte plaat gemeten kan worden. Het voordeel van gebruik van beide methoden is dat ze onderling te vergelijken zijn en dat ze elkaar aan kunnen vullen. Vanuit de literatuur is bekend dat alle weerstandverlagingen zijn gevonden met behulp van windtunnelonderzoek. Voor zover bekend hebben CFD-simulaties nog nooit geresulteerd in weerstandsverlaging. Maar deze numerieke methoden zijn ideaal om de stroming in en om de deuk te visualiseren, wat gemakkelijk zou kunnen zijn bij het onderzoek.

De CFD-simulaties zijn gebruikt om de invloed van de geometrische parameters op de weerstandsverandering te testen. De diepte van de deuken is gevarieerd, wat er toe heeft geleid dat er twee soorten karakteristieke stromingen zijn gevonden. Voor ondiepe deuken zal de stroming blijven aanliggen aan het oppervlak, wat tot gevolg heeft dat zowel de wrijvingsweerstand als de drukweerstand toeneemt. Dus zal ook de totale weerstand, welke de som van de wrijvings- en drukweerstand is, zal toenemen. Voor diepe deuken zal de stroming loslaten van het oppervlak op de locaties waar de deuken geplaatst zijn, wat resulteert in een negatieve wrijvingsweerstand in de deuken. Echter zal, door de diepe deuken, de drukweerstand dusdanig toenemen dat de totale weerstand zal toenemen. Voor alle geteste deukconfiguraties is, bij de opgelegde stromingscondities, een weerstandsverhoging gevonden.

De windtunneltesten die gedaan zijn resulteren, voor specifieke combinaties van deukconfiguraties en stromingscondities, wel in een weerstandsreductie, tot 13%. Hier leveren de ondiepe deuken weerstandreductie op voor het gehele geteste snelheidsbereik, terwijl de diepe deuken voor het gehele snelheidsbereik weerstandverhoging tot gevolg hebben.

Deuken met tussenliggende diepte veroorzaken voor lage snelheden een weerstandverlaging, maar een weerstandsverhoging bij hogere snelheden. Hier is dus aangetoond dat het mogelijk is om met behulp van DSE de weerstand van een oppervlak te verlagen. Ook tonen de windtunneltesten aan dat het patroon waarin de deuken geplaatst worden ook van belang is voor de te bereiken weerstandsreductie. De zijdelingse afstand tussen de deuken is gevarieerd. Dit heeft invloed op de manier waarop de stroming komende uit een deuk zich verder stroomafwaarts zal gedragen.
De reductie van de totale weerstand, met behulp van DSE, wordt waarschijnlijk veroorzaakt door de negatieve bijdrage van de losgelaten stroming in de deuken aan de wrijvingsweerstand, waarbij de toename van de drukweerstand gelimiteerd is tot maximaal de afname van de wrijvingsweerstand. Hierdoor zal de totale weerstand toenemen. Maar, bij de numerieke testen die hier uitgevoerd zijn, is de toename van de drukweerstand te groot. De drukweerstand kan waarschijnlijk worden verkleind door een juiste combinatie van de stominggrootheden, de afmetingen van de deuken (o.a. diepte) en het patroon waarin de deuken geplaatst worden. De interactie hier tussen moet in de toekomst worden onderzocht.

Preface

This thesis describes the research done on the drag reduction in turbulent flows over dented surfaces, by means of both Computational Fluid Dynamic simulations and windtunnel tests. The research has been performed in the framework of a graduation project at the department of Aerodynamics, Faculty of Aerospace Engineering, Delft University of Technology.

Readers interested in the performed CFD-simulations are referred to chapter 3, for the windtunnel test the reader is referred to chapter 4.

I would like to extend my acknowledgments to Dr.ir. L.L.M. Veldhuis, for all the guidance during the course of this study, as well as to Prof.dr.ir. P.G. Bakker and Dr.ir. B.W. van Oudheusden for being part of the graduation committee. I also would like to express my gratitude to Mr. E.W. de Keizer, Mr. N. van Beek, Mr. P.J. Duyndam and Mr. F.J. Donker Duyvis for their support regarding the infrastructure of the project.
Last, but not least, I would like to thank both my parents, Antoon and Petra Vervoort, and my brother Christian, as well as my friends and my fellow-students for their support during the past one and a half years in which I performed this graduation thesis and during the rest of my study.

Delft, August 20, 2007

Erik Vervoort

Table of Contents

List of Figures

List of Tables

List of Symbols

Symbol	Description	Unit
C_D, $C_{D_{total}}$	Total drag coefficient	[-]
$C_{D_{calc.}}$	Simulated drag coefficient	[-]
C_{D_p}	Pressure drag coefficient	[-]
$C_{D_{theory}}$	Theoretical drag coefficient	[-]
C_{D_v}	Viscous drag coefficient	[-]
C_f	Skinfriction coefficient	[-]
$C_{L_{calc.}}$	Simulated lift coefficient	[-]
$C_{M_{calc.}}$	Simulated momentum coefficient	[-]
d_c	Diameter of the dent	[m]
D	Drag	[N]
F_1, F_2	Stretch factors	[-]
h_c	Depth of the dent	[m]
h_{first}	Height of the first cell	[m]
L	Reference length	[m]
M	Mach number	[-]
p_0	Total pressure	[N/m^2]
p_s	Static pressure	[N/m^2]
R_{ahp}	Main radius of the dent	[m]
R_s	Secondary radius of the dent	[m]
Re	Reynolds number	[-]
t	Time	[s]
t_1, t_2	Distances between two neighbouring dents	[m]
U	Free-stream velocity	[m/s]
x	coordinate in streamwise direction	[m]
x^+, y^+ and z^+	Dimensionless coordinates	[-]
y	coordinate perpendicular to the flow and to the surface	[m]
z	coordinate normal to the surface	[m]
γ	Specific heat ratio	[-]
δ_{99}	Boundary layer thickness	[m]
δ^*	Displacement thickness	[m]
μ	Viscosity	[kg/(m·s)]
ρ	Density of the fluid	[kg/m^3]
τ	Skinfriction force	[N]

Chapter 1

Introduction.

Drag reduction has been subject of study for a long time now. Less drag means less energy needed to propel the object through the flow, or with the same amount of energy it is possible to propel an object further, faster, with more payload or a combination of these three. So less drag will increase the efficiency of an object. This object can be a car, train of aircraft, which travel through air, as well as a ship or submarine, which travel through water. Also the transport of fluids and gases through pipelines benefits from a reduction of drag.
All kinds of methods have been developed to reduce drag. Some of the methods that reduce drag in turbulent flows are, for example, the application of grooved surfaces [Pulles, 1988], electromagnetics [Tillack and Morley, 1998] as well as the addition of micro-bubbles [Kodama et al., 2004] or polymer additives to the flow [Gyr and Bewersdorff, 1995]. All these methods reduce drag, but one is more effective than others. For example the addition of micro-bubbles or polymer additives reduces drag up to a maximum of 80%, while blowing/suction and the grooved surfaces only achieve a drag reduction of approximately 10%. Some methods are only applicable in liquid flows, while others are applicable in liquid as well as gasflows. More information about these methods is given in the literature study preceding this graduation thesis. [Vervoort, 2006]

The subject of this thesis is the development of an other method of reducing drag in turbulent flows. A short introduction of this method is given through an analysis of the title of this report, which is *"Drag Effect of Dented Surfaces in Turbulent Flows."*. To understand what this means, the three major terms from this title need to be clarified. First of all: *Drag Effect.* This term implies that the drag of an object in a flow is changed. The term: *Turbulent Flows* implies that the flow around or over an object not laminar, but turbulent. In other words: the flow moves not smooth and orderly, but fluctuating and disorderly. Laminar and turbulent flows behave different near objects and surfaces. The research done by others [Vida, 2004] suggests that the drag reducing phenomenon only occurs when the flow is turbulent. It is not mentioned why only drag of turbulent flow is reduced. Last, and most important, the term *Dented Surfaces* will be explained: The flow together with the dented surface creates a phenomenon which is called Dented Surface Effect (DSE). DSE is a technology which is presumed to have drag reducing capabilities. DSE makes use of dent-like cavities in the surface of an object, which influence the fluid flow over the surface. How these dented surfaces achieves a drag reduction is presently unknown, mainly because the little research done on this

subject technology is kept confidential. Thus it will be the major goal of this thesis to discover the drag-reducing mechanism of DSE.
The drag reducing phenomenon was first encountered at the Kurchatov Nuclear Energy Institute in Russia during the period 1978-1984 [Lashkov and Samoilova, 2002]. Studies performed here were aimed at the enhancement of the heat transfer in the cooling processes in nuclear environments. Dents were produced in smooth cooling surfaces which proved to increase the heat exchange. A side effect of this technique was found in the behaviour of the drag of the cooling agent. Although the dents produced some kind of vortices, the drag was found to be constant compared to the situation with smooth surfaces.

An article in Der Spiegel 14/2004 [Wüst, 2004] presents a phenomenon similar to DSE, in this article the drag reducing technique is called Tornado-Like-Technology (TLT). It is stated that dents in a surface of an object will generate tornado-like vortices that reduces the drag of the object. These vortices are small tornadoes which are causing the drag reducing effect. These tornadoes originate from the dents, and then they jump from dent to dent. In this way they act like a layer of ball bearings between the surface and the airflow further from the wall. This explanation, given by Nikolaus Vida, who patented TLT, in the article in Der Spiegel has not got any scientific background. Research on DSE (or TLT) is needed to clarify how drag is reduced. In the patent on TLT [Vida, 2004] percentages of drag reduction up to 34% are mentioned. Flow parameters are mentioned only briefly. The Reynolds number of the flow is in the order of 10^6 and flow velocities tested are 3, 5 and 7m/s. Other flow parameters are not mentioned. This Reynolds number is low compared to Reynolds numbers of airplanes, trains or cars for which TLT is supposed to reduce drag. The same holds for the velocities at which the tests are done. The reference length used in these tests is the length of the dented plate, this is the reason why in this thesis the reference length will be the length of the plate. The dimensions of the dents are described in detail in Section 2.3, Appendix A.1 and the patent by Vida [Vida, 2004].
Also in the article the research done by DLR, the German aerospace research centre, on TLT, is mentioned. Nothing is mentioned about the geometry and the flow (dent depth, velocities, Reynolds numbers, etc.), but they claim to have found a maximum drag reduction of 16-17%, which could mean a revolution in the aerodynamics of turbulent flows. It can change the design of ships, cars and aircraft completely. Again no explanation is given on how drag is reduced, but it is mentioned that the dents seem to generate some kind of secondary flow structure, which has a decreasing effect on the drag.

1.1 Drag Reduction of Golfballs.

A remark has to be made about the dents present on golfballs. While the golfball dents looks similar to the dents used for the phenomenon researched in this thesis and both dents cause drag reduction, the physical behaviour of the flow is completely different. This will be illustrated here.
If golfballs were smooth, the laminar boundary layer would separate rapidly, creating a very large wake behind the golfball. (see figure 1.1) This large wake creates a high pressure drag. The golfball uses the dents to transition the laminar boundary layer to a turbulent boundary layer. This turbulent boundary layer will separate later, forming a

smaller wake than the laminar boundary layer does. Thus the pressure drag decreases. The friction drag will increase due to the transition of the boundary layer. But since this increase in friction drag will be smaller than the decrease in pressure drag, the total drag will decrease significantly. The decrease of the total drag results in dented golfballs that fly over longer distances than smooth golfballs.

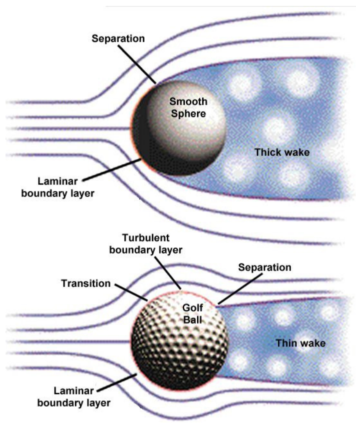

Figure 1.1: Wake behind a golfball.

So the two most important features in drag reduction of a golfball are the transition of the boundary layer and the size of the wake. This is the main difference with the phenomenon investigated in this thesis. It is intended to obtained drag reduction on all kinds of shapes and (flat) surfaces. Also the phenomenon requires a turbulent boundary layer, so the boundary layer is already transitioned from laminar to turbulent.
This makes the DSE phenomenon totally different from the drag reduction of golfballs.

1.2 Research in this Thesis.

This research on drag reduction by DSE consists of two parts. In the first part Computational Fluid Dynamics (CFD) calculations are performed to get further insight in the behaviour of the flow. In the second part of the thesis verification of the possible drag reduction is obtained from windtunnel tests.
The research will cover two main subjects. Firstly: recreation of the results already discovered. These results are obtained from a patent on TLT [Vida, 2004]. A summary of this patent is added to this report as appendix A.1. Secondly: optimization of the drag reduction. DSE uses dents in the surfaces of an object in a flow, to reduce drag. The geometry of these dents is very simple, and it is not probable that this configuration is the most effective one for reducing drag. So optimization of the dent geometry and other parameters, like dent spacing, is the ultimate goal of this thesis.

1.3 Setup of this Report.

The next chapter, chapter 2, will give the problem description, which presents the goals of this thesis. Also the starting point of the research will be presented together with details of the dent geometry. Chapter 3 presents the Computational Fluid Dynamics simulations done during the thesis. The setup and the results of the windtunnel tests are presented in chapter 4. The simulations and windtunnel tests are evaluated in chapter 5, here also an idea is given to the drag reducing principle of DSE and suggestions are made concerning future research on DSE. The report contains the conclusions and recommendations of the research (Chapter 6). Last part of the report contain the appendices. These contain elaborate information about the simulations and windtunnel tests as well as other relevant information concerning this thesis.

Chapter 2

Problem Description.

2.1 Goal of the Research.

An idea how DSE could work is given in the article in Der Spiegel [Wüst, 2004]. Here it is suggested that tornado-like structures are created close to the wall, which act like a kind of bearing to the flow far from the wall. This idea however is not supported by any scientific evidence. In the patent [Vida, 2004] mentioned before, no reason is given why DISA reduces the drag.
The goal of this research is to investigate the influence of dents in the surface of an object on the drag of the object, while the object is subjected to a turbulent flow. The research, done by CFD-simulations and windtunnel tests, is intended to discover the aerodynamic phenomenon of DSE which reduces the drag. And then give a scientific explanation on why and how this phenomenon occurs.
The ultimate goal of this research is to optimize the drag reduction. This is done by investigating which parameters of the dent influence the drag reduction in such a way the reduction can be maximized. For example, the cross-section of the dent and the pattern in which the dents are placed on the surface of the object, are two of these parameters which are to be optimized.

2.2 Starting Point of the Research.

First the research on DSE will be concentrated on the duplication and verification of the TLT-results mentioned in the patent [Vida, 2004]. When the drag reduction matches those in the patent it should be possible to clarify why the drag is reduced (or how DSE/TLT reduces the drag). When the aerodynamic phenomenon that occur are known, the technique can be used to optimize the drag reduction by changing the parameters of the dent geometry or the pattern at which the dents are placed on the object.
Two methods are used for this research. First numerical simulation or Computational Fluid Dynamics (CFD) is used to simulate air flowing over a flat plate containing dents. CFD is useful, because it has the ability of testing all kind of geometries without having to manufacture them. Also with CFD it is possible to investigate the flow without interfering the fluid flow. From the results out of the CFD-calculations a choice is made to which geometry should be tested in the windtunnel. The advantage of windtunnel testing is that once a model is manufactured it is fairly easy to do a lot of tests in a short time, compared to CFD.

2.3 Details of the Dent Geometry.

In the patent about TLT [Vida, 2004] two dents are presented, which are shown in section A.1. The first dent has a relative simple geometry, which has a single main radius (R_{ahp}). The second dent has a more complex geometry, with a main curvature consisting out of three radii. This second dent is not used in this thesis, due to lack of time. Test results given in the patent are obtained with the first dent. Thus it is preferred to start with this dent configuration. Here a problem arises.
The geometry of the dent is described with formulas and parameters. But the given values can not be correct as will be shown here. In figure 2.1 and figure 2.2 the shape parameters are drawn.

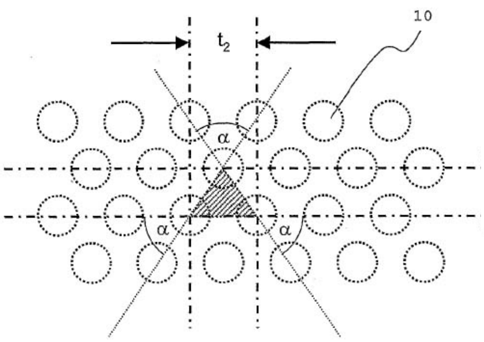

Figure 2.1: Schematic distribution of dents.

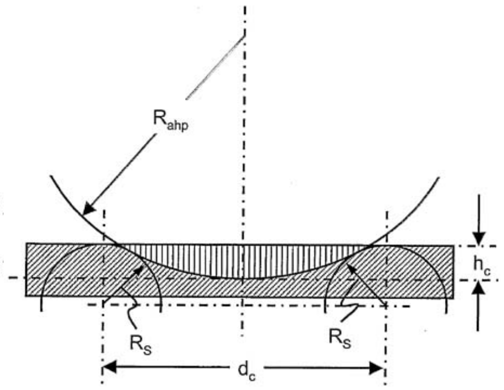

Figure 2.2: Cross-section of dent.

The given values for the parameters are:

$$t_1 = 28.6mm, \qquad t_2 = 33.0mm, \qquad d_c = 20.0mm,$$

$$h_c = 3.0mm, \qquad R_{ahp} = 68.2mm, \qquad R_s = 5.0mm$$

or scaled up or down maintaining essentially the ratios:

$$\frac{t_1}{t_2} = \frac{28.6}{33.0} \approx 0.867, \qquad \frac{R_{ahp}}{R_s} = \frac{68.2}{5.0} = 13.64, \qquad \frac{R_s}{h_c} = \frac{5.0}{3.0} \approx 1.67$$

Now when these numbers are used to draw the dent, then it becomes clear that figure 2.2 can not be correct. In figure 2.3 all the prescribed dimensions are used to draw the dent. As can be seen from this figure, no correct cross-section is created. It is clear that the slope of the cross-section of the dent is not continuous (The black line in figure 2.3 represents the cross-section of the dent.) Three of the parameters (d_c, h_c and R_{ahp}) are interfering with each other.
One of these three parameters has to be altered. The dent diameter d_c is held constant, at 20.0mm, as suggested in the patent. This is done because d_c is the parameter that influences the percentage of coverage by the dent. The coverage should be, according to the patent, about 0.3. In figure 2.4 the dent depth h_c is, as suggested, 3.0mm, now the main dent radius R_{ahp} should be 13.167mm to create a continuous cross-section for the

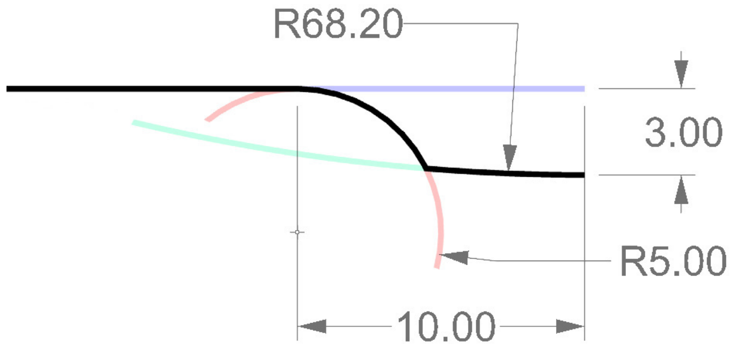

Figure 2.3: Cross-section of dent with suggested parameters.

dent. Another possibility is to hold the dent radius, at 68.2mm, as suggested, then the dent depth should be 0.686mm to create a continuous cross-section. This is shown in Figure 2.5.

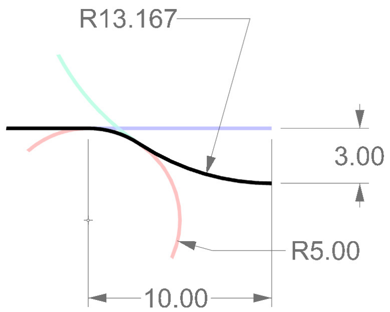

Figure 2.4: Cross-section of dent with suggested depth.

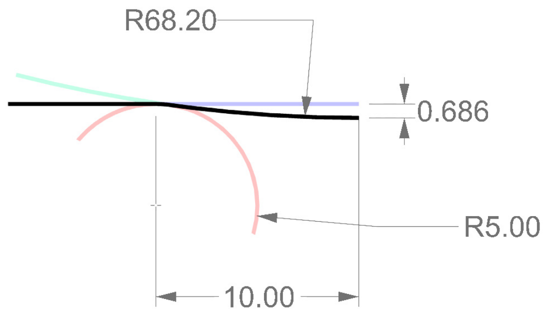

Figure 2.5: Cross-section of dent with suggested radius.

Since it is not clear which of these two suggested cross-sections is correct, it is obvious to test both suggested cross-sections, to see if one or maybe even both cross-sections have drag reducing capabilities.

2.4 Prognosis of the Flow though a Dent.

Here a prognosis will be given of the flow through the cross-section of a dent, it is possible that different flow patterns occur than predicted here.
The flat plate flow, see figure 2.6, the flow is attached to the wall. The skinfriction depends on the x-coordinate, the skinfriction being constant for a fully developed steady flow. No pressure gradient should be present, which is to be realized by correct dimensions and boundary conditions of the domain, otherwise the skinfriction will depend on the x-coordinate.
For shallow dents the flow will follow the contours of the dents, creating a skinfriction distribution which is influenced by the presence of the dents. The skinfriction will

decrease where the flow enters the dent (denoted by "τ^-" in figure 2.6), because the flow is diverging from the wall. The skinfriction in the rear part of the dent experiences a converging flow, which will increase the skinfriction in this part of the dent, denoted by "τ^+" in figure 2.6. It seems unlikely that the sum of the skinfriction in the total dent will be smaller than the skinfriction drag of the flat plate. The dents in the surface create pressure drag. Figure 2.7 (A) shows the pressure vector on a flat plate, which is perpendicular to the surface. For a flat plate this vector is directed vertically, having no horizontal component, thus creating no pressure drag. When a dent is present there will be pressure drag. In the forward part of the dent (figure 2.7 (B)), the pressure vector does have a horizontal component, pointing in upstream direction. This vector creates negative pressure drag. The rearward part is subjected to a pressure vector with a downstream component, creating positive pressure drag. The total pressure drag, the sum of both the pressure drag in the forward and rearward part of the dent, will probably be positive pressure drag, thus creating an increase of total drag.

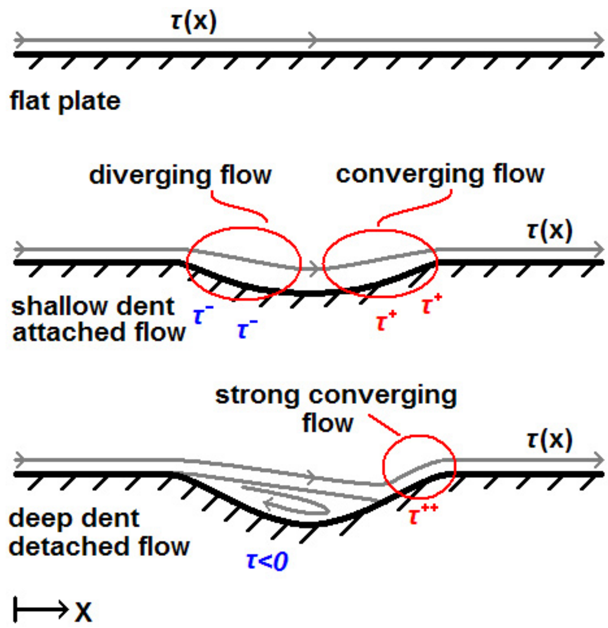

Figure 2.6: Expected change of skinfriction in a 2D-flow through the dents.

For deep dents the cross-section is more curved, possibly creating the flow to separate from the surface, causing an area where the flow rotates or reverses, like shown in the bottom of figure 2.6. This is also suggested in the patent [Vida, 2004], where this phenomenon is called TLT. The reversed flow creates negative skinfriction, which is beneficial for the total drag of the plate. Just after the separated area an area is present with high skinfriction due to the converging pathlines of the flow here. The pressure drag will increase due to the separated flow and attached flow in the rearward part of the dent. It is arguable if the reduction in skinfriction will be larger than the increase in drag due to pressure drag increase. Maybe a certain combination of geometrical parameters combined with the correct flow conditions cause the total drag to reduce. The dents with separated flow is more likely to reduce drag, because of the negative skinfriction present in the dent.

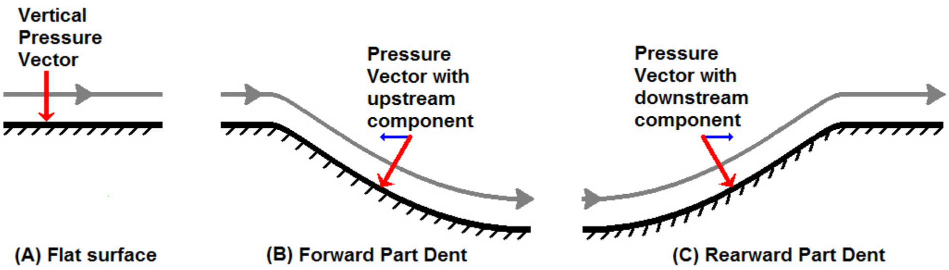

Figure 2.7: Expected change of pressure drag for three types of geometries.

This prognosis is given for a two dimensional situation. For three dimensional situations the flow can be different, especially for the deep dent, with separation. How this three dimensional separation area, with possible vortices present, evolves is hard to predict.

Chapter 3

DSE in Computational Fluid Dynamics Tests.

3.1 Introduction.

In this chapter the Computational Fluid Dynamic-simulations are discussed. The CFD-process consists of a couple of different steps. First the geometry of the problem is defined. Secondly, the volume occupied by the fluid is divided into discrete cells, which altogether form the mesh. Then the physical model, begin conditions and boundary conditions are defined. Next step is to do the actual simulation; this involves solving the flow-equations iteratively. Last step of the CFD-process is to post-process the results of the simulation.
In section 3.2, 3.3 and 3.4 the preparations of the geometry and physical model are explained. In section 3.5 the actual simulations are discussed.

3.2 Geometry of the Problem.

The geometry of the problem consists out of a flat or dented plate and a three dimensional flow-domain. The plates and the flow-domain are modeled with the CAD-program Rhinoceros version 3.0.

3.2.1 Flow-Domain.

The calculation domain is chosen such that its dimensions do not disturb the flow and small enough to limit the calculation time to a reasonable length. The domain is depicted in figure 3.1.
The height of the domain is not limited by the calculation time, because the height of the cells grow as the cells are further placed from the wall. The majority of the cells will be placed in the vicinity of the boundary layer, next to the wall. The limiting factor for the height of the domain is the fact that the pressure gradient in the domain should be zero. The boundary layer causes the flow to have a displacement thickness, which can cause a non-zero pressure gradient if the height of the domain is not large enough. The velocity of the simulations will range from 5.0m/s to 50.0m/s. These velocities are chosen because 5.0m/s is the velocity at which a drag reduction is found in the patent [Vida, 2004] and 50.0m/s is a typical velocity which corresponds with the

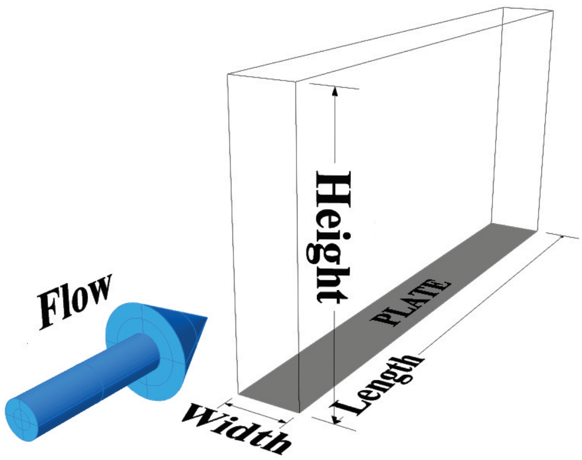

Figure 3.1: Flow-domain.

velocity of trains and fast cars. Probably the dimensions of the drag reducing geometry is depending on the flow conditions. Also the change of velocity is needed to test the behaviour of the phenomenon for varying in Reynolds numbers.

The displacement thicknesses of both these velocities are calculated here. First the Reynolds number and boundary layer thickness are calculated, they are required when calculating the displacement thickness. The reference length used here is 0.50m, which is the length of the plate.

For 5.0m/s:

$$\begin{aligned} Re_L &= \frac{\rho U L}{\mu} = \frac{1.225 \cdot 5.0 \cdot 0.5}{1.7894 \cdot 10^{-5}} \approx 1.71 \cdot 10^5 \\ \delta_{99} &= 0.16L \cdot Re_L^{-\frac{1}{7}} = 0.16 \cdot 0.5 \cdot (1.71 \cdot 10^5)^{-\frac{1}{7}} \approx 0.0143m \\ \delta^* &= \int_0^{\delta_{99}} \left(1 - \frac{u(y)}{u_e}\right) dy = \int_0^{\delta_{99}} \left(1 - \frac{1}{u_e}\left(\frac{y}{d}\right)^{-\frac{1}{7}}\right) dy = \delta_{99}\left(1 - \frac{7}{8u_e}\right) \approx \\ &\approx 0.0143\left(1 - \frac{7}{8 \cdot 5.0}\right) \approx 0.0118m \end{aligned}$$

For 50.0m/s:

$$\begin{aligned} Re_L &= \frac{\rho U L}{\mu} = \frac{1.225 \cdot 50.0 \cdot 0.5}{1.7894 \cdot 10^{-5}} \approx 1.71 \cdot 10^6 \\ \delta_{99} &= 0.16L \cdot Re_L^{-\frac{1}{7}} = 0.16 \cdot 0.5 \cdot (1.71 \cdot 10^6)^{-\frac{1}{7}} \approx 0.0103m \\ \delta^* &= \int_0^{\delta_{99}} \left(1 - \frac{u(y)}{u_e}\right) dy = \delta_{99}\left(1 - \frac{7}{8u_e}\right) \approx 0.0103\left(1 - \frac{7}{8 \cdot 50.0}\right) \approx 0.0101m \end{aligned}$$

So the thickest displacement thickness is 0.0118m and occurs at a velocity of 5.0m/s. The height of the domain needs the have a dimension which is large enough to exclude that the displacement thickness has influence on the pressure gradient. Also the height must be

sufficiently large to include all features that are caused by the dents. A height of 0.25m is selected because this probably will be large enough considering the two conditions mentioned before. If, by accident, the height would be insufficiently large, the height must be increased. In section 3.2.2 this is checked.
The width of the domain is important with respect to the calculation time, because, unlike the height, when the width is increased the number of cells will increase linearly. The width needs to be as small as possible, without interfering the flow to develop in a way it should. The geometry of the plate is symmetric and the smallest symmetric section of the plate is 0.0286m. This is very small compared to the height and length of the plate. Therefore two times the smallest symmetric part is used, which results in a width of 0.0572m. Before the dented plates are used, a series of simulations with only flat plates will be done, to establish the correct physical models. Here a width of 0.050m is used. The width of the domain is correctly chosen, this will appear out of the simulations in section 3.5.1 and 3.5.2.
The length of the domain is set at 0.500m, this length will give the flow space to develop. A larger length is desired, but due to limitations on the simulation time this is not possible.

3.2.2 Flat and Dented Plates

The flat plate has a very simple geometry, it is flat and square with length and width as defined in the previous section. The geometry of the dented plate needs some more explanation. A lot of parameters can be varied in order to make all kinds of different dented plates and to determine the effect of each parameter on the change of drag. It is not possible to make simulations with all combinations of variable parameters, because computation time is limited. So some parameters are fixed. In section 2.3 the geometry of the dent is explained. There also the following dent-parameters are depicted: α, t_1, t_2, d_c, h_c, R_{ahp} and R_s. Since the geometry is incorrect with respect to the depth of the dent, the depth will be the parameter that will be varied first to figure out the correct depth. Three of the parameters are related to the placement of the dents, these are α, t_1, t_2. These three will be fixed at the values used in the patent [Vida, 2004], so $\alpha = 60°$, $t_1 = 28.6$mm, $t_2 = 33.0$mm, thus the ratio $\frac{t_1}{t_2} = \frac{28.6}{33.0} = \frac{13}{15} \approx 0.867$. This results in a fixed position of the dents. Also the diameter of the dents will be fixed at $d_c = 20.0$mm. Now three parameters remain, which together determine the depth and curvature of the dent. These will be varied in a way seven different dents are formed, all with different depths. The values of these parameters are given in table 3.1.

	Variables [mm]			Ratios	
Name	h_c	R_{ahp}	R_s	$\frac{R_{ahp}}{R_s}$	$\frac{R_s}{h_c}$
$Dent_1$	0.343	136.3	10.0	13.63	29.15
$Dent_2$	0.686	68.2	5.0	13.64	7.23
$Dent_3$	1.843	25.0	3.1	8.14	1.67
$Dent_4$	1.988	22.8	3.3	6.88	1.67
$Dent_5$	2.133	21.0	3.6	5.92	1.67
$Dent_6$	2.422	17.9	4.0	4.43	1.67
$Dent_7$	3.000	13.2	5.0	2.63	1.67

Table 3.1: Variable parameters of the different dents tested with CFD.

A short explanation of why these dents are tested is given here: Dent_2 and Dent_7 are

the two dents suggested in section 2.3, figure 2.4 and figure 2.5. As mentioned before in section 2.3 it is not possible to use the dent geometry described in the patent, because of its physical incorrectness.
Dent_1 is produced to check the behaviour of the flow when the dents are even more shallow than Dent_2 (h_{c_2}=0.686mm). The depth of the dent is changed into $h_{c_1} = \frac{1}{2}h_{c_2} =$ 0.343mm. Dent_3, Dent_4, Dent_5 and Dent_6 are deducted from Dent_2 and Dent_7. During the first simulations in which Dent_2 and Dent_7 were used, an aerodynamic effect occurred, from which it was clear that Dent_2 and Dent_7 behaved fundamentally different. To investigate this effect, dents were made with intermediate depths, these were Dent_3 ($h_{c_3} = \frac{1}{2}(h_{c_2} + h_{c_7}) = 1.843$mm), Dent_6 ($h_{c_6} = \frac{1}{2}(h_{c_3} + h_{c_7}) = 2.422$mm), Dent_5 ($h_{c_5} = \frac{1}{2}(h_{c_3} + h_{c_6}) = 2.133$mm) and Dent_4 ($h_{c_4} = \frac{1}{2}(h_{c_3} + h_{c_5}) = 1.988$mm). For these dents the ratio $\frac{R_s}{h_c} = 1.67$ is kept constant, changing R_s to the value prescribed by $1.67h_c$. The main radius is changed in a way it is tangent to R_s and horizontal in the middle of the dent.
An example of a dented plate is given in figure 3.2.

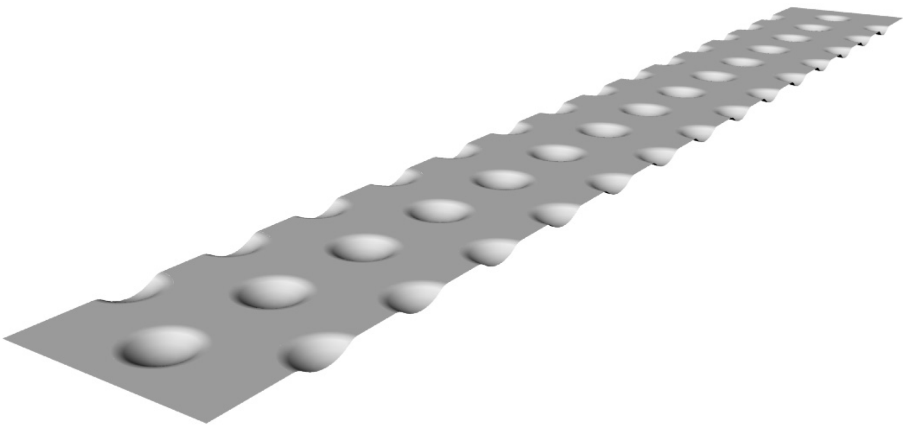

Figure 3.2: Example of dented plate; Depth of dents here is 3.000mm.

3.3 Meshes Used in the Simulations.

The simulations are done with Fluent, a CFD-package which makes use of the finite volume method on a mesh covering the flow-domain. In this thesis, the meshes are made with two grid generators, GAMBIT and Gridgen v15. GAMBIT was used in the first simulations, but due to the lack of control of GAMBIT on the accuracy of the mesh near the surface when using very small elements, Gridgen was used.
Fluent can handle unstructured (triangle-based), structured (square-based) grids and hexagonal meshes. The hexagonal mesh is a relatively new mesh-method. This method is not considered for this thesis, since the available meshing programs are not able to produce hexagonal meshes. Both unstructured and structured grids have advantages and disadvantages. Advantage of the unstructured grid is the possibility of meshing complex geometries. Here the geometry of the plate is simple, which is a requirement for using a structured grid. Also with structured grids the simulations tend to converge faster, especially if the grid is placed in such a way the main direction of the flow is tangent to

the gridcells. So in the simulations done here a structured grid is used.

3.3.1 Grid Resolution.

The simulated flow needs to be turbulent. This turbulent flow requires some special attention here. Not only the no-slip condition affects the flow near the wall, but also by the viscous damping near the wall, which causes a reduction in tangential velocity fluctuations, and by the kinematic blocking, which causes the normal velocities to decrease. Further away from the wall, but still in the near-wall region, the turbulence is increased by the large gradients of the mean velocity.
Fluent can use a number of different turbulence models. The κ-ϵ models, the Reynolds Stress Model (RSM) and the Large Eddy Simulation model (LES) are designed for turbulent core flows. These models need a modification to the mesh to be able to model near-wall flows. The Spalart-Allmaras model and the κ-ω model are designed to be applied throughout the boundary layer, provided the mesh resolution near the wall is sufficient.

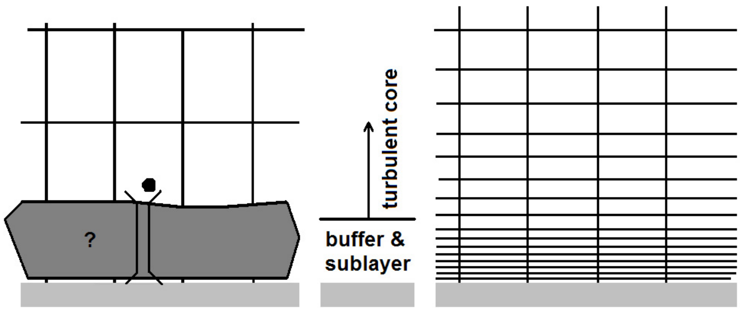

Figure 3.3: Near-Wall Treatment in Fluent.

Fluent includes two methods to model the near-wall region: the Wall-Function Modeling and the Near Wall Resolving. These methods are explained thoroughly in the Fluent User's Guide, [Fluent Inc., 2005b]. Here the most important features will be mentioned. The first method makes use of semi-empirical formulas, called Wall-Functions, which are used to model the turbulence in the near-wall region. In most high-Reynolds number flows, this method saves substantially computational resources, because of the modeling near the wall, which can result in a relative coarse mesh near the wall. Also this method is popular because it is reasonably accurate. An disadvantage of this method is its behaviour when low Reynolds numbers and/or near-wall effects are present in the flow, which is important because this research is focused on near-wall flows. Requirement for the mesh are: $x^+{\sim}100$-600, $y^+ \sim 100$-300, $z^+{\sim}20$-150. x^+, y^+ and z^+ are dimensionless coordinates, which are defined as:

$$x^+ = \frac{\rho U_\tau x}{\mu}$$
$$y^+ = \frac{\rho U_\tau y}{\mu}$$
$$z^+ = \frac{\rho U_\tau z}{\mu}$$

x being the direction of the flow, y being the direction perpendicular to the flow and parallel to the plate and z being the direction perpendicular to the plate, see figure 3.4. A schematic picture of this Wall-Function Method is depicted left in figure 3.3, on the right in this picture the other method, the Near-Wall Approach, is represented. This method solves all the turbulence effects in the flow, even near the wall. The mesh needs to be fine enough to be able to resolve the laminar sublayer. This results in a condition for the height of the first cell at the wall, which has to have a value of $z^+ \leq 1$. For the other dimensions must fulfill: $x^+ \sim 50$, $y^+ \sim 15$.
The height of the first cell, which depends on the z^+-value, can be calculated in the following way:

$$h_{first} = \frac{2z^+ \cdot L}{Re_L \sqrt{\frac{1}{2} C_f}} = \frac{2z^+ \cdot L}{Re_L \sqrt{\frac{0.027}{2} Re_L^{-\frac{1}{7}}}} = \frac{17.21 \cdot z^+ \cdot L}{Re_L^{\frac{13}{14}}}$$

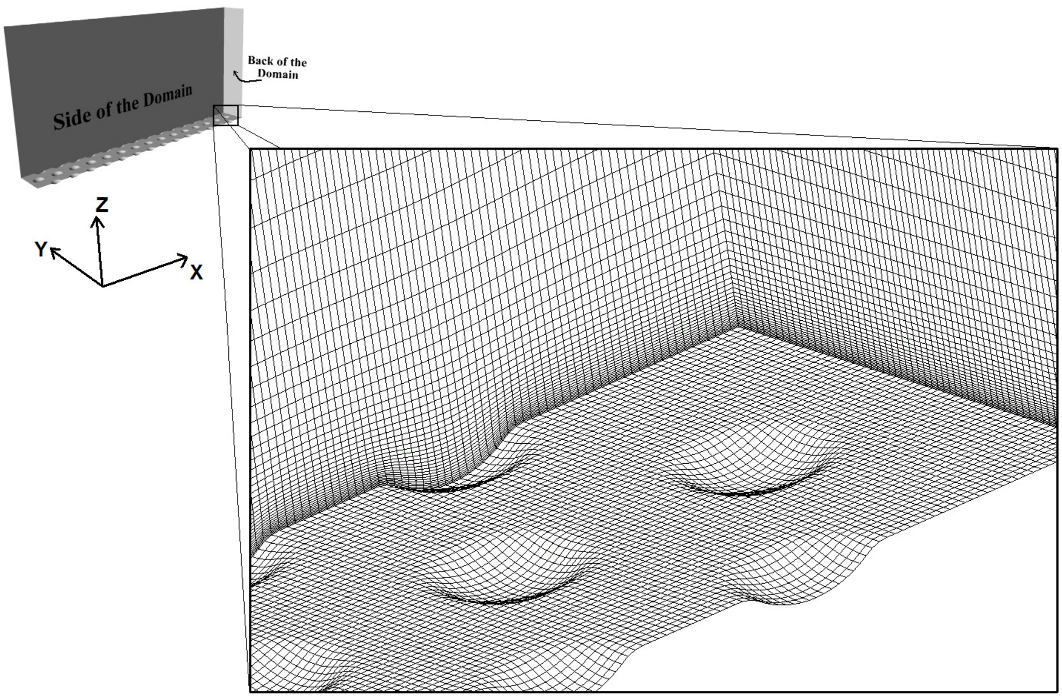

Figure 3.4: Example of the mesh.

For most of the series of simulations different meshes are used. This is because some simulations were performed to obtain more detailed information than others. This results in different meshes. The meshes used are presented for each series individually in the appendices. Figure 3.4 pictures a part of the mesh on the plate and two sides of the domain.

3.4 Physical Model, Begin- and Boundary Conditions.

The CFD-simulations are done with Fluent. Fluent needs input for which physical model it should use, also the boundary conditions on the boundaries of the domain have to be defined in Fluent.

The physical model consists out of settings for the turbulence model, the fluid material and operating conditions:

The turbulence model is of great importance when simulating a flow. The model has to be correct in representing the flow. Multiple turbulence models are available.
In direct numerical simulations (DNS) all the scales of motion are resolved accurately, and no modeling is used. DNS is the most accurate numerical method available at present but is limited by its cost. Present computer resources limit the application of DNS. The method of Reynolds-averaged Navier-Stokes equations (RANS) is a method that is most commonly applied, especially in engineering applications, to calculate the solution of turbulent flow problems. The RANS equations are obtained by time- or ensemble-averaging the Navier-Stokes equations to yield a set of transport equations for the averaged momentum. The effect of all the scales of motion is modeled. Examples of RANS models are the Spalart-Allmaras model, the K-ϵ model, the K-ω model and the Reynolds Stress Model (RSM). Large eddy simulation is a technique intermediate between the solution of the DNS and the RANS methods. In large eddy simulation (LES) the large, energy carrying eddies are computed, whereas only the small, sub-grid scales of motion are modeled. LES can be more accurate than the RANS approach because the small scales tend to be more isotropic and homogeneous than the large ones, and thus more amenable to universal modeling. Furthermore, the modeled sub-grid scale stresses only contribute a small fraction of the total turbulent stresses. Compared with DNS, LES does not suffer from the same strict resolution requirements of DNS. In recent years LES has received increased attention as a tool to study the physics of turbulence in flows at higher Reynolds number, or in more complex geometries, than can be managed with DNS. Its most successful applications, however, have still been for moderate Reynolds numbers. The extension of LES that resolves the wall-layer structures (henceforth called resolved LES) to such flows has been less successful owing to the increased cost of the calculations when a solid boundary is present. [Piomelli and Balaras, 2002]
In simulations series 1 (Section 3.5.1) multiple viscous models have been used to establish the correct model for turbulent flows. The RANS-methods, LES and DES are tested. DNS is not tested, because Fluent is not able to perform DNS simulations. From series 2 (Section 3.5.2) on, the LES-model is used.
The LES-method is the most used method in this thesis. The choice for the using the LES model will illustrated in section 3.5.1. For these simulations the procedure for performing simulations with the LES-model, as well as more elaborate information about the LES turbulence model is given in appendix D.

The air density is taken constant only in some simulations in series 1, where symmetry conditions are used on the top of the domain. In all other simulations the fluid is taken as an ideal gas with varying density, because this is a requirement of the pressure far-field boundary conditions used on the top of the domain.

The operating condition concerns the total pressure in the domain, which for compressible fluids is equal to:

$$p_0 = p_s(1 + \frac{\gamma - 1}{2}M^2)^{(\frac{\gamma}{\gamma-1})}$$

Also a reference point for this total pressure has to be defined. This is a point at which the wall does not perturb the flow. That is why a point is chosen which is placed high and in the front of the domain.

The boundary conditions have to be defined for all boundaries of the domain. An overview of these conditions is given in appendix C. Some boundary conditions imply that changes have to be made to the physical model. For example the Far-Field Pressure boundary condition applied to the top of the domain is allowed only if the density is defined not as a constant (default), but as an ideal gas, which is a variable parameter.

3.5 Analysis and Visualization of the Performed Simulations.

In this section the results of the CFD simulations is presented. A total of nine series of simulations is made during this thesis. In this report only six series will be mentioned. The three series left out of this report were series with no relevant addition to this thesis. The series discussed herein are:

- Two series done to choose the correct turbulence model. In section 3.5.1 a number of different turbulence models are tested. In 3.5.2 the behaviour of the LES turbulence model is tested for different velocities.
- One series with seven different dent depths is tested in section 3.5.3 to test the effect of the depth of the dents to the drag.
- In section 3.5.4 one series with two dent depths is tested for detailed research.
- One series with a deviating free-stream velocity (50m/s in stead of 5m/s) is tested. The purpose of this series is to see if the flow phenomenons encountered at low velocities still exist when higher velocities are imposed.
- To conclude the simulations a simulation is done with a dent which has a non-rotational symmetrical cross-section. (Section 3.5.6)

During the pre- and post-processing of the simulations and for the calculations of the simulations a number of different computer systems are used.
The first three series of simulations (Section 3.5.1-3.5.3) were done on the *lraero1*-computational cluster, also known as the central computational facility Beowulf cluster. For each simulation 4 type A computational nodes were used. Specifications of this cluster are mentioned here:

Master node: Dual Xeon 3 GHz, 1.7 TB Disk in Raid 5 configuration.
8 type A computational nodes: Dual Xeon 3 GHz, 2 GB ECC RAM.
20 type B computational nodes: Dual Opteron 280 dualcore, 8 GB ECC RAM, 160 GB
local disk.
4 type B computational nodes: Dual Opteron 280 dualcore, 16 GB ECC RAM,

160 GB
local disk.

The last three series of simulations (Section 3.5.4-3.5.6) require a graphical interface due to the implication of a UDF at the velocity inlet. These simulations were done on the *lraero2*-workstation. Specifications of this workstation are mentioned here:
Melrow Workstation 2 AMD Opterons 265, 8 GB ECC RAM, 500 GB disk.

The setup and post-processing of the simulations, which both require Fluent, were done on an other workstation. Specifications:
Dell Precision 370. Pentium 4, 3 GHz, 2048 MB ECC RAM, 160 GB disk.

For other applications, like drawing the geometry and the production of the mesh, as well as for writing this report, my own laptop is used. Specifications:
Compaq Presario R3000, AMD Athlon XP Processor 3000+, 797 MHz, 512 MB RAM,
60 GB disk.

3.5.1 Simulations to Establish the Choice of the Viscous Model.

In this section the results of simulation series 1 are presented. The series consists out of 17 simulations. This series is used to test three parameters. The first and most important parameter tested here is the turbulence model. Probably the LES turbulence will be the best model to apply in this situation, as will be explained later in this section, but other methods have to be tested as well. Maybe other turbulence methods are performing the simulations faster then the relatively time consuming LES method, without resulting in large errors. Also the difference between steady and unsteady simulations and the boundary condition at the top of the domain (symmetry or pressure far field) are tested.
First the differences between steady/unsteady simulations are dealt with. Only for Reynolds Average Navier-Stokes (RANS) turbulence methods it is possible to simulate with both steady and unsteady simulations. LES and DES are unsteady turbulence models. Two RANS-methods, the Spalart-Allmaras and the k-ϵ method, are simulated both steady and unsteady. After convergence the calculated values for drag, lift and momentum coefficients are exactly the same for unsteady and steady simulations. (See appendix C.1, table C.2) The only difference between these simulations is the time is takes to converge. The unsteady simulations take up to five times more iterations to converge. From literature [Lashkov and Samoilova, 2002] it is known that sometimes the orientation of the vortices formed in the dents, will change from left to right or from right to left. This shows that the flow is unsteady, which rules out steady methods since these methods cancel all influence of time.
The domain should have no pressure gradient, since a pressure gradient influences the forces at the plate. The boundary condition subjected to the top of the domain have to make sure of this. In figure 3.5 the pressure coefficient in the domain is plotted. In this figure two important things happen.
First it is observed that in both the left and the right picture the pressure coefficient is very high near the beginning of the plate. This is because the flow over the beginning of the plate is not yet developed. The uniform velocity in the inlet of the domain imposes

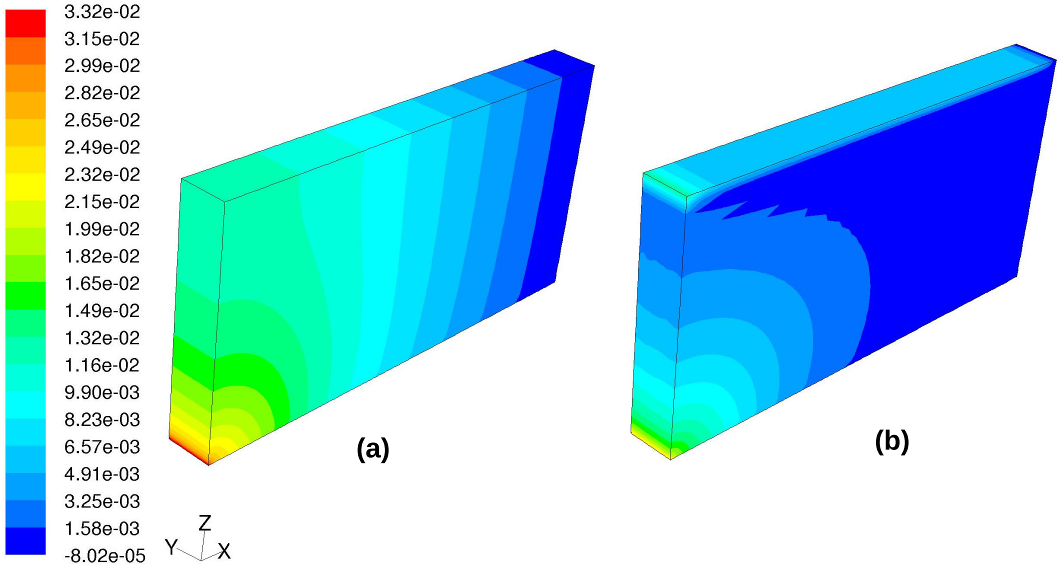

Figure 3.5: Contours of the pressure gradient for symmetry (a) and pressure far-field (b) boundary conditions.

high velocities near the wall, which results in high pressures and wall shear stresses near the beginning of the plate. This is the same for both situations, since the same inlet boundary condition is applied.

The left domain has a symmetry boundary condition at the top of the domain. Due to this symmetry boundary condition it is clear that the pressure in the domain decreases gradually in x-direction. So here a pressure gradient is present. In the right picture, with a pressure far-field boundary condition on top of the domain, the pressure decreases in a limited radial area around the beginning of the plate. Here no pressure gradient in the remains of the domain is present. That is why pressure far-field boundary condition is the correct condition to use on the top of the domain. The pressure far field boundary condition is used to model free-stream compressible flow at infinity, with free-stream Mach number and static conditions specified.

Now the results of the (un)steady simulations of the nine turbulence models, with pressure far-field boundary condition, are considered. The drag coefficients of the converged solutions are shown in table 3.2, the development of the drag coefficient is depicted in figure C.1 (steady simulations) and figure C.2 (unsteady simulations). The change in drag (ΔC_D) is calculated as:

$$
\begin{aligned}
\Delta C_D &= \frac{C_{D_{calc.}} - C_{D_{theory}}}{C_{D_{theory}}} \cdot 100\% \\
with: \qquad C_{D_{theory}} &= 0.031 \cdot Re_L^{-\frac{1}{7}}
\end{aligned}
\tag{3.1}
$$

All RANS turbulence methods results in high values for the simulated drag coefficient, from 9.4% up to 18.2% above the theoretical drag coefficient. Here steady RANS-methods are used, because these converge faster. The flow over a flat plate is steady, thus here it is correct to use steady models, for dented plates this would be incorrect.

DES results in a simulated drag coefficient which is much lower (12.3%) than the theoretically calculated drag coefficient. LES simulates the simulated drag coefficient nearest to the theoretical value. The calculated lift should be zero because a flat plate does not generate lift, which non of the models predicts. But all models simulate lift of approximately the same order (±0.004).

Turbulence Method	(un)steady	$C_{D_{theory}}$ [-]	$C_{D_{calc.}}$ [-]	ΔC_D [%]	$C_{L_{calc.}}$ [-]
Spalart-Allmaras	unsteady	0.00554	0.00622	+12.3	-0.0039
K-ϵ (Standard)	unsteady	0.00554	0.00617	+11.2	-0.0035
K-ϵ (RNG)	steady	0.00554	0.00606	+9.4	-0.0035
K-ϵ (Realizable)	steady	0.00554	0.00615	+11.0	0.0036
K-ω (Standard)	steady	0.00554	0.00655	+18.2	-0.0039
K-ω (SST)	steady	0.00554	0.00644	+16.1	-0.0041
RSM	steady	0.00554	0.00616	+11.2	0.0062
DES	unsteady	0.00554	0.00486	-12.3	-0.0038
LES	unsteady	0.00554	0.00542	-2.1	-0.0040

Table 3.2: Drag and lift coefficients for different turbulence models.

From this comparison and from turbulence model characteristics it is possible to make a choice which turbulence model to use in the upcoming simulations with the dented plates.
It is clear LES performs the best in terms of predicting the drag most accurate.
Also the phenomenon of drag reduction by dents in a surface, is likely to consist out of turbulent vortex structures caused by the interaction of the turbulent flow and the dents in the surface. It is important for the behaviour of the turbulent flow to be independent of the turbulence model. Since RANS-methods model all scales of turbulence in the flow and LES models only the part of the scales smaller than the filter imposed, it makes sense to use the LES model. One major drawback of this model is the need for very small cells near the wall, which results in a large amount of cells needed to fill the domain. And thus the long computational time needed for the detailed simulations.

3.5.2 Behaviour of the LES Turbulence Model at Different Velocities.

It is important to known how the LES model behaves at different velocities. Then it can be established whether LES gives a good representation of the flow or works only for a certain velocity regime. To investigate this a series of six simulations is performed. The only difference between the simulations is the velocity of the free flow. Velocities used in the simulations are: 1m/s, 3m/s, 5m/s, 10m/s, 20m/s and 40m/s. Of course the simulation with 5m/s is not performed here, since it is already done in the previous series.
The mesh used is the same for all simulations and should result in z^+-values which are in agreement with the values needed for the wall function approach which states z^+-values of $z^+ \approx 20$-150. In table 3.3 the z^+-values are presented. The values for the theoretical z^+-value is calculated for each of the velocities and with a first cell height of 2.5mm. The values for $z^+_{calc.}$ vary because the flow does not possess the same characteristics everywhere near the wall. The difference between theoretical and simulated z^+-value is

defined as:

$$\frac{z^+_{calc.} - z^+_{theory}}{z^+_{theory}} \cdot 100\%$$

Although the simulated z^+-values are higher than the theoretical values, almost all values still are in the correct region of $z^+ \approx 20$-150. Only the z^+-values for a velocity of 40m/s is not in accordance with the desired regime. The simulation with this free-stream velocity will nevertheless be performed, keeping in mind that the incorrect mesh can create failures.
When the simulations are finished the simulated z^+-values are computed, these are also shown in table 3.3. The simulated z^+-values for one simulation consist out of a range of z^+-values, because just above the plate the velocity varies for different positions on the plate. For the simulation with a velocity of 1m/s, the simulated z^+-values are much higher than expected. For the other free stream velocities the order of the z^+-values is approximately what was expected.

Velocity [m/s]	z^+_{theory} [-]	$z^+_{calc.}$ [-]	Difference [%]
1	4.7	0 - 27.5	+485
3	13.1	0 - 21.9	+67
5	21.0	0 - 32.9	+57
10	40.1	0 - 59.4	+48
20	76.3	0 - 108.9	+42
40	145.2	0 - 199.8	+37

Table 3.3: z^+-values for the meshes used in series 2.

An more elaborate description of the setup and the results of the simulation is given in appendix C.2. The most important results are also presented here. The drag coefficients are presented in figure 3.6. Also the calculated coefficients are presented here in table 3.4. All values are not averaged values, but the values at the end of the simulations. Since the solutions are converged, there is no difference between the average values and the values at the end of the simulation (t=0.75s), except for the simulation with a velocity of 1m/s. This simulation does not converge like the others. Also this simulations results in lift coefficient which are not, like in all other simulation, close to zero. Previously it was mentioned that the simulated z^+-values deviate from what was expected. Therefore a closer look is needed at the simulation with 1m/s.
The flow in simulation 2-01, which has a free stream velocity of 1m/s, shows an unexpected typical behaviour. In figure 3.7 the skin friction at 0.5s and 1.5s is presented. At 0.5s the first half of the plate shows a gradually decreasing skin friction coefficient, which is in agreement with the other simulations done. But the second half of the plate shows a very irregular pattern. At 1.5s this irregular pattern has shifted and is grown. The skin friction coefficient is zero in some spots. It appears as if the flow is separating from the plate. Also the pathlines through the domain shown an abnormal pattern (Figure 3.8, the pathlines are colored by pathnumber). The pathlines should run almost parallel to the wall in flow direction, but here in some cases the pathlines seem to go almost vertical. Also the velocity is much too high in some regions, even up to 15m/s which is

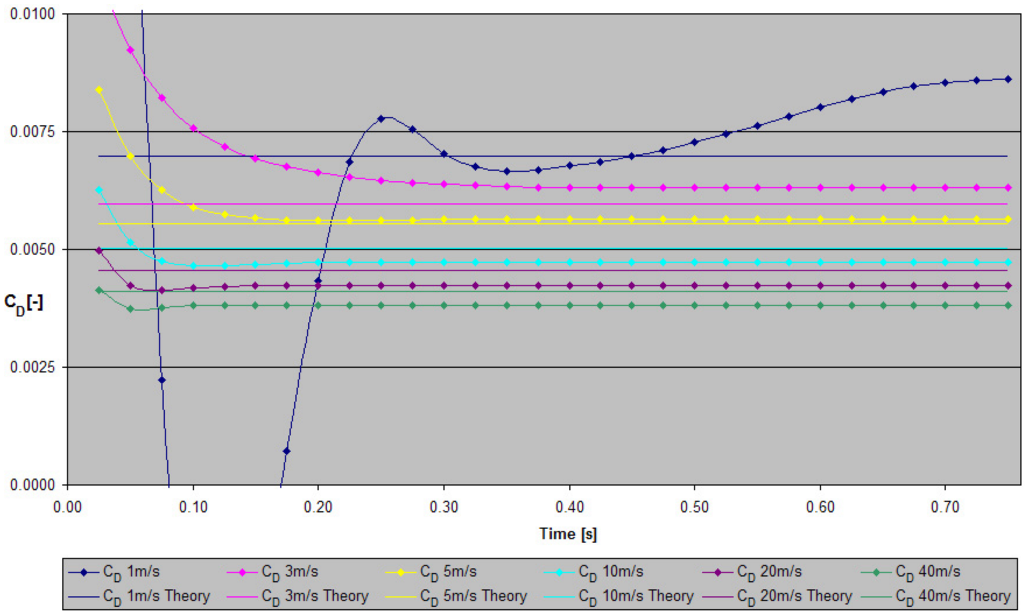

Figure 3.6: Development of the drag coefficients of LES-simulations for varying velocities.

Number of Simulation	Velocity [m/s]	$C_{D_{theory}}$ [-]	$C_{D_{calc.}}$ [-]	ΔC_D [%]	$C_{L_{calc.}}$ [-]
2-01	1	0.00698	0.00862	23.5	-0.0534
2-02	3	0.00596	0.00631	5.8	-0.0049
1-01b	5	0.00554	0.00542	-2.1	-0.0040
2-03	10	0.00502	0.00472	-6.1	-0.0032
2-04	20	0.00455	0.00422	-7.1	-0.0032
2-05	40	0.00412	0.00381	-7.5	-0.0034

Table 3.4: Drag and lift coefficients for different velocities; LES turbulence model.

remarkable since the free flow has only a velocity of 1m/s. The cause of the incorrect flow is probably the extreme low velocity of 1m/s at which the flow enters the domain, which is not compatible with the cell size used here. Also the residuals of the simulation do not seems to converge, see figure C.3. For other velocities the residuals converge nicely, like shown for a velocity of 20m/s in figure C.4.
Since, from literature, no simulations or windtunnel tests with a velocity of 1m/s are known for the dented plates and since all practical implementations of the dented surfaces involve higher velocities, this simulation is not taken into account for the rest of this thesis.
The other five simulations all show the same behaviour. A relatively fast convergence to a value close to the theoretical drag coefficients is found. These coefficients deviate over a range of -7.5% (U=40m/s) to +5.8% (3m/s) from the theoretical drag coefficients. It is important that these deviations are not too large, because if they become larger than the drag change due to the dents, the effect of the dents is not noticed any more. The DSE-phenomenon is reported to result in a drag reduction of up to 15%. Thus the devi-

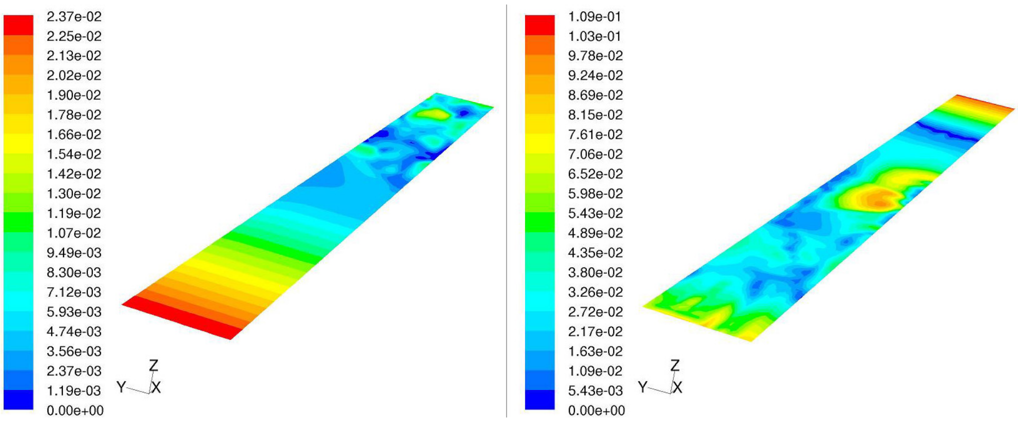

Figure 3.7: Skin friction coefficients of U=1m/s; for left at t=0.5s and right at t=1.5s.

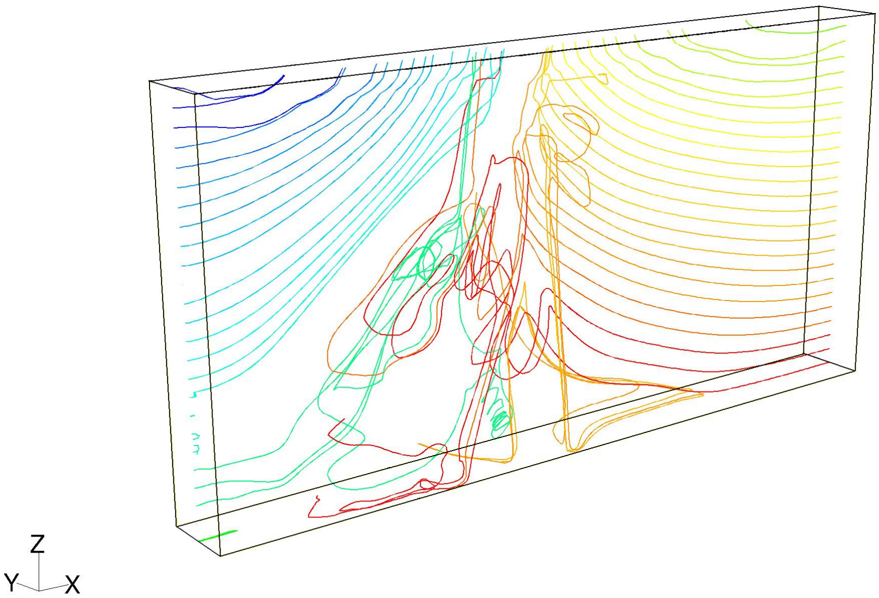

Figure 3.8: Pathlines through domain U=1m/s due to non-converging solution.

ation of the theoretical drag coefficient found here are still small enough to notice drag changes due to the dents, which are to be calculated in the next section. Lift coefficients are nearly zero, so these are as expected.
From the calculations so far it may be concluded that the LES turbulence model simulates the flow in a correct manner for a flow regime of 3-40m/s. From now on the LES model will be used to test dented surfaces.
It is important when performing CFD simulations to have convergence of the solution and grid independence. In this thesis no extensive research is done to insure grid dependency, but is can be proved that the solution is independent from the grid. This is not yet done for this series of simulations, but it is done for following simulations. The solutions

have converged, this is visible in figure 3.4 where the simulations show a converged drag coefficient.

3.5.3 Plates with Different Dent Depths.

Here the first series of simulations with dented surfaces will be discussed. The geometry of the surface will vary, because seven different dents are tested along with the flat plate as reference. Since the only varying parameter is the geometry of the plate, all other parameters are fixed. This also holds for the velocity. The free stream velocity is chosen to be 5m/s, because of two reasons. The first is that in the patent [Vida, 2004] experiments are done with this velocity, so experimental data is available. Also, as seen in the previous section, the simulation with a velocity of 5m/s is most accurate in predicting drag.

For these simulations two important modifications are made in respect to the previous series of simulations. The first, and most obvious modification, is the introduction of the dented plates. Second modification concerns the number of cells, which is increased. The width of the domain is increased with respect to the previous simulations, from 0.05m to 0.0572m. This is because the dented plate have a symmetrical pattern with a width of 0.0572m. A wider domain implies more cells are present. For the simulation of the flat plate still the width of 0.5m is used. This will have important consequences, which will be discussed later when the drag coefficients of different plates are compared. Also the cell size is decreased for two reasons. The dented geometries contain curvatures or radii. It is of great importance that these curves are modeled correctly by the grid. This holds especially for the deeper dents, where the geometry consists out of more severe gradients are present. Smaller cells sizes in the x- and y-direction will provide a better representation of the surface than large cells. This is why the size in x- and y-direction is decreased from 2.5mm (previous simulations) to 1.0mm. The refinement in cell size will lead to an increase by 2.5×2.5=6.25 times as much cells as in the previous simulations, which results in much longer simulation times. Also the z-dimension of the cells in decreased. Previously the wall function method was used to model turbulence near the wall. From now on Near Wall Revolving will be used, to model the near-wall flow in a more detailed manner. The z-dimension needs to be much smaller in for this approach. The requirement here is $z^+ \leq 1$. The height of the first cell should be:

$$h_{first} = \frac{17.21 \cdot z^+ \cdot L}{Re_L^{\frac{13}{14}}} = \frac{17.21 \cdot 1 \cdot 0.5}{(1.71 \cdot 10^5)^{\frac{13}{14}}} = 0.000119m = 0.119mm$$

Which is a very small size, but necessary to fulfill the requirements of the Near Wall Resolving model. The height of the cells will grow as the cells are placed further from the wall. The number of cells can be calculated now: length × width × height = 501 × 58 × 78 = 2,266,524 cells. (For the flat plate, with smaller width, this is 2,233,000 cells.) This is more than ten times are many cells as is used in the previous series. Which, of course, results in a much longer simulation time.

A consequence of these much smaller cells is that it is not possible to compare the results from this series to the results out of the previous simulations. This is why here also the simulation with the flat plate is made once again. The results out of this series are comparable to each other, because the differences in the meshes are only very small, since only the nodes are shifted in z-direction at the position of the dents.

The simulations done result in a drag graph, shown in figure 3.9. Except for the drag

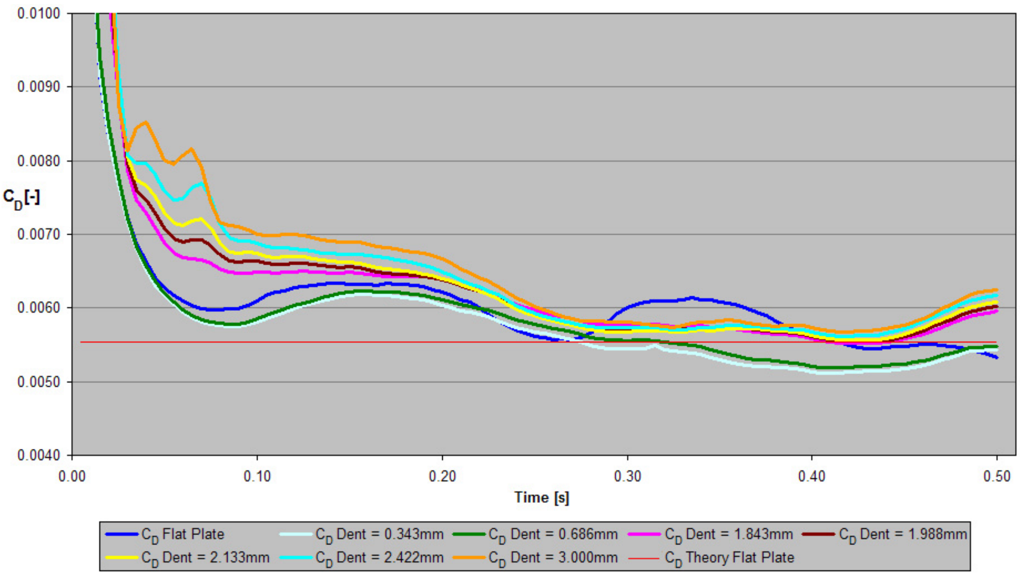

Figure 3.9: Drag coefficients of dented plates with variable depth.

coefficient of the flat plate, all other drag coefficient develop parallel to each other. (The lines in the figure do not cross.) After 0.2s the flat plate drag coefficient shows a deviating behaviour compared to other drag coefficients. It seems that the fluid flow over dented structure is influenced in a different way than the fluid flow over the flat plate. The reason for this different behaviour is the difference in geometry. The width of the flat plate is 0.0072m (12.5%) smaller than the width of the dented plates. This causes a problem with the symmetry boundary conditions defined to the sides of the domain. As will be explained and illustrated in the next section (Section 3.5.4) the symmetry boundary conditions cause the flow to accumulate in one side of the domain. This leads to a small increase in drag. The drag calculated for the flat plate will be overestimated in comparison to the drag of the dented plates. Thus comparing the drag of the flat plate to the others is useless, although they are still shown in table 3.5. This is also the main reason why in the next series of simulations the symmetry boundary conditions will be changed into periodic boundary conditions. The periodic boundary condition will not block the flow near the sides of the domain.
An other remarkable feature of this series is that, unlike previous simulations, the final solution does not converge to a single value for the drag coefficients, but fluctuate a little. At the end of each timestep the residuals are constant, so the solution is converged. (See appendix C.3, figure C.4) This is why the average of these coefficients has to be taken into account. These average values for the force coefficients are shown here, in table 3.5. The average coefficients are taken over the time interval 0.1-0.5s. Here: $C_{D_{theory}} = 0.00554$. The drag of the flat plat is estimated to be 6.3% higher than turbulent flat plate boundary layer theory predicts, this is in accordance with the numbers we found for the LES model in previous simulations.
The results of this series of simulations is presented more elaborate in appendix C.3.

The flat plate will not be considered in relation to the dented plates anymore in this section. The dented plates show a trend of increasing drag for increasing dent depth.

Simulation Number	Dent Depth [mm]	$C_{D_{calc}}$	ΔC_D w.r.t. $C_{D_{theory}}$ [%]	ΔC_D w.r.t. $C_{D_{calc.,flatplate}}$ [%]
3-01	0.000	0.00589	+6.3	n.a.
3-02	0.343	0.00558	n.a.	-5.3
3-03	0.686	0.00566	n.a.	-3.9
3-04	1.843	0.00596	n.a.	+1.2
3-05	1.988	0.00598	n.a.	+1.5
3-06	2.133	0.00600	n.a.	+1.9
3-07	2.422	0.00607	n.a.	+3.1
3-08	3.000	0.00616	n.a.	+4.6

Table 3.5: Drag coefficients for the dented plates with variable depth.

The drag coefficient can be divided into two components, a viscous and a pressure drag component. (See table 3.6) The components are presented for the plates at t=0.5s. A representation of the flow situations for the flat plate, the attached flow over a dented plate and the detached flow over a dented plate are given in figure 3.10. The drag of the flat plate consists out of viscous drag (τ^+) only, since pressure drag is generated by deflections of the flow direction from the free flow direction. The pathlines are parallel to the plate. Thus the flow does not have a component normal the the plate, which causes the pressure drag. For dented plates the flow has a horizontal and a vertical component, which both cause drag. The horizontal component will cause a friction drag, while the vertical component causes pressure drag. Areas were pressure drag is created are denoted in figure 3.10 by $C^+_{D_p}$.
Attached flows through dent were found for depths of 0.343mm and 0.686mm. Deeper dents experience separated flow. It seems that for attached flows the skin friction component, C_{D_v}, is approximately 9% higher than for the detached flows. This is caused by the detached flow areas, where vortices are present, decreases the skin friction (τ^-) due to the negative x-direction in which to fluid is flowing. This is shown in figure 3.10. The pressure drag increases when the dents are deeper, as expected. The deeper the dent, the larger the vertical components of the flow, and thus the pressure drag will be larger. For attached flow the pressure drag is small, since the vertical components of the flow are small. For detached flow, the flow has large vertical components, which cause high pressure drag.
For a decrease in total drag the sum of both drag components should decreases, to below the total drag of the flat plate.

To find an explanation for the drag behaviour a closer look is taken at a number of parameters.
The skinfriction coefficients of the plates are depicted in figure 3.11. The top plate in this figure represents the flat plate, the plates further down in the picture are dented, with the deepest dent situated at the bottom of the picture. This is a static picture, taken at t=0.5s. In time the skinfriction coefficient shows little changes only (this is not illustrated in this report). The situation as it is shown in figure 3.12 represents the average skinfriction coefficient correctly. The dents in the surface influence the skinfriction coefficient in two ways. The skinfriction in the dents changes, due to the shape of the dent. This results in a low skinfriction in the forward part of the dent, where the flow enters the dent. A high skinfriction coefficient is present on the aft side of the dent, where the flow exits the dent. The skinfriction is an absolute parameter,

Simulation Number	Dent Depth [mm]	$C_{D_{total}}$ [-]	C_{D_v} [-]	C_{D_p} [-]
3-01	Flat	0.00532	0.00532	0.00000
3-02	0.343	0.00544	0.00538	0.00006
3-03	0.686	0.00548	0.00526	0.00022
3-04	1.843	0.00595	0.00488	0.00107
3-05	1.988	0.00608	0.00488	0.00120
3-06	2.133	0.00603	0.00488	0.00115
3-07	2.422	0.00617	0.00489	0.00128
3-08	3.000	0.00625	0.00491	0.00134

Table 3.6: Total, viscous and pressure drag of the dented plates; t=0.5s.

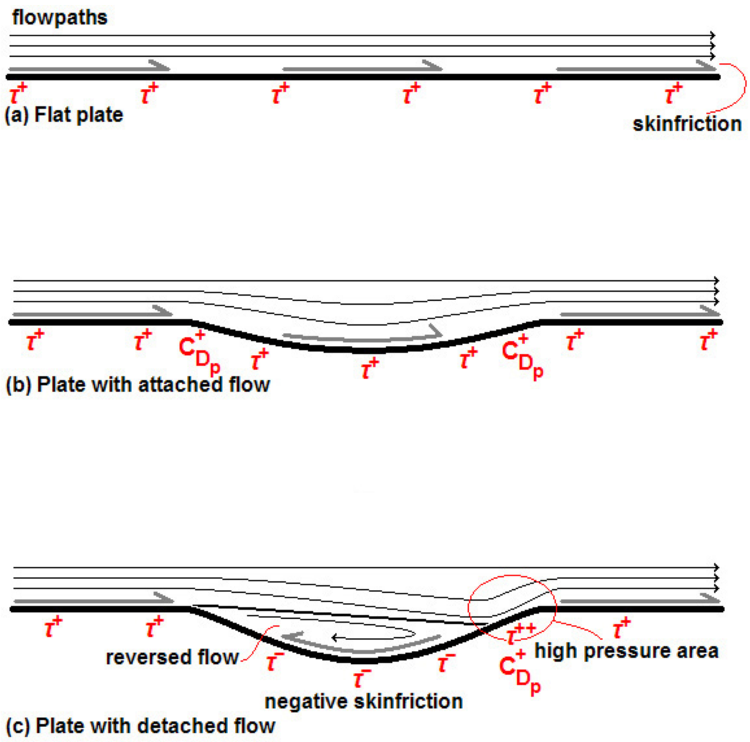

Figure 3.10: Flow effects occurring for different situations.

it is impossible to deduct the direction of the flow from a picture of the skinfriction. When the wall shear stress in x-direction is considered it is possible to find areas where the flow at the plate moves opposite to the free-stream flow. In figure 3.13 the values of the wall shear stresses in x-direction, taken over the average of a selection of dents at a position of y=0.0286m (right through the dent in the middle of the plate) and at a time of t=0.5s, are shown. This selection consists out of the 6^{th} to 15^{th} dent present in the middle of the plate, the first five dents are not part of this selection because they are to close to the edge of the plate where the flow is still developing. Now only a small, negligible, influence of the development of the boundary layer is seen here. The red line represents the position of the dent.

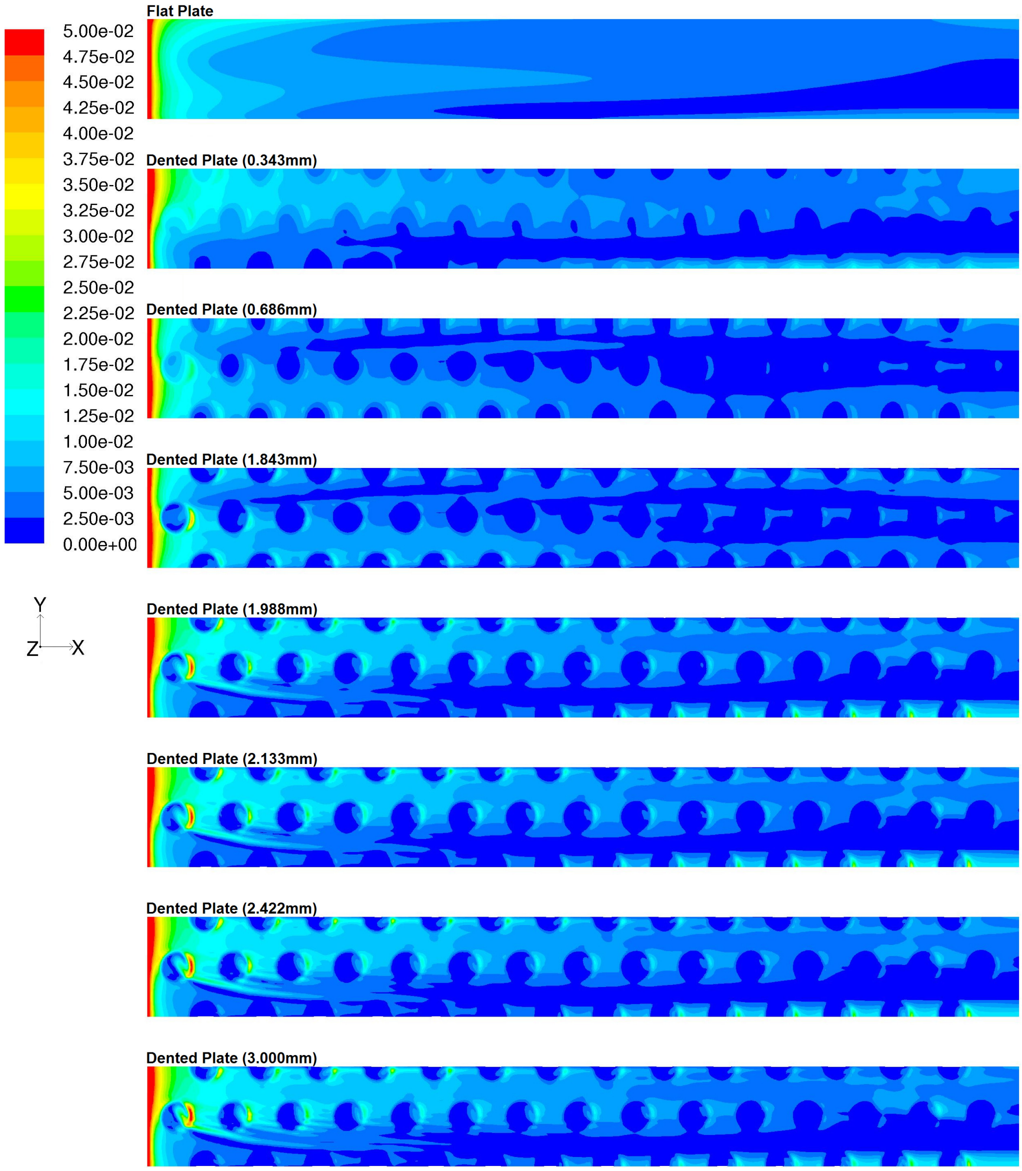

Figure 3.11: Skin friction coefficients of the plates at t=0.5s.

For the dented plate the following is observed: At the position where the flow enters the dent (x=0.0075m), the wall shear stress drops. For the dents with a depth of h_c ≤1.988mm the wall shear stress is positive, for t=0.5s. For dents with depths h_c ≥2.133mm negative wall shear stresses appear (red encircled in the figure).
From figure 3.13 it is concluded that at t=0.5s for dents deeper than h_c =1.988mm cause the flow to detach. For swallower dents, this is not found. But in figure 3.13 the difference between the dent where separation does and does not occur is very small. (separated flow for h_c =2.133mm, attached flow for h_c =1.988mm). If the velocity profiles are plotted, then an other conclusion can be drawn. Figures 3.14, 3.15 and 3.16

feature velocity profiles for the flat plate and two dents (depths are h_c =0.686mm and h_c =1.843mm). For the flat plate one profile is plotted, for the dented plates three profiles are plotted, each at a different position with respect to the dent; just before the dent, in the middle of the dent and just after the dent. The velocity profiles of the flat plate do not change with respect to the chosen position, because the geometry does not change. For the velocity profiles of the dented plates must be mentioned that the height is zero at the level of the flat plate. This causes the velocity profiles for the position in the dent to begin at a negative height. From the velocity profile in figure 3.16 it becomes clear that for depths of h_c =1.843mm the flow separates as well, which was not concluded from the wall shear stress figures discussed before. It is probably due to the averaging of the wall shear stresses over a number of dents that the separated flow is averaged out of the picture.
Also the velocity vector fields in a plane through the dents is taken into account. These are shown in section C.3, figure C.5 and C.6. Although these pictures are unclear, it is possible to find areas with separated flow. Figure C.5 features the flow over a flat plate and the flow over through a shallow dent (depth h_c =0.686mm). Here in both situations the flow is attached to the plate. In figure C.6 the flow through two deeper dents (h_c =1.843mm and h_c =3.000mm) are depicted. As before, when looking at the wall shear stresses in x-direction, the deepest dent will trigger the flow to separate and cause the fluid to flow in reverse direction. Here also the dent with a depth of h_c =1.843mm will cause the flow to separate, like the velocity profiles also have shown.

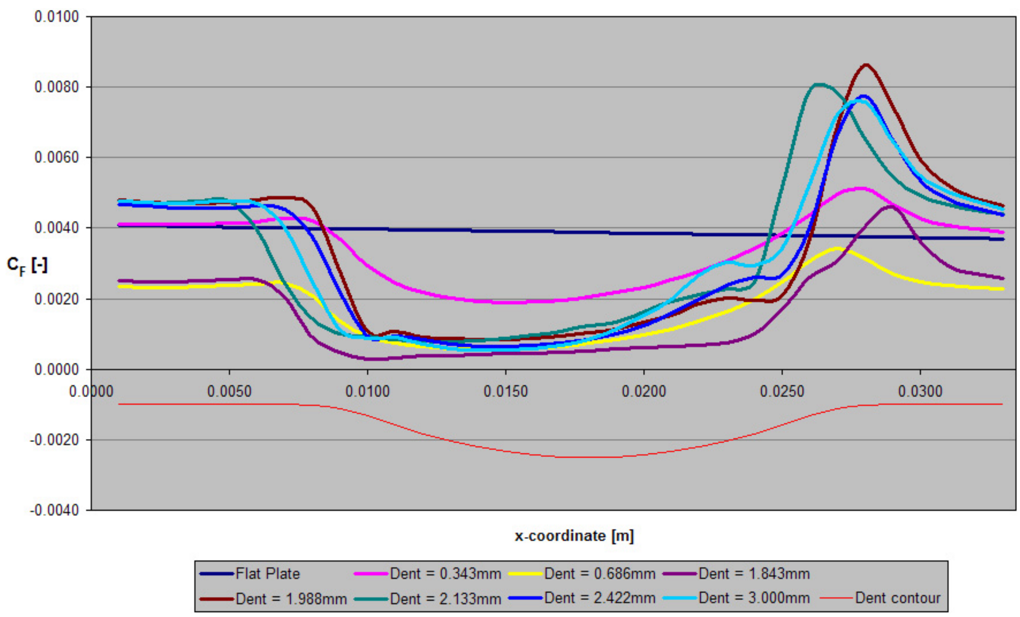

Figure 3.12: Skinfriction coefficient down the middle of the dents; t=0.5s.

Negative wall shear stresses imply that the fluid is flowing in negative direction. Here the flow does not follow the wall anymore, the flow is separated from the wall. This negative wall shear stress causes a huge decrease in shear stress for the deeper dents. The flow near the deep dents is depicted in figure 3.17. For clarification purposes in figure 3.19 the pathline of one singe particle moving through the dent is drawn.

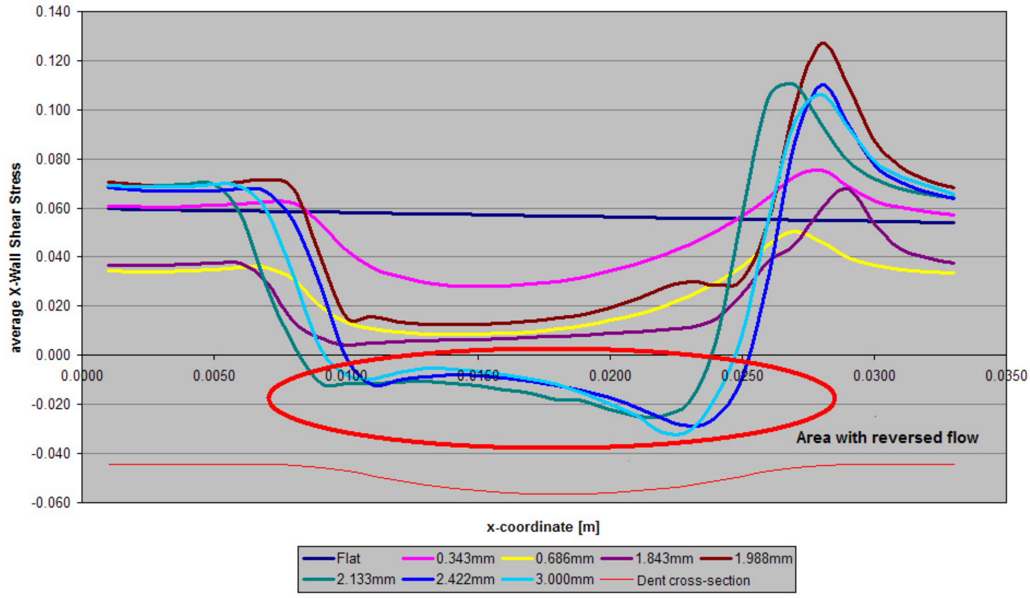

Figure 3.13: Wall shear stress in x-direction, down the middle of the dents, shows reversed flow in dents; t=0.5s.

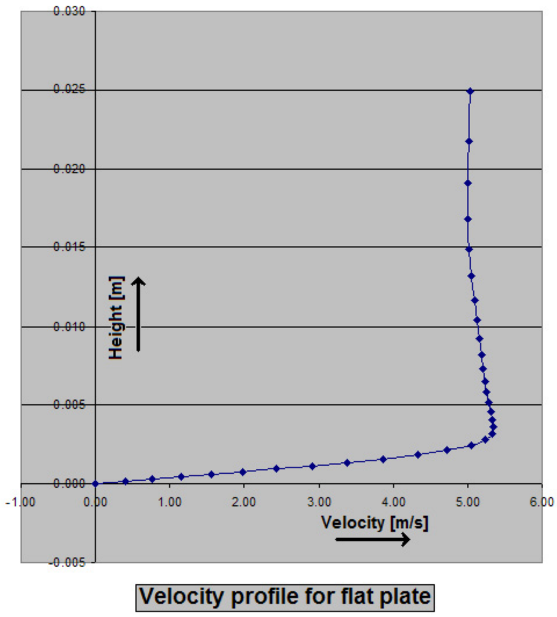

Figure 3.14: Velocity profile for the flat plate.

Figure 3.17 is made in Fluent by making a plane in the dent, perpendicular to the flow. From this plane pathlines are developed in reverse direction, to see where the fluid entering the dent comes from, and in forward direction, to see how and where the

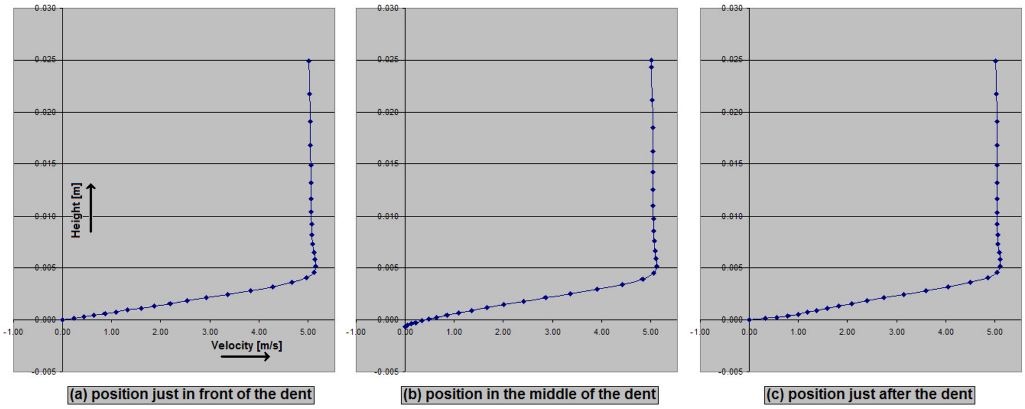

Figure 3.15: Velocity profile for the dented plate, with a depth of 0.686mm, at three positions; just in front of the dent, in the middle of the dent and just after the dent.

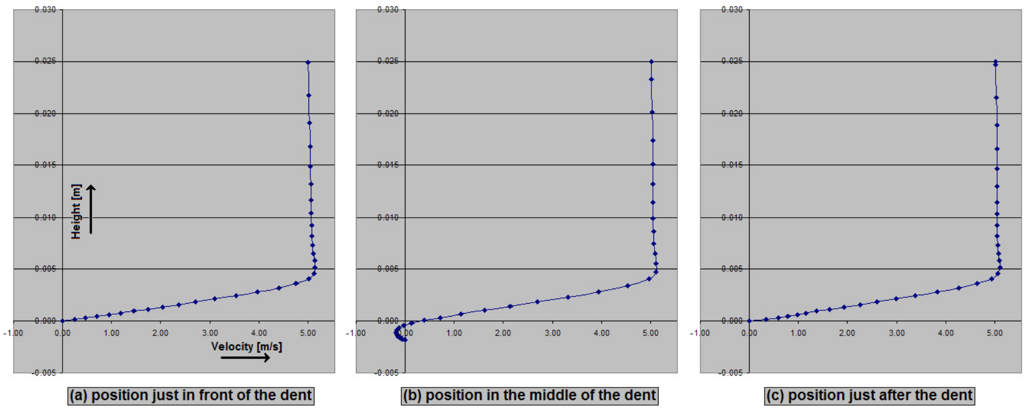

Figure 3.16: Velocity profile for the dented plate, with a depth of 1.843mm, at three positions; just in front of the dent, in the middle of the dent and just after the dent.

fluid exits the dent. From the picture at the right bottom it is clear that the majority of the fluid comes from the left into the dent, then flows through as a single-vortex structure finally exiting the dent at the right aft position. The dent used here has the deepest depth (h_c =3.000mm), because the vortices are best visible in this case. The flow over the dents seems to be similar to the flow found in experiments by New and Lim [New and Lim, 2004], see appendix B. Here symmetric and asymmetric flow fields are encountered for different flow parameters. The asymmetric flow found, present at $Re = 6,000$ and $h_c/d_c = 0.15$ is almost similar to the flow field over the h_c =3.000mm deep dent, calculated in this thesis. The single-vortex structure developing in a dent is called a "tornado-like" vortex. The smaller vortex probably is not visible in the experiment, where the dye used is not able to visualize all features of the flow.

An other study of the flow over a dent is a numerical study done by Isaev [Isaev et al., 2005]. Three-dimensional and plane turbulent flows of an incompressible viscous fluid and the convective heat exchange in the region near a plane wall with a spherical hole or a circular trench with a middle cross-section in the form of a circle

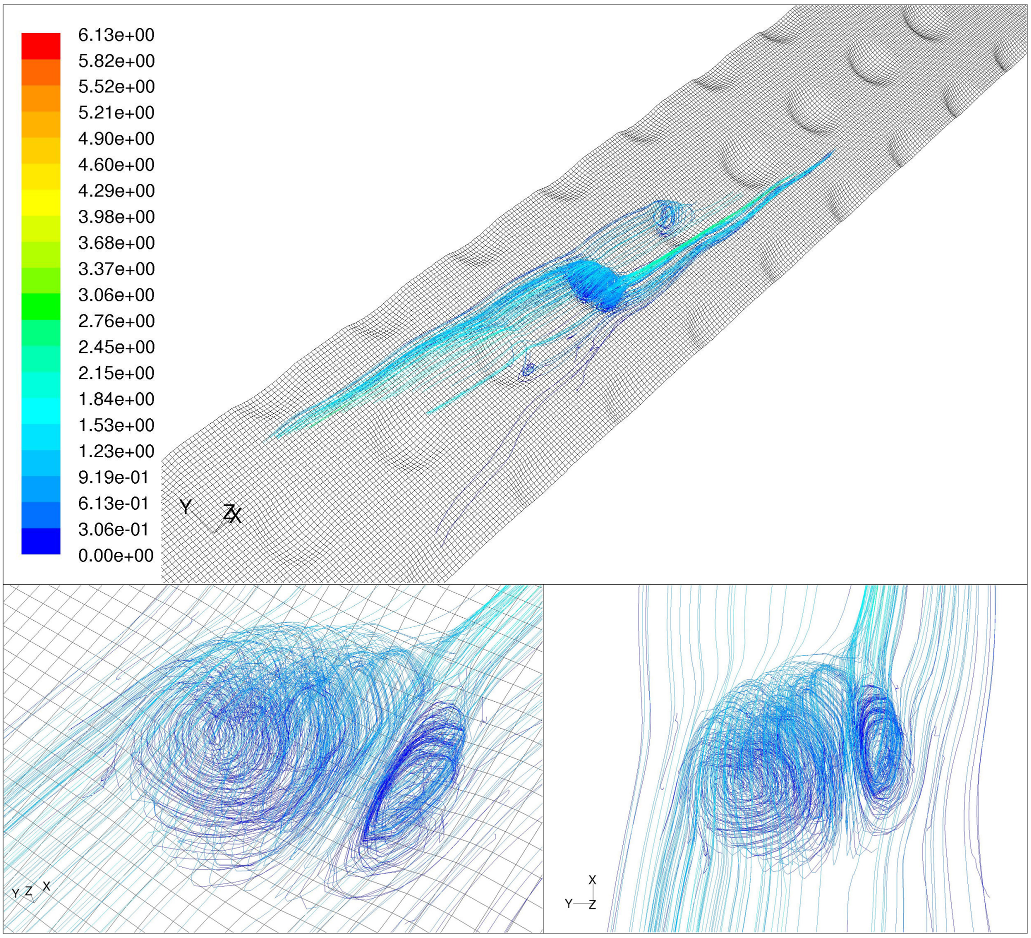

Figure 3.17: Pathlines over a dent (3.000mm) in the plate.

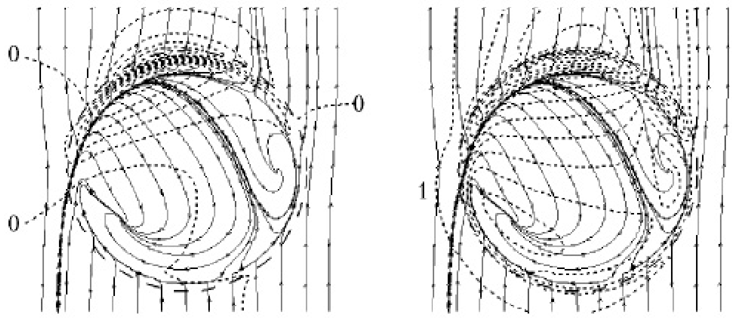

Figure 3.18: Comparative analysis of the patterns of fluid spreading on the surface of a deep hole represented by isobars drawn with a step of 0.02 from the zero level of the excess pressure (left) and isolines of relative heat transfer (right) drawn with a step of 0.025, see [Isaev et al., 2005].

were calculated. This research is aimed at investigating the vortex heat exchange in turbulent flows around a spherical hole on a plane wall, which has been numerically investigated. This numerical study confirms the flow field found in the simulation done in this thesis. Figure 3.18 shows the flow pattern of the fluid through a dent. Both pictures in the figure show the pathlines (arrowed lines). The left picture features also isobars, the right picture contains isolines of relative heat transfer. Both the isobars and the isolines are concentrated near the rear edge of the dent, slightly left from the middle. This is exactly the position were in the simulations done in this thesis high skinfriction coefficients were encountered, see figure 3.11. So both investigation seem to confirm each other to what happens with the flow in a dent.

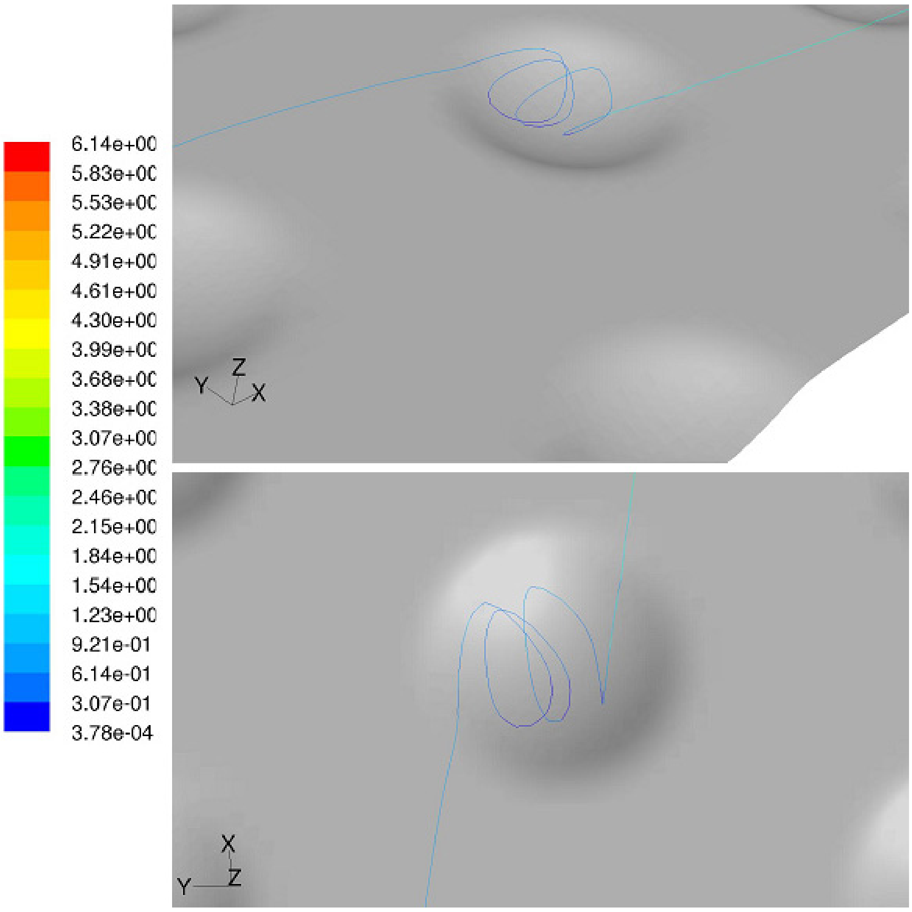

Figure 3.19: Pathline over a dent (3.000mm) in the plate for a single particle.

It has been established by Isaev, that in a flow around a deep hole (h_c/d_c of the order of 0.2) single-vortex structures arise (Figure 3.18) transporting the fluid in the transverse direction with a maximum velocity of the order of 0.2 times the free stream velocity. Although not a lot of flow visualization images are presented in this article, the ones presented seem to correspond very well to the calculations done in this thesis where the vortex structure looks to be the same. Also the maximum velocity in the vortex behaves according to predicted by Isaev, since the velocity is ≈1m/s with a free stream velocity of 5m/s (ratio = 0.2), see figure 3.19 where the pathline is colored corresponding to 1m/s.

The flow coming out of a dent influences the skinfriction in the vicinity of the dent. This is especially visible in the cases where the deep dents with separation are present. A turbulent structure exits the dent and vortex exits the dent and continues it way in a path situated between two rows of dents. When passing the next dent it merges with the flow structure coming out of this dent. The fact that this structure moves between two rows of dents is not what is reported in the previous research done. It was reported in the article in Der Spiegel [Wüst, 2004] that the vortices interact with dents positioned downstream. It seems as if in the simulations done, the lateral distances between the dent are too large, thus making it impossible for the turbulent structure to reach the next dent. See also figure 3.17, where most pathlines coming out of the dent follow a path lying in between two rows of dents.

3.5.4 Simulations for More Detailed Viscous and Pressure Drag Behaviour.

This series of simulations consists out of three simulations, done to get a more detailed view of the phenomenon which influences the drag. An other important goal of this simulation is to investigate what the relation is between the flat plate and the dents plates, since the simulation of the flat plate in the previous series was done incorrectly.
The length of the simulations is increased to 200 time steps (each 0.005s), to simulate one second of real-time fluid flow over the plate. This will result in more accurate averaged parameters. Since the simulations take long to complete (approximately two weeks) only three simulations are done. The plates tested are the flat plate and the dented plates with a dent depth of h_c =0.343mm and h_c =3.000mm. These plates are chosen because the flat plate is needed as reference, the 0.343mm deep dented plate shows an attached flow and the 3.000mm deep dented plate shows a detached flow pattern in the previous set of simulations. So all flow situations encountered previously are included in this series. The size of the plate and domain are equal for all three simulations done here. The shape of the geometry is not changed with respect to the plates in the previous section, but the plate is divided into 120 squares. The first part of the divided plate is shown in figure 3.20. From this figure it is clear that each dent, and the area surrounding the dent, consists out of four squares. The squares in the two rows near the edges of the domain are named L01 to L30 (left side) and R01 to R30 (right side). The two middle rows of squares are named after the dent (D01 to D15) and to the position with respect to the dent (four quadrants: I, II, III and IV). Now Fluent can calculate the properties of each separate square. The meshes made here are deviating only by a small amount to the meshes used in the previous series. The nodal points are shifted in some spots, but the number of nodes and cells is still the same.
Two modifications are made to the boundary conditions used here.
All previous simulations were performed with symmetry boundary conditions at the sides of the domain. This, however, is incorrect. The reason of implementing this symmetry boundary conditions was the symmetry of the geometry. Although the geometry is symmetrical, the flow is not, which makes implementation of symmetry boundaries not correct. The symmetry boundary conditions limit the movement of the flow in the direction perpendicular to the flow. Periodic boundary conditions are used to allow the flow to move through the sides of the domain. In figure 3.21 a schematic picture of the

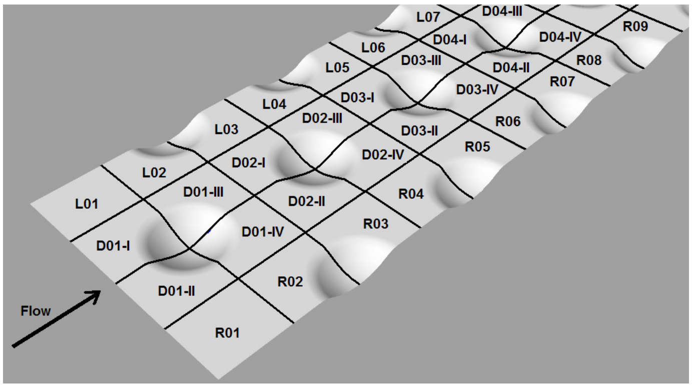

Figure 3.20: The names and order of the squares after division of the plate.

both boundary conditions is drawn. Left the symmetric boundary condition is depicted. If we look at a particle path (black arrow) which points to the right the symmetric boundary condition mirrors an imaginary path on the other side of the boundary (grey arrow). Where these two meet, both paths are bent to a path along the boundary. When the flow is symmetric to this boundary this is correct. But here the flow is not symmetric so it is not. Here the flow near the wall develops as shown in figure 3.22, where it is clearly visible that the flow is concentrating near the right symmetry plane due to the presence of the symmetry boundary conditions. The periodic boundary condition treats the flow in another way. In the right half of figure 3.21 again a pathline is draw in the domain. When the pathline contacts the boundary, the particle exits the domain and enters the domain in the opposite boundary. Periodic boundary conditions always require two identical boundaries.

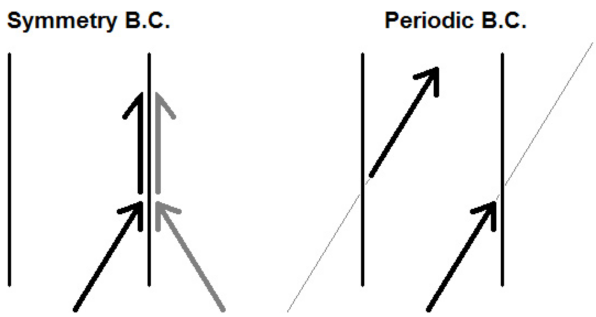

Figure 3.21: Symmetry and periodic boundary conditions.

Another change to the boundary condition is the implementation of a velocity profile at the inlet of the domain. All previous simulations used of a uniform velocity at the inlet. From here on, a velocity profile is implemented at the inlet of the domain. The velocity profile represents the profile of a profile after a development of 0.5m. The advantage is that the flow does not need to develop as much as when a uniform velocity is used, which leads to faster convergence. Also a velocity profile will implement a no-slip condition near the beginning of the plate at x=0m. Here uniform velocities result in very high skinfriction coefficients near x=0. The velocity profile is defined by means

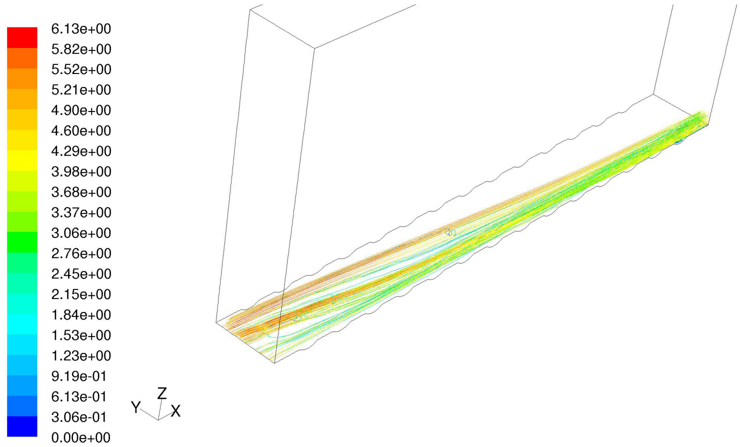

Figure 3.22: Flowlines in case of symmetry boundary conditions.

of a User-Defined-Function (UDF) in Fluent. More information about the velocity profile and the applied UDF is given in appendix E. The applied velocity profile has consequences for calculating the drag ($C_{D_{theory}}$). The formulas used earlier calculate the drag of a turbulent plate from the beginning of the plate. But due to the UDF the first part of the development of the boundary layer is not present in the simulations. Now $C_{D_{theory}}$ is calculated according to this procedure: (see also figure 3.23)

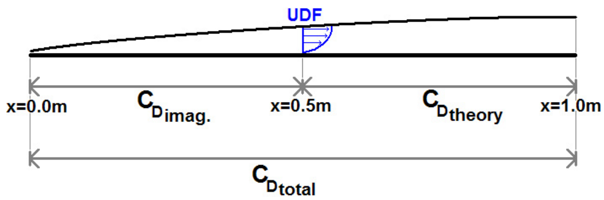

Figure 3.23: Situation for calculating the theoretical drag coefficient.

First the total friction drag of a flat plate with a length of 1m is calculated. The drag coefficient is calculated according to White [White, 1991]:

$$D_{total} = \frac{1}{2}\rho C_{D_{total}} U^2 L$$

$$C_{D_{total}} \approx 0.031 Re_L^{-\frac{1}{7}}$$

Also the drag of a plate of 0.5m can be calculated. This plate is an imaginary part of the plate.

$$D_{imag.} = \frac{1}{2}\rho C_{D_{imag.}} U^2 L$$

$$C_{D_{imag.}} \approx 0.031 Re_L^{-\frac{1}{7}}$$

Now the drag of the plate used in the simulations can be calculated by subtracting the drag of the imaginary part from the drag of the plate with a length of 1m. Also the drag coefficient can be calculated:

$$D_{theory} = D_{total} - D_{imag.}$$
$$C_{D_{theory}} = \frac{2D_{theory}}{\rho u^2 L}$$

For a velocity of 5m/s the theoretical drag coefficient is: $C_{D_{theory}} = 0.00445$.

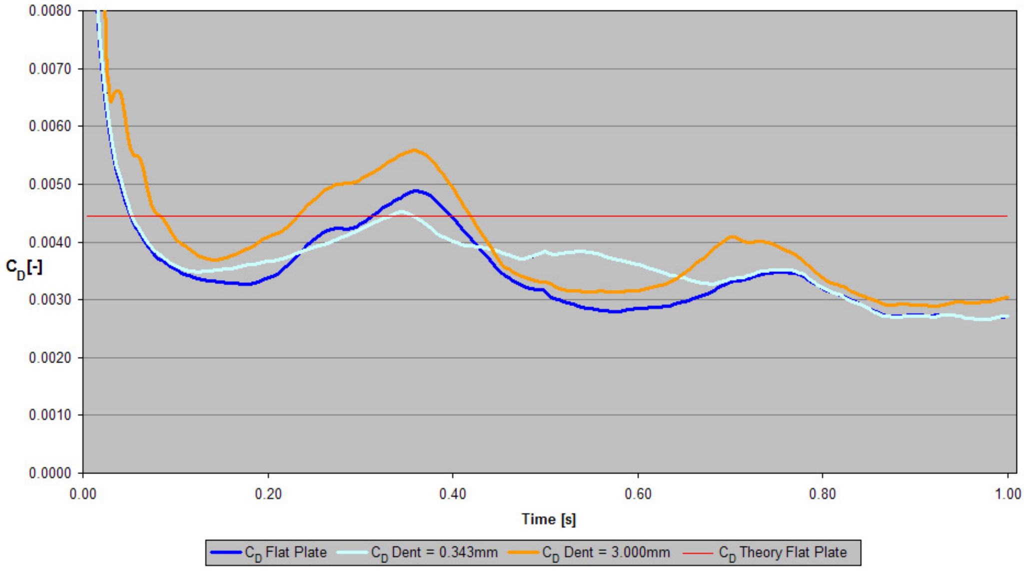

Figure 3.24: Drag coefficients of dented plates.

In figure 3.24 the behaviour of the drag coefficients of the three plates is presented. Here the drag coefficients are developing more random than in the previous simulations. In section 3.5.3 all drag coefficients were developing parallel. Here, for t<0.8s, the drag of the plates is developing not parallel, but they still follow the same trend. For example peaks are present at approximately t=0.4s and t=0.75s for all plates. From t=0.8s on however, the drag coefficients again develop with the same trend, but it is not clear if this behaviour changes when the simulations are continued for t>1.0s. This is not tested in this thesis, because of the duration of these simulations. Each of the simulations done here already took approximately two weeks to simulate one second of the flow.
The averages of the drag coefficient, calculated for $0.2s < t < 1.0s$, are presented in table 3.7. Here a large difference between the theoretical drag coefficient and the calculated drag coefficients is noticed. This can only be caused by the changes in the model. The change of the boundary conditions at the sides of the domain can be of influence to the drag, but only to a small degree. With the symmetric boundary conditions it is possible to create high pressure areas near the sides of the domain, which in combination with the wall, can lead to higher drag than in the situation where periodic boundary conditions are implemented to the sides of the domain. But this difference in drag is to significant to be caused by merely the change of boundary conditions on the sides of the domain. The effect of the changes to the velocity inlet is the main cause for the large drag difference. The uniform velocity, which does not apply no-slip, causes massive wall shear stress near

the beginning of the plate, twice the wall shear stresses caused by the velocity profile, see figure 3.25. This is the main reason why in this series of simulations the drag will be much less that in the previous simulation series.

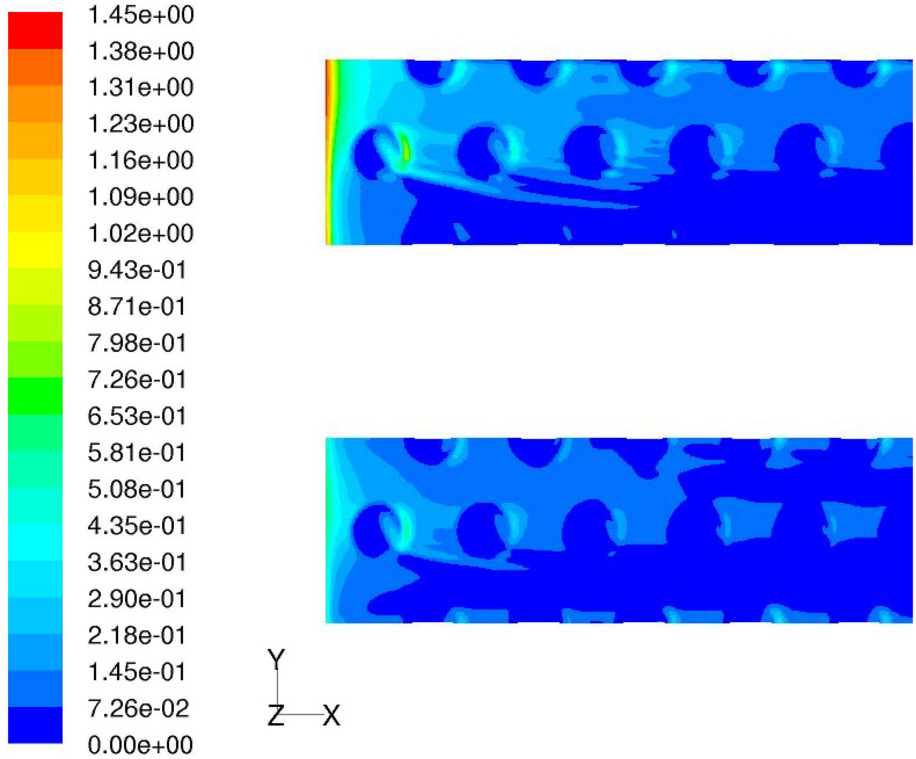

Figure 3.25: High wall shear stresses near the beginning of the plate.

Simulation Number	Dent Depth [mm]	$C_{D_{calc.}}$	ΔC_D w.r.t. $C_{D_{theory}}$ [%]	ΔC_D w.r.t. $C_{D_{calc.,flatplate}}$ [%]
4-01	Flat	0.00338	-24.0	n.a.
4-02	0.343	0.00353	n.a.	+4.4
4-03	3.000	0.00380	n.a.	+12.4

Table 3.7: Drag coefficients for the dented plates.

From table 3.7 it becomes clear that both dented plates show an increase in drag with respect to the flat plate. In the previous simulation series, section 3.5.4, the flat plate could not be compared to the dented plates because of the difference of the width of the domain. Here the domains are equally sized, now a comparison between the flat plate and the dented plates is allowed. From the results here it can be concluded that dented plates, in the geometrical configuration tested here at a free-stream velocity of 5m/s do not result in reduced drag. For all dented plates the drag increases with respect to the flat plate. Thus probably it is justified to assume that in section 3.5.4 also the dented plated will show an increase in drag with respect to the flat plate.

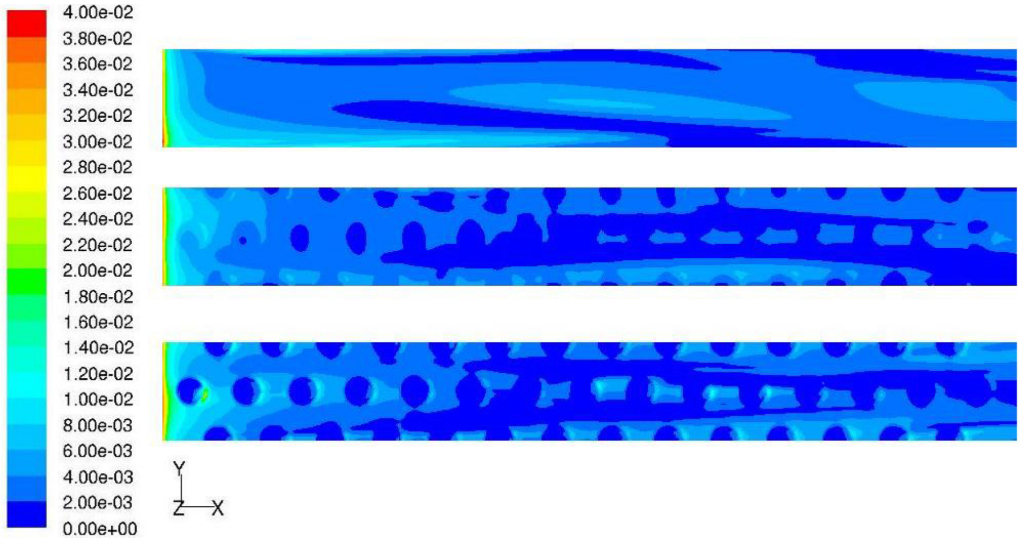

Figure 3.26: Skinfriction of the plates at t=0.5s.

Why does this drag increases? To answer this question a closer look is taken here, more then is done in the previous simulations, to the drag distribution. Table 3.8 shows the division of the drag coefficient in a viscous and a pressure drag component. Of course the pressure drag of flat plate is zero. The shallow dented plate shows an increase of both the viscous and the pressure drag with respect to the flat plate. The deep dented plate shows an increase of the total drag coefficient. This increase is caused by the pressure drag. The viscous drag is reduced with respect to the flat plate, because of the areas with reversed flow (negative skinfriction). It is not satisfactory to known if and how drag changes, but it is relevant to know in which part of the dents the drag changes. Therefore the surface of the dents is divided into four quadrants to investigate to influence of each quadrant to the skinfriction drag and pressure drag.

Simulation Number	Dent Depth [mm]	$C_{D_{total}}$ [-]	$C_{D_{visc.}}$ [-]	$C_{D_{pres.}}$ [-]
4-01	0.000	0.00304	0.00304	0.00000
4-02	0.343	0.00317	0.00314	0.00003
4-03	3.000	0.00343	0.00270	0.00073

Table 3.8: Total, viscous and pressure drag of the plates.

In this series of simulations the drag coefficients averaged over time ($0.2s < t < 1.0s$) and over dents (dent no. 6 to 15) are calculated. Each dent is divided into four quadrants, called I, II, III and IV, as is seen in figure 3.20. In table 3.9 the average values for the total, viscous and pressure coefficients, averaged over time ($0.2s < t < 1.0s$) and over dents (dent 6 to 15), are presented. This table needs some explanation. The coefficients in the table are grouped in small 2x2 groups. Each group of four numbers represents a dent. These four numbers are geometrically arranged in the table in a way the flow is coming from above. For example: if $C_{D_{total}}$ of the dented plate (0.343mm) is considered, the flow creates drag coefficients of 0.0000453 (left) and 0.0000456 (right) in the forward half of the dent and 0.0000497 (left) and 0.0000501 (right) in the rearward half of the dent.

	Flat 0.000mm				
$C_{D_{total}}$	0.0000443	0.0000473			
	0.0000433	0.0000472			
$C_{D_{visc.}}$	0.0000443	0.0000473			
	0.0000433	0.0000472			
$C_{D_{pres.}}$	0.0000000	0.0000000			
	0.0000000	0.0000000			
Average values over the four quadrants $C_{D_{total}}$=0.0000453 $C_{D_{visc.}}$=0.0000453 $C_{D_{pres.}}$=0.0000000					
	Depth 0.343mm			Δ0.343mm [%]	
$C_{D_{total}}$	0.0000456	0.0000453		+0.7	+0.1
	0.0000501	0.0000497		+10.8	+9.8
$C_{D_{visc.}}$	0.0000450	0.0000448		-0.5	-1.1
	0.0000495	0.0000491		+9.4	+8.5
$C_{D_{pres.}}$	0.0000005	0.0000006		n.a.	n.a.
	0.0000006	0.0000006		n.a.	n.a.
	Depth 3.000mm			Δ3.000mm [%]	
$C_{D_{total}}$	0.0000450	0.0000468		-0.6	+3.5
	0.0000586	0.0000602		+29.5	+33.0
$C_{D_{visc.}}$	0.0000379	0.0000395		-16.2	-12.8
	0.0000428	0.0000443		-5.3	-2.1
$C_{D_{pres.}}$	0.0000175	0.0000172		n.a.	n.a.
	0.0000147	0.0000135		n.a.	n.a.

Table 3.9: Division of the drag coefficients in the dent quadrants.

The flat plate is expected to show an equal distribution for the coefficients, since the quadrants are geometrically identical. But this is not true according to the numbers in table 3.9, where a difference in the coefficients is shown between the left and right quadrants. This is probably due to the irregular flow over the flat plate, which causes an imbalance when averaging the coefficients like is done here. It is not correct to compare these quadrants to the quadrants of the dented plate, because the differences found will be caused by the flat plate simulation and not by the dents in the dented plates. For correctly comparing the quadrants of the dents the average coefficients of the quadrants of the flat plate are used.

When the drag coefficients of the dented plates are compared with the averaged coef-

ficients from the flat plate, the total drag coefficients will increase for both dents with respect to the flat plate. But the way this drag increase originates is different for both dented plates.
For the shallow dented plate (h_c =0.343mm) the viscous drag decreases in the forward part of the dent with 0.5% and 1.1% (left and right) and increases in the rearward part of the dent 9.4% and 8.5% respectively. The pressure drag increases in all part of the dent. At the positions where the flow exits the dent, the skinfriction is increased. This is because the pathlines of the flow bent downwards, by the diverging geometry of the forward part of the dent, encounter the converging geometry of the rearward part of the dent. Here an area of dense pathlines is formed, which cause the skinfriction to increase, see figure 3.27. At the position where the flow enters the dent, the opposite happens. Here the pathlines converge a bit, creating a small decrease of skinfriction. The increase of skinfriction is the rearward part of the dent is much larger than the decrease is the forward part, increasing the total skinfriction coefficient.The pressure drag coefficient also increases, due to the fact that the flow through the dent has a vertical component, which results in pressure drag.
The deeply dented plates shows a separated flow pattern. This results in reversed flow, which causes a large area with negative skinfriction. This separated area is situated in both the forward and the rearward part of the dent, see figure 3.28. The rearward part, similar to the attached flow situation, still experiences some skinfriction increase due to the flow exiting the dent, this is why the skinfriction coefficient decreases more in the forward quadrants of the dent. The separated flow however, causes the pressure drag to increase more than the skinfriction decreases, resulting in an increase of the total drag.

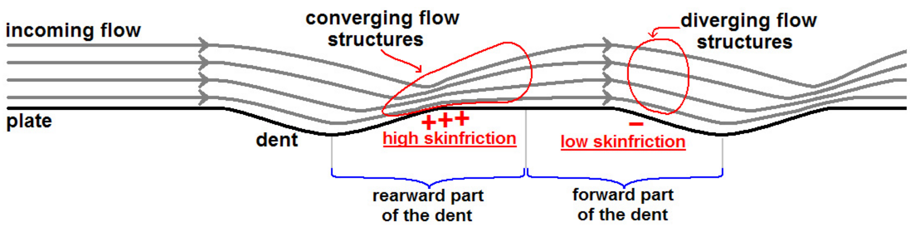

Figure 3.27: For attached flows the skinfriction is increased due to the compression flow where the flow exits the dent.

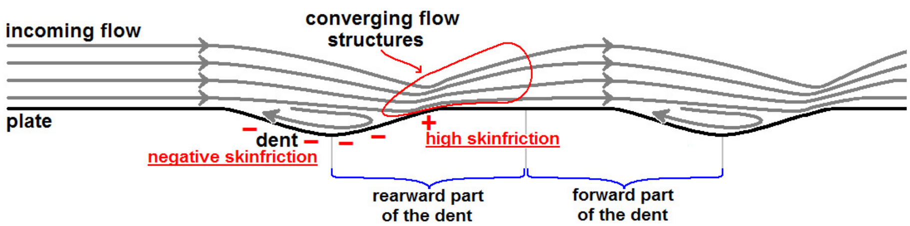

Figure 3.28: For detached flows the skinfriction is decreased due to the reversed flow in the separated areas.

Figure 3.29 shows the wall shear stress in x-direction. This figure shows the same behaviour of the wall shear stress as encountered in the previous section. The shear stress drops where the flow enters the dent. For deep dents the flow separates and creates negative shear stresses. At the position where the flow exits the dent, the shear stress of the dented plates will be larger than the shear stress of the flat plate.

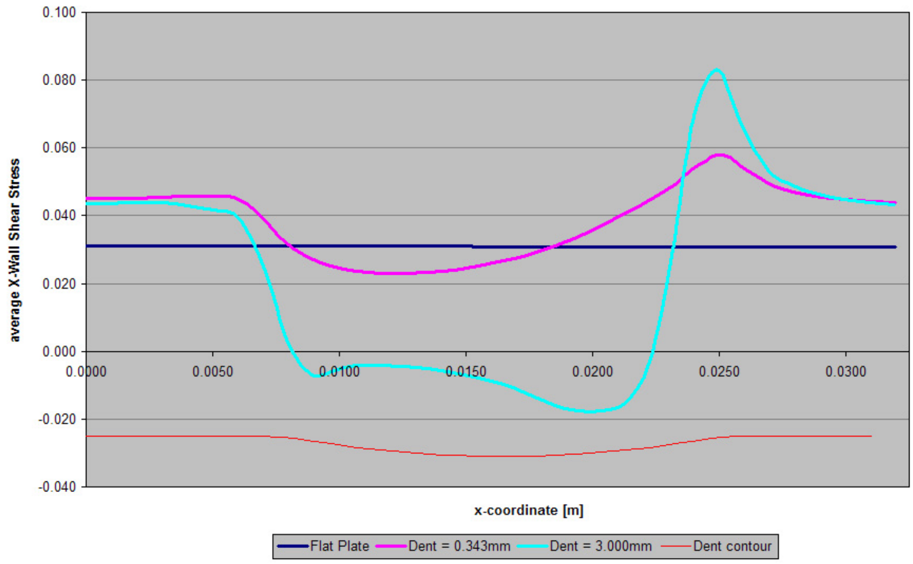

Figure 3.29: Average wall shear stress in x-direction of the plates.

3.5.5 Simulations with Free-Stream Velocity of 50m/s.

This series of simulation is done to test the dented surfaces at a velocity higher than velocities suited for practical use. For example high speed trains, like the one mentioned in an article in Der Spiegel [Wüst, 2004]. These simulations are done to investigate the behaviour of high velocity flow over dented surfaces. Another goal of this series is to check if the characteristic flow patterns of attached and detached flow, which were encountered in section 3.5.3 and 3.5.4, still occur at high velocities. It is also important to know how the drag change will be for high velocities (U=50m/s). Maybe, here the dents will result in drag reduction, unlike for low velocities (U=5m/s).
A remark has to be made about the position of this series of simulations in this report with respect to the chronological place of this series within the performance of all simulations. This series of simulations is performed, not as fifth series as expected from the fifth position of this series in this report, but as fourth. Thus this series is performed between the series presented in the two previous sections (3.5.3 and 3.5.4). The idea for the simulation series with the split plate arose after this series was performed. Thus the analysis made in the previous section, about the changes in viscous and pressure drag coefficient in the quadrants of the dent, can not be made in this section for the simulation series with a free-stream velocity of 50m/s.

The geometry used here were chosen by reviewing the simulations in section 3.5.3. The flat plate has to be tested to provide the reference simulation. Further two characteristic flows were encountered, attached and detached flow. Two plates are investigated which each have shown one type of these characteristic flow patterns. The dented plates tested have dents with a depth of h_c =0.343mm (attached flow for U=5m/s) and h_c =3.000mm (detached flow for U=5m/s).

The application of the high velocity has consequences for the mesh used in the simulations. Since the velocity is a parameters determining the z^+-value, increasing the velocity will result in a decreased height for the cell size if the z^+-value must remain constant. This causes the number of cells in the domain to increase. The height of the first cell becomes:

$$h_{first} = \frac{17.21 z^+ L}{Re_L^{\frac{13}{14}}} = \frac{17.21 \cdot 1 \cdot 0.5}{(1.71 \cdot 10^6)^{\frac{13}{14}}} = 0.000014m = 0.014mm$$

The total number of cells for the mesh will be: length×width×height = 501×58×83 = 2,411,814 cells, which is approximately 145,000 cells more then was used in simulations with a free-stream velocity. This will increase the time to complete the simulation. The size of the timesteps in decrease because of the increase in free-stream velocity, from Δt =0.05s for U=5m/s to Δt =0.002s for U=50m/s.

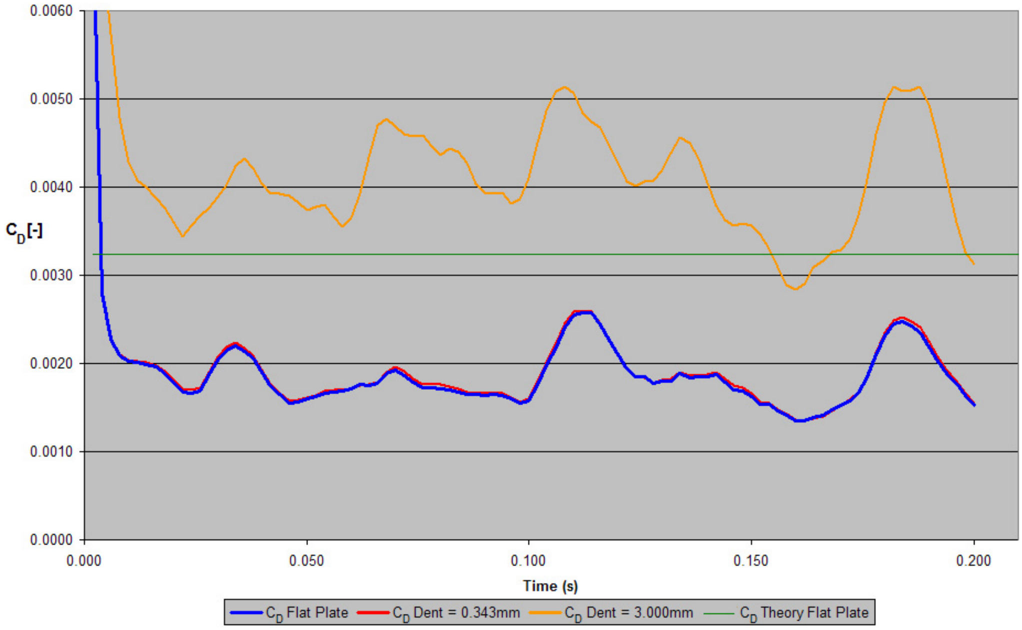

Figure 3.30: Drag coefficients for the plates with a free-stream velocity of 50m/s.

Simulation Number	Dent Depth [mm]	$C_{d,calc}$	ΔC_d w.r.t. $C_{d,theory}$ [%]	ΔC_d w.r.t. $C_{d,calc,flatplate}$ [%]
5-01	Flat	0.00182	-43.8	n.a.
5-02	0.343	0.00184	n.a.	+1.1
5-03	3.000	0.00409	n.a.	+124.7

Table 3.10: Drag coefficients for the dented plates for plates subjected to a flow with a free-stream velocity of 50m/s.

The development of the drag coefficients is shown in figure 3.30. Large fluctuations appear in the development of all drag coefficients. Due to these large fluctuations it is required to simulate the flow over a large time interval to have an average which represents the correct value. Here an interval of 0.20s is simulated, because of limited calculation time available. The average values are shown in table 3.10, these coefficients calculated by averaging the drag coefficients over the time interval $0.04 \leq t \leq 0.20$. The theoretical drag coefficient is $C_{D_{theory}}$=0.003237. For calculation of $C_{D_{theory}}$ see section C.5. The large difference between the theoretical are simulated drag coefficient of the flat plate is remarkable, here a difference in drag with respect to the theoretical flat plate drag of -43.8% appears. This large difference also appeared in the previous section, due to the UDF at the velocity inlet of the domain.

Simulation Number	Dent Depth [mm]	$C_{D_{total}}$ [-]	$C_{D_{visc.}}$ [-]	$C_{D_{pres.}}$ [-]
5-01	0.000	0.00172	0.00172	0.00000
5-02	0.343	0.00174	0.00170	0.00004
5-03	3.000	0.00373	0.00193	0.00179

Table 3.11: Total, viscous and pressure drag of the plates, free-stream velocity is 50m/s.

The difference between the flat plate and the shallow dent, with a depth of 0.343mm, is very small (1.1%), smaller then was calculated for a flow velocity of 5m/s where a difference of +4.4% was encountered. The flow through the dent is attached, similar to encountered in the previous sections for a free-stream velocity of 5m/s. It seems that the dents disturb the flow in a less negative manner for higher velocities. However for the deep dent (3.000mm), where the flow separated the drag increase is substancially larger for high velocities. The situation still is comparable as sketched in figure 3.27.
The wall shear stress in x-direction, figure 3.31, shows for these simulations approximately the same trends as encountered in the previous section for a free-stream velocity of 5m/s. For the shallow dent, the behaviour is almost identical, but for the deep dent is behaviour differences. The peak-values are still at the same position in the dent, but they are much higher compared to the flat plat values. This will result in much higher wall shear stresses near the exit of the dent.
Now the drag coefficient is split into a viscous and a pressure drag coefficient. The shallow dent shows similar behaviour as is encountered with velocities of 5m/s. The viscous drag coefficient is not changing much for attached flows. Compared to the viscous drag coefficient of the flat plate here viscous drag coefficient is decreased a little. The difference is that small that it is not clear is this is due to actual viscous drag reduction or due to incorrect averaging caused by the large fluctuations in the flow. The pressure drag increases by a small amount, due to the fact that the fluid flowing over the plate will have a vertical component a the positions where the dents are situated. This, small, vertical component causes a small increase of the pressure drag coefficient.
The deeply dented plate (3.000mm) shows different behaviour for U=50m/s than was encountered with a free-stream velocity of 5m/s. The total drag is more than twice the drag of the flat plate. Here both the viscous and the pressure drag coefficients increase for the dented plate with respect to the flat plate. The viscous drag increases because the very high skinfriction near the exit of the dents (See figure 3.32) is not compensated for by the negative skinfriction in the dent caused reserved flow. It seems that the exit of the dent is to steep. A more gradually slope of the backward of the dent should result

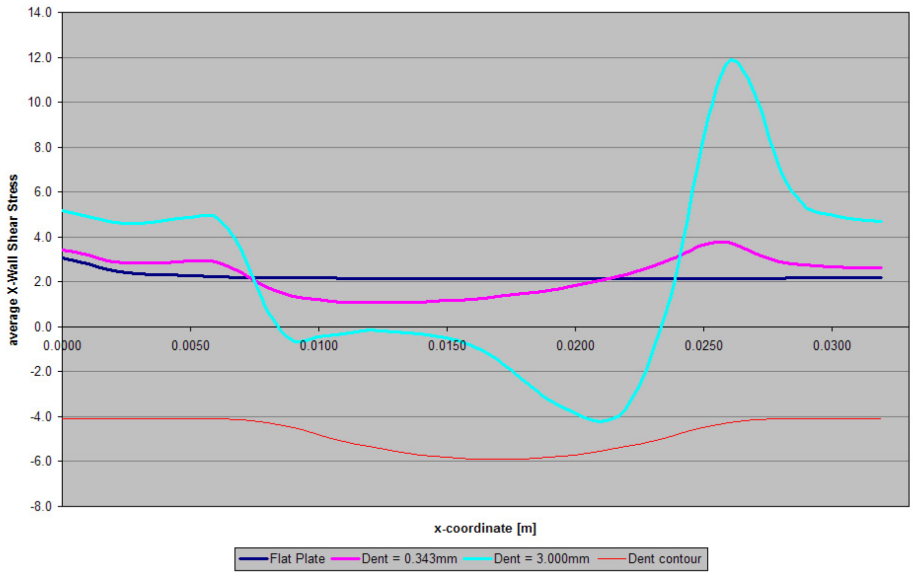

Figure 3.31: Average wall shear stress in x-direction of the plates for a free-stream velocity of 50m/s.

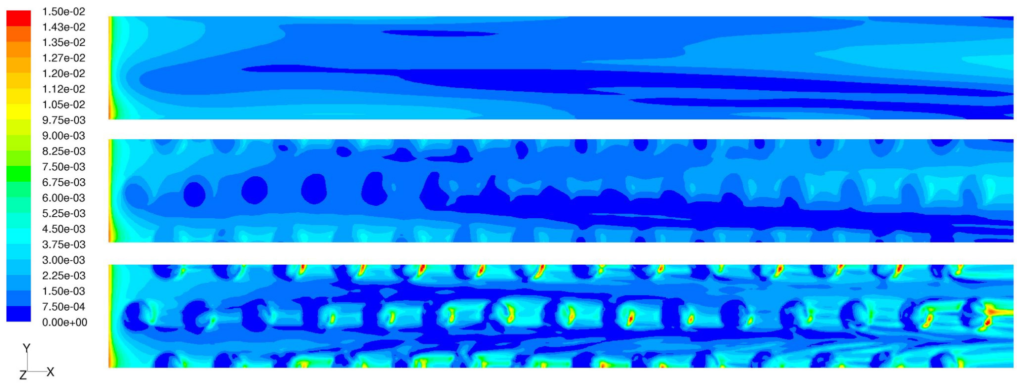

Figure 3.32: Skinfriction coefficient of the plates for a free-stream velocity of 50m/s at 0.2s.

in lower skinfriction. This geometry should be considered for future simulations. The next section (Section 3.5.6) is dedicated to these kind of dents. The pressure drag is very high for this configuration. Due the combination of high velocity flow and separated flow structures large vertical velocity components emerge. In section 3.5.3, figure 3.19 features pathlines of a particle with a free-stream velocity of 5m/s, this pathline is a smooth line. In figure 3.33 similar particle path is shown for a free-stream velocity of 50m/s. This path is not smooth but irregular, also is shows more complicated three dimensional path of the particle.
Generally it is concluded that for 50m/s, just like for 5m/s, no drag reduction is encountered for the dent geometries tested here. The simulations show a small increase in drag for the dent with a depth of 0.343mm and a very large drag increase for the dent

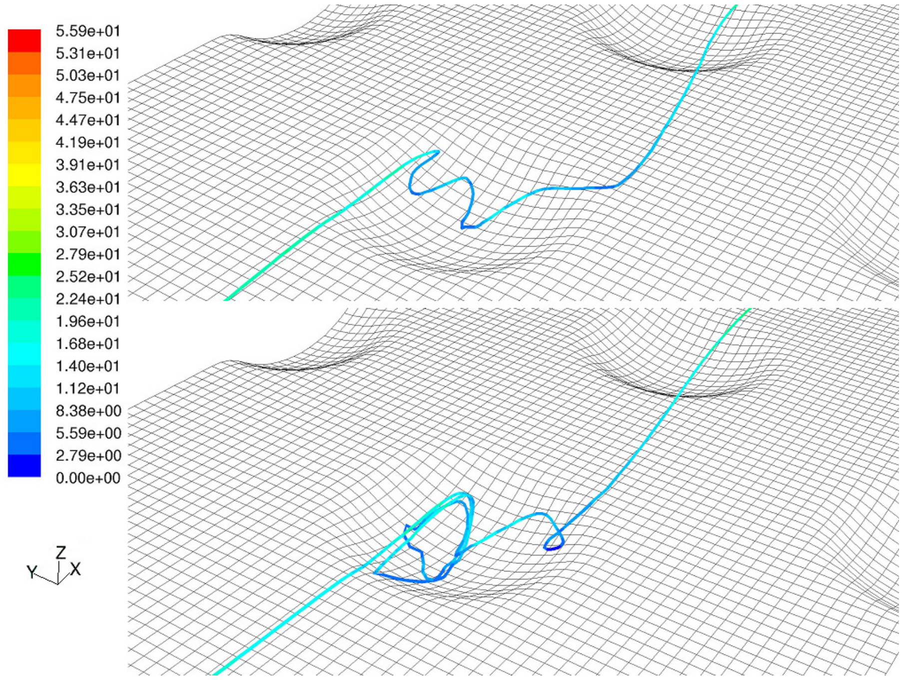

Figure 3.33: Pathlines of two particles through a dent (depth 3.000mm), the flow is detached from the plate and a vortex structure is created.

with a depth of 3.000mm. In this series of simulations the same physical phenomenon (attached and detached flows, vortices) are found to exist as are present in the previous section.

3.5.6 Simulation with a Dent with Non-Rotational Symmetric Cross-Section.

The research of flows through non-rotation symmetrical dent shapes is not described by literature as far as known. Still this can be of great importance for optimizing the drag reducing capabilities of dented surfaces.
This section will contain data for a simulation done with a dent with a non-rotational symmetry. In this section the geometry will be presented in a form of a single algebraic formula. The results of the simulation of one dent-geometry is given. At the end of this section some suggestions will be given to further develop the geometry of the dent.

Geometry of the Non-Rotational Symmetric Dent.

The geometry is presented by a single algebraic formula which defines the complete geometry of the three dimensional dent. The curvature of the rotational symmetric dent, which is used in all simulations done before, is used as the starting point for building the dent. This shape is represented by the dark-blue line in figure 3.34. When this shape is compressed or stretched in radial direction (other lines in figure 3.34) then shapes with smaller or larger inclinations are formed. When these are combined a lot of different cross-sections can be made. Figure 3.35 features a number of possible cross-sections that can be obtained, (a) is the original rotation symmetrical cross-section. A cross-section with a very steep front part and a shallow backward part is depicted at (b). In figure 3.35 the cross-sections are not drawn to scale, the depth and curvature are exaggerated for clarification purposes.

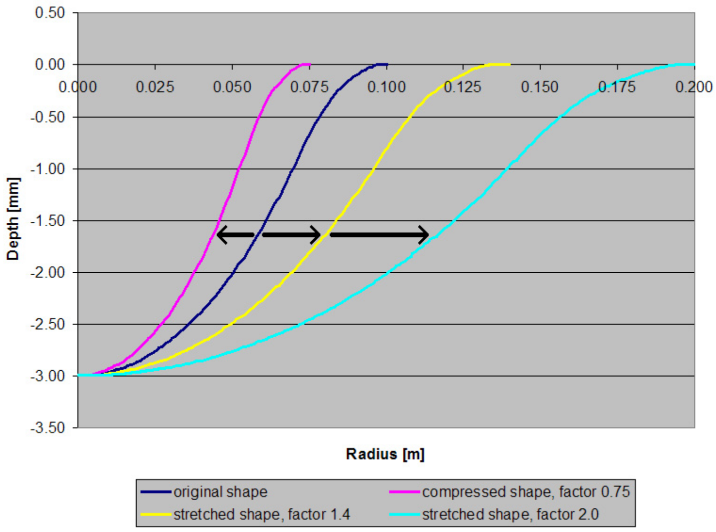

Figure 3.34: Compressing and stretching of the original shape of the cross-section on the dent.

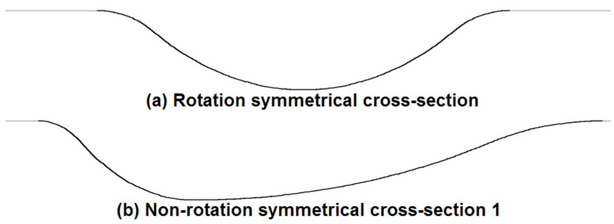

Figure 3.35: Different cross-sections with compressed and/or stretched curvatures.

Now the cross-section shown in figure 3.35 have to be turned into three dimensional dents. Appendix F contains the procedure of building a three-dimensional dent shape. This shape is determined by the depth of the dent and by two pre-defined stretch-factor. These three parameters are needed as input for an m-file, with which Matlab produces the dent geometry. This m-file, as well as a more elaborate explanation of how the dent geometry is created is included in appendix F.

Simulation with the Non-Rotational Symmetric Dent.

The idea behind this simulation is to maximize the negative skinfriction in the separated area and minimize the pressure drag.
The geometry is of type (b) in figure 3.35. The depth is chosen to be h_c =3.000mm, because in previous simulations this always resulted in separated flow patterns. The

forward part of the dent, where the flow enters the dent, is radially compressed (factor $F_1 = 0.5$) to allow the flow to separate almost immediately. The large separation area should create a large surface with negative skinfriction, which should be the main cause of the total drag reduction. The backward part of the dent is stretched (factor $F_2 = 2$). Here the less steep slope of the dent should result in low pressure and low skinfriction as the fluid flow exits the dent. An example of the plate tested here is shown in figure 3.36.

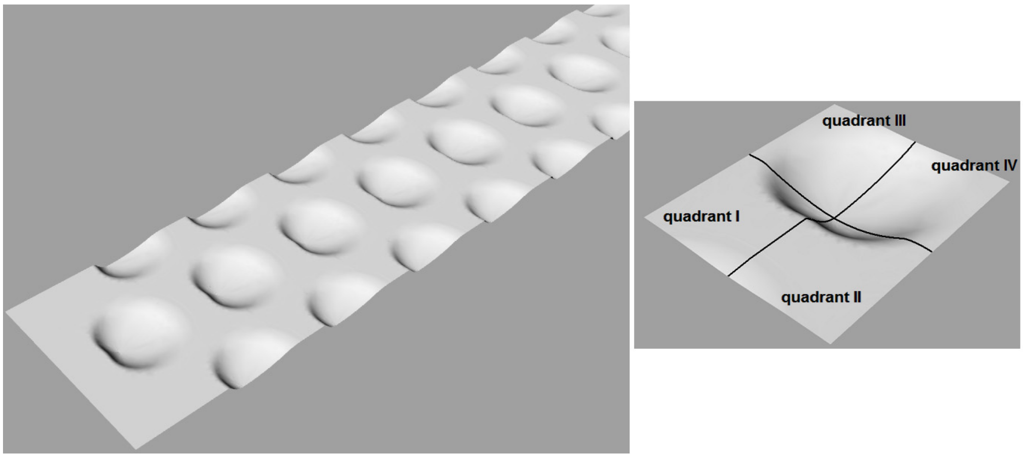

Figure 3.36: Plate with non-rotational symmetric dents (left), the division of the dent into four quadrants (right).

Since the velocity inlet of the domain is defined by a UDF, like done in the section 3.5.4, it is likely to compare the dented plate tested here to the simulations done in section 3.5.4. The development of the drag coefficient is shown in figure 3.37. It is noticed that although the drag of the non-rotational symmetrical dent is much higher, the development of the drag coefficients follow approximately the same trend. From table 3.12 is becomes clear that the drag is 73% higher for the non-rotational symmetric with respect to the flat plate. The difference between the simple dent and the non-rotational symmetric dent is 53.9%. It is clear that the objective of drag reduction by changing the shape of the dent is not yielded by this geometry. Of course the cause of this unexpected result has to be clarified.

Simulation Number	Dent Depth [mm]	$C_{D_{calc.}}$	ΔC_D w.r.t. $C_{D_{theory}}$ [%]	ΔC_D w.r.t. $C_{D_{calc.,flatplate}}$ [%]
4-01	Flat	0.00338	-24.0	n.a.
4-03	3.000	0.00380	n.a.	+12.4
6-01	Asym. 3.000	0.00585	n.a.	+73.1

Table 3.12: Drag coefficient for the non-rotational symmetric dented plate w.r.t. flat and simple dented plates.

First the skinfriction of the non-rotational symmetric dented plate is plotted in figure 3.38 for t=0.5s. Compared to figure 3.26 the skinfriction for the non-rotational symmetric dents is very high near the exits of the dents. Also in the dents itself the skinfriction is slightly higher. Figure 3.26 shows large areas of low skinfriction between the rows of

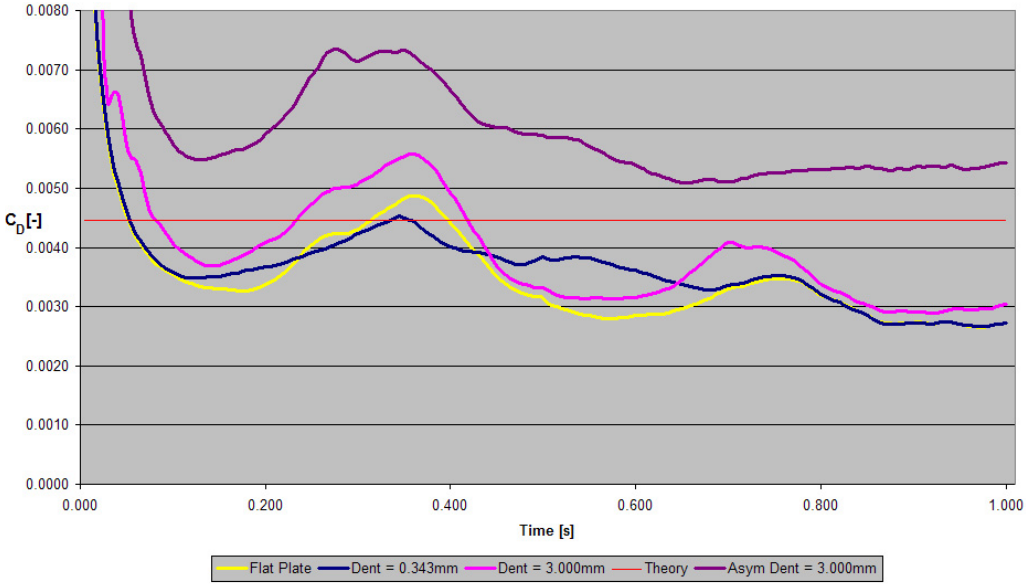

Figure 3.37: Drag coefficient of the non-rotational symmetrical dent.

dents (large dark-blue areas) for the simple 3.000mm deep dent in section 3.5.4, these areas are much smaller in for the dent tested in this section, see figure 3.38.
The wall shear stresses in x-direction the middle of the dent are plotted in figure 3.39, this figure also features the wall shear stresses in x-direction obtained in section 3.5.4. The wall shear stress develops all dents approximately the same. But this not shown in the figure because of the displacement of the non-rotational symmetric dent with relation to the simple dents. Due to the stretched geometry of the dent, the dented area in the forward quadrants is much smaller than the dented area in the rearward quadrants. All dent show a decrease of wall shear stress when the flow enters the dent. If the flow separates, like it does in the non-rotational symmetric dent, the wall shear stress will become negative. In the rearward part of the dent, where the flow exits the dent, the wall shear stress increases to a peak value just after the dent. Because the non-rotational symmetric dent stretched up to the end of the rearward quadrants (III and IV), the maximum wall shear stress is obtained in the forward part of the dent downstream. The magnitude of the negative wall shear stress indicates a stronger separated flow, decreasing the drag more than the simple dent geometry does. But the area where the wall shear stress is larger than for the simple dent is larger as well as the magnitude of the peak is. This will cause the drag to increase in this area. The sum of these two areas will determine is the wall shear stress will increase or decrease and here for the non-rotational symmetric dent the total wall shear stress increases.
If the drag is split into viscous (skinfriction) drag and pressure drag, see table 3.13, then it is also noticed that the viscous drag for the non-rotational symmetric dented plate is much higher than for the flat plate (+34.5%) and even higher compared to the 3.000 deep simple dent (+51,5%). This was also concluded from the wall shear stresses were high maximum stresses were encountered.

Each dent consists of four quadrant, see figure 3.36. For these quadrants the averages of

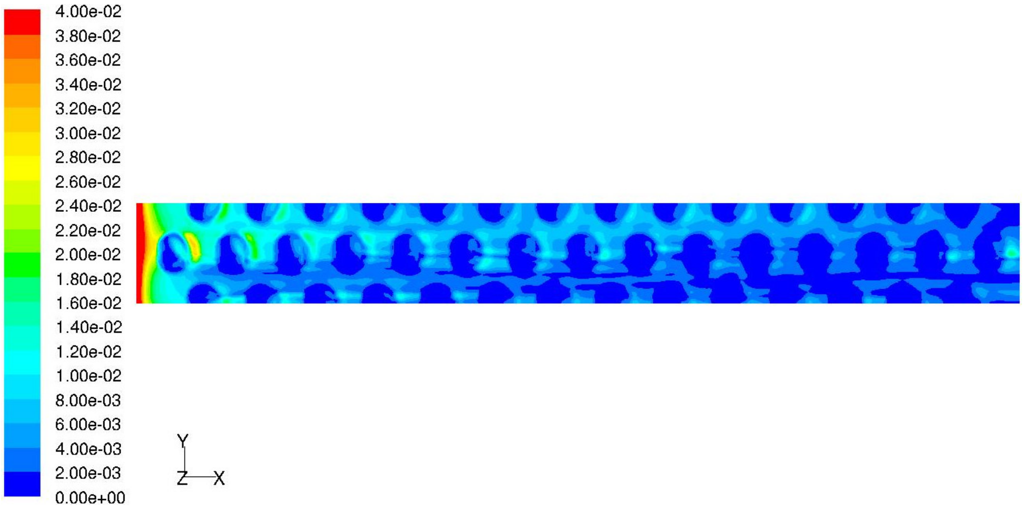

Figure 3.38: Skinfriction coefficient of a plate with a non-rotational symmetrical dent; t=0.5s.

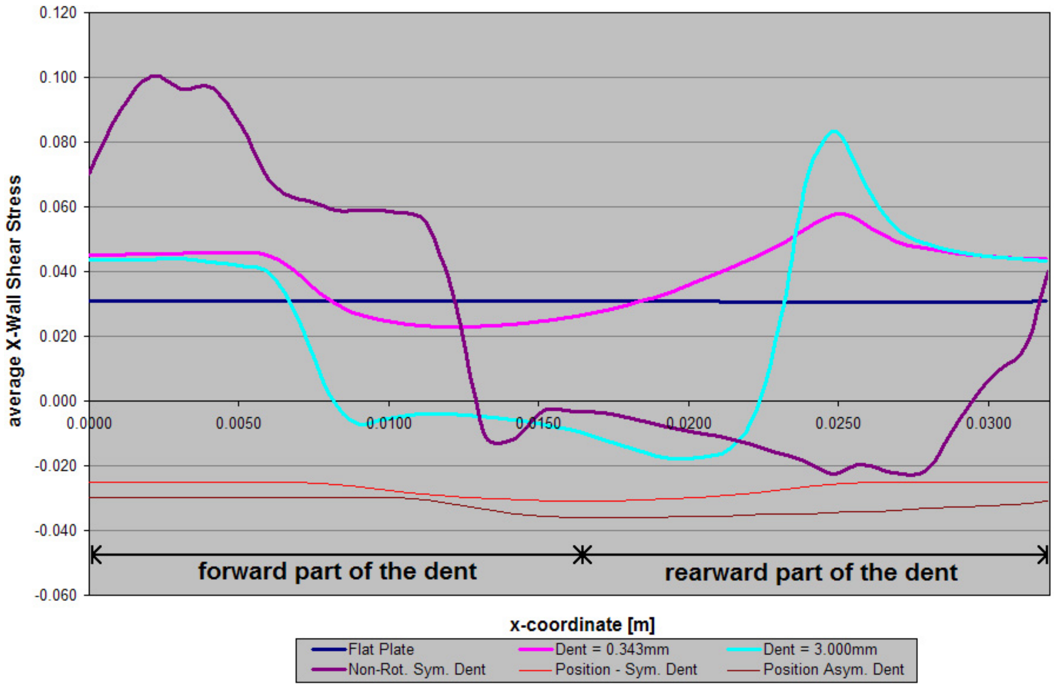

Figure 3.39: Wall shear stress in x-direction of the non-rotational symmetrical dent.

the viscous and pressure drag coefficient, in time ($0.2s \leq t \leq 1.0s$) and for dents 6 to 15, are depicted in table 3.14, together with the differences between the coefficients of the non-rotational symmetrical dented plate and both the flat and the simple dented plate. The total drag increases, especially in the front part of the dent, quadrants I and II. Here the drag increases, because the separated area, with negative skinfriction, is small since

Simulation Number	Dent Depth [mm]	$C_{D_{total}}$ [-]	$C_{D_{visc.}}$ [-]	$C_{D_{pres.}}$ [-]
4-01	0.000	0.00304	0.00304	0.00000
4-03	3.000	0.00343	0.00270	0.00073
6-01	Asym. 3.000	0.00579	0.00409	0.00170

Table 3.13: Total, viscous and pressure drag of the non-rotational symmetrical dented plate.

only a small part of the dent is placed in these quadrants. The maximum values for the skinfriction are situated in these quadrants, because these maximum values are situated downward from the end of the dent, which is just after the rearward quadrants, placing the high friction area in the forward part of the next dent. The pressure drag coefficient does not change much (+8.0% and -13.1%) with respect to the simple dented plate, probably because area of separated flow is smaller, but due to the steeper inclination of the dent, the separation is more severe, resulting in approximately the same of pressure drag coefficient as was encountered for the simple 3.000mm dent.
A large separated area is present in the rearward quadrants of the dents, quadrant III and IV. This results in a large area with negative skinfriction. A viscous drag reduction of ±44%, with respect to the flat plate, and ±42%, with respect to the simple 3.000mm deep dented plate, is obtained. In this area the pressure drag coefficients increases with more than 100% with respect to the simple 3.000mm deep dented plate, due to the vertical velocity components which are caused by the vortices in the separated areas.

	Non-rotational symmetric dent		Difference w.r.t. flat plate [%]		Difference w.r.t. 3.000mm dent[%]	
$C_{D_{total}}$	0.0000748	0.0000738	+65.2	+63.0	+66.1	+57.5
	0.0000660	0.0000606	+45.9	+33.8	+12.7	+0.6
$C_{D_{visc.}}$	0.0000671	0.0000674	+48.2	+48.8	+77.0	+70.7
	0.0000257	0.0000249	-43.2	-45.1	-40.0	-43.9
$C_{D_{pres.}}$	0.0000077	0.0000064	n.a.	n.a.	+8.0	-13.1
	0.0000403	0.0000357	n.a.	n.a.	+156.2	+124.8

Table 3.14: Division of the drag coefficients in the dent quadrants for comparing the quadrants of the non-rotational symmetrical dented plate to the flat plate and the simple dent with h_c =3.000mm.

Chapter 4

Windtunnel Experiments.

4.1 Introduction.

The phenomenon of DSE is also studied in the windtunnel. In this section the windtunnel tests are described. In section 4.2 the windtunnel used in the experiments is described, while section 4.3 contains information about the measurements and the programs which collect the data. In 4.4 discusses the geometry of the plate and the dents are described. Section 4.5 the procedures for taking the measurements are explained. Finally in section 4.6 the results of the force measurements and velocity profile measurements are presented.

4.2 Windtunnel.

The windtunnel tests are performed in the M-tunnel, located at the Aerodynamics department of the faculty of Aerospace Engineering. The M-tunnel is a tunnel which can be used in two configurations: with an open or a closed circuit. Here the open circuit configuration is used. The maximum speed of the windtunnel is 35m/s. In the configuration of the closed circuit the maximum velocity of the windtunnel is higher, approximately 50m/s, but this is not required for these tests. The test section has a width and a height of 0.40m×0.40m, the length of the section is 1.0m. The tunnel produces a low amount of turbulence. A schematic picture of the windtunnel layout is shown in figure 4.1, figure 4.10 shows a photograph of the measurement section of the windtunnel.

4.3 Measurement Systems.

To be able to measure the drag of the installed plate at various Reynolds numbers (by varying windtunnel velocity) various quantities have to be measured.

1. The windtunnel velocity is calculated from of the dynamic pressure measured in the tunnel. The dynamic pressure is measured by a Pitot-static probe, which is placed in the tunnel, just in front of the measurement section. The measurement instrument is a Mensor Digital Pressure Gauge 2400. The measurement signal is transferred, with LabVIEW, into the windtunnel velocity, as explained later in this section.

2. The velocity in the boundary layer is calculated from of the total pressure measured by a flattened pressure probe. The height of the probe is adjustable, thus the velocity profile can be measured. The measurement instrument is a Mensor Digital Pressure Gauge Model 2101 SN531918, range 0 to 0.5 psig. The pressure signal from the probe is transferred, with LabVIEW, into the probe velocity as explained later in this section.

3. The temperature is measured by a thermometer, which is placed in a side of the settling chamber. Since velocities calculated from pressures require also a temperature input, the temperature is inserted in the LabVIEW programs. This happens manually, although it is recommended to automate this process.

4. The drag of the plate is measured by a horizontal force balance, installed underneath the testsection, see figure 4.1.

5. The flow over the plate needs to be turbulent. The flow is made turbulent by placing zig-zag tape onto the deflector plate, just in front of the dented plate, see figure 4.1. This deflector plate will guide all fluid over the plate. To check if the flow is turbulent, the noise created by the flow is measured by a microphone. Laminar flow produces a monotone noise; turbulent flow however produces a fluctuating noise. Thus with the microphone it is possible to establish the turbulence level.

As mentioned before programs were developed to calculate, visualize and write the measurement data. The software used here is LabVIEW 8.2. In total three different LabVIEW programs are used in the measurements. These three programs are explained here. For more information the LabVIEW User Manual [Nat.Instr. Corp., 2006] should be consulted.
The first program (or Virtual Instrument as it is called in LabVIEW), called *"Data - Speed_Force.vi"*, is used for the force measurements. A LabVIEW-program consists of a frontpanel and a block diagram. The frontpanel is the graphical interface when the program is running and is depicted in figure 4.2. The block diagram holds the blocks that receives, calculates and exports information. The block diagram in this program consists out of three blocks: one block measuring the tunnel velocity, one block for the force measurements and a final block for writing the measurements to a file.
The block for measuring the speed of the tunnel is displayed figure 4.3. Part A (encircled in the figure) represents the communication with the pressure measuring device, the Mensor DPG 2400. This part sends a communication string to the device and receives a string with the dynamic pressure. The velocity is calculated, in part B, out of the total pressure, the static pressure and temperature (both require manual input in the frontpanel). A local variable is made from the signal with the velocity (C). This local variable is used as input in the write block. An indicator (D) represents the velocity at the frontpanel. The dynamic pressure is also converted to a local variable and represented on the frontpanel, by an indicator.
The drag force is measured and calculated in another block, see figure 4.4. A Data Acquisition assistant (DAQ-assistant) reads the signal from the force-balance. This signal is scaled by a factor. The offset is not used here, because the offset is calculated in the post-processing. The calibration coefficients are not used here, the signal does not need to be calibrated. The force parameter is stored as local parameter and it is displayed on the frontpanel by an indicator.
Each block in the block diagram is placed inside a while-loop, this is represented by the thick grey line (see figures 4.3 to 4.9) encircling the content of the block. This is

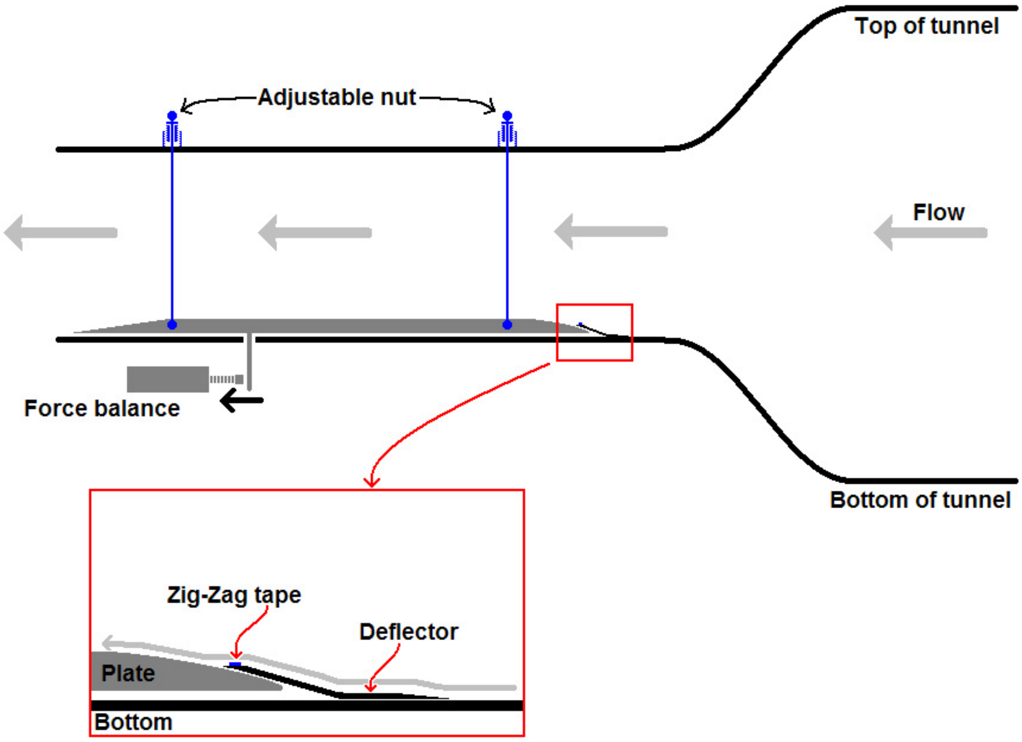

Figure 4.1: Schematic layout of the windtunnel.

required to repeat the measurements until the measurement is stopped by the user.

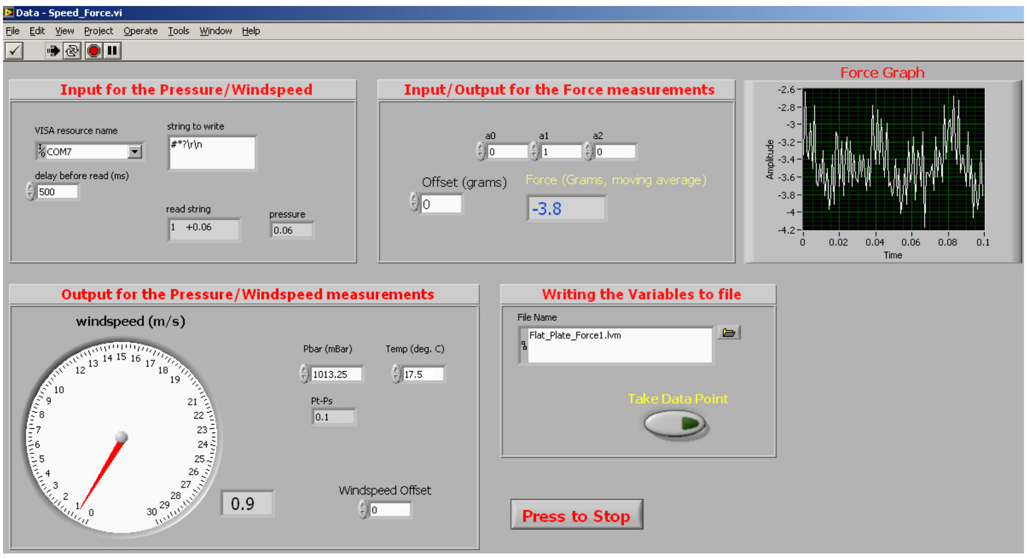

Figure 4.2: Frontpanel of LabVIEW force measurement program.

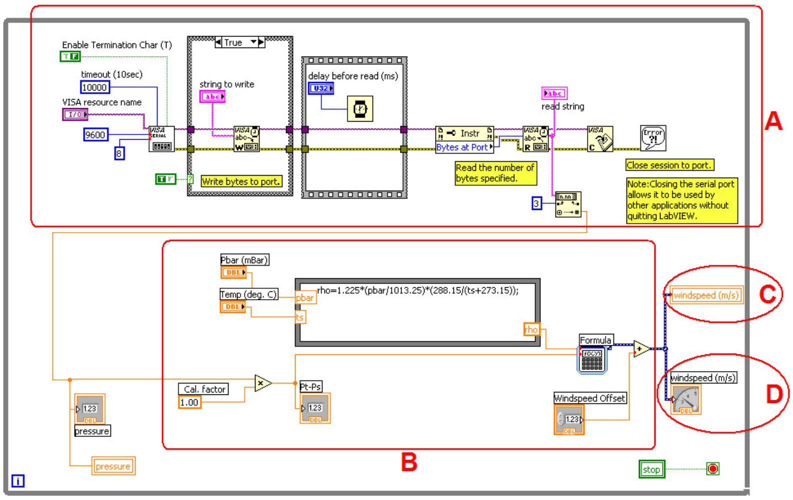

Figure 4.3: Part of the block diagram: Velocity of the tunnel.

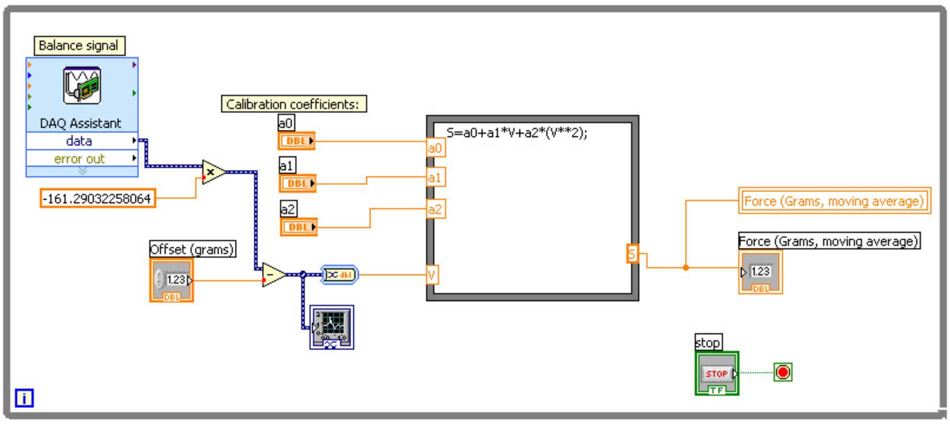

Figure 4.4: Part of the block diagram: Drag force on the plate.

The third and last block in this program is the block that produces the output-file of the measurement, see figure 4.5. In this program the output-file contains four parameters: the velocity in the tunnel, the dynamic pressure in the tunnel, the drag force of the plate and the drag-coefficient of the plate. The first three parameters are obtained, via local variables, from the two previous blocks (A). The drag coefficient is calculated here (B). Also the four parameters are written to an output file (C). These actions are placed in a true/false loop, which is controlled by a switch (D), which is visible at the frontpanel.
The second program, called *"Data - Speed_Pressure - Simple.vi"* is used when boundary layer profiles are to be measured. The frontpanel is displayed in figure 4.6. This program consists of three blocks: one block measuring the tunnel velocity, one block for writing the measurements to a file and a final block for the velocity measurements of the probe. The first two are identical the corresponding blocks in the force measurement program.
The block which measures the velocity of the probe is added here. (See figure 4.7) The pressure form the digital pressure measurement device (Mensor 2101) is read by an

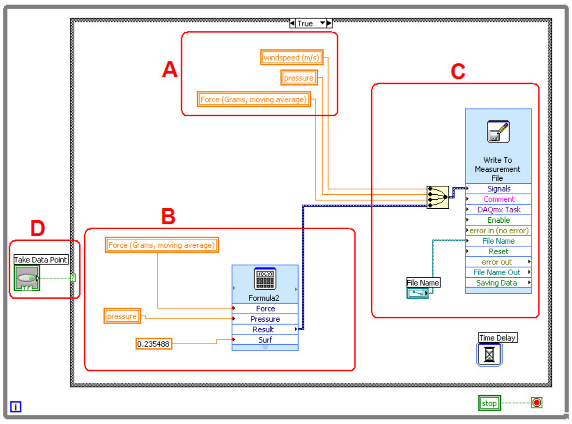

Figure 4.5: Part of the block diagram: Writing the output file.

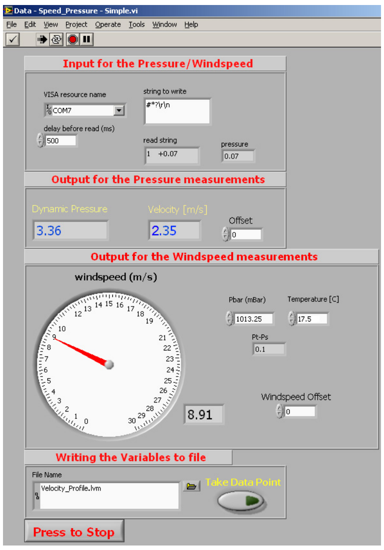

Figure 4.6: Frontpanel of LabVIEW velocity probe measurement program.

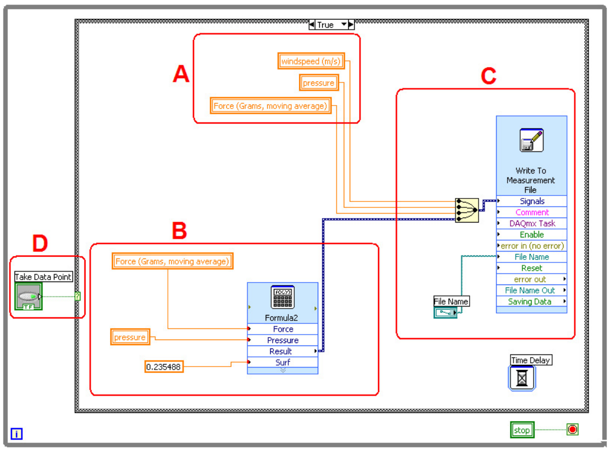

Figure 4.7: Part of the block diagram: Probe velocity.

Instrument I/O Assistant. This device does not communicate by receiving and sending strings with information, it simply sends the required information to the LabVIEW program. From the measured pressure, the velocity is calculated.

The third program, called *"geluid1.vi"* is used to assess if the flow is turbulent, which is done by measuring the noise level of the flow. First the noise is measured in middle of the tunnel, where the flow is not influenced by the wall. The flow in the middle of the tunnel is laminar, or turbulence is very small. The difference between the minimum and maximum noise level is used to assess whether or not the flow near the wall is laminar or turbulent. The frontpanel is shown in figure 4.8. This program consists of only one block (Figure 4.9) which measures noise. The noise data is imported into the program by a DAQ-assistant and shown in a graph on the frontpanel.

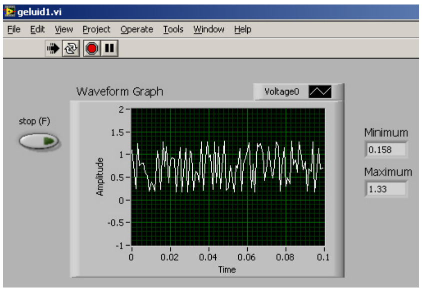

Figure 4.8: Frontpanel of LabVIEW noise measurement program.

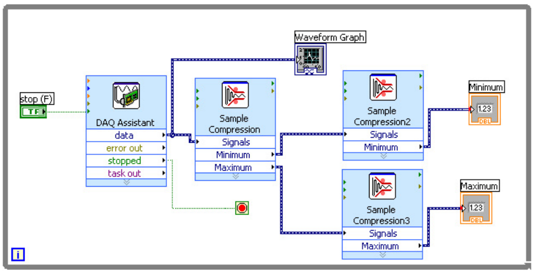

Figure 4.9: Block diagram: Probe velocity.

4.4 The Model.

In this section the model will be described. The plate model is milled out of a single block of aluminium. In the middle of the plate a cavity is made. In this cavity a layer of plasticine is placed. The bottom of this cavity is grooved to hold the plasticine into place and to allow the plasticine to be pushed down when the dents are created. The advantage of this plasticine is its property to change the shape of the surface. If the plate was made entirely out of aluminium, for every dent configuration a new plate has to be milled, which is very time-consuming and costly.
Pictures of the plate can be seen in figure 4.10 and figure 4.1. In the picture the plate is mounted into the testsection of the windtunnel. One of the sides of the testsection is removed for displaying purposes only. The front and rear of the plate are milled in a way that the flow will stay attached to the surface. Since the plate is positioned just over the tunnelfloor, an aluminium strip (placed just in front of the plate on the tunnel floor) will guide the flow over the plate. A zigzag-tape is placed on this aluminium strip to ensure a turbulent flow over the plate. It is of importance that the plate can move without friction in the direction of the flow. This is achieved by hanging the plate in the tunnel by four cables. The plate now moves like a pendulum, when it moves in horizontal direction it automatically moves vertically. This vertical movement is not favourable because now gravity limits the horizontal movement. But this vertical movement is very limited due to the weight of the plate and, when measuring the drag force, the plate is fixed to a force-balance, restricting the horizontal (and thus also the vertical) movement. These cables are placed outside of the tunnel and thus will not interact with the flow. At the end of each cable a pin is situated, which sticks through a small hole in tunnelwall, into the side of the plate. The plate needs to be in a horizontal position in the tunnel, also the plate needs to be placed as low as possible without touching the tunnelfloor. This is achieved by adjusting the length of each cable by (un)tightening a nut at the top of the cable.
A pin is fixed to the bottom side of the plate. A hole in the bottom of the tunnel is made for the pin. The force-balance is placed on a rail, touching the pin and thus measuring the drag force when the plate is pushed rearward by the airflow in the tunnel.
In the upper side of the plate two small holes are made. Two screws, connected by a

wire can be placed inside these holes. Thus it is much easier to place the plate inside the tunnel, or to remove the plate from the tunnel.
The plasticine used to make the dents in the plate is quite hard to handle. First a layer of plasticine is applied in the plate in a way the plasticine is perfectly flat. The plasticine is not very flexible when it is cold. When the plasticine is heated it is flexible and therefore easier to apply. But when heated the plasticine becomes sticky. This is a problem when a flat surface has to be created, because the plasticine then sticks to the tools. This is why it is best to not heat the plasticine before or during the production of the flat plate or when pressing the dent-geometries into the plasticine. Empirically it is found that for temperatures up to 20 °C the plasticine can be handled without problem.
When making the surface flat, two tools are used (See figure 4.11). The first one is a cylindrical roller, used to flatten the plasticine to approximately a flat surface. An important characteristic of the plasticine is elasticity. After the plasticine is compressed by the cylinder, it expands a little. Now the other tool, a large knife, is used to remove all redundant plasticine.
The dents are created by pressing a stamp into the surface of the plasticine. (Figure 4.14) The stamps are made out of aluminium. The form of this stamp can have all kinds of shapes. Here only rotation-symmetric dents are created, but it is possible to create all other kinds of dents as well. The advantage of the plasticine allows measurements of different dents within a short period of time. Now it is possible to create and test one dent configuration in approximately six hours. The same dent-geometries are used as simulated in the CFD-simulations done earlier in the project. The depth of the dents in CFD ranges from h_c=0.343mm to h_c=3.000mm. When making a comparison between CFD and windtunnel results, it is desired that the tested dent-configuration are the same.

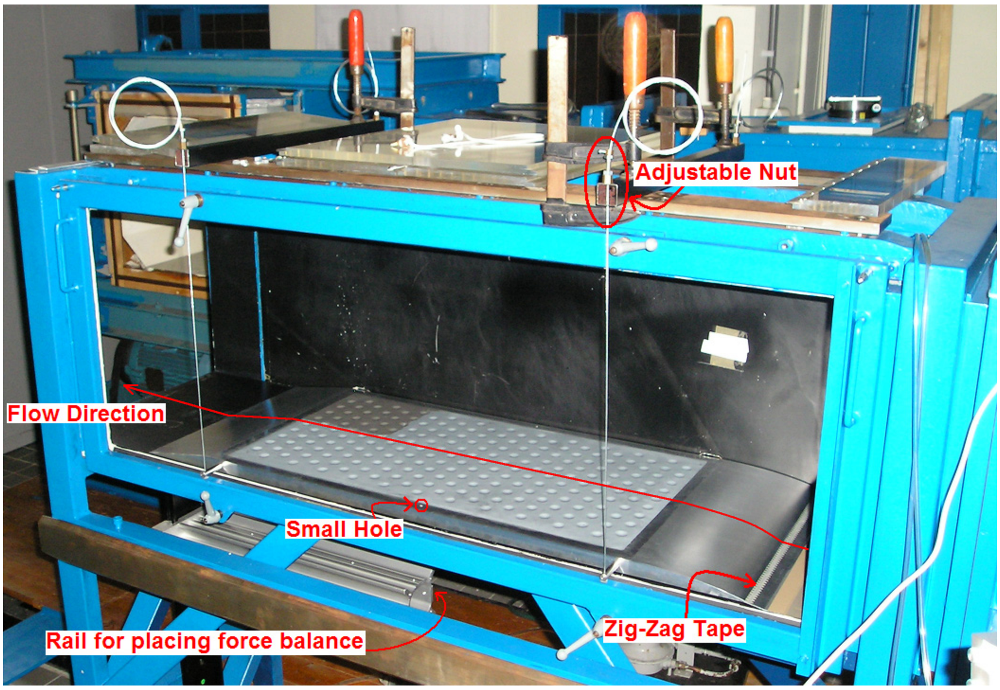

Figure 4.10: The dented plate in the windtunnel testsection.

Thus approximately the same dent depths are used. The stamps used have dent depths of: h_c=0.343mm, h_c=1.0mm, h_c=2.0mm, h_c=3.0mm and h_c=4.0mm. When designing the dents no consideration was given to the fact that the plasticine is elastic. After the production of the dent it was found that the dent depth is reduced by approximately 0.5mm, due to the elastic characteristics of the plasticine. The stamp with a dent height of h_c=0.343mm, did not create a dent structure visible by the naked eye. But a very shallow dent structure is present; it is noticeable when stroking the surface. The other dent depths are reduces by 0.5mm and become: h_c=0.5mm, h_c=1.5mm, h_c=2.5mm and h_c=3.5mm. These depths are not the exact depths tested by the CFD-simulations, but since the same range of depths is covered it is still possible to make a qualitative comparison between the CFD-simulations and the windtunnel tests.
The dents are arranged in a pattern. In the test two patterns are tested. The first pattern (pattern 1) originates from the patent, [Vida, 2004], and is also used in CFD. Here the dents are arranged in a triangular pattern. Pattern 2 uses the same triangular positioning of the dents as is used in pattern 1, but there the pattern is rotated over an angle of 90°, see figure 4.12 and figure 4.13. The black arrow in both figures represents the flow direction. Clearly it is visible that with pattern 1 that perpendicular to the flow direction there is space between the dents. Pattern 2 shows an overlap of the dents perpendicular to the flow.
From CFD-simulations and windtunnel tests (Section B) it is clear that a vortex-like structure emerges from a dent. With pattern 1, this vortex-like from the dents come together in the space between the dents. This is not possible with pattern 2, since here the dents overlap. The vortex-like structures from one dent will interact with the next dent they encounter. Pattern 2 tests the effect of this interaction between the dents.

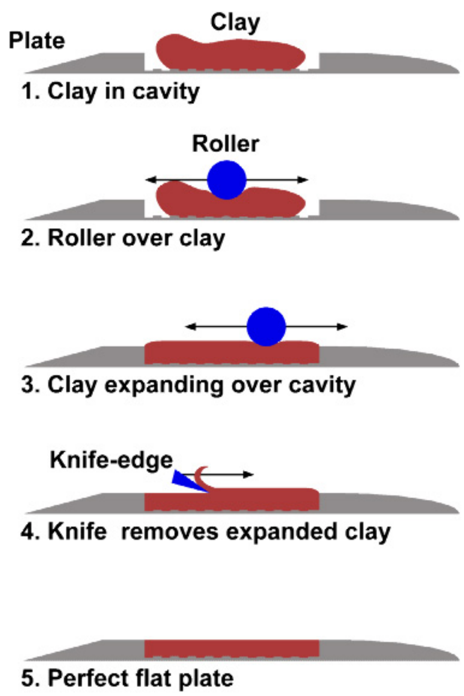

Figure 4.11: Procedure to create a flat plate with plasticine.

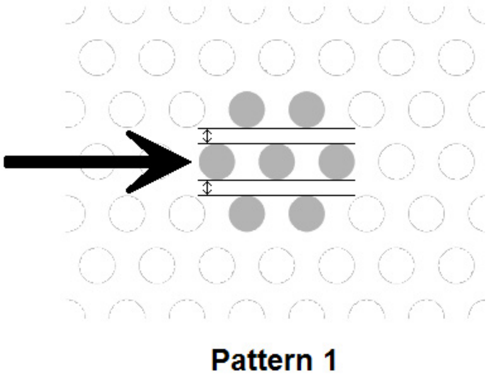

Figure 4.12: Dent pattern 1.

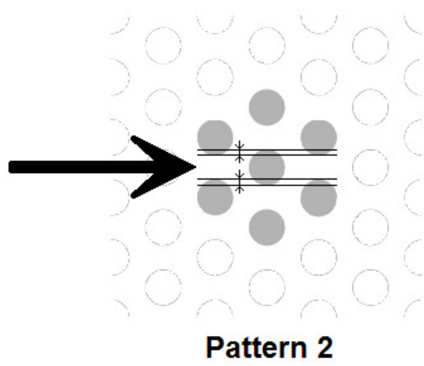

Figure 4.13: Dent pattern 2.

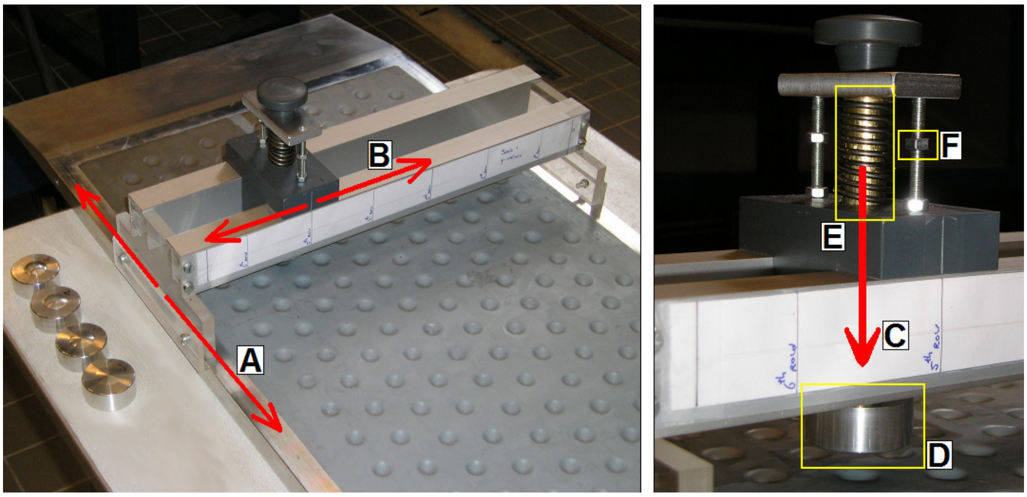

Figure 4.14: Stamp device to make the dent pattern.

For the production of the dents a device is developed which makes it possible to stamp each dent in the correct position. This device, figure 4.14, allows the stamp (D) to move in streamwise direction (A) and perpendicular to the flow direction (B). Of course the stamp can move downwards (C) to push the stamp into the plasticine. This vertical movement is stopped by two nuts (F), to prevent the stamp from going to deep in the plasticine. A spring (E) makes sure the stamp retracts from the plasticine after the dent has been made.

4.5 The Measurements.

A total of eleven tests are done. These can be divided into two series of tests. One series with pattern 1 and one series with pattern 2. Each series consists of a flat plate measurement (reference) and a number of measurements with dented plates. Of course first the flat plate measurement is done, followed by the most shallow dented plate, then increasing depth, up to the deepest dented plate.

Each plate is subjected to two kinds of measurements: a force measurement and a velocity profile measurement. These will be explained in more detail.

4.5.1 Force Measurements.

The force measurement consists of three separate force-measurements. Between each force-measurement the plate is removed from the windtunnel and reinstalled again. This is to ensure the independence of the measurements. One measurement consists of 40 points. The first point is taken without the tunnel running; this is to determine the offset in the force balance and in the pressure gauge. For the other 39 points the velocity ranges from just over 0m/s to almost 29m/s (Tunnel speed settings range from 0-20 to 9-00). This range of velocities is chosen because the CFD-simulations are done at 5 m/s as well as some experiments found in the patent [Vida, 2004]. It is necessary to measure at higher velocities because almost all practical applications are related to higher velocities. Trains and trucks travel at velocities of 25-30m/s.
A measurement point, which is the average of the points taken during five second period ($\approx$100 points), is taken when the force is approximately constant. This average of the measurement point is calculated during the post-processing of the test. Recommended is to improve the LabVIEW programs automatically producing the averages in an output file. A second order polynomial is fitted through the 40 points. This is done by using a program called CurveExpert, Version 1.37, which is a curve fitting system for Windows. The reason why a second order polynomial is used is because the drag force is proportional to the square of the velocity. Since three separate force measurements are performed, three polynomials will be produced. The average of these polynomials form one single polynomial, which will be used when the results of the tests are compared.

4.5.2 Velocity Profile Measurements.

The velocity profile is measured at one location on the plate only. This location is positioned in the middle of the plate, in the middle of triangle formed by three dents. The pressure probe is traversed from a position just above the plate ($\approx$0mm) to 17mm. At the latter position it is found that the probe is outside of the boundary layer flow. In total at 29 points the total pressure is measured. Each measurement point is, just like in the force measurements, an average of the values measured over a period of five seconds. The boundary layer profile is measured using five free-stream velocities: 3m/s, 5m/s, 7.5m/s, 10m/s and 15m/s. The velocity is calculated as explained in section 4.3.

4.6 Results.

The results include both the force measured and velocity profiles measured. The data and the graphs of the tests are shown in appendix G. First the two series with both patterns are presented. Also a comparison between the two patterns will be made.

4.6.1 Test Series 1: Pattern 1.

The force measurements for this pattern are presented in appendix G.1. Figure 4.15 is a graph of the drag measured in all six series. All plates show a quadratic relation between velocity and drag, which is expected since: $D = \frac{1}{2} C_D \rho U^2 L$. From this figure it is clear that the drag of the three plates with the deepest dents (h_c=1.5mm, h_c=2.5mm and h_c=3.5mm) is higher than the drag of the flat plate. The drag of the two most shallow dents (h_c=0.343mm and h_c=0.5mm) are almost equal to the drag of the flat plate. To allow comparison between the flat and shallow dented plates, the drag increase has to be calculated.

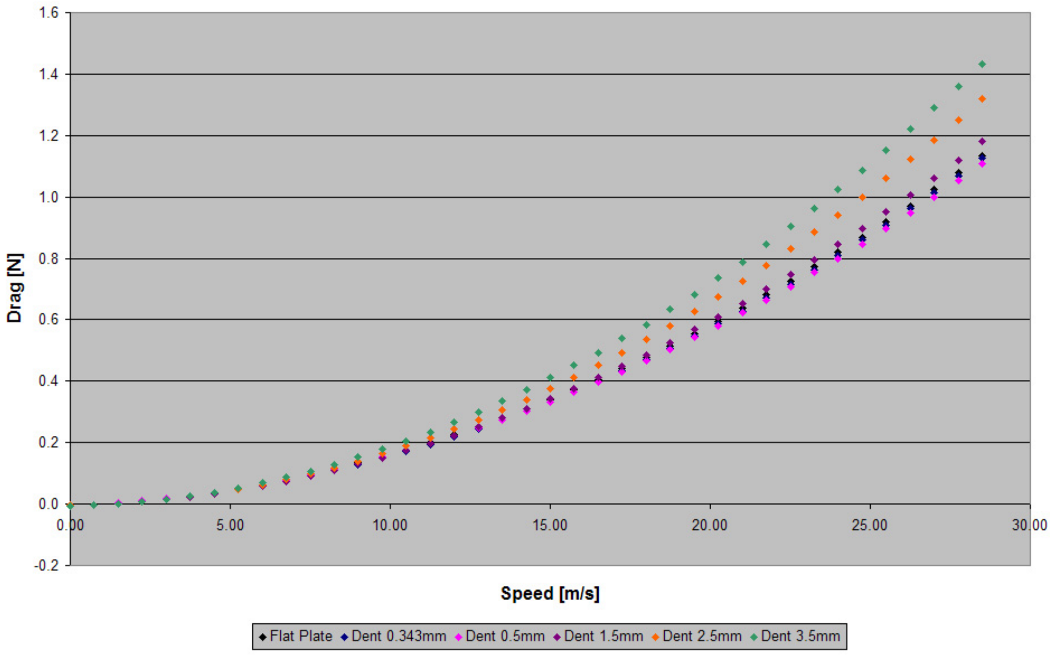

Figure 4.15: Forces measured on dented plates with pattern 1.

In figure 4.16 the absolute increase of drag with respect to the flat plate is plotted for pattern 1. And figure 4.17 presents the percentage of drag increase with respect to the flat plate. The drag increase in force [N] and percentage [%] are defined as:

$$\Delta D[N] = D_{dented} - D_{flat}$$
$$\Delta D[\%] = \frac{D_{dented} - D_{flat}}{D_{flat}} 100\%$$

From the figure 4.16 and 4.17 it is clear that both the plate with dent depths of h_c=0.343mm as well as the plate with dents with a depth of h_c=0.5mm have less drag than the flat plate for almost the entire velocity regime. The dent of h_c=0.343mm has a maximum drag reduction at U=4m/s of 5%. For higher velocities still there is a drag reduction of 1%. The dent of h_c=0.5mm has a maximum drag reduction for velocities above U=5m/s, this reduction is 2.5% for velocities higher than 10m/s. Also it is noticed that for dent $h_c \leq 2.5mm$ no drag reduction is obtained. The plate with dents of

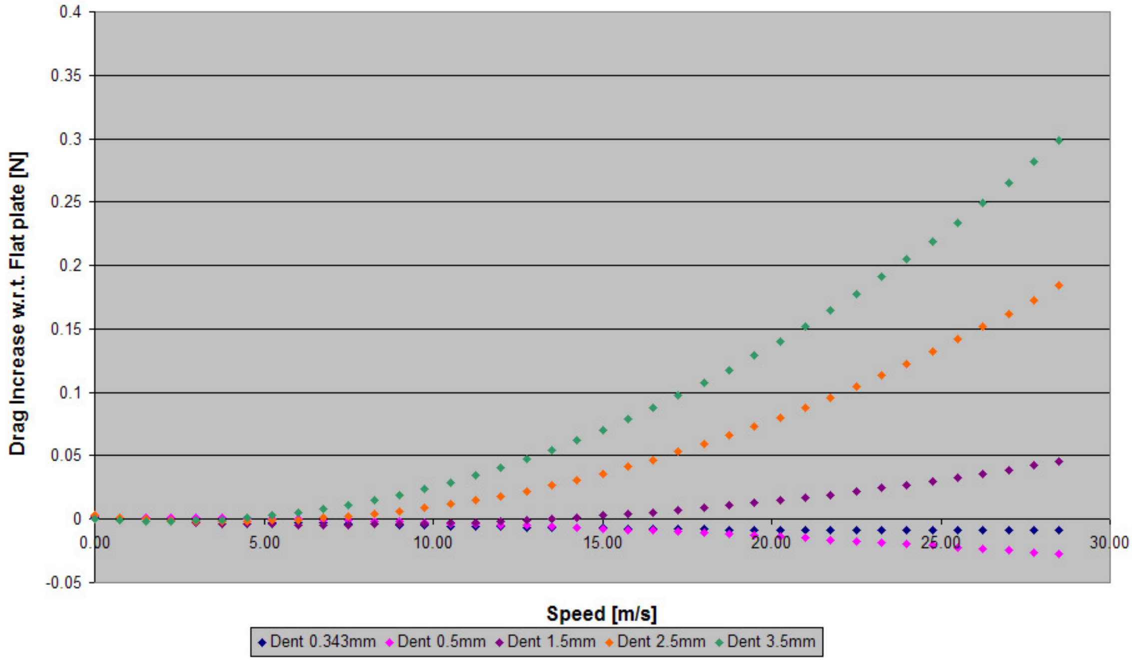

Figure 4.16: Forces increase [N] on dented plates with pattern 1.

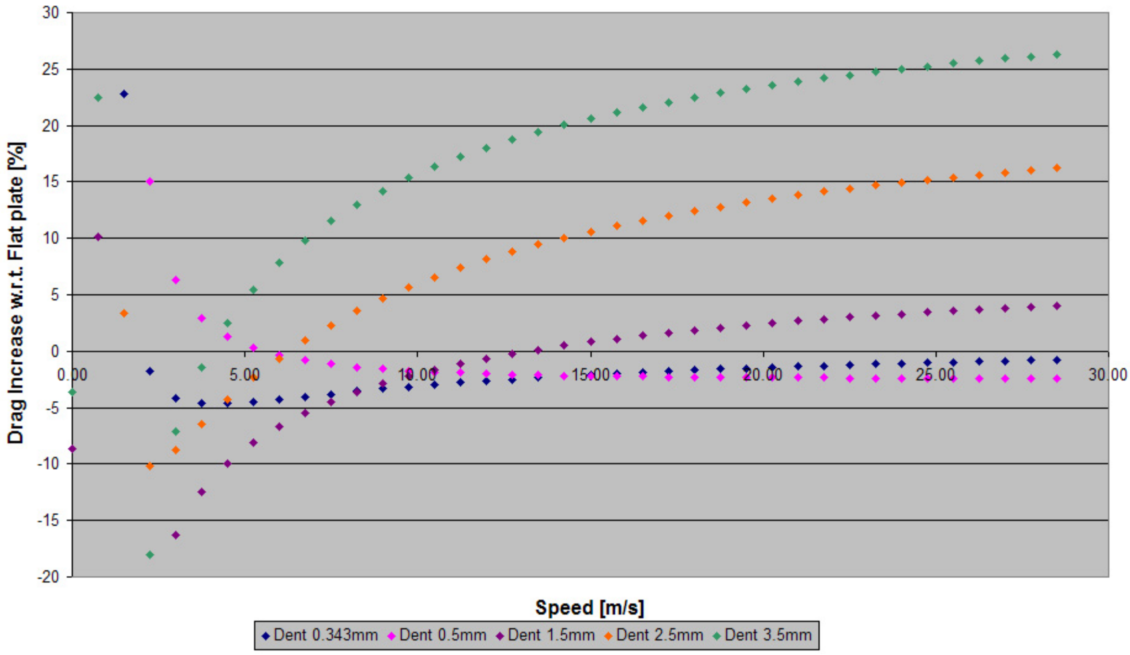

Figure 4.17: Forces increase [%] on dented plates with pattern 1.

h_c=1.5mm shows a small drag reduction for velocities up to U=12.5m/s.
A remark has to be made about the size of these drag reductions. The drag force of a plate is an average of three force measurements. The original measurements points deviate from this average. If this difference between the individual measurements is much larger than the drag differences between the plates with different dent configurations, it is not clear that the drag change is produced by real physical changes in the flow or by one (or more) deviating measurements. For every plate, out of all three measurement series, an average error can be calculated. In table 4.1 the errors are given.

$$Error[N] = \frac{1}{n}\sum_{i=1}^{n}\sqrt{(D_m - D_{av})^2}$$

$$Error[\%] = \frac{1}{n}\sum_{i=1}^{n}\sqrt{\left(\frac{D_m - D_{av}}{D_{av}}\right)^2} 100\%$$

Where:

n = number of points
D_m = measured drag in a point
D_{av} = average drag corresponding to the velocity of the point of D_m.

	All measured points		Only points >5m/s		Only points >10m/s	
	Error [N]	Error [%]	Error [N]	Error [%]	Error [N]	Error [%]
Pattern 1						
Flat plate	0.0207	133.97	0.0229	6.40	0.0259	4.79
Dent 0.343mm	0.0176	73.97	0.0193	6.37	0.0219	3.97
Dent 0.500mm	0.0200	71.33	0.0221	8.42	0.0248	5.67
Dent 1.500mm	0.0174	83.24	0.0192	7.96	0.0213	4.60
Dent 2.500mm	0.0218	77.87	0.0242	7.29	0.0274	5.27
Dent 3.500mm	0.0123	253.09	0.0135	4.47	0.0151	2.52

Table 4.1: Error margins for the measurements, Pattern 1.

When the absolute errors for all measurements points are considered, these errors are of the same order. But when the errors calculated in percentages are considered, these vary a lot, from 71% to 253%. This is because relative large errors are made at the lower end in the speedregime, where the variation of the measured points is much larger than the average of the points. These errors should be neglected. Therefore the errors of two other speedregimes are considered. In the first only points with a velocity of U>5m/s are regarded. The second considers only points with a velocity of U>10m/s. These two regimes cause the absolute error to increase, because error of the points in the lower part of the speed regime, which are left out, are smaller, in absolute sense, than the errors at higher velocities. Removing these small errors increases the size of the average error. The percentual error decrease when the lower speeds are neglected.
Since drag reduction is defined as a percentage of drag decrease, the errors in percentages are of more importance than the absolute errors. The drag increase is, for velocities higher than U=10m/s, of the same order as the error margin found in the measurements in case of the dents of h_c=0.343mm, h_c=0.5mm and h_c=1.5mm. For the deeper dents, h_c=2.5mm and h_c=3.5mm, the measurement margin is smaller than the drag increase,

this holds for velocities higher than U=5m/s. Thus, in general, for velocities over U=5m/s the measurement margin is equal or smaller than the obtained drag increase. For these velocities the drag change is presumed as valid, not depending on the quality of the measurements.

The velocity profile reveals a very important error made in the experiments. The flow should be turbulent, as was reported in literature [Vida, 2004]. As reported previously in this chapter, the turbulence level is checked with a microphone. And for the zigzag-tape used here the noise level of the flow was thought to be high enough to ensure the flow to be turbulent. But during post-processing the velocity profiles, it is concluded that for low free-stream velocities (U≤5m/s) the measured velocity profiles do not match at all with the theoretical turbulent velocity profiles, see figure G.7. The measured velocity profiles do match the theoretical laminar velocity profile. Both the laminar and the turbulent velocity profile are calculated according White [White, 1991]:

$$u_{laminar} = U\Big(\frac{2y}{\delta} - \frac{y^2}{\delta^2}\Big)$$
$$u_{turbulent} = U\Big(\frac{y}{\delta}\Big)^{1/7}$$

with:

$$\delta_{laminar} = \frac{5.5x}{\sqrt{Re_x}}$$
$$\delta_{turbulent} = 0.37xRe_x^{-1/5}$$

For higher free-stream velocities, U≥7.5m/s, the velocity profiles will match the theoretical turbulent velocity profile. Thus it can be concluded that somewhere in the velocity range 5m/s≤U≤7.5m/s, the flow transits from laminar to turbulent. Now does this have consequences for the conclusions made earlier in this section?
For velocities higher then 7.5m/s nothing changes. The two most shallow dented plates (h_c=0.343mm and h_c=0.5mm) show a drag reduction with respect to the flat plate of respectively 1% and 2.5%, while all deeper dented plates show an increase of drag.
For low velocities (0m/s<U<5m/s) it is difficult to conclude anything about the measurements, because the force increase in percentage are changing a lot in this velocity regime, see figure 4.17. Also the drag increases are less or equal than the errors of the measurements. Finally the flow is transiting from laminar to turbulent which is a third important reason not to extract conclusions about the drag change in this velocity range.

The velocity profiles are measured at one point on the plate. This point is situated in between the dents, approximately in the middle of the plate. Since only one point is used to measure the velocity profile it is not possible to gather lots of information out of the velocity profile measurements. It is clear from all measured velocity profiles that the fluid always flow downstream, since $\big(\frac{\partial u}{\partial y}\big)_0 > 0$ in figures G.7 to G.11. Thus there are no separated flow areas near the surface. From the CFD-simulations it was found that the separated areas only exist in the dents. The velocity profile measured here confirms this.
Figures G.7 and G.8 represent the velocity profiles over the flat plate and five dented plates for free-stream velocities of 3m/s and 5m/s. Here all velocity profiles of all dented plates look alike. It seems the dents have no influence on flow at this position between

the dents. This can be explained by the fact that the flow inside the dent is attached to the wall, even inside the dents. In chapter 3 this situation is encountered, for example, for shallow dented plates subjected to a low free-stream velocity. For higher velocities the velocity profiles do show different behaviour. Probably, here the dents cause the flow to separate and vortices are created which influence the flow at the position where the velocity profiles are measured, resulting in differences in the profiles.

For more detailed analysis more velocity profiles need to be measured, at different positions of the plate. Also positions inside the dent should be considered, but this is difficult because measuring the velocity profile with a probe will influence the flow. It is possible the probe will disturb vortices inside the dents.
Another measurement that should be considered is to measure the pressure inside boundary layer with a rake of probes, to determine the change of impulse, which is related to the change of drag of the plate.

4.6.2 Test Series 2: Pattern 2.

The force measurements done for pattern 2 are presented in appendix G.3. A graph of the drag measured in all five series is shown below. See figure 4.18. In the previous series a dent depth of h_c=3.5mm is tested. This dent depth is not tested in this series. From series 1 can be concluded that the plate with dent depth h_c=3.5mm behaves similar to the plates with a dent depth of h_c=1.5mm and h_c=2.5mm. If due to the change in the pattern the plates with dent depths h_c=1.5mm and h_c=2.5mm show a difference in behaviour to each other or to the behaviour found in series 1, then the plate with dent depth h_c=3.5mm could still be added to this series.
The results of the drag measurements are plotted in figure 4.18. The drag change in force [N] and percentages [%] are presented in figures 4.19 and 4.20. Like in the previous section, the drag changes are of the same or larger order than the deviation of the measurement points with respect to the averages when U>5m/s. Thus, for velocities over 5m/s the drag increase is presumed as valid, not depending on the quality of the measurements. Remarkable is that for velocities of $\leq 25m/s$ the dent with a depth of h_c=1.5mm results in a drag reduction. Even the dent with a depth of h_c=2.5mm results in a drag reduction for velocities of $\leq 15m/s$. The drag reduction found for the plates with dents of h_c=0.343mm and h_c=0.5mm is 3% and 5% respectively. The plate with dents of h_c=0.5mm even has an optimal drag reduction of approximately 13%, at 6m/s.

The velocity profiles, for velocities up to 5m/s, measured here also match the laminar theoretical velocity profile. While the velocity profile for U≤7.5m/s match the turbulent theoretical velocity profile. This is similar to what is found when pattern 1 was tested.

4.6.3 Results.

For the comparison of both pattern only velocities higher than 7.5m/s are taken into account, because as illustrated before, for lower velocities the validity of the measurement is questionable.
Pattern 1 shows drag reducing capabilities for shallow dents of ≈1% for dent depth of

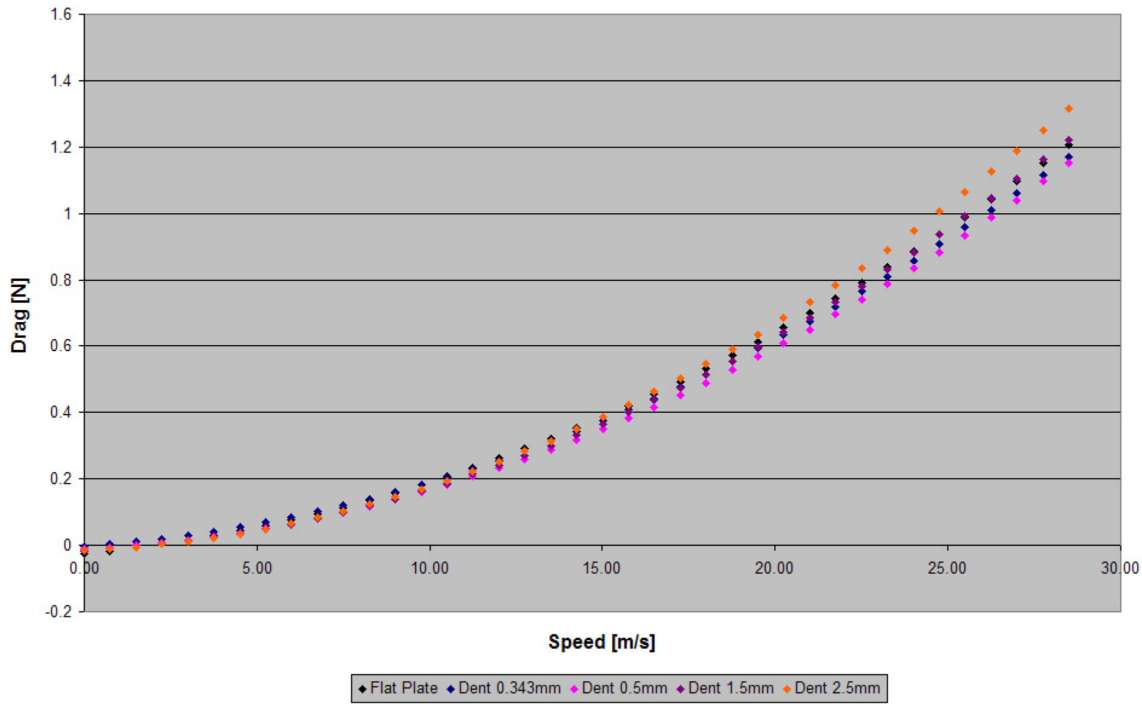

Figure 4.18: Forces measured on dented plates with pattern 2.

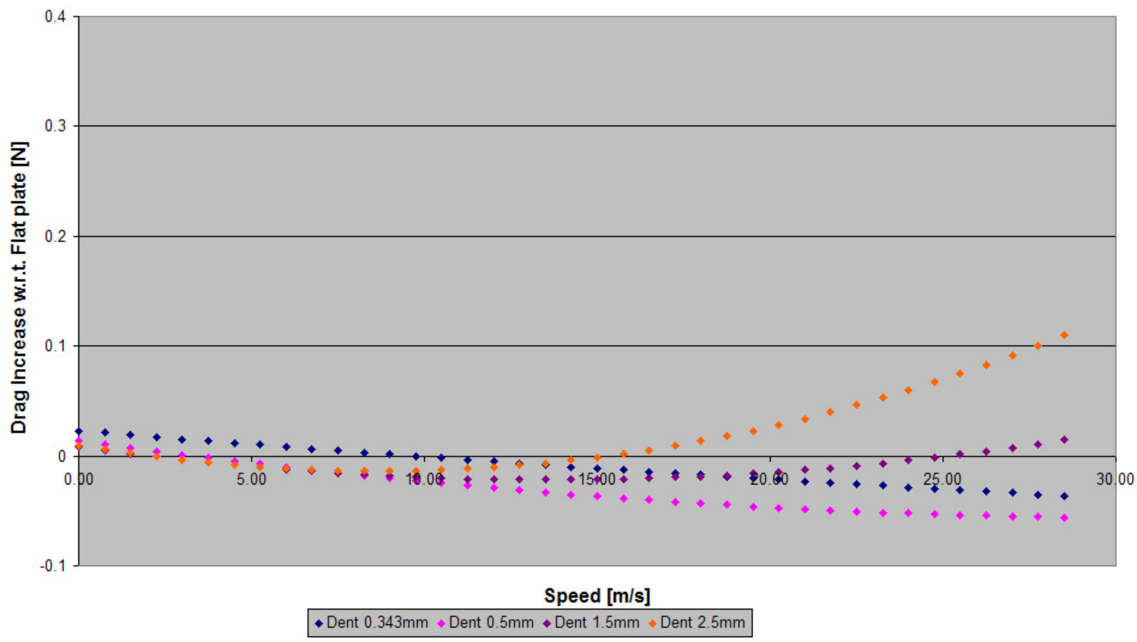

Figure 4.19: Forces increase [N] on dented plates with pattern 2.

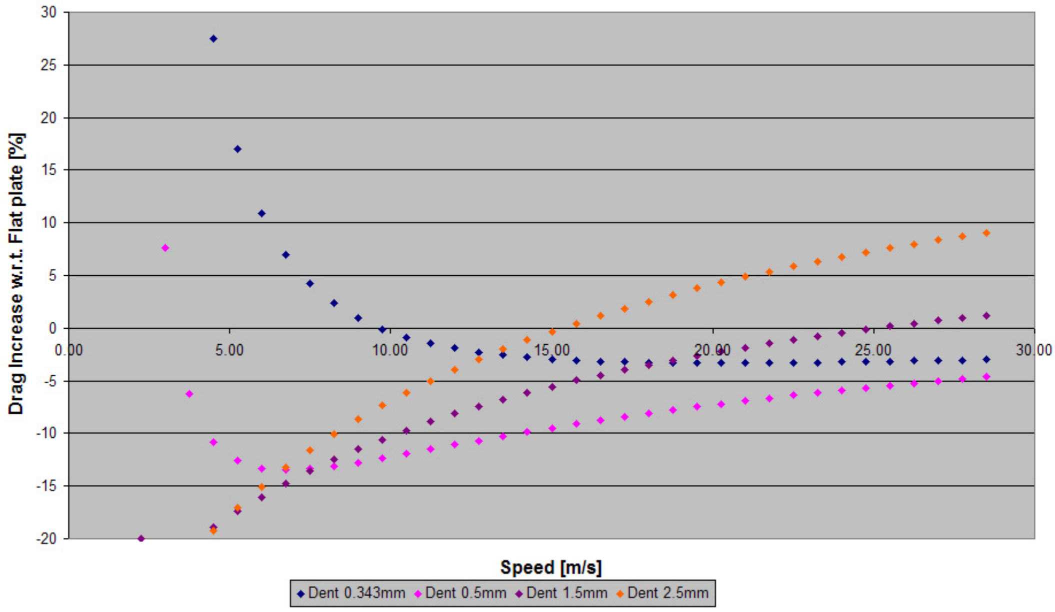

Figure 4.20: Forces increase [%] on dented plates with pattern 2.

	All measured points		Only points >5m/s		Only points >10m/s	
	Error [N]	Error [%]	Error [N]	Error [%]	Error [N]	Error [%]
Pattern 2						
Flat Plate	0.0253	65.75	0.0270	11.09	0.0285	4.86
Dent 0.343mm	0.0238	907.60	0.0246	13.16	0.0248	5.33
Dent 0.500mm	0.0121	78.75	0.0130	6.76	0.0141	3.26
Dent 1.500mm	0.0216	73.17	0.0235	7.98	0.0263	4.83
Dent 2.500mm	0.0169	83.23	0.0183	7.04	0.0202	4.44

Table 4.2: Error margins for the measurements, Pattern 2.

h_c =0.343mm and ≈2.5% for dents with depths of h_c=0.5mm. The dent with a depth of h_c=1.5mm only reduces drag for velocities lower than 12.5m/s. For dent depths of $h_c \geq$2.5mm the drag increases always.
For dent pattern 2 it is found that for velocities of $\leq 25m/s$ the dent with a depth of h_c=1.5mm results in a drag reduction. Even the dent with a depth of h_c=2.5mm results in a drag reduction for velocities up to 15m/s. The drag reduction encountered for the plates with dents of h_c=0.343mm and h_c=0.5mm is 3% and 5% respectively.
For all dented surfaces pattern 2 shows, for shallow dented plates where drag decrease is encountered, better drag reducing capabilities then pattern 1. For deep dented surfaces the increase in drag is lower for pattern 2 than for pattern 1. Thus it is concluded that pattern 2, where the rows of dents are positioned closer together, does has better drag reducing capabilities than pattern 1.
It is highly recommended that, by means of flow visualization in the windtunnel or by means of CFD-simulations, the effect of the placement of the dents is investigated.

Chapter 5

Results and evaluation of the research on DSE

In this chapter the results of the research on DSE by means of Computational Fluid Dynamic simulations and windtunnel tests are compared with each other and with available information from literature. Also an idea is given on how the phenomenon of DSE should be able to result in a reduction of drag. Finally this chapter will give some ideas and/or suggestions for future research to drag reduction by DSE.

5.1 CFD-simulations vs. Windtunnel tests.

All CFD-simulations done during this thesis have shown a increase of drag, which is not confirmed by the windtunnel tests, where a both drag decrease and increase are encountered. From both tests it is clear that when dent are shallow, to flow will stay attached to the wall, even in the dents. Deeper dents will trigger the flow to separate from the wall and cause reversed flow in the dents and a vortex coming out of the dent. The drag is influenced by the dented surface. From the CFD-simulations it is known how the drag is changed. The skinfriction drag for attached flow will always be higher for dented plate with respect to the plate plate. For separated flows, however, the skinfriction is reduction by a substantial amount. But the separated flow causes a vortex to appear in the dent, which is not only found in this research but also by others ([Wüst, 2004], [Vida, 2004], [New and Lim, 2004]). This vortex will increase the pressure drag according to the CFD-simulations. The increase in pressure drag is found to be larger then the decrease of skinfriction drag, resulting in an increase of total drag. This effect was also found in an experimental investigation of a turbulent boundary layer flow over a wavy wall, performed over 35 years ago in the Ph.D. study of A. Sigal, see [Sigal, 1971]. Here also the skinfriction was decreased, but increase in pressure drag caused the total drag to increase.

The author suggests that the solution to obtaining a reduction in total drag is obtained by limiting the increase of the pressure drag. This should by obtained by controlling to flow coming out of the dent after it is separated. The positioning of the dents is crucial here. From the CFD-simulation it is known that the positioning of the dents tested resulted in a separated flow, which exits the dent and does not interact

with any of the dents downstream. From the windtunnel tests, where two dent patterns are tested, it is known that the placement of the dents does influence the drag behaviour to a great extent. It was found that the pattern, for which the lateral distance between the dents is smaller, results in lower drag than for a pattern with larger lateral distances between the dents. If the lateral distance between the dents is decreased then the flow will encounter the dent downstream, which is presumed to influence the pressure drag, (see figure 5.1). The influence of the position of the dents is very important and should be investigated, by means of windtunnel tests or by means of CFD-simulations. The latter is preferred because of the possibility very accurate flow visualization without interfering the flow.
Another geometry that can be used for influencing the pressure drag are dents with non-axis symmetric geometries. For CFD-simulations and from literature it is found that the flow is not symmetric, thus it seems highly unlikely that symmetric dent are optimal drag reducing geometries. Figure 5.2 features oval shaped dents, which possibly can influence the flow in a way drag is reducted.

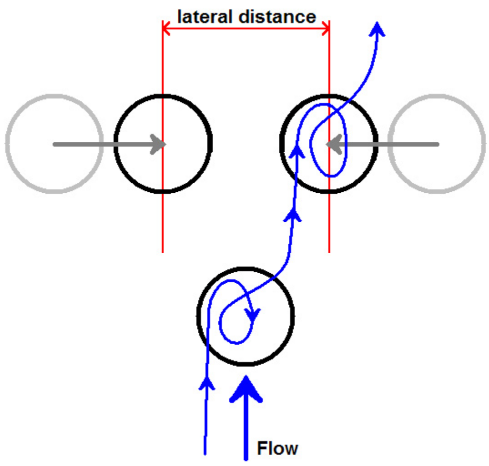

Figure 5.1: Decreasing of the lateral distance between the dents; topview.

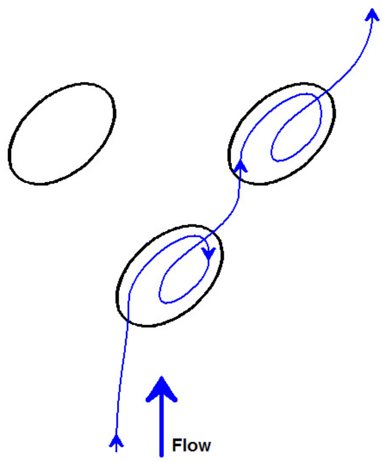

Figure 5.2: Non-axis symmetric dent geometry; topview.

An even more exotic idea is the application of dents which have much more difficult shape. Figure 5.4 shows a dent based on a NACA-duct, here (a) shows a three-dimensional sketch of the separated flow in the dent. Figure 5.4 features a view from the side of the same separated flow. The NACA duct is designed as an air-intake for aircraft, of which the shape should produce as little drag possible, see figure 5.3. If this NACA duct is reversed it is possible a separated flow area is formed. Maybe this low drag property, combined with a negative skinfriction caused by the separated flow in the dent will reduce drag. This NACA-duct-like dent is just one of the limitless amount of dent geometries which possibly can reduce drag.
The goals of this thesis were threefold: to investigate if it is possible to reduce drag adding dents to surfaces, to investigate why the drag is reduced and finally to optimize the drag reduction. The first goal is fulfilled: the windtunnel tests proves it possible to reduce drag by adding dents to a flat surface, like claimed in literature ([Wüst, 2004] and [Vida, 2004]). The reason why to drag is reduced is clarified, with aid of the

Figure 5.3: Example of NACA-duct; source: www.carbonmods.co.uk.

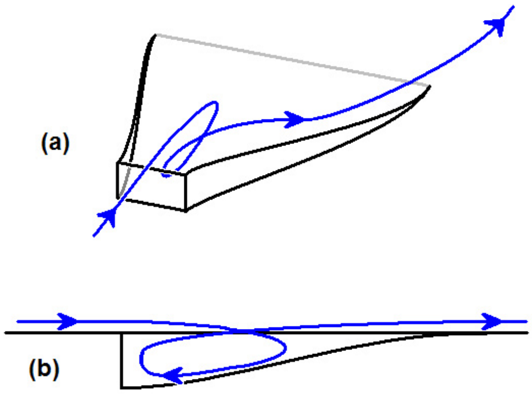

Figure 5.4: Dent based on reversed NACA-duct.

CFD-simulations, although not completely. More research is needed therefore. Just as more research is needed to optimize the drag reduction, which is an unfulfilled goal of this thesis.
If, after future research, DSE is a more understood phenomenon is can be used to apply to more difficult geometries, suited for practical applications. This is a challenge as well, because these geometry (for example the body of a high-speed train) consists of curves surfaces, angles and other irregular surfaces. The surfaces tested in the research done in this thesis always were dented with a uniform pattern of identical dents, but for practical application it is possible dent geometries and pattern vary, because of the varying flow conditions on different part of an object.

Chapter 6

Conclusions and Recommendations.

6.1 Conclusions.

The conclusions about the simulations are:

- The CFD-simulations seem to give a very good representation of the flow over dented plates. Compared to numerical research and windtunnel test performed in other dent related research, the same kind of flow patterns are encountered.
- Here an increase in drag is found for all simulations compared to the flat plate drag. Two characteristic flow situations have occurred: For shallow dents, the flow will stay attached to the plate, here the curvature of the dent will increase viscous drag and create pressure drag, both increasing the total drag. The deep dents, where the flow through the dent separates from the wall, also shows an increase in drag, but here the increase is entirely caused by the increase of pressure drag. The skinfriction drag of the plate decreases, due to the reversed flow in the separated areas.
- When a flow with high velocity, representing practical implication of DSE, is tested, the drag increases for all applied dent geometries. The characteristic attached and detached flow patterns encountered at low velocities are also present at high velocities.
- A dent with a non-rotational symmetric cross-section is tested. The geometry is designed to increase the separation area, which should lead to a large separation area with negative skinfriction. Also geometry is designed to reduce pressure drag. The simulations results in high skinfriction and pressure drag. The tested geometry, for applied flow conditions, does not result in reduced drag.
- The decreasing skinfriction for separated flows is presumed to be the cause for a possible reduction of the total drag. But for all dent geometries numerically tested in this thesis the increasing pressure drag dominates the decreasing skinfriction. For a total drag reduction the pressure drag should be limited, which is presumed to happen if the flow exiting a dent interacts in a specific way with dents downstream. This interacting should be investigated in future research.

The conclusions about the windtunnel tests are:

- Most important conclusion from the windtunnel test is that it is possible to reduce the drag, up to 13%. Shallow dents are proven to reduce drag on the entire velocity regime, while very deep dents are found to always create an increasing drag. Dent with intermediate depths cause drag reduction fot low velocites, while high velocities result is drag increase.

- The two patterns tested show that pattern 2 contains better drag reducing capabilities than pattern 1. The difference between the two pattern is the placement of the dents. The lateral space between the dents in pattern 2 is smaller than the space used in pattern 1, which results in a flow exiting a dent and interacting with a dent downstream. This interaction effect proves to be important for the amount of drag of the plate and should be investigated to a further extent.

General conclusions from this thesis are:

- For a reduction of drag to occur it seems that the viscous drag should be decreased by the dents, this is caused by negative skinfriction in separated areas. The separated areas are caused by specific combinations of the geometry of the dent and the flow properties. The pressure drag should not increase or should increase less than the decrease of the viscous drag. The pressure drag can probably be controlled by adjusting the placements of the dents. From the CFD-simulations it is known that the flow exiting from a dent does not encounter other dents. If the dents are placed in a pattern in which the flow encounters more than one dent, the pressure drag can be decreased. This is confirmed by windtunnel test with the different patterns.

- The CFD-simulations and the windtunnel tests do not agree about the possibility of drag reduction by dented plates. Windtunnel tests show drag reduction is possible, while this is not encountered in CFD-simulations. From literature it is known that only drag reduction is found in experimental research. Numerical research where drag reduction is encountered is not known to exist.

6.2 Recommendations

Recommendations for further research on the subject of dent induced drag reduction are:

- For future research, which involves CFD-calculation as well as windtunnel tests, it is probably better to perform the windtunnel tests before CFD-simulations are made. Changes to models are made easily and it is very easy and fast to test at different velocities, while this takes lots of time using CFD-simulations. Also CFD is ideal to research details on why the drag is reduced, but this is only possible if is known for geometries and flow conditions the drag is reduced, which can be found using windtunnel tests.

- The research on the influence of the geometric parameters of the dent to the drag should be continued. Here only the dent depth is varied over a wide range of depths. The change in placement of the dents and the free-stream velocity are varied, but here more research is needed to investigate the behaviour of these parameters. The patterns and distances between the dents seem to be of great importance in controlling the pressure drag, this is why these two parameters are to be researched first. But also other dent shapes are to be tested, for example asymmetric dent of NACA-duct based dents, which maybe influence the flow in a way drag is reducted.

- A recommendation for future windtunnel tests is the application of more measurement systems. Here only drag forces and a single velocity profile are measured. While, with for example particle image velocimetry or hot wire anemometry it is possible to measure flow vectors, and/or visualize vortices. Although it is difficult to apply hot wire anemometry, because of the probe disturbing the flow. Non-intrusive research methods are needed preferred. Added smoke to the fluid flow may also result in a better understanding of the flow structures present in the dent. The velocity profiles should be measured at positions all over the plate, also inside the dents, for identifying separated areas. Also a rake of pressure probes can be used to measure the loss of impulse of the flow, which relates to the drag of the plate.
- The LabVIEW programs used in the windtunnel tests should be modified, to allow automated input for the temperature. Also the averaging of the results should be automated, this saves post-processing time.
- The CFD-simulations take lots of time to complete. It would be beneficial to shorten these calculation times, by using faster computers or faster software, if available.

Chapter 7

Bibliography

[Fluent Inc., 2005a] Fluent Inc. (2005a). *Fluent 6.2 UDF User Manual.* [130]

[Fluent Inc., 2005b] Fluent Inc. (2005b). *FLUENT 6.2 User's Guide.* [15, 123, 130]

[Fluent Inc., 2005c] Fluent Inc. (2005c). *Introductory Fluent Notes - Fluent v6.2 - Modeling Turbulent Flows.* [123]

[Gyr and Bewersdorff, 1995] Gyr, A. and Bewersdorff, H. (1995). *Drag Reduction of Turbulent Flows by Additives.* Kluwer Academic Publishers. [1]

[Isaev et al., 2005] Isaev, S., Leont'ev, A., Kiknadze, G., Kudryavtsev, N., and Gachechiladze, I. (2005). Comparative analysis of the vortex heat exchange in turbulent flows around a spherical hole and a two-dimensional trench on a plane wall. *Journal of Engineering Physics and Thermodynamics*, no.78:749–761. [xv, 32, 34]

[Kiknadze et al., 2000] Kiknadze, G., Gachechiladze, I., and Oleinikov, V. (2000). *Method and Apparatus for Controlling the Boundary or Wall Layer of a Continuous Medium.* [87]

[Kodama et al., 2004] Kodama, Y., Kakugawa, A., Takahashi, T., Nagaya, S., and Kawamura, T. (2004). *Drag Reduction of Ships by Microbubbles.* National Maritime Research Institute of Japan. [1]

[Lashkov and Samoilova, 2002] Lashkov, Y. and Samoilova, N. (2002). On the viscous drag of a plate with sperical recesses. *Fluid Dynamics*, no. 2:231–236. [2, 19]

[Nat.Instr. Corp., 2006] Nat.Instr. Corp. (2006). *LabVIEW User Manual.* National Instruments Corporation. [54]

[New and Lim, 2004] New, T. and Lim, T. (2004). On the occurence of asymmetric flow within a circular concavity. *42nd AIAA Aerospace Sciences Meeting and Exhibit.* [32, 71, 91, 92]

[Piomelli and Balaras, 2002] Piomelli, U. and Balaras, E. (2002). Wall-layer models for large-eddy simulations. *Annual Reviews Fluid Mechanics*, 34:349–374. [17]

[Pulles, 1988] Pulles, C. (1988). *Drag Reduction of Turbulent Boundary Layers by means of Grooved Surfaces.* PhD thesis, Technische Universiteit Eindhoven. [1]

[Scheidegger, 2005] Scheidegger, T. (2005). *Overview: LES in Fluent 6.2.* [123]

[Sigal, 1971] Sigal, A. (1971). *An Experimental Investigation of the Turbulent Boundary Layer over a Wavy Wall.* PhD thesis, California Institute of Technology. [71]

[Tillack and Morley, 1998] Tillack, M. and Morley, N. (1998). *Magnetohydrodynamics.* McGraw Hill. [1]

[Vervoort, 2006] Vervoort, E. (2006). *Methods for Drag Reduction in Turbulent Flows - Literature Study.* Delft University of Technology. [1]

[Vida, 2004] Vida, N. (2004). *Three Dimensional Surface Structure for Reduced Friction Resistance and Improved Heat Exchange.* World Intellectual Property Organization. [v, vii, 1, 2, 3, 5, 6, 8, 11, 13, 25, 60, 62, 66, 71, 72, 81]

[White, 1991] White, F. (1991). *Viscous Fluid Flows.* Mechanical Engineering Series. McGraw-Hill International Editions, second edition. [37, 66, 129]

[Wüst, 2004] Wüst, C. (2004). Dellen im dach. *Der Spiegel*, no. 14:pp. 170–172. [2, 5, 35, 43, 71, 72]

Appendix A

Summary of TLT-patents.

A.1 TLT-patent EP1604122A1; Three Dimensional Surface Structure for Reduced Friction Resistance.

Three Dimensional Surface Structure for Reduced Friction Resistance and Improved Heat Exchange.[Vida, 2004]
It is known that the process when a continuous medium like a gas, or a liquid flows along a surface covered with very special three-dimensional concave reliefs, named the TLT-reliefs, is accompanied by self-organization of secondary twisted tornado-like jets originating in each concavity of the relief and flowing out of it into the parent flow. It is known that friction could be reduced by means of dents located at said surface and that in addition heat transfer between said surface and the streaming media, e.g. gases, liquids and two-phase mixtures containing gases and liquids could be increased. Accordingly the invention proposes a surface, which comprises dents, wherein the edges of said dents are rounded, thereby forming a central dent area and at least one curvature area for each dent to the surrounding surface. Such a geometry of a surface especially improves the flow properties with respect to friction resistance as also with respect to heat and mass transfer for surfaces, along which a medium flows, which consists of a gas, a liquid, a two-phase mixture, or a mixture of multiple phases.
The underlying principle are secondary vortices, which originate in the dents and lead to an organized transportation of medium from the surface to the main flow. Due to the reduced pressure inside the vortex flows the boundary layer is sucked in, so that the thickness of the boundary layer does not increase.
Especially suitable for drag reduction, i.e. reduction of friction resistance, is a surface comprising dents having a relatively low depth in relation to the diameter. Dents having a diameter d_c and a depth h_c with a ratio between said depth and said diameter of $h_c/d_c = 0.1$, show an especially low friction resistance. Two curvature areas are very advantageous in order to achieve a gentle transition from the dent to the surrounding surface, thereby reducing the probability of destruction of the advantageous secondary vortices, which originate in the dents.
The dents are arranged periodically on the surface. In order to realize a good coverage of the surface, the centres of three adjoining dents preferably form a triangle. (Figure A.3) The maximum coverage can be reached in this kind of arrangement when the curvature areas of said three adjoining dents are in contact with each other. Even in this arrangement a small area of flat surface remains in the centre of three respective adjoining dents. In this location preferably additional smaller-sized dents are provided,

by which the flow properties can be further improved.

Detailed description of the invention
Figure A.1 shows schematically a preferred distribution of dents *10* on a surface. The dents are arranged periodically, wherein the centres of the three directly adjoining dents *10* form an equilateral triangle. The angle therefore has a value of 60°. The distance between the centres of two adjoining dents *10*, which is equal to the length of a side of the triangle, have a constant value t_1. The distance between two rows of dents *10*, which equals the height of the triangle, has a constant value t_2. The parameters t_1 and t_2 can have different values depending on the purpose for which the surface shall be utilized. Figure A.2 shows a cross section through the centre of one of the dents *10* shown in

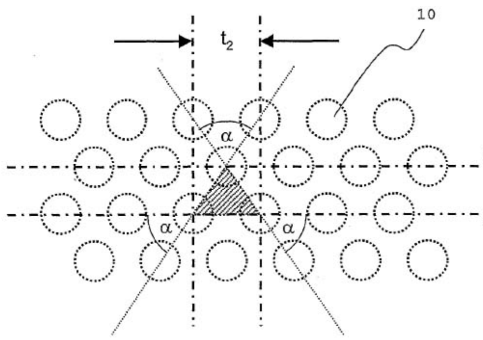

Figure A.1: Schematic distribution of dents.

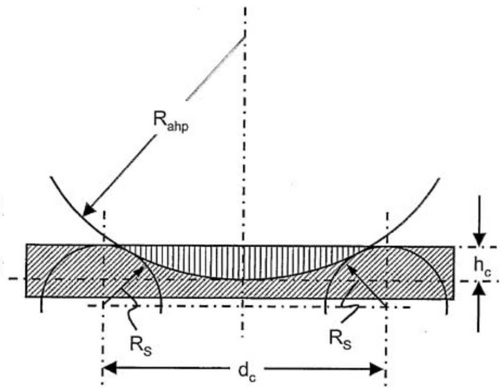

Figure A.2: Cross-section of dent.

figure A.1, perpendicular to the surface. In this embodiment the dent essentially has the form of a calotte with radius R_{ahp}, height h_c and diameter d_c. Further the dent *10* is rounded at the edges with a rounding radius R_s. Thereby in this example the dent is symmetrical with respect to rotation around an axis through the centre of the dent and perpendicular to the surface.
In this embodiment the dents are the type shown in figure A.1 and figure A.2, preferably with the following values:

$$
\begin{aligned}
t_1 &= 28.6mm \\
t_2 &= 33.0mm \\
d_c &= 20.0mm \\
h_c &= 3.0mm \\
R_{ahp} &= 68.2mm \\
R_s &= 5.0mm
\end{aligned}
$$

or scaled up or down keeping essentially the ratios:

$$\frac{t_1}{t_2} = \frac{28.6}{33.0}, \qquad \frac{R_{ahp}}{R_s} = \frac{68.2}{5.0}, \qquad \frac{R_s}{h_c} = \frac{5.0}{3.0}$$

The above named values result in a fraction of the surface, which is covered by the dents, of about 0.3.

Figure A.3 shows schematically a top view of a distribution of dents comprising a central dent area *110*, a first curvature area 120 and a second curvature area *130*, the named areas being arranged consecutively from the centre of the dent to the outside. The central dent area has a diameter of d_1, the first curvature area has a diameter of d_2 and the second curvature area has a diameter of t_1. The dents are arranged to figure A.1, but in this preferred embodiment the outer rims of two adjoining dents are in contact with each other for a maximum surface coverage. Again, the centres of the three adjoining dents form an equilateral triangle, the distance between the centres of the two adjoining dents having a constant value t_1 and the distance between two rows of dents having a constant value t_2. In this embodiment therefore the diameter of the second curvature area equals the distance between two adjoining dents t_1. A small area of surface remains in the centre between three adjoining dents. In this location preferably additional smaller-sized dents *200* can be provided, thereby further improving the flow properties of the surface.

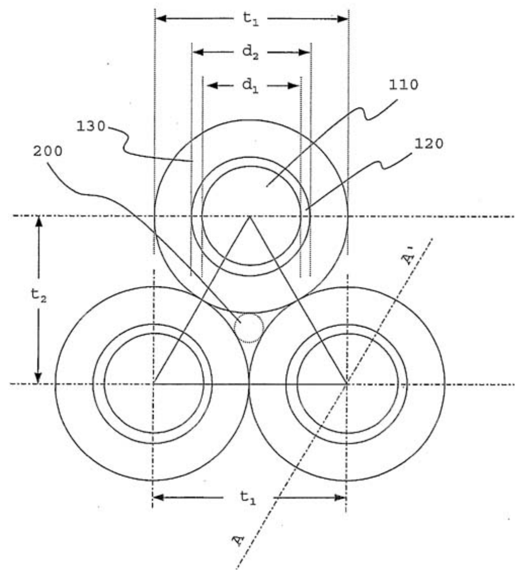

Figure A.3: Schematic distribution of dents *110*.

A cross-section AA' through the centre of a dent perpendicular to the surface is shown in more detail in figure A.4. The central dent area *110* essentially has the form of a section of a sphere, followed in the outward direction by two consecutive curvature areas. Since the curvature areas can be described as an arc, which is rotated in space, they have a surface formed as a part of a torus or similar thereto.
There is one point, in which the circle with radius R_1, being part of the sphere that forms the central dent area, and the circle with radius R_2, defining the curvature of the first curvature area, have a mutual tangent. Further, there is a point, in which the circle with radius R_2 and the circle with radius R_3 have a mutual tangent. To completely describe the form of the dent a set of parameters, in particular the parameters d_1, a_1,

a_2, R_2/R_1 and f, are chosen according to the necessities of the specific purpose the surface shall be used for and depending on whether drag reduction or improved heat exchange has priority. For most purposes the coverage of the surface by the central dent areas lies below 70%.

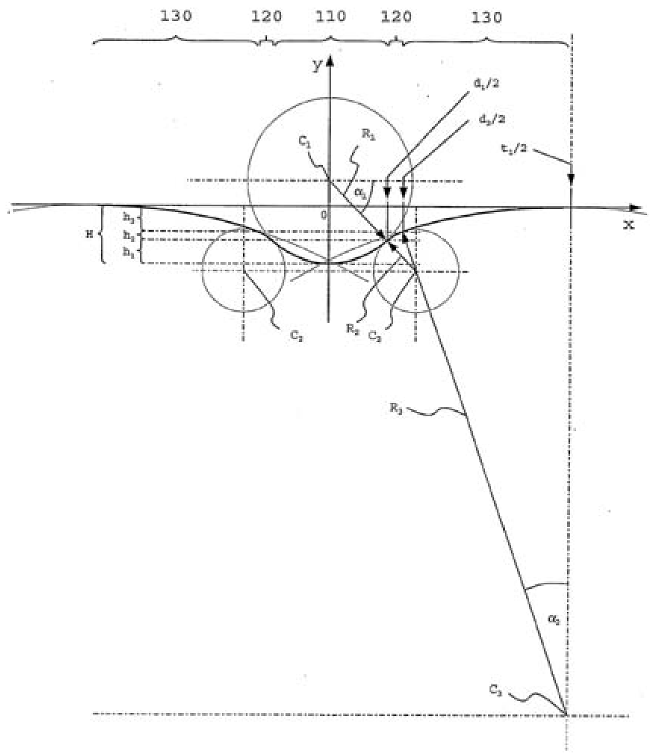

Figure A.4: Cross-section of dent *110*.

In figure A.5 a high-speed train *300* is shown schematically, which is provided with an inventive outer surface *310*, which comprises a multitude of dents, the form, size and distribution of which is adapted according to the speed and geometry of the train *300*. The train is characterized by improved flow properties in comparison to a similar train with a flat surface. In particular the forming of drag vortices is reduced as also the forming of lee wave in case side winds. Consequently the overall friction resistance is also reduced.
A further effect of the inventive surface lays in the separation point of the flow being moved further downstream or in certain circumstances the complete disappearance of a separation point. This effect allows for instance for providing completely new wing profiles. In figure A.6 a conventional wing profile *400* is shown in comparison with a modified wing profile *410*, the use of which becomes possible for example as a wing of an airplane, when the surface is provided with an inventive dent structure.
During the experiment performed by the inventors the hydrodynamic characteristics of the following objects were compared:

- The TLT-relief metal plate with the smooth surface metal plate;
- The adjustable elastic TLT-relief plate with the smooth plate with no holes on the

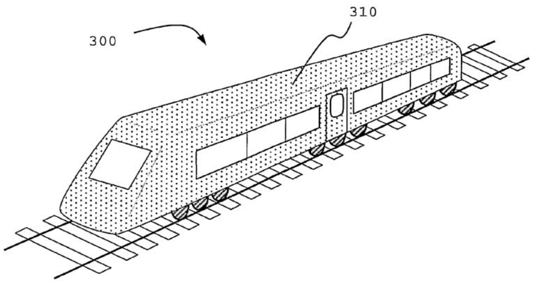

Figure A.5: High speed train with dents.

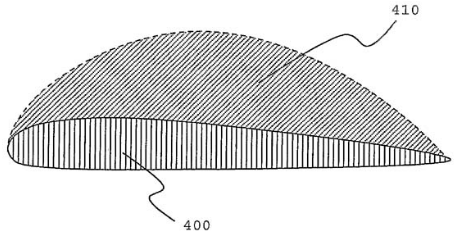

Figure A.6: Wing profile with dents.

support plate having the same elastic coating;

- The plates with various TLT reliefs on the metal surface with the plates with membranes and different TLT reliefs on the elastic surface.

The measurements were carried out in a cavitation tunnel of the Hamburgische Schiffbau-Versuchanstalt GmbH (HSVA), in which the flow was characterized by the Reynolds numbers defined as follows:

- Along the plate length considering the preliminary section within the range: $9 \cdot 10^5 \leq Re \leq 7,5 \cdot 10^6$
- Along the TLT relief concavity diameter within the range: $2,5 \cdot 10^4 \leq Re \leq 6 \cdot 10^5$

The onflowing stream turbulence rate was high and according to the laser measurements comprised:
$0,1 \leq \sigma \approx \sqrt{u'^2}/u_\infty \leq 0,3$
The water temperature in the flow was measured within the range:
$15\,^\circ\mathrm{C} \leq T \leq 22\,^\circ\mathrm{C}$

The velocity profiles were measured at thirty points arranged on the surface of the plate. The profile speed measurements on the ambient surfaces of the flat plates and the plates with TLT relief were performed at these points. The experimental data are represented in Table A.1 shown below. It follows from the table that the friction resistance of the metallic surface with the TLT relief is ∼22% lower than that of the smooth metallic surfaces. The friction resistance of the surface with elastic rough rubber coating and the TLT relief on it is ∼34% lower than that of the smooth elastic rough rubber coated surface.

Speed of undisturbed flow	Reynolds number to length plate	Position data of points, where the speed profiles over plate are measured		Displacement layer thickness of line of flow over the plate		Thickness of loss of impulse in the flow over plate		Local friction ratio	Total friction ratio
U_∞ m/s	$Re = U_\infty \cdot L/\nu$ 10^6	1. Section X_1 [m]	2. Section X_2 [m]	1. Section $\delta_1(X_1)10^3m$	2. Section $\delta_1(X_2)10^3m$	1. Section $\delta_2(X_1)10^3m$	2. Section $\delta_2(X_2)10^3m$	C'_f 10^3	C'_f 10^3
Measurement on metal plates with smooth and formed streamlined surfaces									
3	2,415			0,80	1,71	0,62	1,34	3,70	4,20
5	4,025	0,239	0,626	0,72	1,53	0,58	1,19	3,27	3,73
7	5,640			0,67	1,43	0,52	1,12	3,10	3,54
3	2,415			0,67	1,42	0,52	1,11	3,03	3,47
5	4,025	0,239	0,626	0,60	1,27	0,47	0,99	2,70	3,10
7	5,640			0,56	1,18	0,44	0,92	2,50	2,85
Measure results of the elastic, smooth and formed surface with rough rubber cover									
3	2,415			1,01	2,14	0,80	1,69	4,63	5,30
5	4,025	0,239	0,626	0,90	1,90	0,71	1,50	4,08	4,67
7	5,640			0,83	1,75	0,66	1,38	3,74	4,28
3	2,415			0,78	1,63	0,61	1,28	3,76	3,95
5	4,025	0,239	0,626	0,69	1,45	0,54	1,14	3,10	3,53
7	5,640			0,63	1,34	0,50	1,05	2,87	3,27

Table A.1: Experimental data of friction reduction.

A.2 TLT-patent US6119987A1; Method for Controlling the Boundary Layer of a Continuous Medium.

Method and Apparatus for Controlling the Boundary or Wall Layer of a Continuous Medium.[Kiknadze et al., 2000]
It is an object of this paper to provide a method for providing control of the boundary layer or the wall layer of a continuous medium comprising gases, liquids and/or mixtures thereof, for changing the flow structure, the turbulence level, the transfer of the impulse, the transfer of heat and/or admixtures in said layers is adapted to take advantage of a reduced hydraulic resistance, an increased heat and impulse transfer and may accordingly be used in huge variety of technical applications.
It has to be noted that the inventors have found a very fundamental solution of secondary tornado-like vortices as function of the speed of the streaming medium, which solution may be realized by a plurality of different physical forces and influences. The fundamental solution is directed to the flow structure itself, especially to the generation of secondary tornado-like vortices having a nonzero helicity $v \cdot rot(v) \approx 0$ and shall not be limited by any distinct device or preferred embodiment.

The continuous medium flow is influenced by a field of forces at least in the wall region of the flow within a range of distances y_n along the normal from the streamlined surface, the said range being from 0.005 to 0.3 of the thickness δ of the boundary layer. The influence is used to cause the velocity vectors of the continuous medium particles to turn alternately in space and/or in time through angles α=0.02 to 0.5 radian with regard to the streamlined surface and away from this surface, as well as through angles β=0.02 to 0.3 radian to the left and right with regard to the direction of motion of the wall flow of the continuous medium. In this case the intensity of the influence is such that the minimum curvature radius R_{min} of the trajectories of the continuous medium particles, which are under the influence of the field of forces within the range of the indicated distances from the wall, is from 2 to 30 average distances S along the normal from the streamlined wall to the curved trajectory of the particle. Whereas the spatial repetition of the influence is $\lambda \parallel$=(3 to 30) y_n along the direction of the wall flow and $\lambda \perp$=(1 to 10) y_n across the direction of the wall flow. The repetition time T being from 3 to 30 distances y_n, divided by the average velocity v in the boundary or wall layers, and this provides for the formation of secondary tornado-like vortex flows that create the structure of the boundary or wall layer, determining the level of intensity, of transfer of the impulse and heat.
In the case when the averaged velocity vectors turn toward the streamlined surface, this involves a decrease of the pulse and heat transfer from the following continuous medium to the surface, past which the flow runs, the pulse and heat transfer increases. Turns of the velocity vectors to the left or to the right with regard to the direction of the wall flow involve a transfer of the pulse across the said flow and perpendicular with regard to the normal to the surface, past which the flow runs.
The turns of the velocity vectors have an influence on the shift of the averaged velocity, i.e. on the derivatives of the absolute averaged velocity value with regard to the directions, which are perpendicular to the averaged velocity vectors. The changed Reynolds stresses also involve changes of the derivatives of the velocity components with regard to the coordinates. These factors, along with the extension of the tubes of flow under conditions of a three-dimensional change of the averaged velocity, result in the formation of various vortex structures, including tornado-like ones. The vortex

structures in their turn influence the transfer of the pulse, heat and admixtures.
The distance y_n from the wall, within which the field of forces exercises its influence on the continuous medium flow and which involves turns of the continuous medium particle velocity vectors, corresponds to the zone of formation and transformation of coherent large-scale structures, which play an important role in the wall turbulence mechanism. At a turbulent flow of the continuous medium this distance is normally enclosed within the range from 0.005 to 0.3 times the thickness d of the boundary layer.

The influence on the flow may be exercised by a magnetic field alternating in space and/or in time or jointly by a magnetic field and an electric field, concentrated in the wall region within a range of distances $y_n = (0.005 - 0.3)\delta$.
The influence on the flow may be accomplished by the shape of the streamlined surface alternating as deformable membranes, which are held at the circumference thereof, in space and/or in time, whereby pressure gradients are generated, which undergo changes in value and direction.
The flow may be influenced by blowing the continuous medium in and by sucking it off alternately in space and/or in time in various sections of the surface, past which the flow runs.

The method of controlling the boundary or wall layer of the continuous medium may be realized in the following way. The continuous medium flow is influenced by the field of forces F at least in its wall region within a range of distances y_n along the normal from the streamlined surface B, this range being from 0.005 to 0.3 of the boundary layer thickness δ. By means of such an influence the vectors of continuous medium particle velocities are caused to turn alternately in space and/or time through angles $\alpha = 0.02$ to 0.5 radian to the direction of the wall flow v or $\underline{v}$ of the continuous medium. In this case the influence intensity is such that the minimum curvature radius R_{min}, of trajectory A of the continuous medium particles, which are under the influence of the field of forces F within the range of the indicated distances from the wall is from 2 to 30 average distances S along the normal from the streamlined surface B to the particle curved trajectory A, whereas the spatial repetition of the influence is $\lambda \parallel= (3to30)y_n$ along the direction of flow, $\lambda \perp= (1to10)y_n$ across the direction of flow, time repetition T is from 3 to 30 distances y_n divided by the average velocity v in the boundary or wall layers, and this provides for the formation of secondary tornado-like vortex floes, which form the structure of the boundary or wall layer, and this structure determines the level of turbulence, transfer of the pulse, heat and admixtures. The created three-dimensional tornado-like structures are characterized by the nonzero helicity $v \cdot rot(v) \approx 0$.
In accordance with the modern knowledge, the vortex flow regions with the nonzero helicity, such as tornado-like structures, lead to the effects of the anomalous energy transfer along the turbulence spectrum, to the negative turbulent viscosity and to the disturbance of the Reynolds analogy in the direction of the heat transfer. So tornado-like vortex flows control and form the boundary or wall flow structure and create the helicity turbulence.

At first a source of influence should be located in the vicinity of, or in the surface; and testing of the flow structure provides information of the directional change of the velocity vector, i.e. also of the average velocity vector v, and is providing information about the distribution of angles of the velocity of the flow in the direction of the normal and in a plane extending parallel to the surface, see for instance figure A.7

and figure A.8.

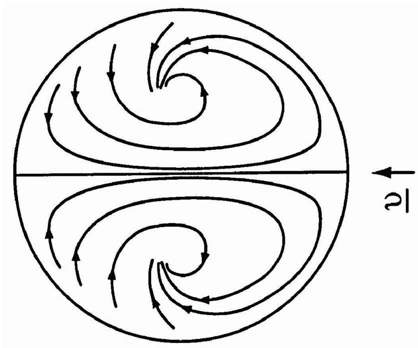

Figure A.7: Flow velocity normal to the surface.

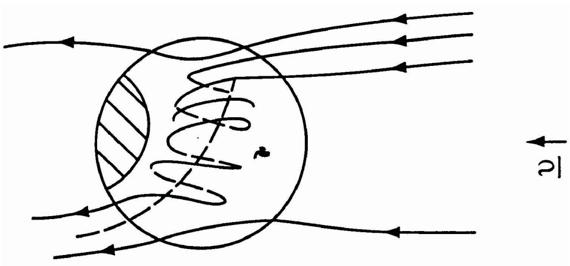

Figure A.8: Flow velocity parallel to the surface.

Based on the obtained results the intensity of the employed fields, i.e. the strength of the induced forces of the depth of deformation may be amended, essentially in view of a distribution in the direction of the normal to the surface.
After optimization of the first source the second and further sources may be located at a distance as defined in the claims. The grid of adapted sources may be obtained stepwise for substantially any surfaces and any shape and for basically all technically relevant devices, see e.g. figure A.9) for an embodiment of such a grid. Additionally, the sources may be randomly or statistically distributed.

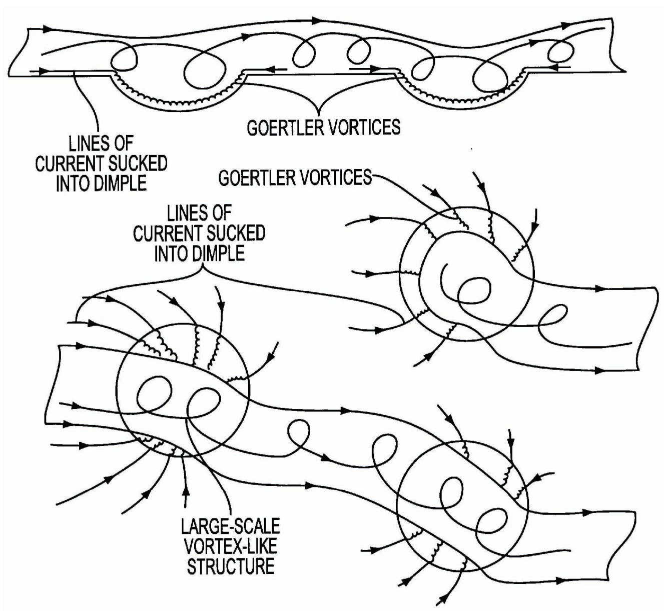

Figure A.9: Grid of dents on a surface.

It is obvious, in case of the body of a ship, in case of the wing of a plane or a body

of a vehicle, that there are different local velocities at different places. Consequently, the resulting positions of the sources will vary in accordance. Furthermore, not only to use a field of sources which are placed at the respective distances for the respective as described above, but to use a very dense field of sources which are not all energized at the same time. By omitting the energization of the respective misplaced sources it is possible to control the local influence also for different velocities, respectively.
Figure A.10 shows the C_D-coefficient of an inventive surface as function of the speed of the streaming medium in comparison to a prior art surface. Both surfaces were introduced into a windtunnel and the C_D-coefficient was measured. The inventive surface was containing spherical indentation, i.e. concavities having a maximum depth relative to the plane surface of about 0.5mm, a radius of about 4.5mm and a longitudinal spacing, i.e. spacing in streaming direction, of about 2.0mm between the edges of the indentations. Several rows of indentations were placed beneath each other in a staggered array with a spacing of the rows relative to each other of coarsely about 9.5mm. The speed of the streaming medium, which medium in this case was air, is given as Mach number. For 0.75 Mach it can be seen that the hydraulic resistance of curve 4 for the plane prior art surface is more than about 15% higher than the resistance of curve 3, i.e. the hydraulic resistance of the inventive surface.
To show the influence of a tilt angle on the inventive effect the inventive surface and the prior art surface were tilted relative to the speed of the streaming medium. As expected the lowest resistance, i.e. lowest C_D-coefficient was obtained for a tilt angle of zero degrees which is the same case as shown in figure A.11 where the medium was streaming essentially parallel to the surfaces. It clearly may be seen that the inventive reduction of the hydraulic resistance is effective for a wide range of tilt angles which tilt also may be called the angles of attack.

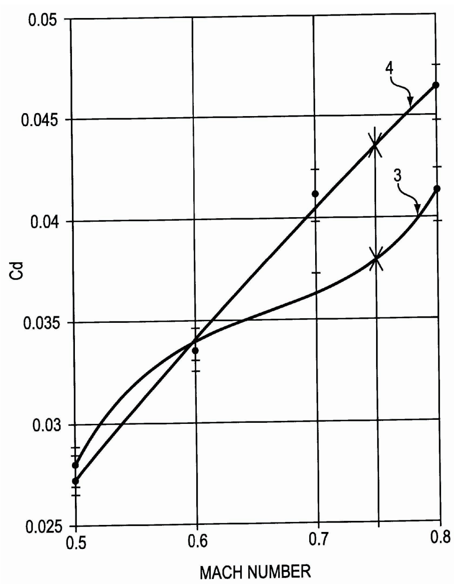

Figure A.10: C_D-coefficient of an inventive surface.

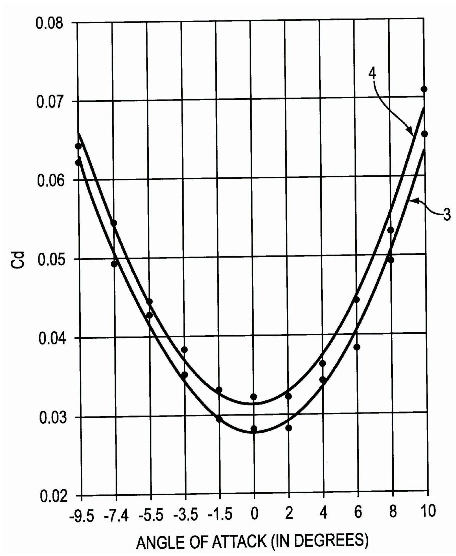

Figure A.11: The influence of a tilt angle on the C_D-coefficient.

Appendix B

Flow Visualization from literature.

An experiment, concerning experimental research of the flow through a single dent, is done by T.H. New and T.T. Lim of the National University of Singapore. [New and Lim, 2004]
An study has been carried out on a flow past a circular concavity embedded on a flat surface. Flow visualization using conventional point dye-injection of coloured dye was performed at various concavity depth-to-diameter ratios with Reynolds numbers ranging from 1500 to 6000. The results showed that, depending on exact Reynolds number of the flow and the depth-to-diameter ratio, the normally anticipated symmetric recirculating flow state within the concavity might not be sustainable. Instead, the flow state was observed to transit to an asymmetric one with a dominant vortex formed diagonally across the concavity. The presence of the vortex also seemed to lead to enhanced mass transport into and across the concavity. Reynolds number was found to be the driving factor behind the various major flow states occurring within the circular concavity, as the transition between the flow states remained almost invariant for the concavity depth-to-diameter ratios for this study.
The usefulness of concavities extends beyond the context of reduced form drag, as apparent in their application in areas where heat transfer is important. While it may be intuitive as to why they are favoured over a nominally flat surface for heat transfer purposes with respect to the increase in the effective heat transfer surface area, the higher-than-proportional increase in the heat transfer rate than could be explained by the increased surface area suggests that critical flow phenomena may be responsible for the observation. Many earlier studies have confirmed this fact, these concavities have, to a lesser extent, been associated with reduction in turbulent skin friction drag. However, the experimental results gathered so far has proved to be inconclusive.
Self-organization of vortex flows within the concavities has been pointed out as the basis for the observation of increased mass and heat transfer when such three-dimensional surface profiles exist on the flow surfaces. It has been argued earlier that the formation of symmetric and/or asymmetric vortex structures within the concavities could be the source of disproportional increase in mass and heat transfer rate. However, the exact natures of these vortex systems still remained elusive till these days despite several attempts to explain and formulate a mechanism for their appearance. Moreover, their transitions to various flow states with different flow parameters further impede our understanding of these concavities flow behaviour. Adding to these difficulties are the

highly three-dimensional resultant flow fields, which could cause practical experimental problems when one tries to examine the flow field qualitatively and/or quantitatively.
The flow field of a flow past a circular concavity is the first step to a better understanding of its basic flow physics and certainly, the most basic building block toward good grasp of the flow field resultant of a flow past an array of such concavities. The lack of clear and distinct understanding of the most basic flow configuration surrounding a circular concavity prompted this flow visualization study. While flow images similar to the configuration here have been obtained previously, they were usually the results of isolated specific work conducted at arbitrary flow parameters. Consequently, it might have led to many conflicting viewpoints regarding the exact flow structures involved. Therefore, this study attempts to explore in a systematic manner the evolution of a flow past a single circular concavity with increasing concavity depth-to-diameter ratio as well as Reynolds number, so as to map out the flow regimes of interest for future studies.
Point dye-injection flow visualization has been carried out for a flow past a circular concavity with a depth-to-diameter ratio (h_c/d_c) of 0.1, 0.15 and 0.2, with Reynolds number ranging from 1500 to 6000 (Re=1500 interval).

Remark by E. Vervoort; Research of New and Lim in relation to the graduation thesis:
New and Lim use a different definition of the reference length (L = dent diameter) then used in the thesis presented in this report where the reference length is the length of the tested plate. According the the definition of New and Lim, in the graduation thesis most research is performed at a Reynolds number of $Re_L = \frac{\rho U L}{\mu} = \frac{1.225 \cdot 5 \cdot 0.02}{1.7894 \cdot 10^{-5}} = 6846$ and size parameters of $h_c/d_c = 0.343/20.0 = 0.017$ and $h_c/d_c = 3.0/20.0 = 0.15$. The deepest dent is closest represented by the experiments done with $Re = 6000$ and $h_c/d_c = 0.15$ in the article by New and Lim [New and Lim, 2004]. These results are presented here:
End of remark

According to figure B.1, the dye-streaks were observed to convect into the concavity but instead of forming the expected recirculating regions, a single tornado-like vortex was observed to form diagonally across the concavity with its axis orientated at about 45° in the downstream direction. Occasionally, the vortex would flip over to the opposite side of the concavity and back again but they ultimately remained sporadic events. A closer look at the video recordings and the still images indicated that the rotational sense of this singular vortex was the same as in the one observed for the symmetrical case described earlier, suggesting that this vortex might be derived from the stable horseshoe vortex system observed previously at other Reynolds number and h_c/d_c-values. But on the other hand, its origin seemed to stem from a point on the concavity wall which was distinctly marked out by a small recirculating pool of coloured-dye. Clearly, more conclusive experimental data is needed to resolve this issue. Nevertheless, the subsequent behaviour of the vortex was intriguing, to say the least. It demonstrated what could best be described as a visually strong scourging action within the concavity and remained the largest vortex structure observed throughout the entire study. The figures showed the dye-streaks spiraling around throughout the vortex axes until the vortex ended just as abruptly at the other diagonal end of the concavity. There existed regular ejections of coloured-dye near the location where the vortex diffused, indicating that mass ejection from the concavity was periodic and common as well.
The above observations suggested that the appearance of the tornado-like vortex might lead to an increase in the mass transfer not only diagonally across but into the concavity.

One could certainly imagine the usefulness of these concavities in the area of heat transfer whereby a suitably arranged pattern of them are able to alter the flow field such that the cooling fluid is being continuously drawn across and into the concavities to cool the surface. The scourging action would further enhance the process by transferring heat away from the fluid within the concavities to the cooler fluid further away from the surface.

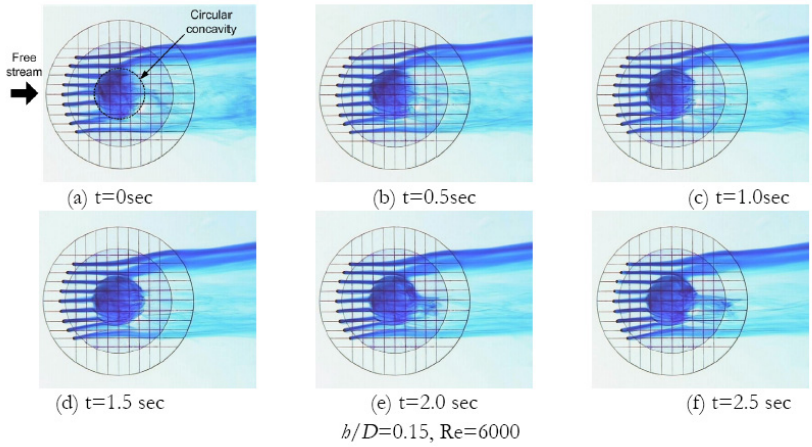

Figure B.1: Flow (Re=6000) through dent (h_c/d_c=0.15).

Figure B.2 shows a close-up view of the tornado-like vortex at a reduced rate of coloured-dye injection for better observation. The image clearly showed the dye-streak flowed into the concavity and terminated at a small recirculatory point acting very much like a source thereafter. The dye was subsequently entrained into the vortex and spiraled about until it was ejected at the downstream edge of the concavity. With this, the difference in the flow field between the symmetric and asymmetric scenario could be schematically shown in figure B.3, from both side cross-section as well as plan view. However, these flow differences were established to be preliminary and much work still needed to be covered to improve the overall understanding of flows past these three-dimensional concavity and subsequent optimization.
Conclusions:
An experimental study has been carried out to visualize the flow field associated with flow past a circular concavity with h_c/d_c=0.1, 0.15 and 0.2 at Re=1500 to 6000. Results have shown that it is possible for the normally anticipated symmetrical flow field within the concavity to breakdown into an asymmetrical one. Evidences suggested that flow unsteadiness might be the cause of the transition; even though under no circumstances during the investigation did the asymmetrical flow field revert back to symmetrical state at the same flow configurations when the former occurred. It is believed that the tornado-like vortex observed during flow asymmetry is linked to the stable horseshoe vortex system in the concavity when the flow is symmetric. Realignment of the vorticity associated with the horseshoe-like vortex system triggered by flow unsteadiness caused the tornado-like vortex to form diagonally across the concavity and resulted in subsequent regular mass ejection across and from the concavity. These observations supported previous claims regarding the existence of these tornado-like asymmetric vortices which purportedly increase mass and heat transfer. However, the exact nature

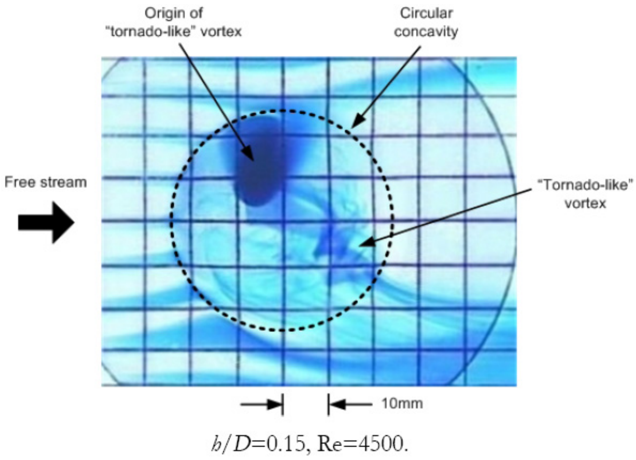

Figure B.2: Close-up view of the asymmetric tornado-like vortex (Re=4500, h_c/d_c=0.15).

of the transition between the symmetrical and asymmetrical flow states remains to be explored further.

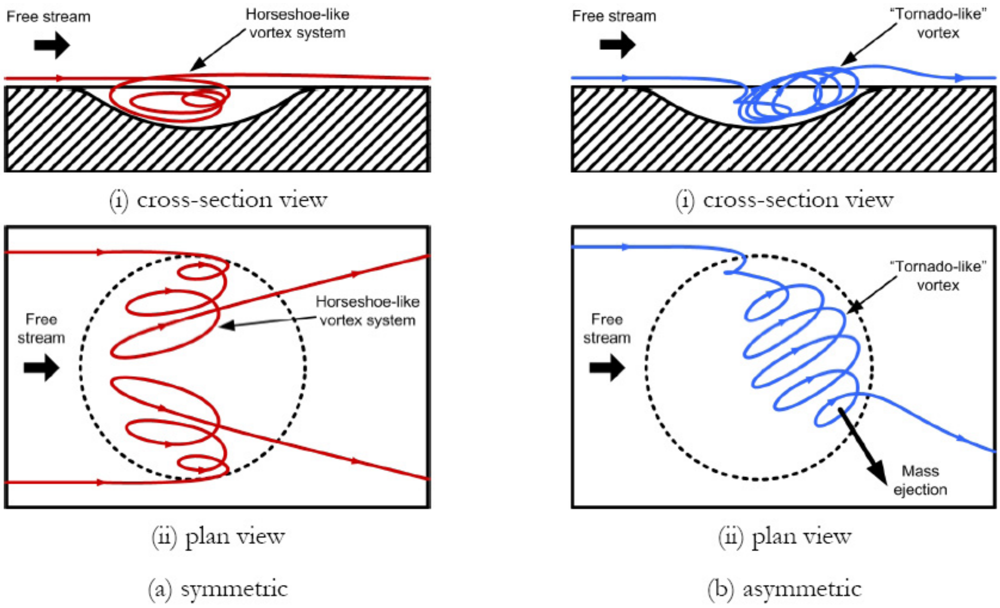

Figure B.3: Schematic drawings for both symmetric and asymmetric flow fields encountered.

Appendix C

Simulations Data.

In this appendix the most important results of the simulations are presented. Also a brief explanation of the setup of the simulations is given.
Appendix C.1 concerns the first series of simulations. The main focus of this series of simulations is to find the correct turbulent model. In this series the only geometry used is the flat plate.
Appendix C.2 contains simulations to test the behaviour of the Large-Eddy Simulation method at different velocities, ranging from U=1m/s up to U=40m/s. Only the flat plate geometry is used in the series of simulation.
Appendix C.3 features the first series of simulations where dents are added to the geometry. In this series the flat plate (reference value) and seven dent-configurations are tested, each with a different dent depth, all at a velocity of 5m/s.
Appendix C.4 contains the setup and results of simulations done with "split" plates. Here the objective is to investigate the drag at the different places in the dents. Three different geometries are tested; the flat plate and two dents, one with a depth of 0.343mm and the dented plate with a dent depth of 3.00mm.
Appendix C.5 contains data of simulations done with a free-stream velocity of 50m/s, instead of 5m/s used in C.3 and C.4. Here only three simulations are done. The flat plate and the dents with a depth of 0.343mm and 3.000mm are tested.
Appendix C.6 contains data of a simulation done with a non-rotational symmetric dent-shape.

C.1 Simulation - Series 1; Simulations to Establish the Choice of the Viscous Model.

Title: Simulations with 6 Turbulence Models at 5m/s.	
Numbers of Simulations:	1-01, 1-02, 1-03, 1-04, 1-05 & 1-06
Dents Used:	Flat plate only
Objective of the Series of Simulations: This set of simulations is performed to compare the behaviour of six turbulence models to a flow of 5m/s over a flat plate.	
Brief Description: In this series of simulations six turbulence models are tested. These are: - The Spalart-Allmaras model - The k-ε model (three submodels: the Standard, RNG and Realizable k-ε model) - The k-ω model (two submodels: the Standard and SST k-ω model) - The Reynolds Stress model (RSM) - The Large Eddy Simulation model (LES) - The Detached Eddy Simulation model (DES) For the Spalart-Allmaras and the Standard k-ε model steady as well as unsteady simulations are performed. This is done to check the differences in results and convergence speed.	
Case Setup	
Geometry: The geometry used here consists out of a flat plate, with a length of 500mm and a width of 50mm. The height of the domain is 250mm.	
Boundary Conditions: - Flat Plate: This is a non-moving wall - Left & Right boundaries: Symmetry boundaries, since the geometry is symmetric with respect to these boundaries. - Inflow: a velocity inlet is used here, with a uniform velocity. - Outflow: a pressure outlet is used here. - Top of domain: symmetry or pressure far-field. The domain should have a zero-pressure gradient. A symmetry boundary is sufficient if the domain is high enough, otherwise the pressure far-field has to be implemented. Disadvantage of the pressure far-field is the need to model the density as an ideal gas. For an ideal gas the density is variable, which increases calculation time.	
Flow Properties: Free-stream flow velocity = 5.0m/s Reynolds number = $\frac{\rho \cdot U \cdot L}{\mu} = \frac{1.225 \cdot 5.0 \cdot 0.5}{1.7894 \cdot 10^{-5}} = 1.71 \cdot 10^5$ Theoretical drag coefficient: $C_{D_{theory}} = 0.031 \cdot Re_L^{-1/7} = 0.031 \cdot (1.71 \cdot 10^5)^{-1/7} = 5.543 \cdot 10^{-3}$	

this table continues on the next page

Mesh:
All simulations are performed making use of the same mesh. This mesh is used only for establishing the correct turbulence model. The mesh used is a coarse mesh. For this series of simulations it is decided to make use of the wall function method to model the flow near the wall. This method does not require as much time to perform the simulations as the near wall approach does. Also since for this series of simulations it is not important to simulate details near the wall, the wall function method is the correct method to use. Since the geometry used is the flat plate the coarse mesh does not leave any geometric details out of the simulation. In later simulations, where dented plates are tested, a finer mesh is need required.
For the wall function method the z^+-value has to be between 20 and 150. The height of the first cell is 2.5mm. Which, in theory, must result in: $z^+ = 0.0581 \cdot \frac{h_{first}}{L} \cdot Re_L^{13/14} = 0.0581 \cdot \frac{0.0025}{0.5} \cdot (1.71 \cdot 10^5)^{13/14} = 21.0$. But the z^+-value will not be exactly the same in the simulations as expected. After the simulation is performed the z^+-values need to be checked. (Figure C.3)
The height of the cell grows for each layer of cells with a factor of 1.02.
The length and width of the cells is 2.5mm. These dimension is chosen because the height is the cells of the first row is also 2.5mm, thus resulting in cubic cells which have a minimal skewness. The x^+-value and y^+-value are both equal to 21.0. This are low values for the wall functions model. Low x^+-, y^+-, or z^+-values do not cause problems when performing simulations, only the simulation will take longer because more cells are used then necessary for the turbulence model.
Number of cells: length×width×height =189×19×51=183,141 cells

Table C.1: Series 1: Setup of the simulations.

Results:								
Simulation	Numb.	Timesteps	Size ts.	It./ts.	$C_{D_{sim.}}$	ΔC_D	$C_{L_{sim.}}$	$C_{M_{sim.}}$
1-01: LES Model (unsteady; Symmetry & Far Field BC's)								
symBC	1-01a	75	0.025	200	0.00564	1.7	-0.0099	0.0026
FFBC	1-01b	85	0.025	150	0.00542	-2.1	-0.0040	0.0005
1-02: Spalart-Allmaras Model (steady & unsteady; Symmetry & Far Field BC's)								
st symBC	1-02a	n.a.	n.a.	600	0.00644	16.1	-0.0087	0.0022
st FFBC	1-02b	n.a.	n.a.	600	0.00622	12.3	-0.0038	0.0004
unst symBC	1-02c	15	0.025	200	0.00643	16.1	-0.0087	0.0022
unst FFBC	1-02d	15	0.025	200	0.00622	12.2	-0.0039	0.0005
1-03: DES Model (unsteady; Symmetry & Far Field BC's)								
symBC	1-03a	15	0.025	150	0.00511	-7.9	-0.0093	0.0021
FFBC	1-03b	30	0.025	150	0.00486	-12.3	-0.0038	0.0013
1-04: k-ε Model, Standard (steady & unsteady; Symmetry & Far Field BC's)								
st symBC	1-04a	n.a.	n.a.	600	0.00630	13.7	-0.0087	0.0024
st FFBC	1-04b	n.a.	n.a.	600	0.00616	11.22	-0.0035	0.0005
unst symBC	1-04c	15	0.025	200	0.00630	13.7	-0.0087	0.0024
unst FFBC	1-04d	25	0.025	200	0.00617	11.2	-0.0035	0.0006

this table continues on the next page

1-04: k-ε Model, RNG (steady & Far Field BC's)								
st FFBC	1-04e	n.a.	n.a.	800	0.00606	9.40	-0.0035	0.0006
1-04: k-ε Model, Realizable (steady & Far Field BC's)								
st FFBC	1-04f	n.a.	n.a.	1600	0.00615	11.02	0.0036	-0.0014
1-05: k-ω Model, Standard (steady & Far Field BC's)								
st FFBC	1-05a	n.a.	n.a.	425	0.00655	18.17	-0.0039	0.0003
1-05: k-ω Model, SST (steady & Far Field BC's)								
st FFBC	1-05b	n.a.	n.a.	425	0.00644	16.13	-0.0041	0.0005
1-06: Reynold Stress Model (RSM) (steady & Far Field BC's)								
st FFBC	1-06	n.a.	n.a.	500	0.00616	11.17	0.0062	-0.0006

Table C.2: Series 1: Results.

Simulation number	z^+_{theory} [-]	$z^+_{sim.}$ [-]	Difference [%]
1-01a	21.0	17.8-33.4	-15.2 - +59.0
1-01b	21.0	17.3-32.9	-17.6 - +56.7
1-02a	21.0	22.0-33.1	+4.8 - +57.6
1-02b	21.0	21.6-32.5	+2.9 - +54.8
1-02c	21.0	22.0-33.2	+4.8 - +58.1
1-02d	21.0	21.6-32.5	+2.9 - +54.8
1-03a	21.0	15.9-33.2	-24.3 - +58.1
1-03b	21.0	15.5-32.5	-26.2 - +54.8
1-04a	21.0	22.4-29.0	+6.7 - +38.1
1-04b	21.0	22.9-28.8	+9.0 - +37.1
1-04c	21.0	23.3-29.1	+11.0 - +38.6
1-04d	21.0	22.9-28.7	+9.0 - +36.7
1-04e	21.0	22.8-28.4	+8.6 - +35.2
1-04f	21.0	22.0-29.2	+4.8 - +39.0
1-05a	21.0	21.7-32.4	+3.3 - +54.3
1-05b	21.0	21.3-32.4	+1.4 - +54.3
1-06	21.0	22.1-28.8	+5.2 - +37.1

Table C.3: z^+-values for the meshes used in series 1.

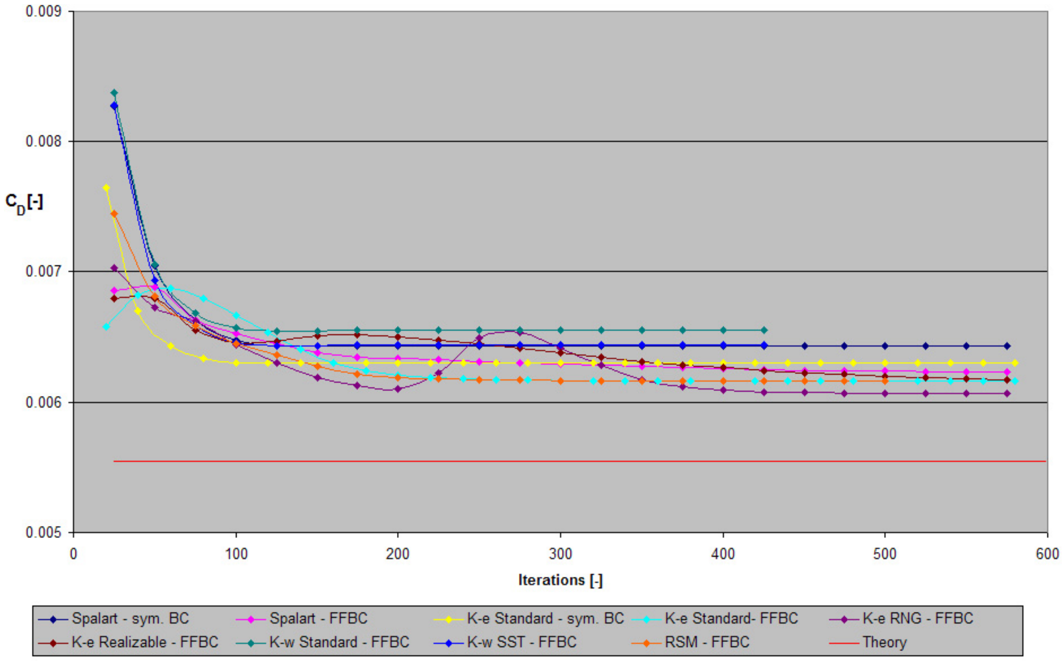

Figure C.1: Development of the dragcoefficients for the steady simulations.

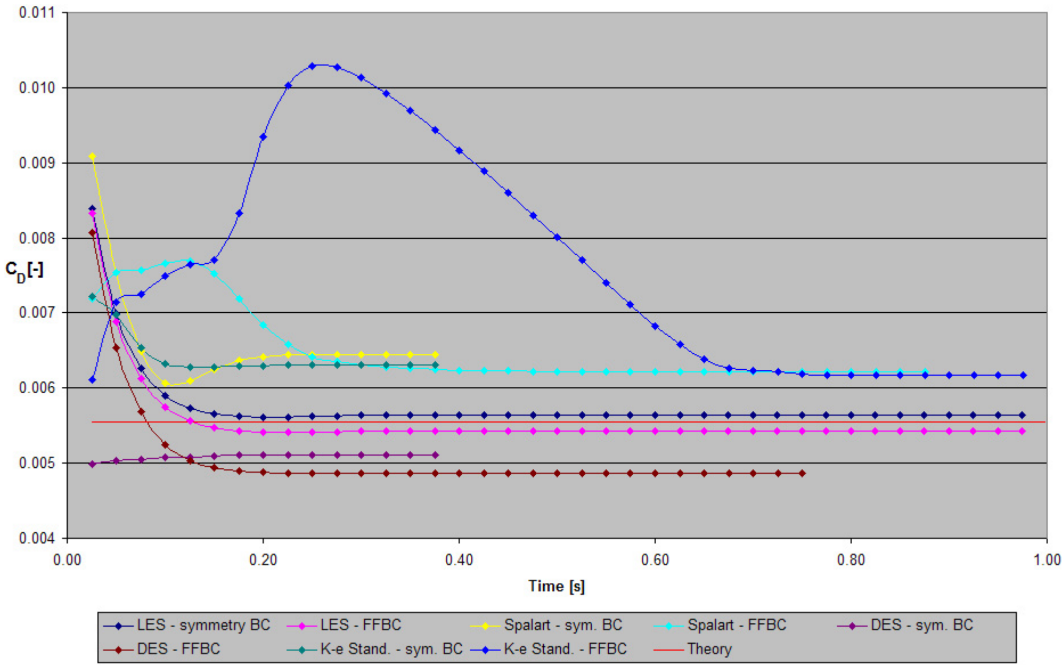

Figure C.2: Development of the dragcoefficients for the unsteady simulations.

C.2 Simulation - Series 2; Behaviour of the LES Turbulence Model at Different Velocities.

Title: Simulations with the LES Turbulence Model at Different Speeds.	
Numbers of Simulations:	2-01, 2-02, 1-01b, 2-03, 2-04 & 2-05
Dents Used:	Flat plate only
Objective of the Series of Simulations: This series of simulations is performed to check the behaviour of the LES turbulence model at different velocities.	
Brief Description: In this series of simulations six different velocities are used to simulate the flow over a flat plate. These velocities are: 1m/s, 3m/s, 5m/s, 10m/s, 20m/s and 40m/s. The simulation with 5m/s is taken from simulation series 1.	
Case Setup	
Geometry: The geometry used here consists out of a flat plate, with a length of 500mm and a width of 50mm. The height of the domain is 250mm. (The same geometry as used in series 1.)	
Boundary Conditions: - Flat Plate: This is a non-moving wall - Left & Right boundaries of the domain: These are set as symmetry boundaries, since the geometry is symmetric with respect to these boundaries. - Inflow: A pressure inlet is used here, with a uniform pressure. The pressure inlet is used because Fluent issues that velocity inlet boundary conditions are not appropriate for compressible flow problems, although no major problem are encountered when using velocity inlets. - Outflow: A pressure outlet is used here. - Top of domain: pressure far-field, to insure a zero-pressure gradient.	
Flow Properties: Free-stream flow velocity varies: 1m/s, 3m/s, 5m/s, 10m/s, 20m/s and 40m/s. Reynolds number ($Re_L = \frac{\rho \cdot U \cdot L}{\mu}$) and theoretical drag coefficient ($C_{D,theory} = 0.031 \cdot Re_L^{-1/7}$) vary, because they both are a function of the velocity. These are shown in Table C.5	
Mesh: All simulations are performed making use of the same mesh. This will result in different z^+-values, but as long as all z^+-values activate the wall function approach for the fluid flow near the wall, then this approach is allowed. The length and width of the cells is 2.5mm. The height of the first cell is 2.5mm. The height of the cell grows for each layer of cells with a factor of 1.02, with no maximum. The z^+-value varies because it depends on the velocity, see table3.3. ($z^+ = 0.0581 \cdot \frac{h_{first}}{L} \cdot Re_L^{13/14}$) Number of cells: length×width×height=189×19×51=183,141 cells	

Table C.4: Series 2: Setup of the simulations.

Results:						
Simulation number	Velocity [m/s]	Time-steps	Size ts.	It./ts.	Reynolds number	$z^+_{expected}$
2-01	1	30	0.025	200	34,229	4.7
2-02	3	30	0.025	200	102,688	13.1
1-01b	5	20	0.025	150	171,147	21.0
2-03	10	30	0.025	200	342,294	40.1
2-04	20	30	0.025	200	684,587	76.3
2-05	40	30	0.025	200	1,369,174	145.2
Simulation number	Velocity [m/s]	$C_{D_{theory}}$	$C_{D_{sim.}}$	ΔC_D	$C_{L_{sim.}}$	$C_{M_{sim.}}$
2-01	1	0.00698	0.00862	23.5	-0.0534	0.0177
2-02	3	0.00596	0.00631	5.8	-0.0049	0.0006
1-01b	5	0.00554	0.00542	-2.1	-0.0040	0.0005
2-03	10	0.00502	0.00472	-6.1	-0.0032	0.0005
2-04	20	0.00455	0.00422	-7.1	-0.0032	0.0005
2-05	40	0.00412	0.00381	-7.5	-0.0034	0.0007

Table C.5: Series 2: Results.

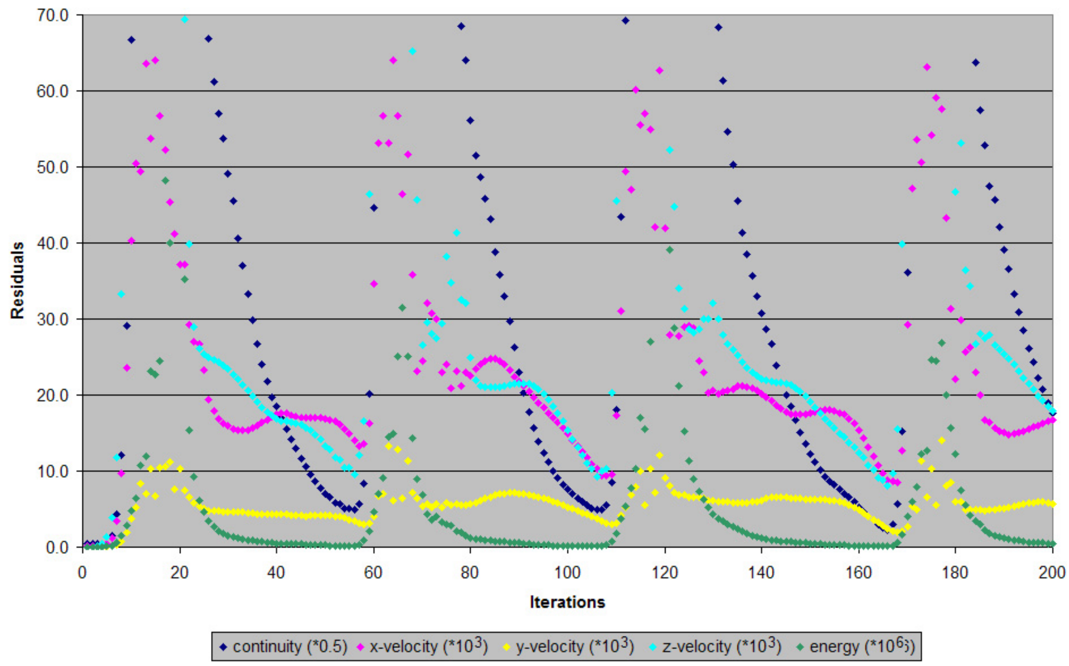

Figure C.3: Residuals of the first timestep for the simulation with 1m/s.

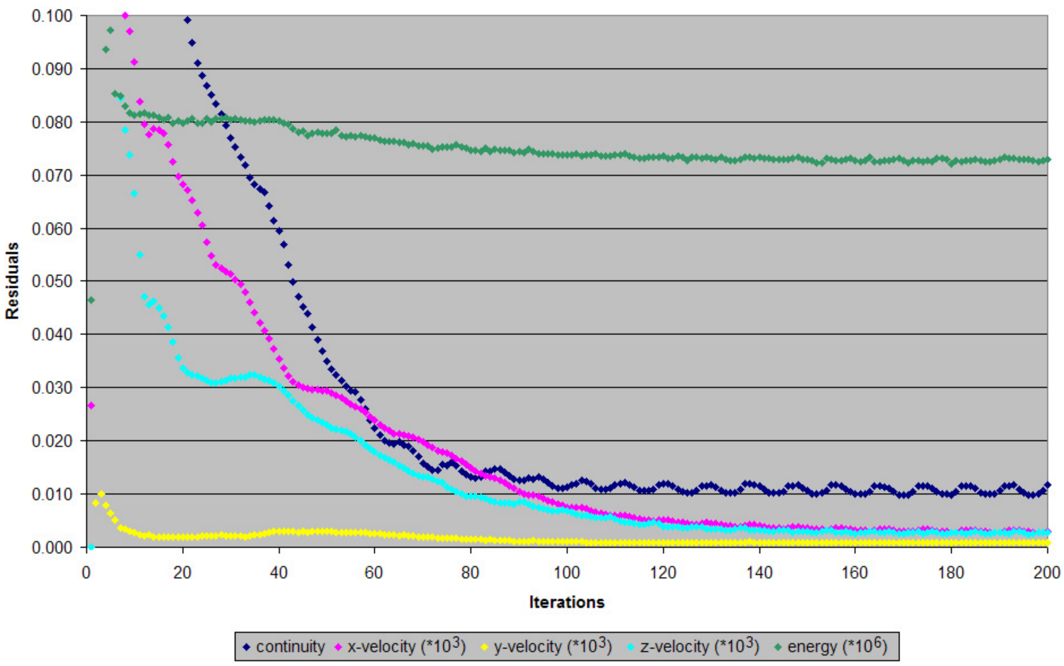

Figure C.4: Residuals of the first timestep for the simulation with 20m/s.

C.3 Simulation - Series 3; Plates with Different Dent Depths.

Title: Simulations with seven dents, all with different depths.	
Numbers of Simulations:	3-01, 3-02, 3-03, 3-04, 3-05, 3-06, 3-07 and 3-08
Dents Used: Flat plate (reference value) and seven dented plates. The only difference between the dented plates is the depth of the dents. The depths used are: 0.343mm, 0.686mm, 1.843mm, 1.988mm, 2.133mm, 2.422mm and 3.000mm.	
Objective of the series of Simulations: The series of simulations is performed to investigate the relation between the depth of the dents and the drag of the plate. Goal is to find a drag change caused by the dents in the surface of the plate and to explain why this drag change occurs.	
Brief Description: The flow over seven dented plates and one flat plate is simulated. Flow properties are identical for all cases. The meshes are not identical, because of the differences in geometry, but the differences are small.	
Case Setup	
Geometry: The geometry used here consists out of a plate, with a length of 500mm and a width of 57.2mm, for the flat plate a width of 50.0mm is used. The height of the domain is 250mm. The width of the dented plates is larger then the width used in previous simulations. This is done to still ensure symmetry of the geometry. In each dented plate three rows of dents are constructed, one in the middle of the plate and two on the edges of the plate. These last two rows are consist solely out of half dents, to make the geometry symmetric. (see figure 3.2)	
Boundary Conditions: - Plates: These are all non-moving walls. - Left & Right side of the domain: These are set as symmetry boundaries, since the geometry is symmetric with respect to these boundaries. - Inflow: A velocity inlet is used here, with a uniform velocity. - Outflow: A pressure outlet is used here. - Top of domain: pressure far-field, to insure a zero-pressure gradient.	
Flow Properties: Free-stream flow velocity for all simulations in this series is 5m/s. Reynolds number $Re_L = \frac{\rho \cdot U \cdot L}{\mu} = \frac{1.225 \cdot 5.0 \cdot 0.5}{1.7894 \cdot 10^{-5}} = 1.71 \cdot 10^5$ $C_{D_{theory}} = 0.031 \cdot Re_L^{-1/7} = 0.031 \cdot (1.71 \cdot 10^5)^{-1/7} = 5.543 \cdot 10^{-3}$	
Mesh: GRIDGEN is used to make the meshes, this program provides more control over the mesh, especially when small cells need to be constructed near the wall, than GAMBIT (which was used to create the mesh in all previous simulations). Width and length of the cells are decreases (compared to previous series of simulations) to a size of 1mm. This is done to allow more detailed simulations. The height of the cells varies. The first cell should have a height corresponding with an z^+-value of 1. Thus: $h_{first} = 17.21 \cdot z^+ \cdot L \cdot Re^{-\frac{13}{14}} = 17.21 \cdot 1 \cdot 0.5 \cdot (1.71 \cdot 10^5)^{-\frac{13}{14}} = 0.119mm$.	

this table continues on the next page

The height of the cells grows linear to a value of 4.68mm, from there the cells have a constant height of 4.92mm. Number of cells: length×width×height= $501 \times 58 \times 78 = 2,266,524$ cells
Simulation properties: For all simulation in this series holds: - Number of timesteps: 100 - Iterations in one timestep: 200 - Size of a timestep: 0.005s, thus the total simulated time is 0.5s.

Table C.6: Series 3: Setup of the simulations.

Results:						
Simulation Number	Depth [mm]	$C_{D_{sim.}}$	ΔC_D w.r.t. $C_{D_{theory}}$	ΔC_D w.r.t. $C_{D_{sim.,flatplate}}$	$C_{L_{sim.}}$	$C_{M_{sim.}}$
3-01	0.000	0.00589	6.3	n.a.	-0.0011	0.0001
3-02	0.343	0.00558	n.a.	-5.3	-0.0009	0.0003
3-03	0.686	0.00566	n.a.	-3.9	-0.0012	0.0005
3-04	1.843	0.00596	n.a.	1.2	-0.0015	0.0006
3-05	1.988	0.00598	n.a.	1.5	-0.0014	0.0005
3-06	2.133	0.00600	n.a.	1.9	-0.0014	0.0005
3-07	2.422	0.00607	n.a.	3.1	-0.0014	0.0004
3-08	3.000	0.00616	n.a.	4.6	-0.0013	0.0004

Table C.7: Series 3: Results.

Simulation number	z^+_{theory} [-]	$z^+_{sim.}$ [-]	Difference [%]
3-01	1.0	0 - 4.3	+334
3-02	1.0	0 - 4.4	+337
3-03	1.0	0 - 4.2	+322
3-04	1.0	0 - 4.4	+336
3-05	1.0	0 - 4.4	+336
3-06	1.0	0 - 4.3	+333
3-07	1.0	0 - 4.4	+335
3-08	1.0	0 - 4.4	+335

Table C.8: z^+-values for the meshes used in series 3.

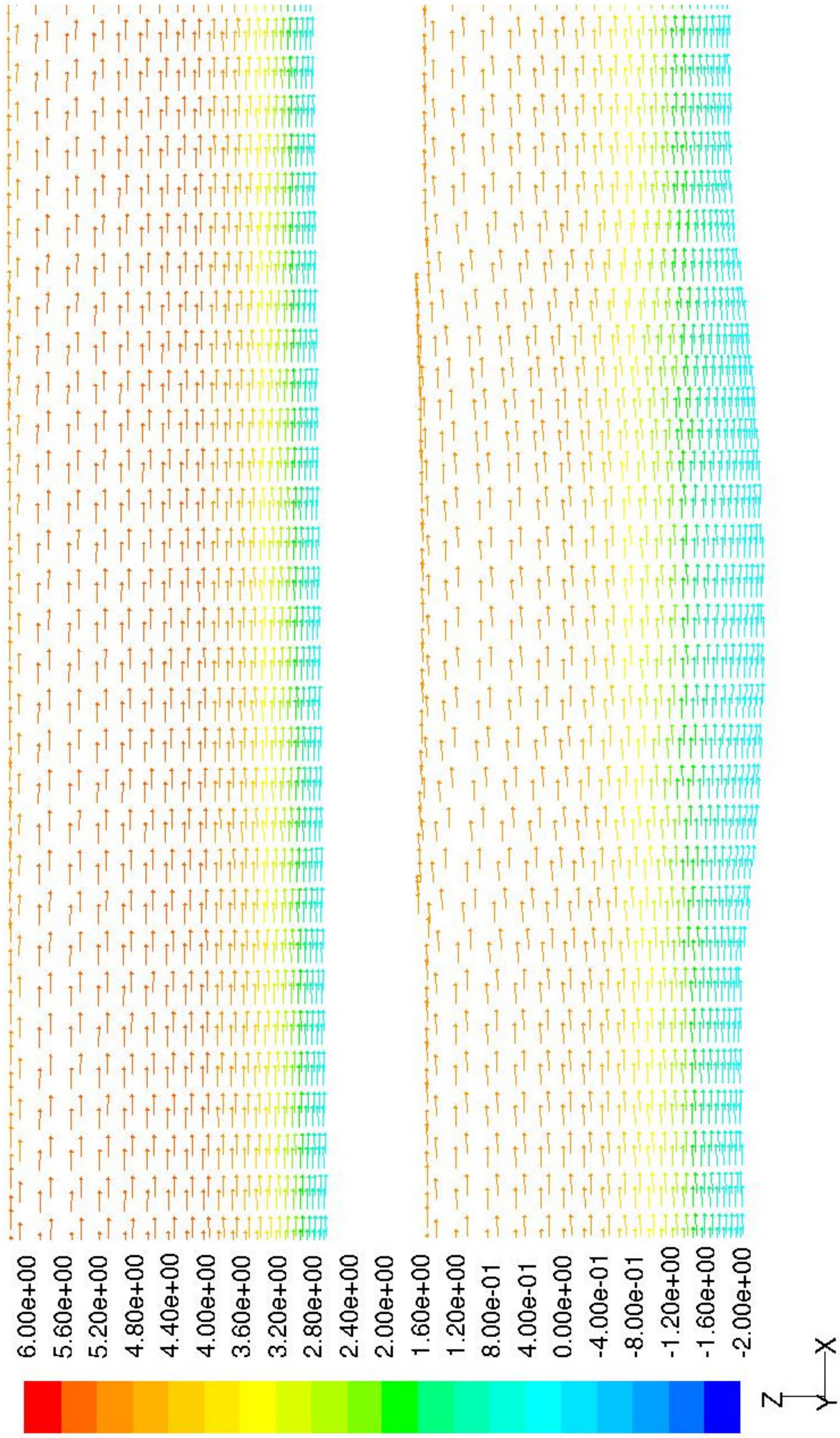

Figure C.5: Velocity vectors in cross-section in the middle of the dents; attached flow for the flat plate (left) and for the dent with depth 0.686mm (right).

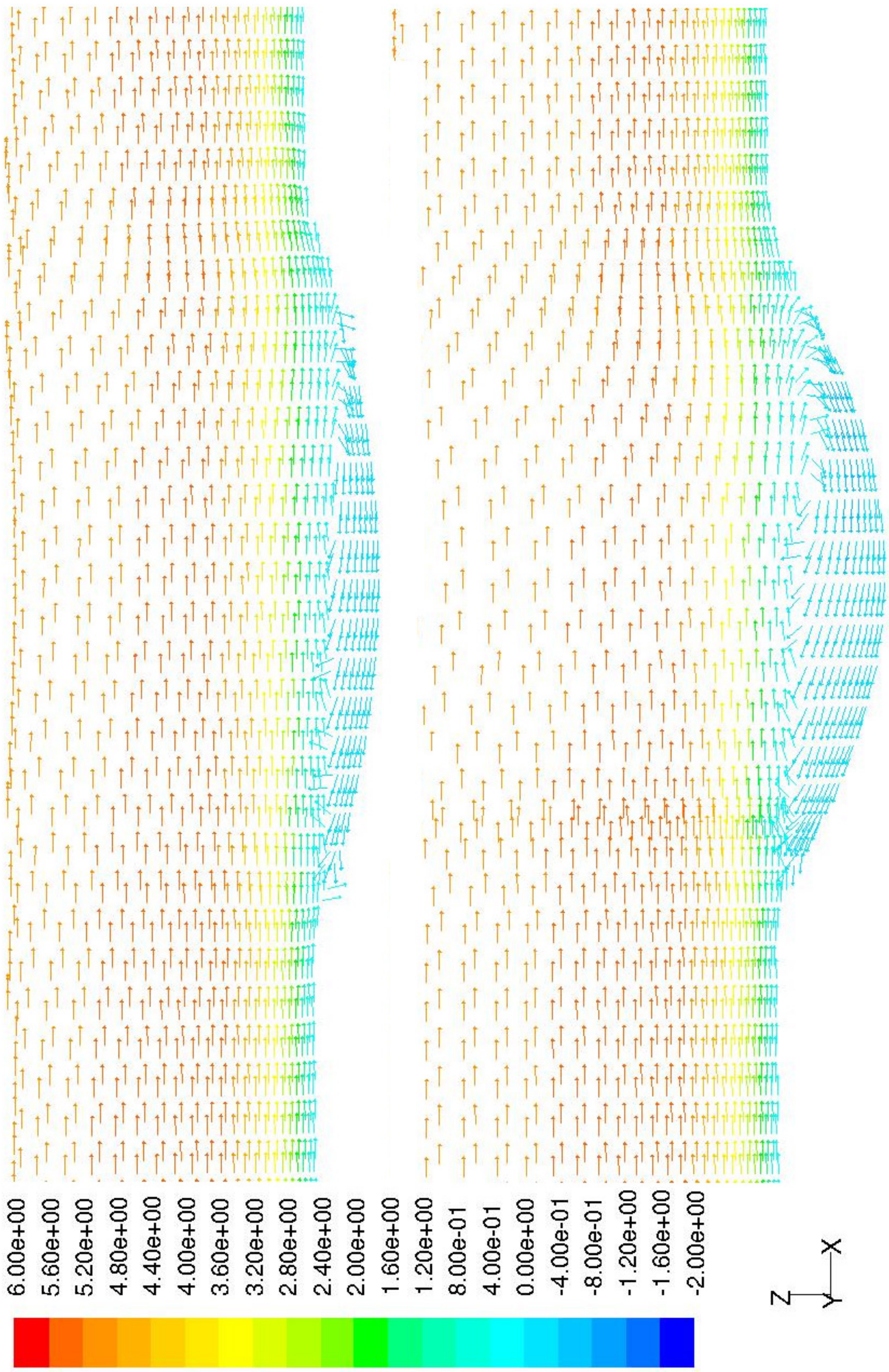

Figure C.6: Velocity vectors in cross-section in the middle of the dents; detached flow for the dent with depth 1.843mm (left) and for the dent with depth 3.000mm (right).

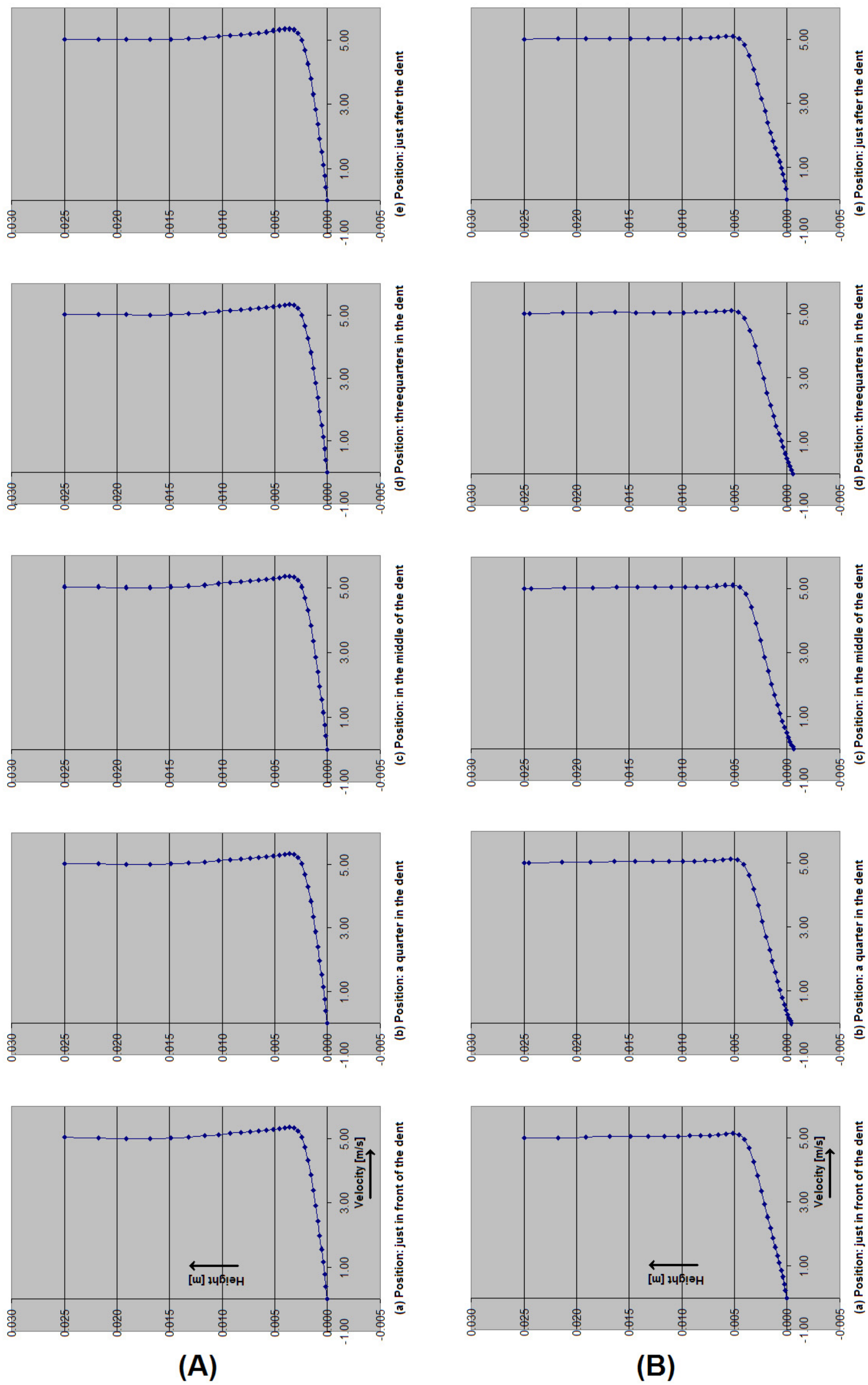

Figure C.7: Velocity profiles at five position in the dent for the flat plate (A) and a dented plate (B)(depth 0.686mm).

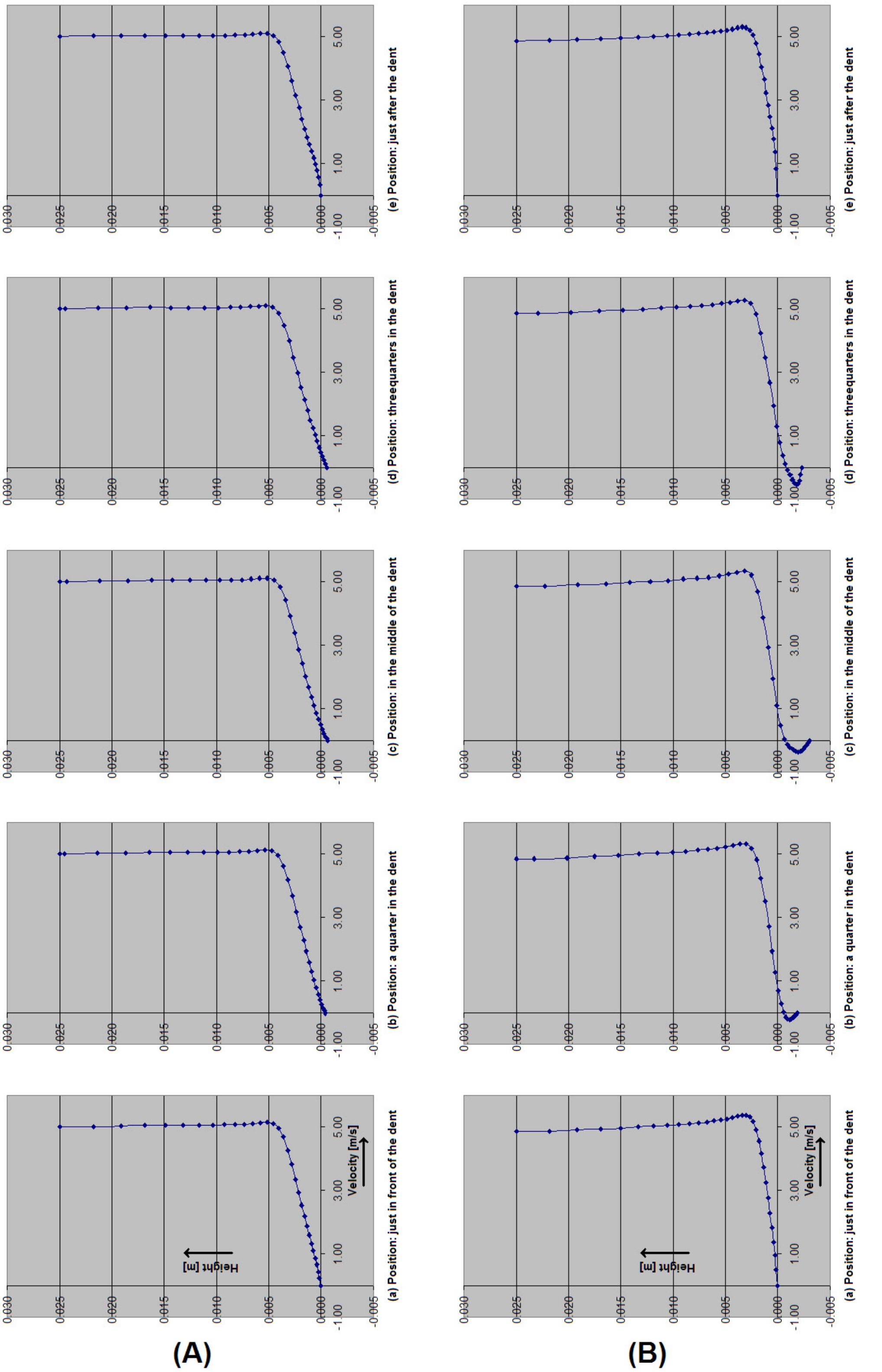

Figure C.8: Velocity profiles at five position in the dent for two dented plates (depth 1.843mm (A) and 3.000mm(B)).

C.4 Simulation - Series 4; Simulations for More Detailed Viscous and Pressure Drag Behaviour.

Title: Simulations for More Detailed Viscous and Pressure Drag Behaviour.	
Numbers of Simulations:	4-01, 4-02 and 4-03
Dents Used: Flat plate (reference value) and two dented plates with depths of 0.343mm and 3.000mm.	
Objective of the series of Simulations: This series of simulations is done to investigate the influence of different parts of the dents on the drag.	
Brief Description: The plates in this simulations are divided into 120 small surfaces, each containing a quarter of a dent. This division is depicted in figure 3.20. Now it is possible to compare the drag characteristics of each quarter of the dents. The simulations are done on the flat plate, as a reference case, and the dents with a depth of 0.343mm and 3.000mm.	
Case Setup	
Geometry: The geometry is exactly equal to the geometry used in simulation series 3. The plates are split, but this does not change the geometry.	
Boundary Conditions: - Plates: These are all non-moving walls. - Left & Right side of the domain: periodic boundary condition. The symmetry boundary conditions used in earlier simulations are not correctly implemented due to the fact that although the geometry is symmetric, the flow is not symmetric. The symmetric boundary conditions blocked the development of the flow, the flow was "reflected" as it neared the sides of the domain. With the periodic boundary condition the flow can "exit" the domain at the sides. When it does exit on one side, it will enter the domain at the same position on the other side, see section 3.5.4. - Inflow: still a velocity inlet is used, but now a variable inflow velocity is used in stead of the constant velocity used in earlier simulations. A velocity profile is modeled, using a User-Defined-Function (UDF) in Fluent, see appendix E. - Outflow: A pressure outlet is used here. - Top of domain: pressure far-field, to insure a zero-pressure gradient.	
Flow Properties: Free-stream flow velocity for all simulations in this series is 5m/s. Reynolds number $Re_L = \frac{\rho U L}{\mu} = \frac{1.225 \cdot 5.0 \cdot 0.5}{1.7894 \cdot 10^{-5}} = 1.71 \cdot 10^5$ It is now, due to the fact that a velocity profile on the inlet is used, more difficult to calculate the theoretical drag coefficient. The velocity profile is the theoretical velocity profile after developing for 0.5m. The total drag of the plate, including an imaginary plate where the flow is developing, is: $D_{total} = \frac{1}{2}\rho U^2 L C_{D_{total}}$, with $C_{D_{total}} = 0.031(Re_{L=1m})^{-1/7}$ and $Re_{L=1m} = \frac{\rho U}{\mu} = 3.42 \cdot 10^5$ $D_{total} = \frac{1}{2} \cdot 0.031 \rho U^2 (\frac{\rho U}{\mu})^{-1/7} = 0.076874N$	

this table continues on the next page

The total drag of the imaginary part of the plate is: $D_{imag.} = \frac{1}{2}\rho U^2 L C_{D_{imag.}}$, with $C_{D_{imag.}} = 0.031 \cdot (Re_{L=\frac{1}{2}m})^{-1/7}$ and $Re_{L=\frac{1}{2}m} = \frac{\rho U L}{\mu} = 1.71 \cdot 10^5$ $D_{imag.} = \frac{1}{2} \cdot \frac{1}{2} \cdot 0.031 \rho U^2 (\frac{\rho \cdot U}{2\mu})^{-1/7} = 0.042438N$ Thus the drag of the real part of the plate is: $\Delta D = D_{total} - D_{imag.} = 0.034436N$ And the drag coefficient of the real part of the plate is: $C_{D_{theory}} = \frac{2\Delta D}{\rho U^2 L} = 0.004450$
Mesh: The meshes in all domains are built using the same method, this method was also used in simulation series 3. The meshes created in this series are not identical to the meshes created in series 3, because of the division of the plates. The nodes are not situated on the exact same positions, but the amount of nodes and cells is equal. Width and length of the cells are 1mm. The height of the cells vary. The first cell should have a height corresponding with an z^+-value of 1. Thus: $h_{first} = 17.21 \cdot z^+ \cdot L \cdot Re^{-\frac{13}{14}} = 0.119$mm. The height of the cells grows linear to a value of 4.68mm, from there the cells have a constant height of 4.92mm. Number of cells: length×width×height $= 501 \times 58 \times 78 = 2,266,524$ cells
Simulation properties: For all simulation in this series holds: - Number of timesteps: 200 - Iterations in one timestep: 200 - Size of a timestep: 0.005s, thus the total simulated time is 1.0s.

Table C.9: Series 4: Setup of the simulations.

The value of $C_{D_{sim.}}$ is determined by the average of the calculated C_D-values of the timesteps 40 to 200, or 0.2s<t<1.0s. This also holds for $C_{L_{sim.}}$ and $C_{M_{sim.}}$.

Results:				
Simulation Number	Depth [mm]	$C_{D_{sim.}}$	ΔC_D w.r.t. $C_{D_{theory}}$	ΔC_D w.r.t. $C_{D_{sim.,flatplate}}$
4-01	0.000	0.00338	-24.0	n.a.
4-02	0.343	0.00353	n.a.	+4.4
4-03	3.000	0.00380	n.a.	+12.4

Table C.10: Series 4: Results.

Simulation number	z^+_{theory} [-]	$z^+_{sim.}$ [-]	Difference [%]
4-01	1.0	2.74	+174
4-02	1.0	2.74	+174
4-03	1.0	2.74	+174

Table C.11: z^+-values for the meshes used in series 4.

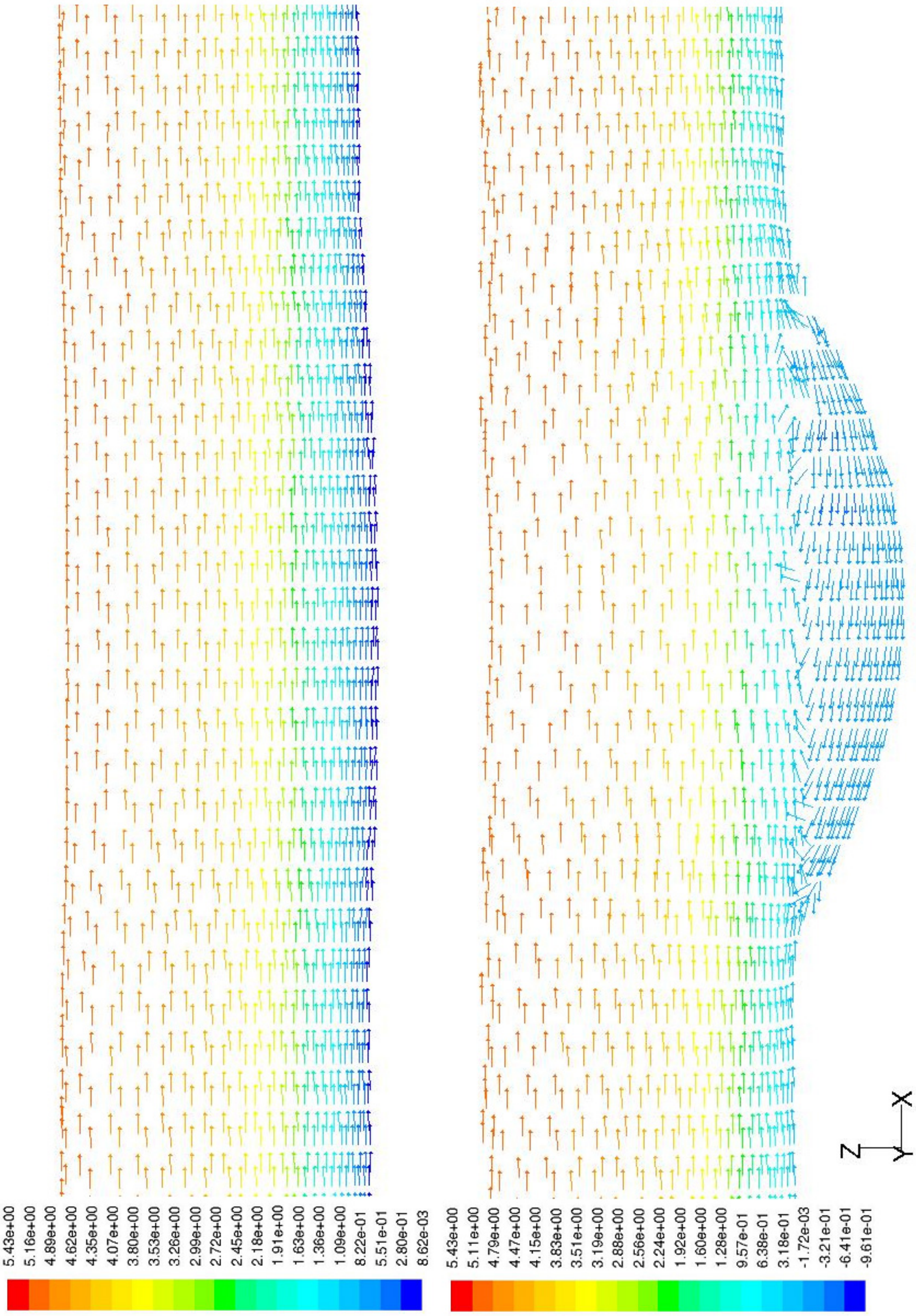

Figure C.9: Velocity vectors in cross-section in the middle of the dent; attached flow for the dent with depth 0.343mm (left) and for the dent with depth 3.000mm (right); U=5m/s.

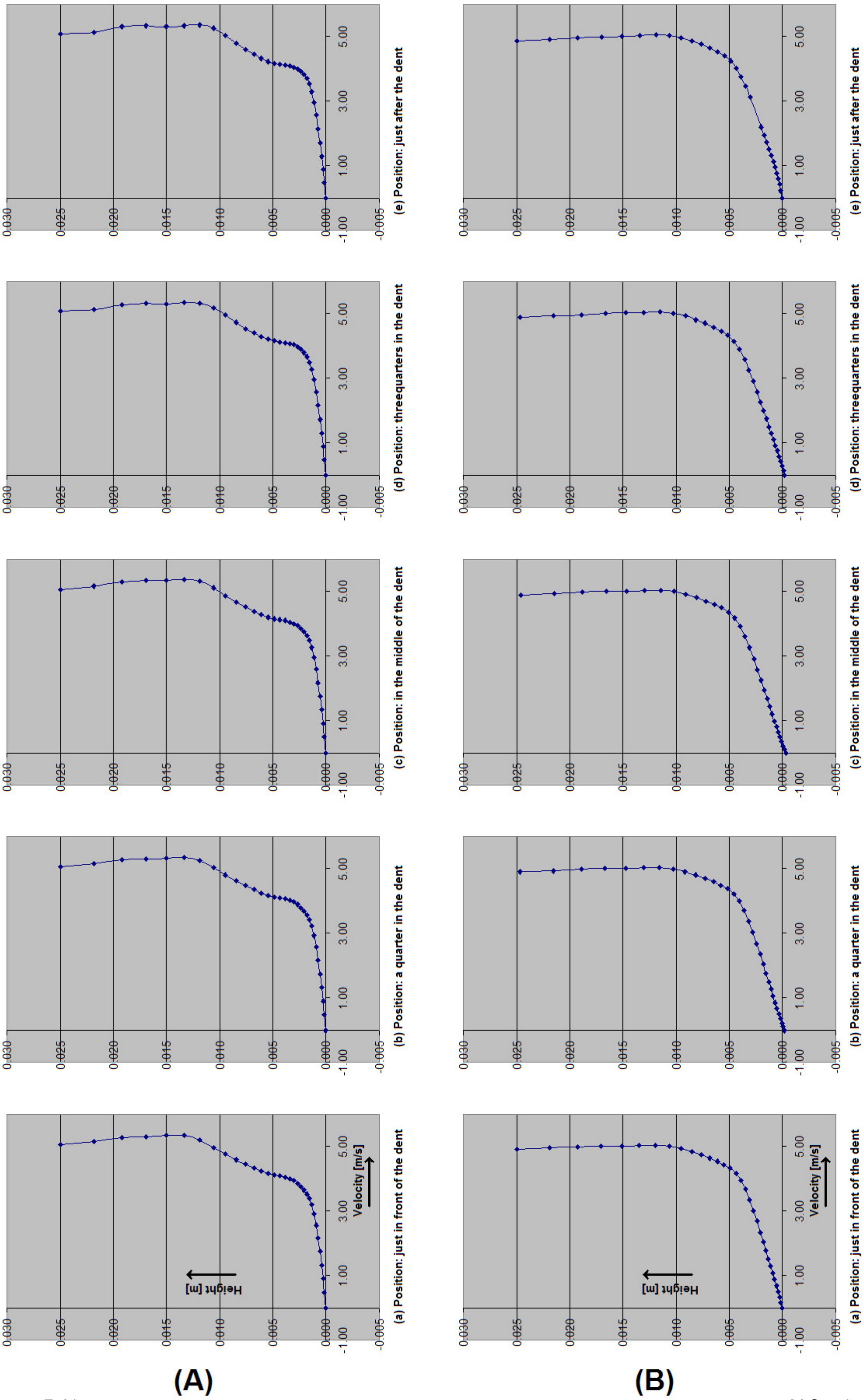

Figure C.10: Velocity profiles at five position in the dent for flat plate (A) and dented plate with attached flow (B) (depth 0.343mm).

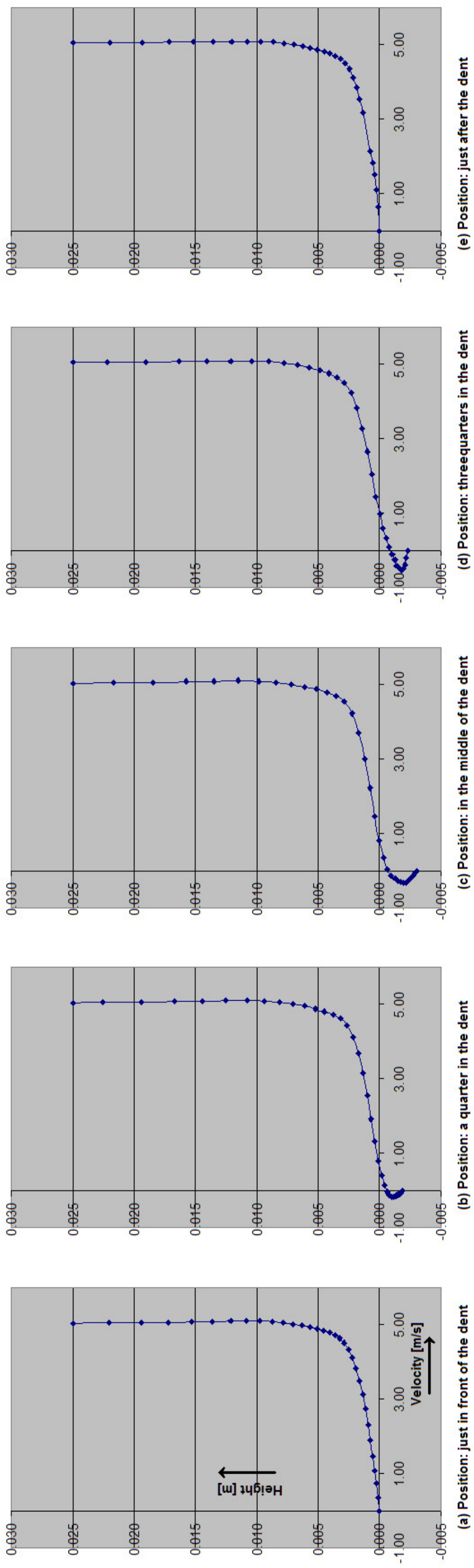

Figure C.11: Velocity profiles at five position in the dent for dented plate with detached flow (depth 3.000mm).

C.5 Simulation - Series 5; Simulations with Free-Stream Velocity of 50m/s.

Title: Simulations with a free-stream velocity of 50m/s.	
Numbers of Simulations:	5-01, 5-02 and 5-03
Dents Used: Flat plate (reference value) and two dented plates, with depths of 0.343mm and 3.000mm.	
Objective of the series of Simulations: This series of simulations is done to investigate the drag(increase) at a velocity which corresponds with the velocity reached in practical applications. Also this series is used to investigate if the characteristic flow patterns found with a free-stream velocity of 5m/s also occur when using higher free-stream velocities.	
Brief Description: Three plates are subjected to a flow with a free-stream velocity of 50m/s. This is a velocity which corresponds to practical application of DSE. The plates tested are the flat plate and the dented plates with depths of 0.343mm and 3.000mm.	
Case Setup	
Geometry: The geometry is exactly equal to the geometry used in simulation series 3.	
Boundary Conditions: - Plates: These are all non-moving walls. - Left & Right side of the domain: periodic boundary condition. - Inflow: Velocity inlet with a modeled velocity profile, using a UDF in Fluent. - Outflow: A pressure outlet is used here. - Top of domain: pressure far-field.	
Flow Properties: Free-stream flow velocity for all simulations in this series is 5m/s. Reynolds number $Re_L = \frac{\rho U L}{\mu} = \frac{1.225 \cdot 50.0 \cdot 0.5}{1.7894 \cdot 10^{-5}} = 1.71 \cdot 10^6$ Due to the application of the velocity profile at the inlet the theoretical drag coefficient is calculated as described in section 3.5.4. The drag coefficient is: $C_{D_{theory}} = \frac{2 \Delta D}{\rho U^2 L} = 0.003237$	
Mesh: The meshes used in this series are built using the same method as used in previous series. Width and length of the cells are 1mm. The height of the cells vary. The first cell should have a height corresponding with an z^+-value of 1. Thus: $h_{first} = 17.21 \cdot z^+ \cdot L \cdot Re^{-\frac{13}{14}} = 0.014$mm. Number of cells: length×width×height $= 501 \times 58 \times 83 = 2,411,814$ cells	
Simulation properties: For all simulation in this series holds: - Number of timesteps: 100 - Iterations in one timestep: 200 - Size of a timestep: 0.002s, thus the total simulated time is 0.2s.	

Table C.12: Series 5: Setup of the simulations.

The value of $C_{D_{sim.}}$ is determined by the average of the calculated C_D-values of the timesteps 40 to 200, or 0.2s<t<1.0s. This also holds for $C_{L_{sim.}}$ and $C_{M_{sim.}}$.

Results:						
Simulation Number	Depth [mm]	$C_{D_{sim.}}$	ΔC_D w.r.t. $C_{D_{theory}}$	ΔC_D w.r.t. $C_{D_{sim.,flatplate}}$	$C_{L_{sim.}}$	$C_{M_{sim.}}$
5-01	Flat	0.00182	-43.8	n.a.	-0.00232	0.00063
5-02	0.343	0.00184	n.a.	+1.1	-0.00261	0.00086
5-03	3.000	0.00409	n.a.	+1247	-0.00432	0.00112

Table C.13: Series 5: Results.

Simulation number	z^+_{theory} [-]	$z^+_{sim.}$ [-]	Difference [%]
5-01	1.0	0.24	-76
5-02	1.0	0.20	-80
5-03	1.0	0.20	-80

Table C.14: z^+-values for the meshes used in series 5.

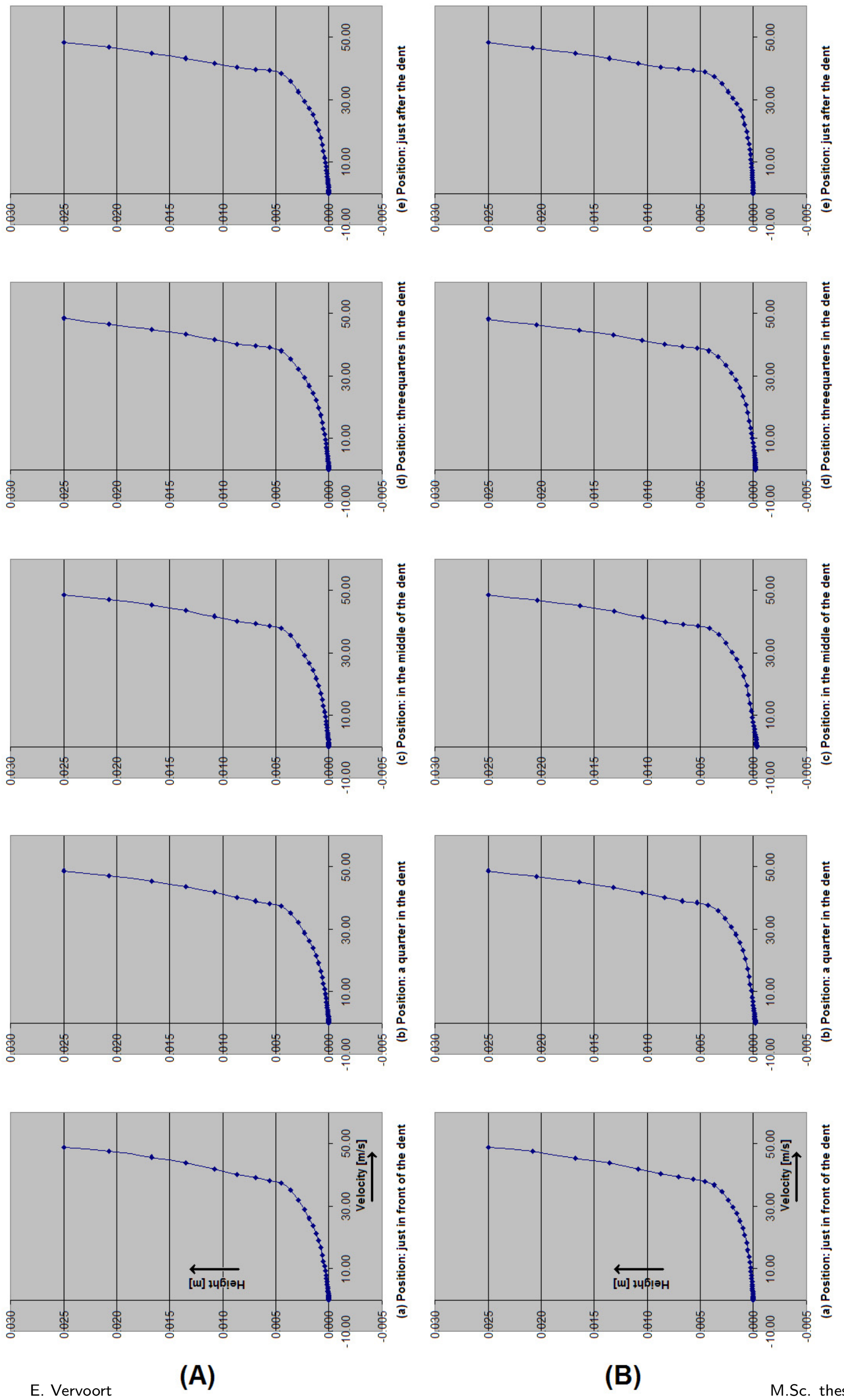

Figure C.12: Velocity profiles at five position in the dent for flat plate (A) and dented plate with attached flow (B) (depth 0.343mm) U=50m/s.

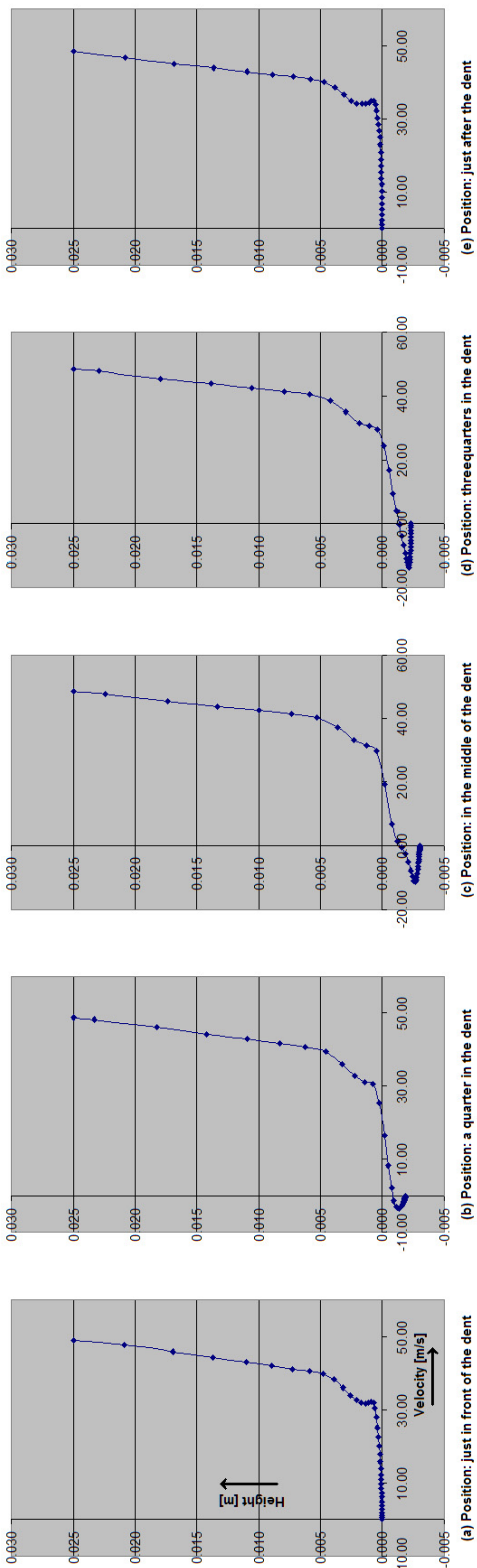

Figure C.13: Velocity profiles at five position in the dent for dented plate with detached flow (depth 3.000mm); U=50m/s.

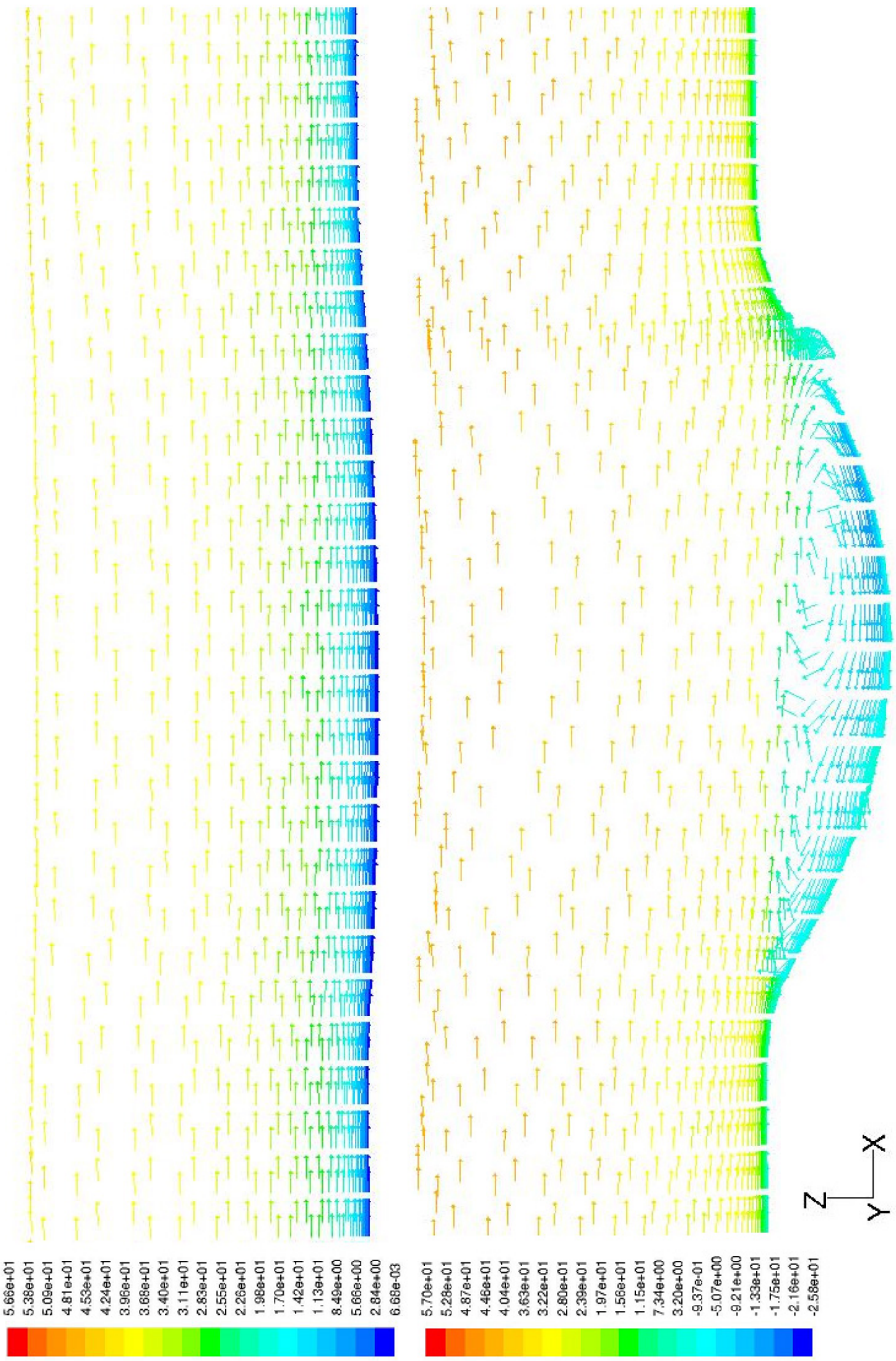

Figure C.14: Velocity vectors in cross-section in the middle of the dent; attached flow for the dent with depth 0.343mm (left) and for the dent with depth 3.000mm (right); U=50m/s.

C.6 Simulation - Series 6; Simulation with a Dent with Non-Rotational Symmetric Cross-Section.

Title: Simulations with a non-rotational symmetric dent geometry.	
Numbers of Simulations:	6-01
Dents Used: Here a non-rotational symmetric dent is used. The geometry is explained in Section 3.5.6. The forward part is compressed by a factor F_1=0.5, creating a steep entrance of the dent. The backward part of the dent is stretched by a factor of F_2=2. (see figure 3.35)	
Objective of the series of Simulations: The goal of this simulation is to optimize drag reduction by maximizing the negative skinfriction area and by minimizing the pressure drag.	
Brief Description: From previous series it is known that deep dents will cause the flow to separate. Here an area with negative skinfriction is created. This area should be maximized triggering the separation early on in the dent which is likely to happen if the forward part of the dent is steep. The high skinfriction and pressure drag just after the dent should be kept as small as possible, by reducing the slope of the backpart of the dent. This simulation confirms if this geometry indeed will result in a reduction of drag.	
Case Setup	
Geometry: The dented plate uses dent with a non-rotational symmetric cross-section, described in section 3.5.6 and appendix F. The dimensions of the plate are the same as for previous dented plates (57.2mm×500mm). The dents are split into quadrants like is done in simulation series 4, section 3.5.4.	
Boundary Conditions: - Plates: These are all non-moving walls. - Left & Right side of the domain: periodic boundary condition. - Inflow: Velocity inlet with a modeled velocity profile, using a UDF in Fluent. - Outflow: A pressure outlet is used here. - Top of domain: pressure far-field.	
Flow Properties: Free-stream flow velocity for all simulations in this series is 5m/s. Reynolds number $Re_L = \frac{\rho U L}{\mu} = \frac{1.225 \cdot 50.0 \cdot 0.5}{1.7894 \cdot 10^{-5}} = 1.71 \cdot 10^5$ Due to the application of the velocity profile at the inlet the theoretical drag coefficient is calculated as described in section 3.5.4. The drag coefficient is: $C_{D_{theory}} = \frac{2\Delta D}{\rho U^2 L} = 0.003237$	
Mesh: The meshes in all domains are built using the same method, this method was also used in simulation series 3 and series 4. Width and length of the cells are 1mm. The height of the cells vary. The first cell should have a height corresponding with an z^+-value of 1, corresponding to a height of 0.119mm. The height of the cells grows linear to a value of 4.68mm, from there the cells have a constant height of 4.92mm. Number of cells: length×width×height $= 501 \times 58 \times 78 = 2,266,524$ cells	

this table continues on the next page

Simulation properties:
For all simulation in this series holds:
- Number of timesteps: 200
- Iterations in one timestep: 200
- Size of a timestep: 0.005s, thus the total simulated time is 1.0s.

Table C.15: Series 6: Setup of the simulations.

Results:				
Simulation Number	Depth [mm]	$C_{D_{sim.}}$	$C_{L_{sim.}}$	$C_{M_{sim.}}$
6-01	3.000	0.00585	-0.00635	0.00188

Table C.16: Series 6: Results.

Simulation number	z^+_{theory} [-]	$z^+_{sim.}$ [-]	Difference [%]
6-01	1.0	4.4	+340

Table C.17: z^+-values for the meshes used in series 6.

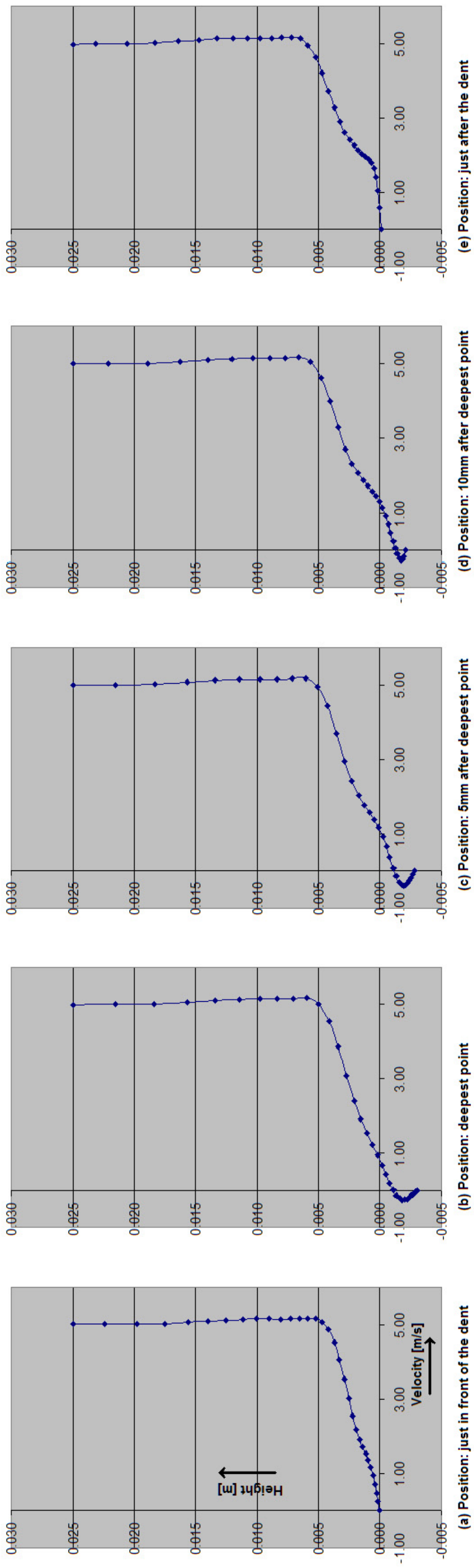

Figure C.15: Velocity profiles at five position in the dent for plate with detached flow through non-rotational symmetric cross-section (depth 3.000mm).

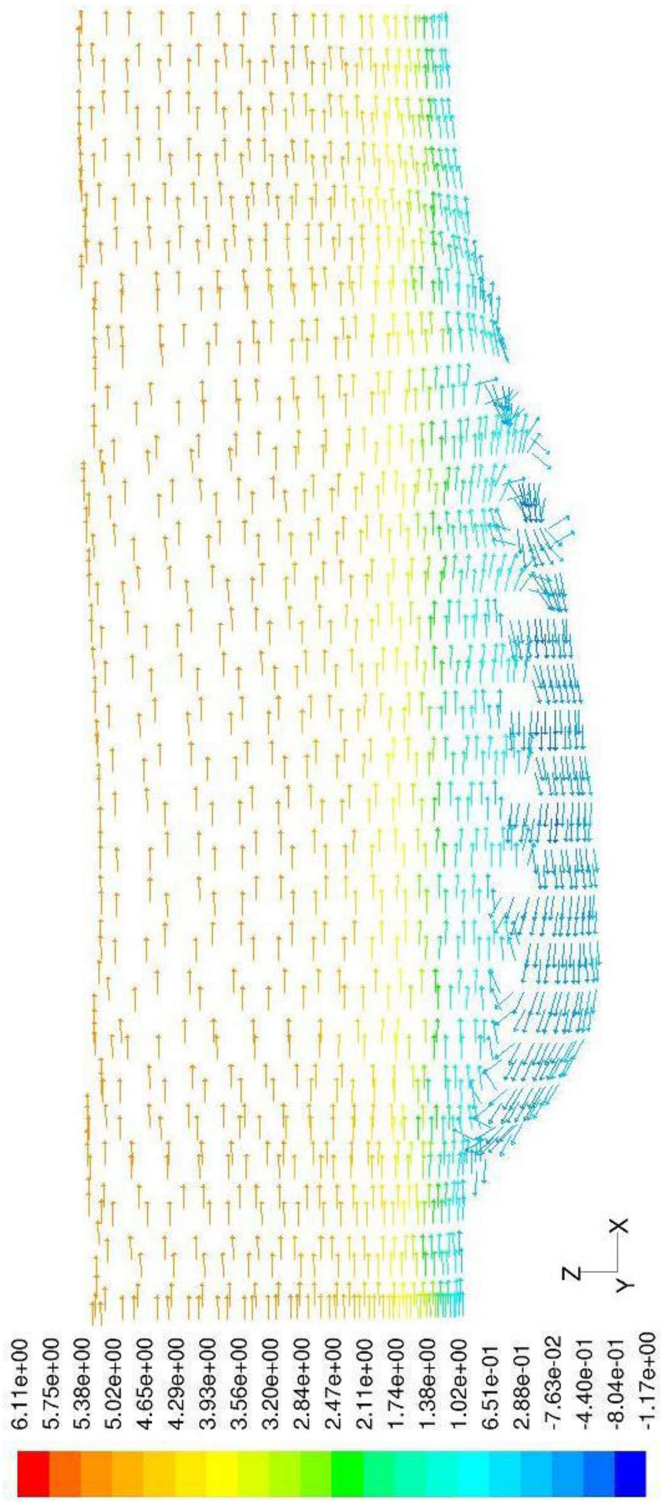

Figure C.16: Velocity vectors in cross-section in the middle of the dent; non-rotational symmetric dent (depth 3.000mm).

Appendix D

Large Eddy Simulation (LES) Model and Simulation Setup.

The Large-Eddy Simulation model is one of the turbulence models that can be applied in Fluent to simulate fluid flows around objects. Here the LES method will be explained. Information in this section about LES is obtained from the Fluent manual [Fluent Inc., 2005b], out of introductory Fluent nodes about the modeling of turbulent flows [Fluent Inc., 2005c] and out of an overview of LES in Fluent [Scheidegger, 2005].

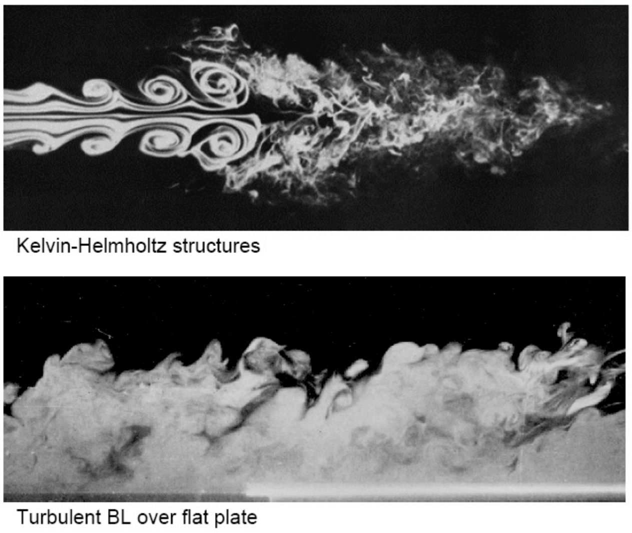

Figure D.1: Two examples of turbulent flow structures.

Turbulent flows consist of eddies (structures) with wide range of length and time scales. The largest eddies are typically comparable in size to the characteristic length of the mean flow. The smallest scales are responsible for the dissipation of turbulence kinetic energy. Figure D.1 feature two examples of turbulent flows. Here the top picture is showing a jet flowing into a stationary fluid. The jet creates vortices, these vortices gradually fall apart into smaller vortices, which will decay into a very chaotic structure. The lower picture shows a turbulent boundary layer over a flat plate.
A number of different methods are available when performing the simulations, these

are shown in figure D.2. It is possible to directly resolve the whole spectrum of turbulent scales using an approach known as direct numerical simulation (DNS). No modeling is required in DNS. However, DNS is not feasible for practical engineering problems involving high Reynolds number flows. The cost required for DNS to resolve the entire range of scales is proportional to Re_t^3, where Re_t is the turbulent Reynolds number. Clearly, for high Reynolds numbers, the cost becomes prohibitive. The Reynolds-Averaged Navier-Stokes (RANS) Equations Models solve ensemble-averaged Navier-Stokes equations, which involves the modeling of all turbulence scales. This is the most widely used approach for calculating industrial flows. The LES model will solve the spatially averaged Navier-Stokes equations. Large eddies are directly resolved, but eddies smaller than the mesh sizes are modeled. In general the more turbulent scales are resolved, the longer it takes to perform the simulations. Large eddy simulation (LES) thus falls between DNS and RANS in terms of the fraction of the resolved scales, see figure D.2.

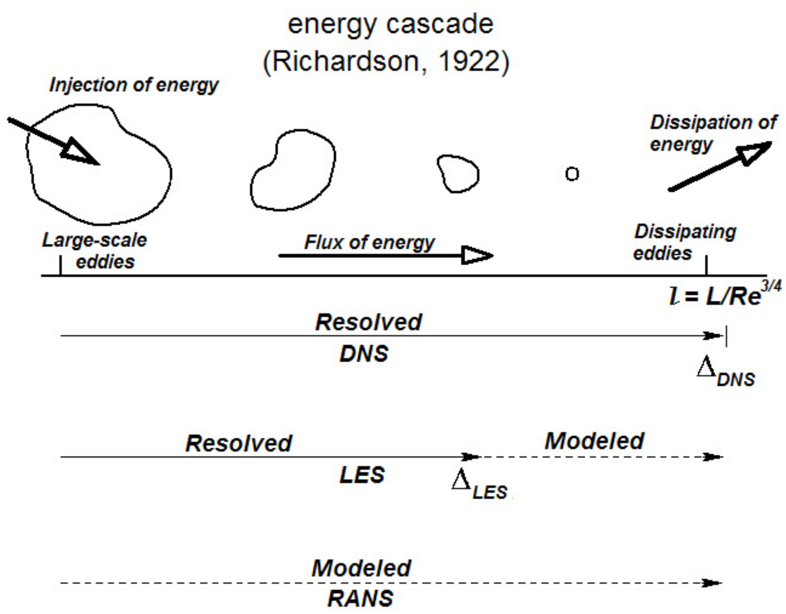

Figure D.2: Turbulent scales and prediction methods.

The rationale behind LES can be summarized as follows. Momentum, mass, energy, and other passive scalars are transported mostly by large eddies. Large eddies are more problem-dependent. They are dictated by the geometries and boundary conditions of the flow involved. Small eddies, on the other hand, are less dependent on the geometry. They tend to be more isotropic and are consequently more universal. The chance of finding a universal turbulence model is much higher for small eddies.
Resolving only the large eddies allows one to use much coarser mesh and larger timestep sizes in LES than in DNS. However, LES still requires substantially finer meshes than those typically used for RANS calculations. In addition, LES has to be run for a sufficiently long flow-time to obtain stable statistics of the flow being modeled. As a result, the computational cost involved with LES is normally orders of magnitudes

higher than that for steady RANS calculations in terms of memory and CPU time. Therefore, high-performance computing (e.g., parallel computing) is a necessity for LES, especially for industrial applications.

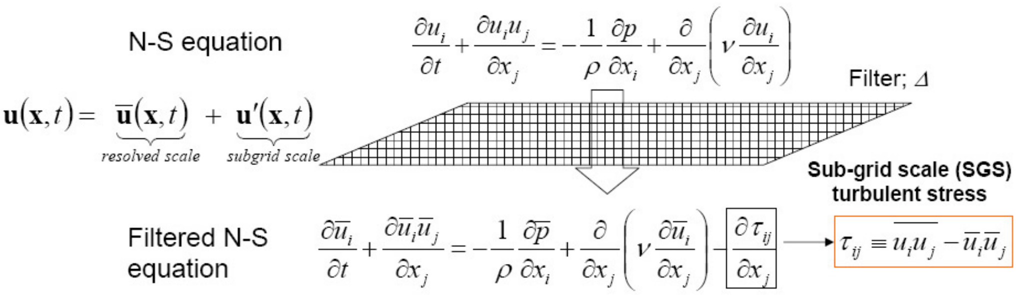

Figure D.3: Filtering of the eddies by gridsize for the LES turbulence model.

The spectrum of turbulent eddies in the Navier-Stokes equations is filtered. The filter is a function of grid size. Eddies smaller than the grid size are removed and modeled by a sub-grid scale (SGS) model. Here the Smagorinsky-Lilly model is used. The Smagorinsky-Lilly model is an algebraic model in which subgrid-scale stresses are parameterized using the resolved velocity scales. The underlying assumption is the local equilibrium between the transferred energy through the grid-filter scale and the dissipation of kinetic energy at small subgrid scales. Eddies larger than the grid size are directly solved numerically by the filtered transient Navier-Stokes equations.

Table D.1 can be used as a step-by-step manual to setup the model for performing the simulations. This setup manual does not deal with the creation of the geometry and the production of the grid. It is assumed that for the geometry already a mesh-file (*.MSH) or a CAS-file (*.CAS) is created.

Fluent Version:	*3d* (for single node mode)	
Define → User-Defined → Functions → Interpreted	First: Browse to the file Then: Interpret	
File → read → case	Reading the *.MSH-file or *.CAS-file.	
Grid → Check	Checking the volume mesh for errors	
Grid → Reorder → Domain	Reorder domain to reduce bandwidth and thus computational time	
Grid → Scale	Grid was created in *mm* → Scale	
Define → Models → Viscous → Large Eddy Simulation	Subgrid Scale Model: User/Defined Functions - Subgrid-Scale Turbulent Viscosity	Smagorinsky/Lilly *None*
Define → Materials	Change Density from *constant* to *ideal-gas* (needed for Pressure Far Field B.C.) press: *Change/Create*, energy equation is enabled.	

this table continues on the next page

Define → Operating Conditions	Operating Pressure ≈ Mean flow pressure Operating Pressure = *101340 Pa* (5m/s) Reference point: point in the undisturbed flow: *x=0.01m, y=0.0286m, z=0.24m*	
Define → Boundary Conditions	BOUNDARY	SETTINGS
	interior-domain	interior
	fluid	fluid
	inlet	*Velocity Inlet* Magnitude: *Velocity Profile (UDF)* Total Temperature: *288.15K* Fluc. Vel. Algorithm: *Vortex Method* Turbulence Intensity: *7.5%* Turbulence Length Scale: *0.035m*
	outlet	*Pressure Outlet* Gauge Pressure *0* Total Temperature: *288.15K*
	plate left/right sides top of domain	*Wall* *Periodic B.C.* *Pressure Far Field* Gauge Pressure *0* Mach number *0.014693* for 5m/s Total Temperature: *288.15K*
Define → Periodic Conditions	Upstream Bulk Temperature: *288.15K*	
Solve → Monitors → Residuals	*Uncheck* Convergence Criterion of all parameters	
Solve → Monitors → Force	Force Vector C_D: (1,0,0) (Default) Force Vector C_L: *(0,0,1)* Momentum Centre C_M: (0,0,0) about *Y-axis* Options: Check *Print* & *Write* Wall Zones: *Plate* File Name: *Define unique name*	
Report → Projected Areas	Projection Direction: *Z* Surfaces: *Plate* Min. Feature Size (m): *0.005m* *Compute*	
Report → Reference Values	Compute From: *Velocity Inlet* Check/Set: Area *Reference Area* Check/Set: Length *0.5m* Pressure is gauge pressure so: 101325Pa	

this table continues on the next page

Solve → Controls → Solution	Equations: Select ALL Pressure: *0.2* Density: *0.8* Body Forces: *0.8* Momentum: 0.7 Energy: *0.8*
	Discretization: Pressure: Standard Density: *Central Differencing* Momentum: *Central Differencing* Energy: *Central Differencing*
	Pressure Velocity Coupling: SIMPLE
Solve → Initialise	Compute from: *Inlet* *Absolute* *Initialise*
Solve → Monitors → Force	Time step size: 0.005s (for 5m/s) Number of time steps: *100 or 200* Max. Iterations per time step: *200* Reporting interval: *25* *Enable*: Data Sampling for Time Statistics
Optional: Parallel → Partition	Method: *Cartesian X-Coordinate* Number: *4* *Partition*
File → write → CAS and DAT	Saving the created *.CAS-file and *.DAT-file Or: Save as *.CAS.gz (zipped files will save diskspace)

Table D.1: Setup procedure for a LES-simulation in Fluent.

Appendix E

Velocity Profile and the User-Defined Function.

During some of the simulations (section 3.5.3, 3.5.4 and 3.5.5) velocity profiles are used at the velocity inlet of the domain to speed up the development of the flow and to get rid of the extreme high skinfriction areas near the beginning of the plate.
According to White [White, 1991] a turbulent velocity profile which approximately applies to the flow over turbulent flat plates is that of a simple one-seventh power-law profile, taken from pipe flow data. This profile looks like:

$$\overline{u} = U_e \left(\frac{z}{\delta}\right)^{1/7}$$

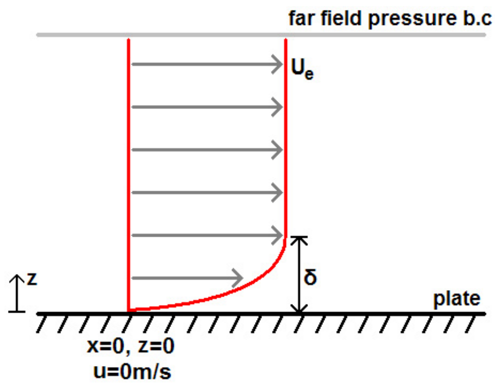

Figure E.1: Velocity profile defined at the inlet.

Figure E.1 represents a schematic drawing of the velocity profile a cross-section of the domain used in this thesis. The no-slip condition at the plate defines the velocity to be zero at the wall. The velocity will increase as the height from the wall is increased according to the power-wall to the free-stream velocity (U_e), until the free-stream velocity (U_e) is reached at z=δ. For $z > \delta$ the velocity is equal to the free-stream velocity. At the top of the domain the no-slip condition is not applied, because of the far field condition defined here.

Since the shape of the boundary layer is defined by the power-law, only two parameters determine the velocity profile. These are the free-stream velocity (U_e) and the thickness of the boundary layer (δ) which is defined as:

$$\delta = 0.16 x Re_x^{-1/7} = 0.16 x \Big(\frac{\rho x U_e}{\mu}\Big)^{-1/7}$$

Here x is the characteristic length, which is chosen to be the length of the plate, x=0.5m. Now the boundary layer implemented at the inlet of the domain represents the boundary layer developed after a distance of 0.5m.
For U_e=5m/s the boundary layer thickness is: δ=0.0143m.
Now the boundary layer profile has to be implemented into Fluent. This is done by using a User-Defined Function.

A User-Defined Function (UDF) is a function that can be dynamically loaded into the Fluent solver to enhance the standard features of the Fluent code. UDF's are written in the C programming language. They are defined using DEFINE macros that are supplied by Fluent. They access data from the Fluent solver using predefined macros and functions also supplied by Fluent Inc. Every UDF contains the udf.h file inclusion directive (#include "udf.h") at the beginning of the source code file, which allows definitions for DEFINE macros and other Fluent-provided macros and functions to be included during the compilation process. UDFs are either interpreted or compiled and are hooked to the Fluent solver using a graphical user interface panel. This is a disadvantage, because the computer cluster available does not allow the use of a graphical interface panel. Therefore the simulations can not be performed with the fast computer cluster, but a slower workstation has to be used.
UDFs allow Fluent to be customized to fit your particular modeling needs. UDF's can be used for a variety of applications, of which some are: customization of boundary conditions, material property definitions, surface and volume reaction rates, adjustment of computed values on a once-per-iteration basis, initialization of a solution, post-processing enhancement, and many more. Here a UDF is used to implement a velocity profile at the inlet to improve the convergence and to get rid of the development of the boundary layer at the beginning of the plate.

A short explanation of this UDF will now be given here, for more elaborate information about UDF, see the Fluent manual [Fluent Inc., 2005b] or the Fluent UDF-manual [Fluent Inc., 2005a]. Values that are passed to a solver by a UDF or returned by the solver to a UDF are specified in SI units.
In the first part of the UDF the parameters are defined. The UDF is suited for all free-stream velocities, by changing the value for the free-stream velocity (called Ufree) in the value of the desired free flow velocity and changing boundary layer thickness (called d) into the value corresponding to the velocity.
After the definition of the parameters a loop is defined which calculates the velocity profile. In Fluent this velocity profile, when assigned to the inlet of the domain, will be applied to the whole plane of the inlet (complete y-range).
The UDF used for simulations with a velocity of 5m/s is shown here:

UDF source file

```
#include <udf.h>

#define B 1./7.
#define Ufree 5.0
#define d 0.0143
DEFINE_PROFILE(inlet_velocity,t,i)
{
    real x[ND_ND];
    real z;
    face_t f;

    begin_f_loop(f,t)
    {
      F_CENTROID(x,f,t);
      z = x[2];
      if (z <= d)
        {
          F_PROFILE(f,t,i) = Ufree * pow(z/d, B);
        }
      else
        {
          F_PROFILE(f,t,i) = Ufree;
        }
    }
    end_f_loop(f,t)
}
```

Appendix F

Building the Geometry of an Non-Rotational Symmetric Dent.

Here the method of designing the non-rotational symmetric dent will be explained. The basis for the dent is half a cross-section of a rotational symmetric dent with a depth of 1mm. The shape of this cross-section will be stretched and rotated at the same time, creating a non-rotational symmetric dent. Two stretch-factors (F_1 and F_2) are defined as respectively the factor stretching the dent in forward (Θ=0) and rearward direction with respect to the lowest point of the dent. This is also explained in section 3.5.6. These factors can chosen to be identical, then a rotational symmetric dent will be formed. When these factors are not identical a smooth function should be made which relates both factors to each other. This is required to connect to front part of the dent to the rearward part in a proper manner.

For example: If the stretch-factors are prescribed, then it is possible to develop the stretch factor linear and with a cosine, according to the formulas:

$$F_{linear}(\Theta) = \begin{cases} F_1 + \frac{F_2 - F_1}{\pi}\Theta & 0 \leq \Theta \leq \pi \\ F_2 - \frac{F_2 - F_1}{\pi}(\Theta - \pi) & \pi \leq \Theta \leq 2\pi \end{cases}$$

$$F_{cosine}(\Theta) = \frac{F_1 + F_2}{2} - \frac{F_2 - F_1}{2}\cos\Theta \qquad 0 \leq \Theta \leq 2\pi$$

Figure F.1 features both the linear and the cosine stretch-factors for $0 \leq \Theta \leq 2\pi$, for F_1=0.5 and F_2=2. The linear function shows non-smooth behaviour at 0° and 180°, while the cosine function is smooth everywhere on the domain. If the top view of the dents are considered, see figure F.2 , then it is clear that the linear development results in a irregular dent geometry. Especially at locations where the stretch-factor is not smooth, the dent geometry is distorted (points [-5,0] and [20,0]). The geometry developed with the cosine shows a much better behaviour, which results in a geometry suited for use in simulations.

Now for all the angles (Θ) the stretch-factors are determined. These factors have to be multiplied with the original shape of the dent. This original shape is not represented by a mathematical formula yet, the shape is composed out of two separate arc-shaped lines. With CurveExpert, a curve fitting program, it is possible to fit a mathematical curve onto the original dent shape. CurveExpert can fit all kinds of formula through an array of points. Here it is found that an 18^{th}-degree polynomial represents the original shape almost perfectly. Thus this polynomial will be used to create the three dimensional

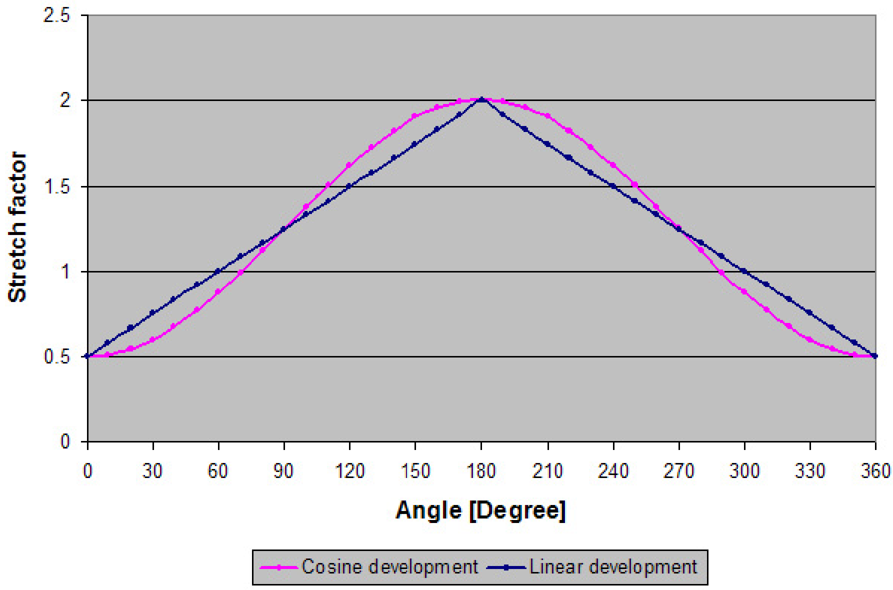

Figure F.1: Development of the stretch-factor around the dent.

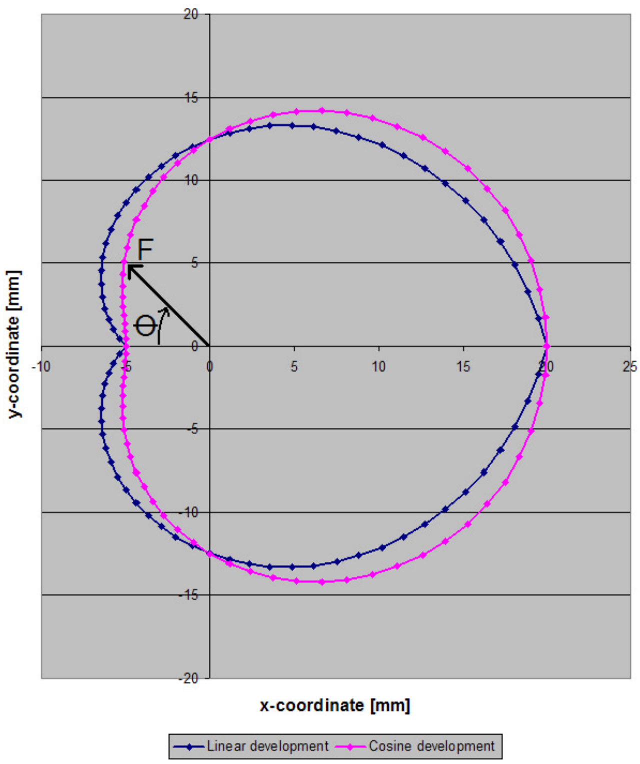

Figure F.2: Top view of the dent for a linear and a cosine development.

shape of the non-rotational symmetric dent.
The m-file used for making the dent is shown below. The m-file is depicted below. In this file only three parameters determine the shape of the dent. The stretch-factors F_1 and F_2 (F1 and F2 in the m-file) and the depth have to be adjusted to create different shapes. Four other parameters (R_j, R_N, T_J and T_N) determine the number of points calculated to represent the dent. The points created are shown in a figure, like figure F.3, where the dent corresponding to the m-file below is presented. The points are also exported to a output-file (here called: *dent.out*), which can be imported into the CAD-program to create the geometry for the simulation.

m-file for producing the non-rotational symmetric dent geometry

```
clc; clear; close all;

% Model for visualising the dent-shape making use of a polynomial

% Constants
F1 = 0.5;      % Stretch-factor for the front half of the dent.
F2 = 2;        % Stretch-factor for the back half of the dent.
R_j = 45;      % number of steps on R.
R_N = 20;      % size of R: R should be at least 10 times F1 or F2 (largest of both values).
T_j = 30;      % number of steps of Theta.
T_N = 12;      % size of step of Theta.
               % T_j * T_N = 360, for making a complete dent-geometry.
Depth = 3;     % Dent Depth [mm].

% Polynomial Constants
P00 = 0.0010666195;
P01 = 0.0059783229;
P02 = -0.044143825;
P03 = -0.044146725;
P04 = 0.10477612;
P05 = -0.088511638;
P06 = 0.037583879;
P07 = -0.008730778;
P08 = 0.0010693816;
P09 = -0.000053318527;
P10 = 0.0000011340285;
P11 = -0.00000071969012;
P12 = 0.00000011194426;
P13 = -0.0000000022830268;
P14 = -0.0000000002576733;
P15 = -0.000000000068373455;
P16 = 0.000000000013137372;
P17 = -0.00000000000078036706;
P18 = 0.00000000000001627368;
```

m-file continues on next page

```
% Calculated parameters
A = (F1+F2)/2;
B = (F2-F1)/2;

for i= [1:T_j]
    for j=[1:R_j]
        R(i,j) = j * R_N / R_j;
        Th(i,j) = i;
        F = 10-j*R_N/R_j/(A-B*cos(i*T_N*pi/180));
        H(i,j) = Depth*(P00 + P01*F + P02*F∧2 + P03*F∧3 + P04*F∧4 + ...
            ... + P05*F∧5 + P06*F∧6 + P07*F∧7 + P08*F∧8 + ...
            ... + P09*F∧9 + P10*F∧10 +P11*F∧11 + P12*F∧12 + ...
            ... + P13*F∧13 + P14*F∧14 + P15*F∧15 +P16*F∧16 + ...
            ... + P17*F∧17 + P18*F∧18);
        Vec((i-1)*R_j+j,1) = -R(i,j)*cos(T_N*Th(i,j)*pi/180);
        Vec((i-1)*R_j+j,2) = R(i,j)*sin(T_N*Th(i,j)*pi/180);
        Vec((i-1)*R_j+j,3) = H(i,j);
            if Vec((i-1)*R_j+j,3) ¿= 0;
                Vec((i-1)*R_j+j,3) = 0;
            end
    end
end

figure(1)
plot3(Vec(:,1),Vec(:,2),Vec(:,3),'.')
axis([-25 25 -25 25 -10 1]);
xlabel('x-coordinate');
ylabel('y-coordinate');
zlabel('z-coordinate');

save dent.out Vec -ASCII
```

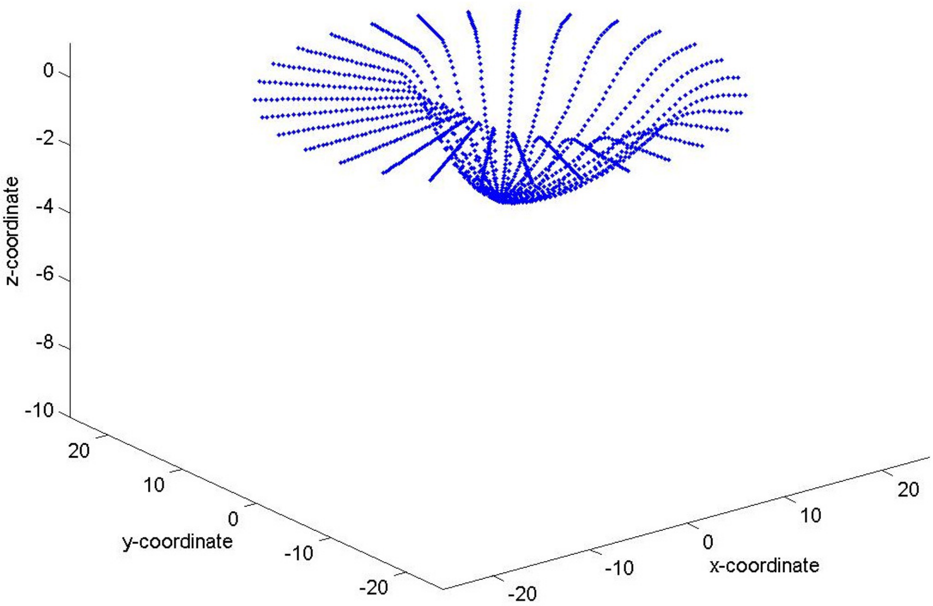

Figure F.3: Example of non-rotational symmetric dent; F_1=0.5, F_2=2 and depth=3mm.

Appendix G

Windtunnel Tests.

In this appendix all data and figures obtained from the tests in the windtunnel are presented.

G.1 Drag Force Figures for all six dents tested; Pattern 1.

Here the drag forces are presented for all six plates measured for pattern 1.

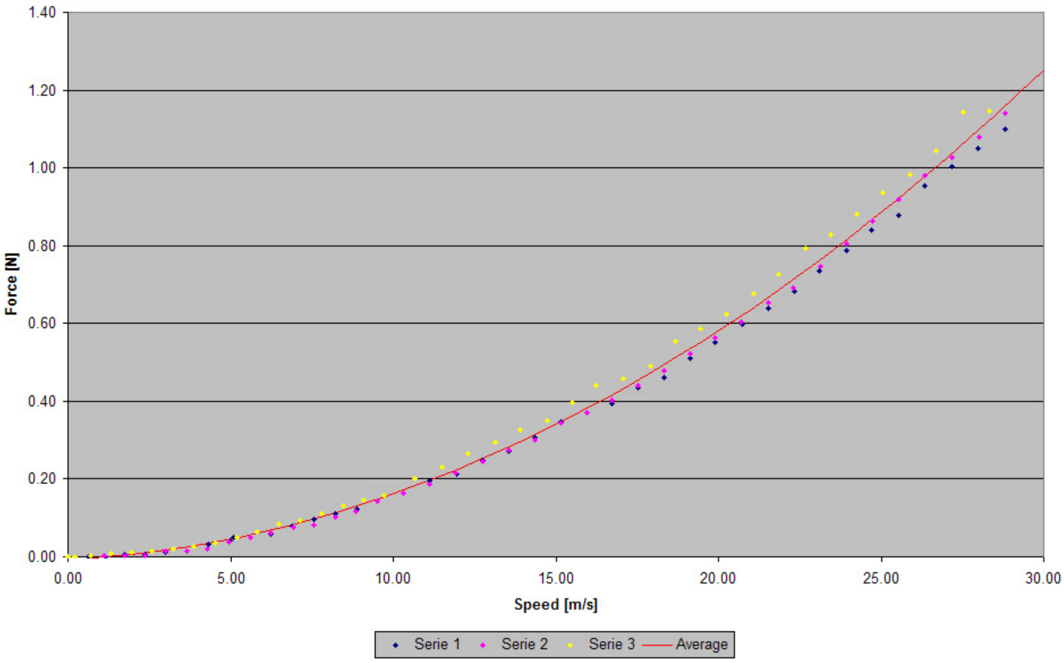

Figure G.1: Drag force, data for test 1: Flat plate.

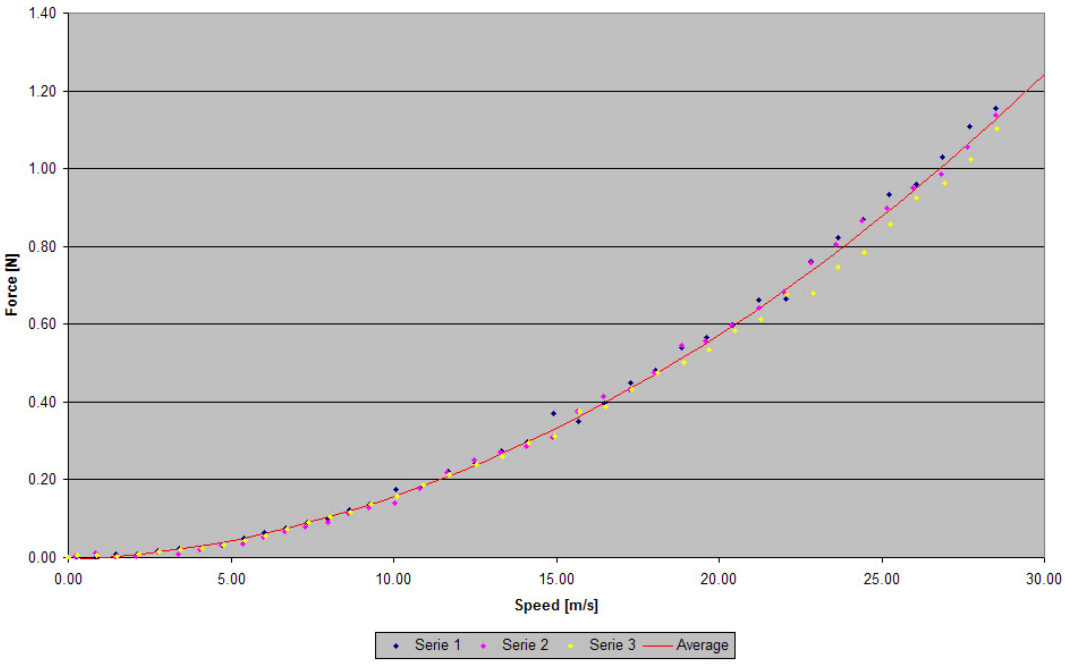

Figure G.2: Drag force, data for test 2: Dent 0.343mm.

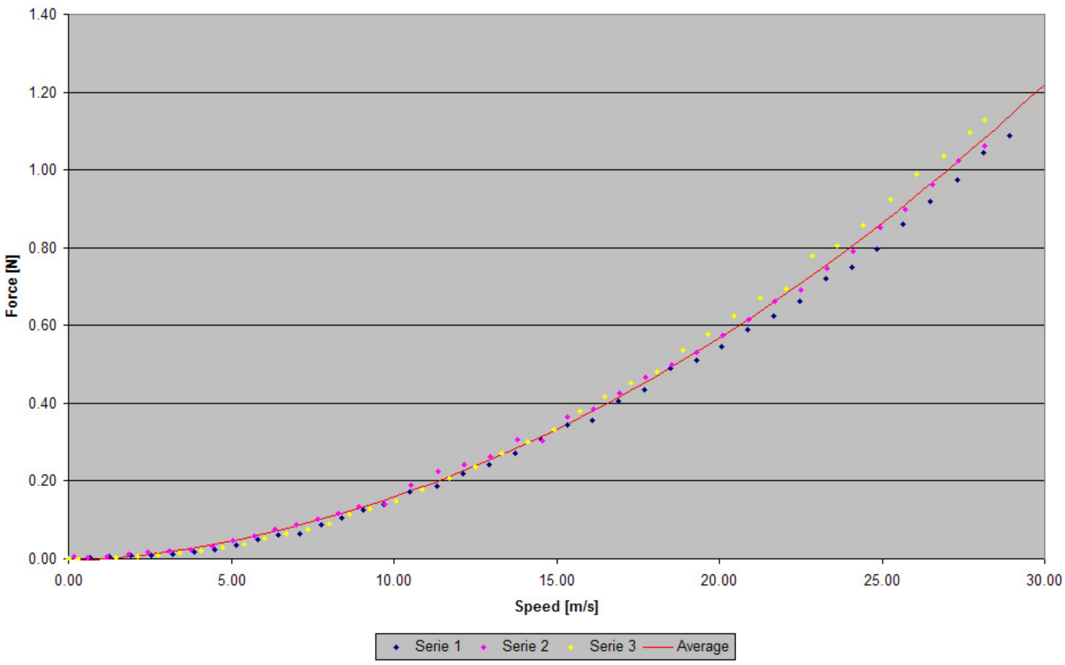

Figure G.3: Drag force, data for test 3: Dent 0.5mm.

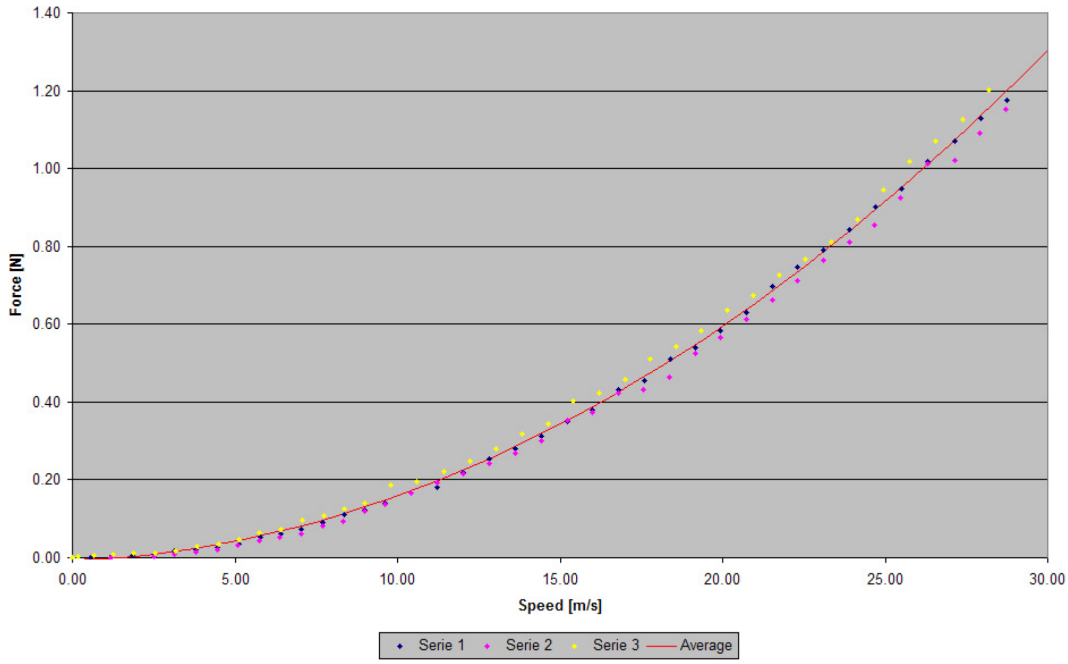

Figure G.4: Drag force, data for test 4: Dent 1.5mm.

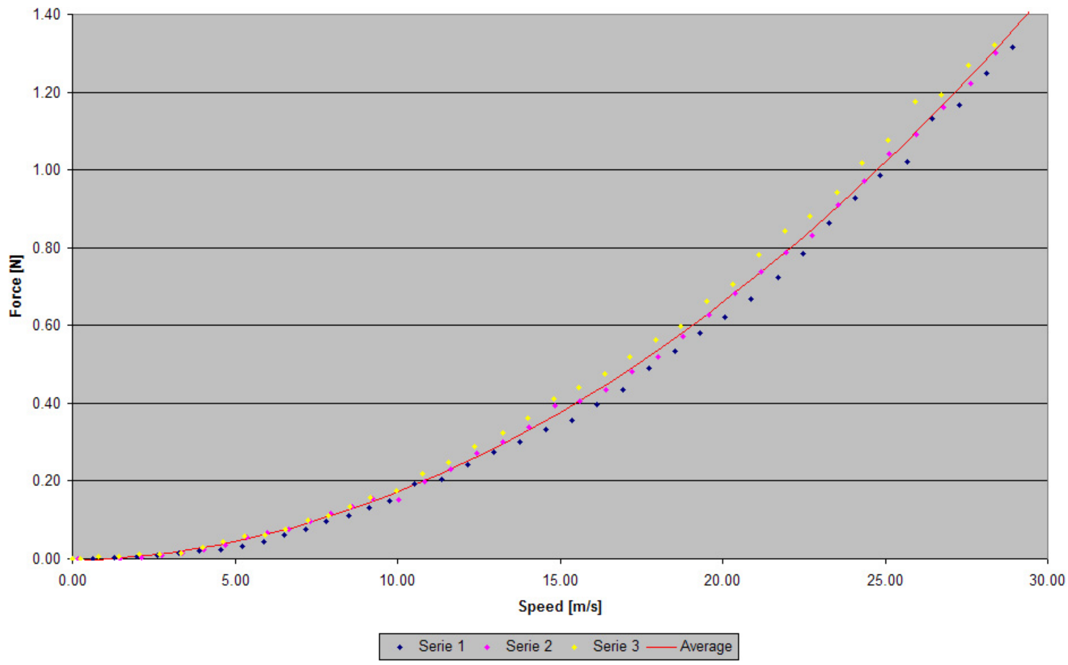

Figure G.5: Drag force, data for test 5: Dent 2.5mm.

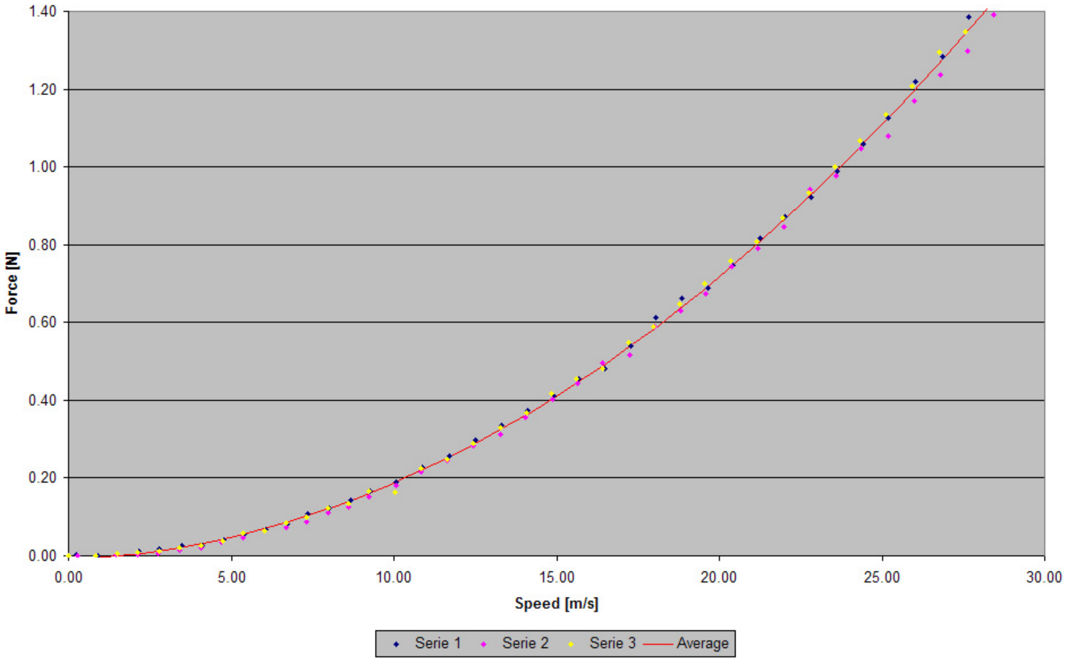

Figure G.6: Drag force, data for test 6: Dent 3.5mm.

G.2 Velocity Profiles for Pattern 1.

Here the velocity profiles are presented for all five velocities measured: 3.0m/s, 5.0m/s, 7.5m/s, 10.0m/s and 15m/s.

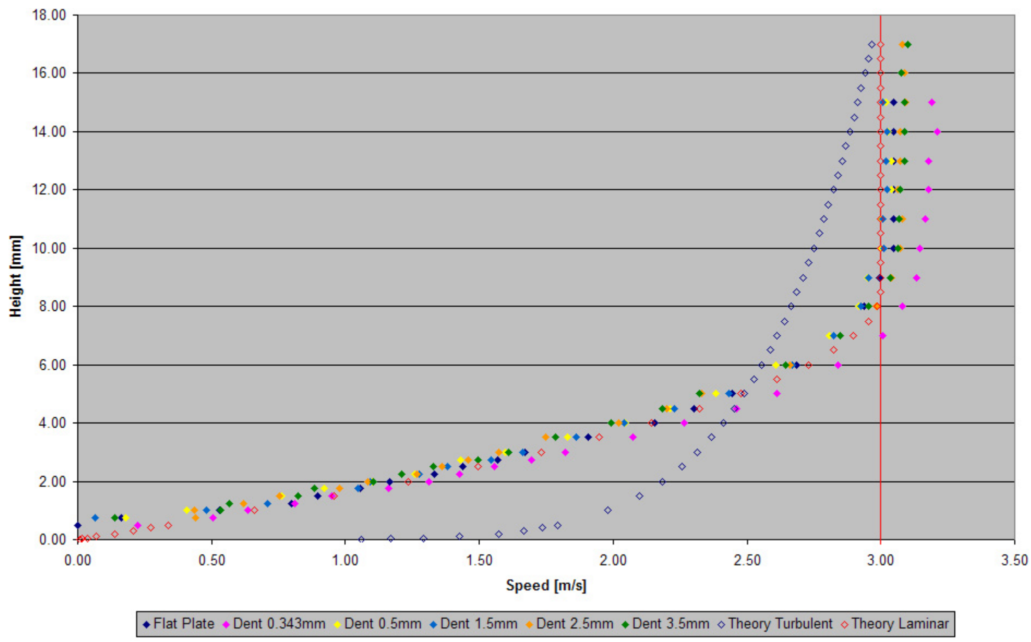

Figure G.7: Velocity profiles of the flow in between the dents; pattern 1, free-stream velocity is 3m/s.

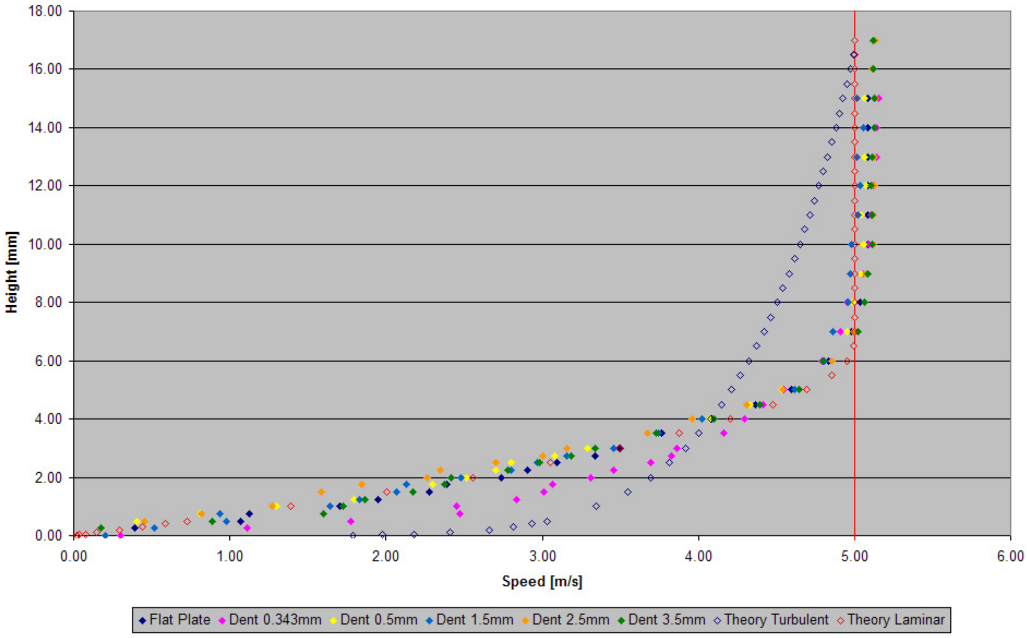

Figure G.8: Velocity profiles of the flow in between the dents; pattern 1, free-stream velocity is 5m/s.

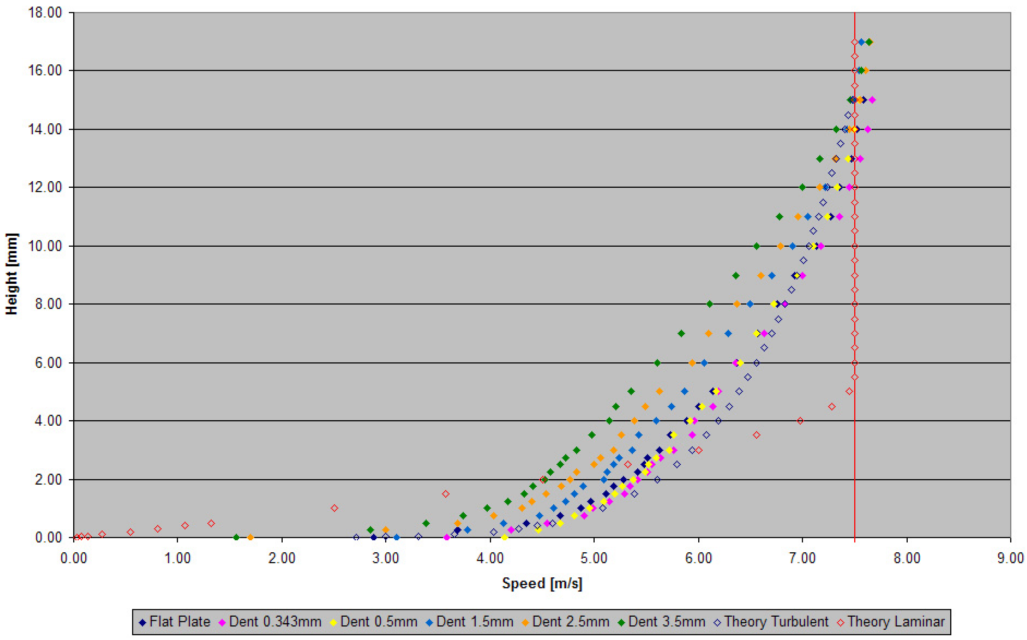

Figure G.9: Velocity profiles of the flow in between the dents; pattern 1, free-stream velocity is 7.5m/s.

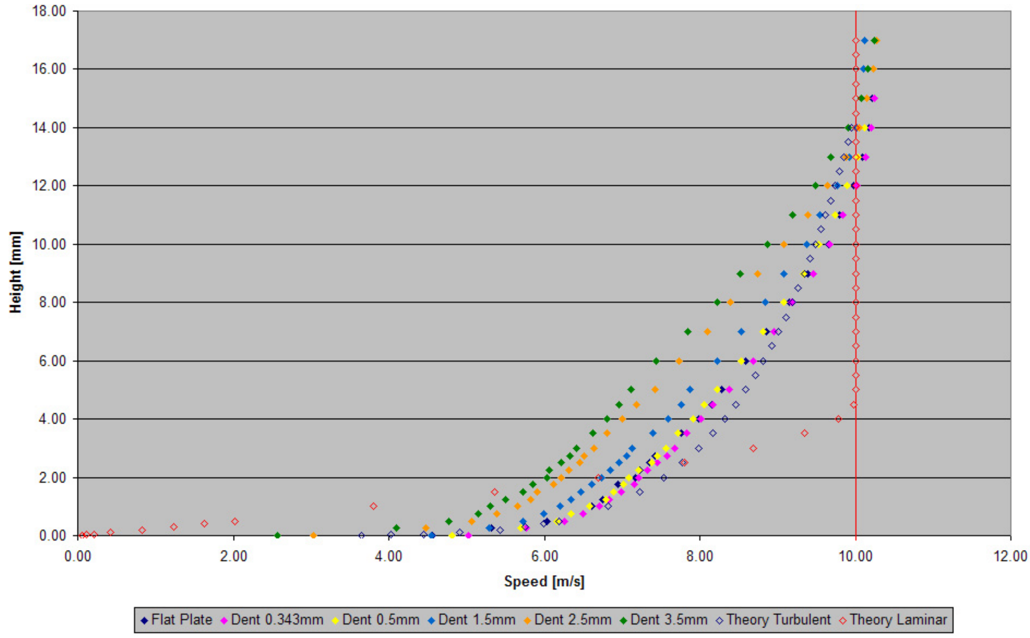

Figure G.10: Velocity profiles of the flow in between the dents; pattern 1, free-stream velocity is 10m/s.

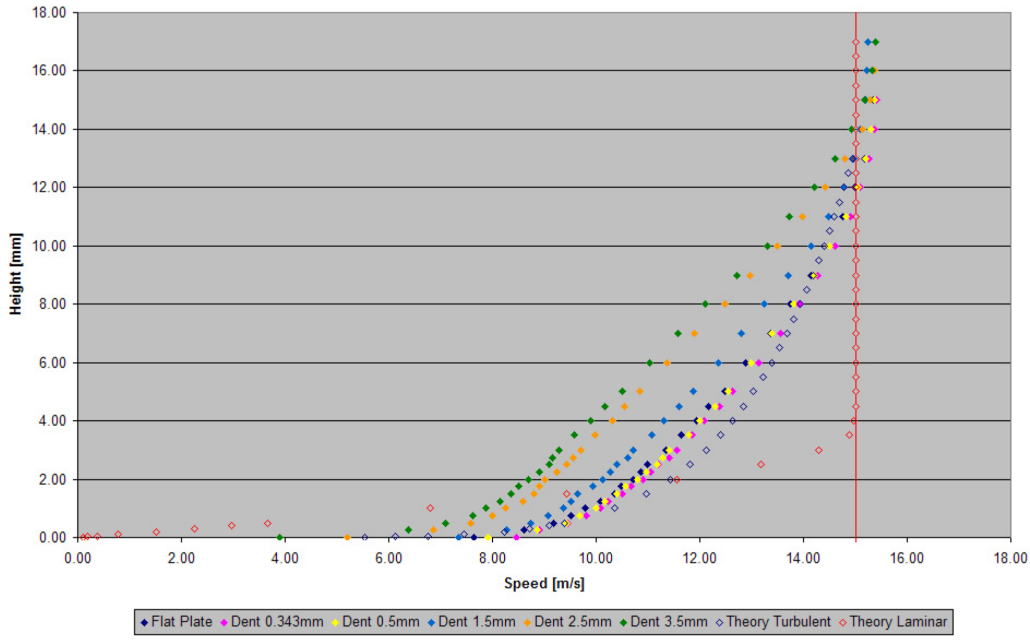

Figure G.11: Velocity profiles of the flow in between the dents; pattern 1, free-stream velocity is 15m/s.

G.3 Drag Force Figures for all five dents tested; Pattern 2.

Here the drag forces are presented for all five plates measured for pattern 2.

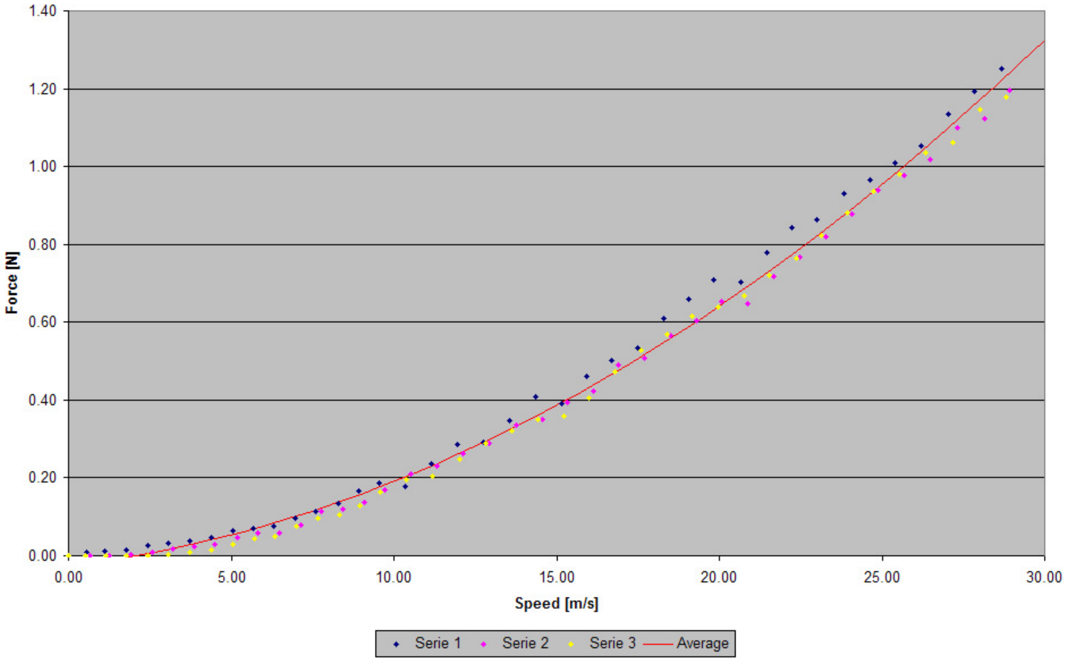

Figure G.12: Drag force, data for test 7: Flat Plate.

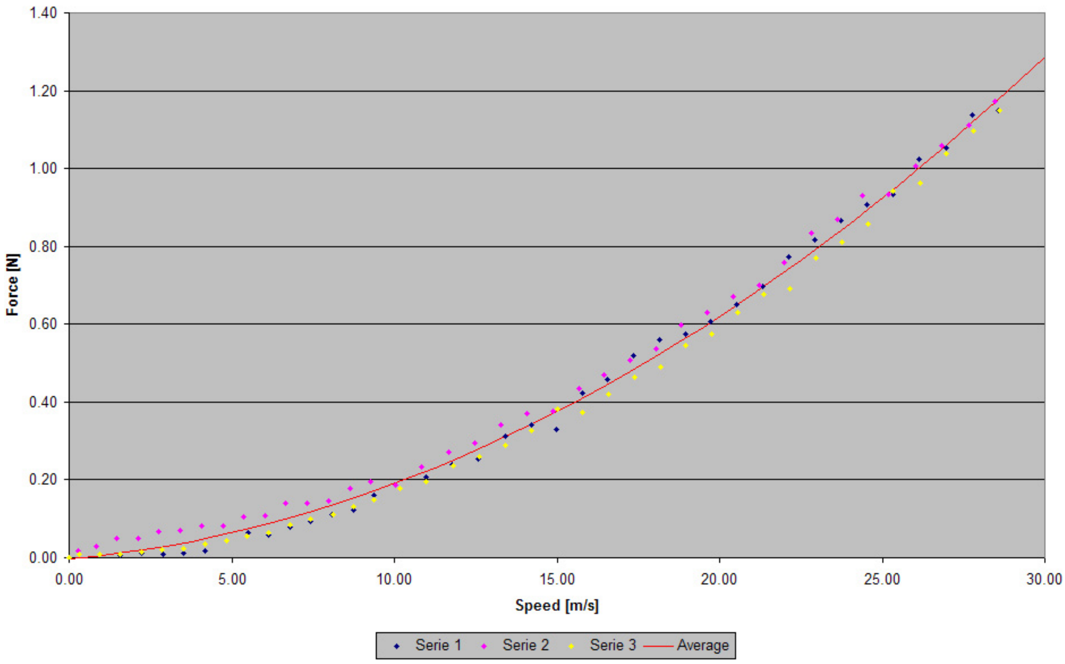

Figure G.13: Drag force, data for test 8: Dent 0.343mm.

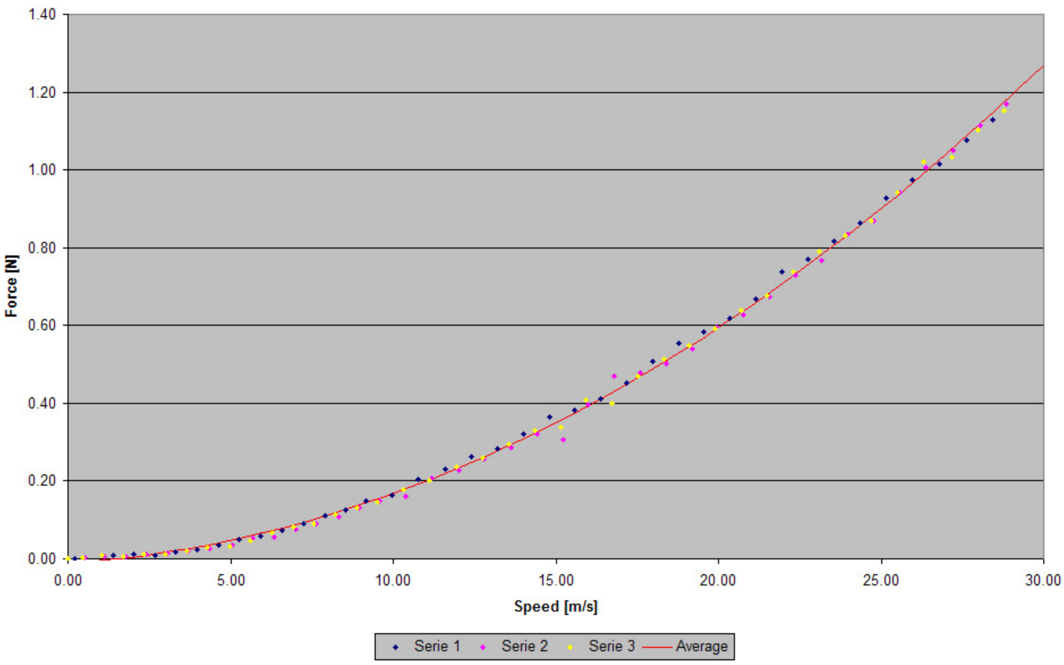

Figure G.14: Drag force, data for test 9: Dent 0.5mm.

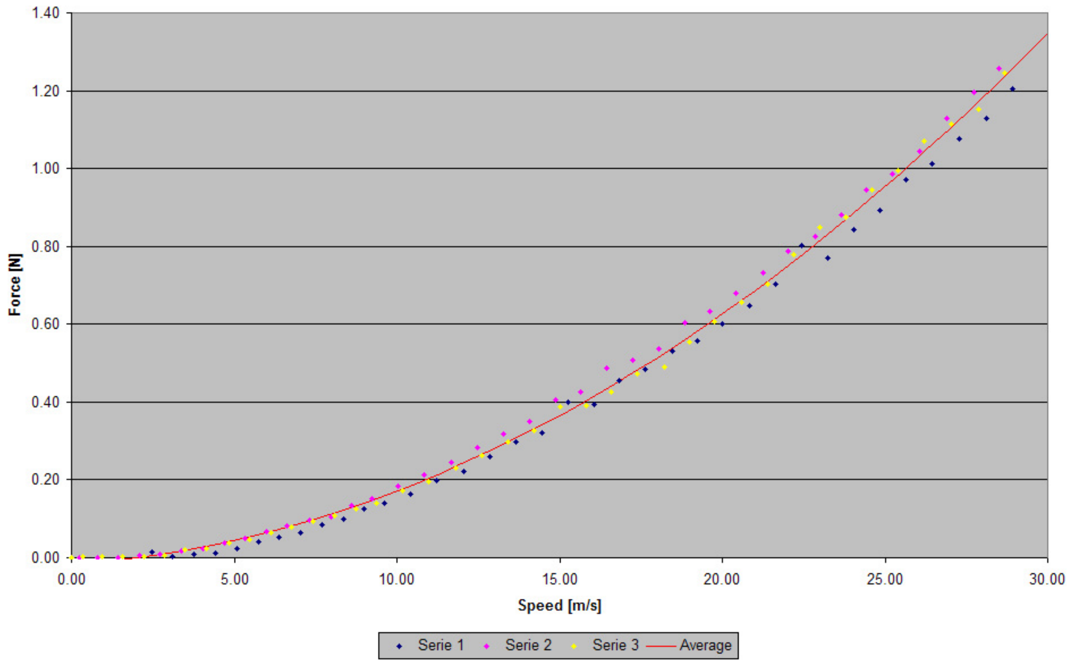

Figure G.15: Drag force, data for test 10: Dent 1.5mm.

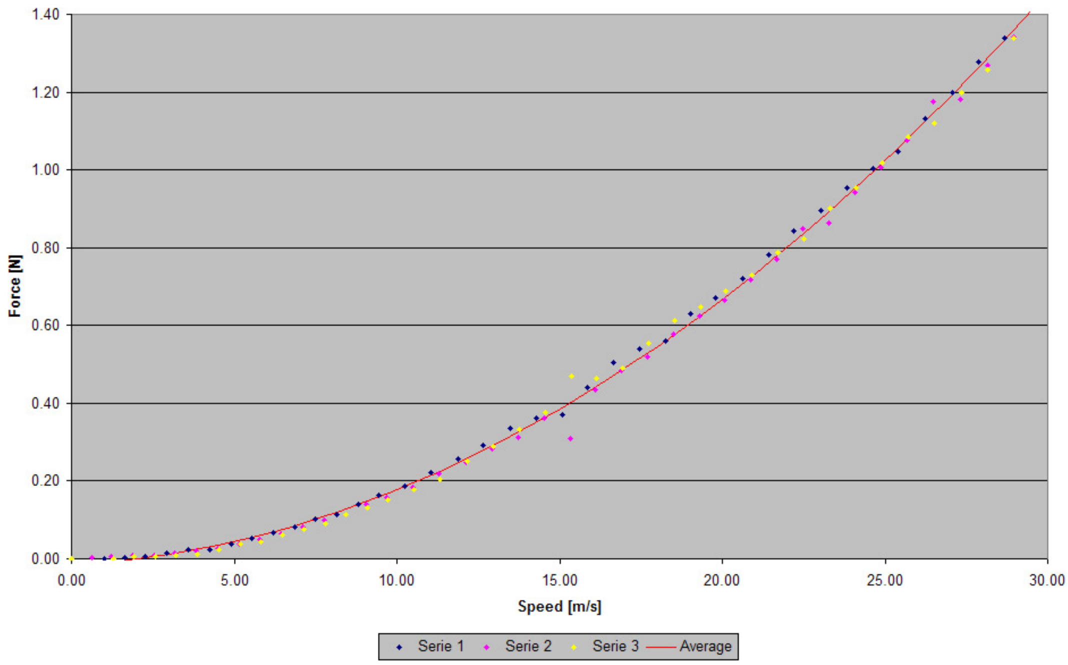

Figure G.16: Drag force, data for test 11: Dent 2.5mm.

G.4 Velocity Profiles for Pattern 2.

Here the velocity profiles are presented for all five velocities measured: 3.0m/s, 5.0m/s, 7.5m/s, 10.0m/s and 15m/s.

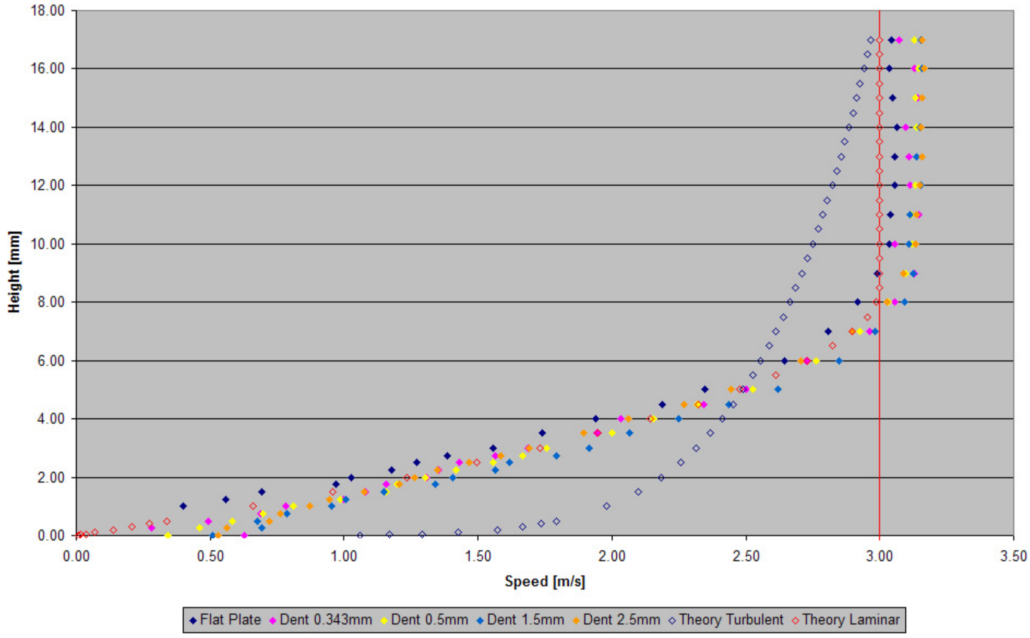

Figure G.17: Velocity profiles of the flow in between the dents; pattern 2,free-stream velocity is 3m/s.

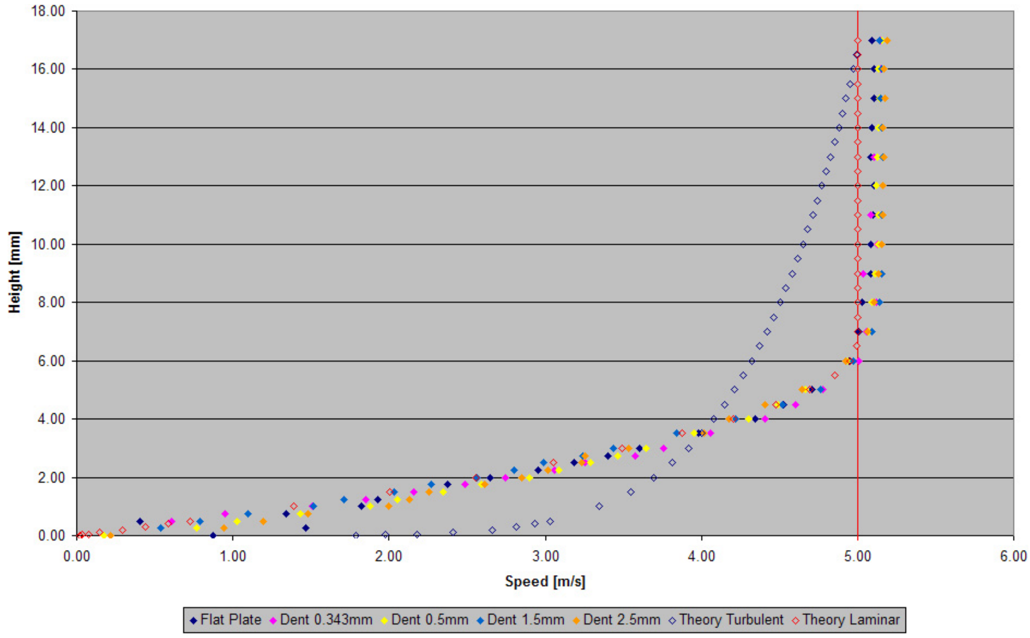

Figure G.18: Velocity profiles of the flow in between the dents; pattern 2,free-stream velocity is 5m/s.

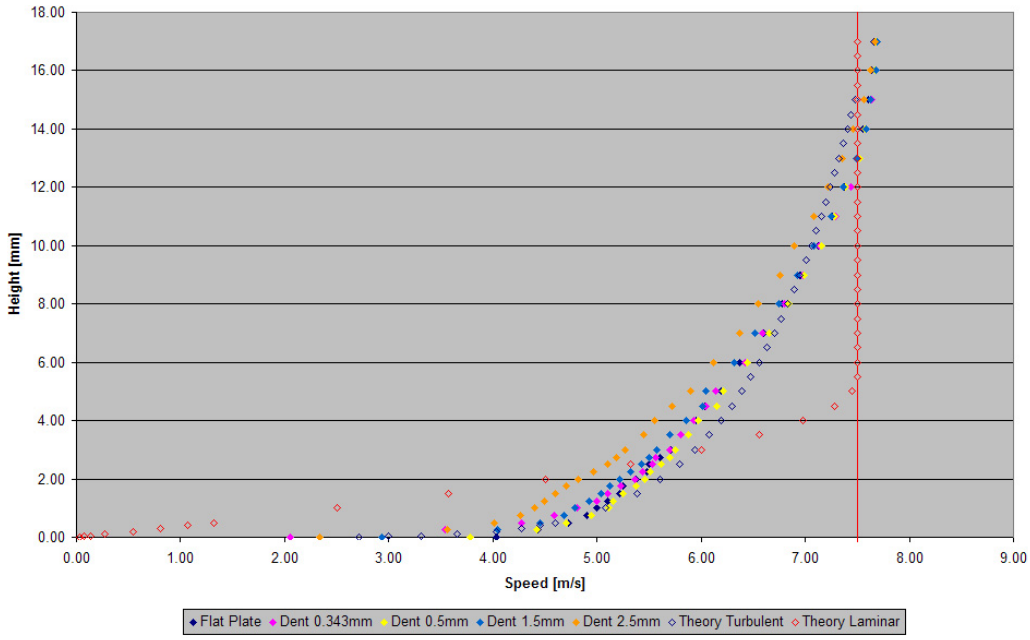

Figure G.19: Velocity profiles of the flow in between the dents; pattern 2,free-stream velocity is 7.5m/s.

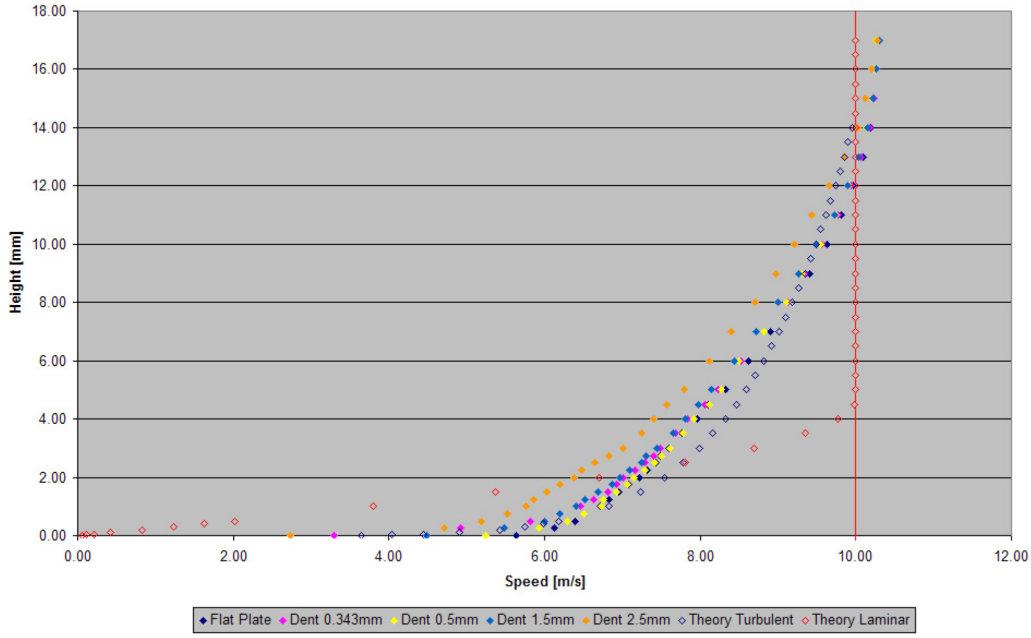

Figure G.20: Velocity profiles of the flow in between the dents; pattern 2,free-stream velocity is 10m/s.

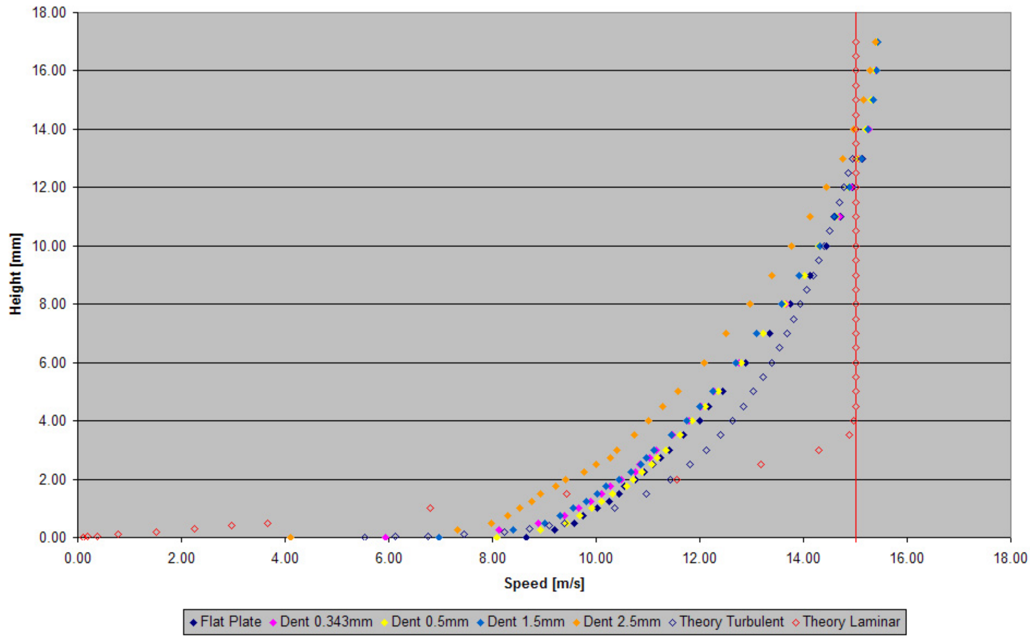

Figure G.21: Velocity profiles of the flow in between the dents; pattern 2,free-stream velocity is 15m/s.